Surviving Quantum Chaos: Weak Thermalization, Prethermalization and Quantum Many-Body Scar States

Thesis by

Cheng-Ju Lin

In Partial Fulfillment of the Requirements for the
Degree of
Doctor of Philosophy in Physics

Caltech

CALIFORNIA INSTITUTE OF TECHNOLOGY
Pasadena, California

2019
Defended May 22, 2019

ACKNOWLEDGEMENTS

I am deeply grateful for the guidance, inspirations and supports I received from my thesis advisor, Professor Olexei I. Motrunich. Lesik has always been patient, dedicated and supportive to my research. He never felt too tedious to explain physics or calculation details to me when I have questions. He let me pursue different research topics and problems freely. He also shared my excitements when we found interesting problems or when we had some breakthroughs in my research. His warm and kind attitude to his students and his insightful and constructive advice on his students' research are things that a student cannot ask for more.

I thank my friends who have made my life in Caltech a fun journey, especially Christopher White, Brenden Roberts, Alex Turzillo, Zack Erickson and Marcus Teague. I also thank my loving family for their supports.

Finally, I would like to thank the people who fought for freedom and human rights, for they made it possible for me to have the privilege to do science in this world.

ABSTRACT

Quantum chaos and the eigenstate thermalization hypothesis are based on the assumption of the validity of random matrix theory description on the spectrum and eigenstates. They provide the foundation and descriptions for the typical dynamics and thermalization in generic closed quantum systems. In this thesis, we investigate situations where the systems show atypical dynamics or anomalous thermalization, conflicting with the usual expectations from quantum chaos and eigenstate thermalization hypothesis.

We first examine *weak thermalization* in a nonintegrable spin chain. The system shows long-lived strong oscillations and relaxes to the thermal equilibrium weakly. We identify the dynamics describable by quasiparticles and recognize the oscillation frequency to be the quasiparticle mass gap. We also estimate the damping time for the oscillations.

Next, we study *prethermalization*, a phenomenon where a system relaxes to an intermediate almost-equilibrium stage before reaching the true thermal equilibrium. We study a nonintegrable spin chain in the strong coupling limit, where an almost-conserved quantity emerges and gives rise to the prethermalization.

We also study a newly proposed diagnostic for quantum chaos: *out-of-time-ordered correlators*. Contrasting to the chaotic systems, we inspect their behaviors in various noninteracting integrable models.

Finally, we dig into the *quantum many-body scar states* in the PXP model which describes a Rydberg atom chain. These special states do not satisfy the random matrix theory description nor the eigenstate thermalization hypothesis, therefore defying quantum chaos.

PUBLISHED CONTENT AND CONTRIBUTIONS

[1] C.-J. Lin, and O. I. Motrunich, “Exact Quantum Many-Body Scar States in the Rydberg-Blockaded Atom Chain”, Phys. Rev. Lett. **122**, 173401 (2019), DOI: 10.1103/PhysRevLett.122.173401; C.-J. L. is the main contributor in the project and in the writing of the manuscript.

[2] C.-J. Lin, and O. I. Motrunich, “Out-of-time-ordered correlators in a quantum Ising chain”, Phys. Rev. B **97**, 144304 (2018),
DOI: 10.1103/PhysRevB.97.144304; C.-J. L. is the main contributor in the project and in the writing of the manuscript.

[3] C.-J. Lin, and O. I. Motrunich, “Out-of-time-ordered correlators in short-range and long-range hard-core boson models and in the Luttinger-liquid model”, Phys. Rev. B **98**, 134305 (2018),
DOI: 10.1103/PhysRevB.98.134305; C.-J. L. is the main contributor in the project and in the writing of the manuscript.

[4] C.-J. Lin, and O. I. Motrunich, “Explicit construction of quasiconserved local operator of translationally invariant nonintegrable quantum spin chain in prethermalization”, Phys. Rev. B **96**, 214301 (2017),
DOI: 10.1103/PhysRevB.96.214301; C.-J. L. is the main contributor in the project and in the writing of the manuscript.

[5] C.-J. Lin, and O. I. Motrunich, “Quasiparticle Explanation of the Weak-Thermalization Regime under Quench in a Nonintegrable Quantum Spin Chain”, Phys. Rev. A **95**, 023621 (2017),
DOI: 10.1103/PhysRevA.95.023621; C.-J. L. is the main contributor in the project and in the writing of the manuscript.

TABLE OF CONTENTS

Chapter 1

INTRODUCTION

From quantum chaos to the eigenstate thermalization hypothesis

"It has been said something as small as the flutter of a butterfly's wing can ultimately cause a typhoon halfway around the world." Though not entirely scientifically correct, thanks to the movie *The Butterfly Effect (2004)*, such a phenomenon has become a widely-known signature of classical chaos. More specifically, the butterfly effect refers to the statement that a small perturbation in the initial condition will result in an exponential divergence of the trajectory in the phase space:

$$\frac{\partial q(t)}{\partial q(0)} = \{q(t), p\}_{\text{P.B.}} \sim e^{\lambda_L t} \,, \tag{1.1}$$

where q denotes the generalized coordinate of a classical dynamical system, p is the corresponding conjugate momentum, $\{A, B\}_{\text{P.B.}}$ is the Poisson bracket, and λ_L is the Lyapunov exponent, which quantifies the rate of the exponential divergence. Other characterizations of classical chaos such as *mixing* and *ergodicity* provide mathematical justifications for the statistical mechanics, which is perhaps the most ubiquitous and successful physics framework.

While chaos is mathematically well-established in classical dynamics, can it be defined in quantum systems? On the one hand, an important ingredient for chaos in the classical system is the nonlinearity in the equation of motions. On the other hand, dynamics in quantum systems is entirely governed by the Schrödinger equation, which is linear! If there is no chaos in the quantum system, how can statistical mechanics emerge from quantum systems? Moreover, if one starts from some pure initial state, under a closed quantum dynamics, how is it possible that a unitary evolution takes a pure state into a thermal ensemble, which is a mixed state?

In fact, in the quantum mechanics, so far there is no unique definition of quantum chaos. One therefore can have different definitions of quantum chaos, provided they have some meaningful connections to the classical chaos or some intriguing concepts.

One important advance regarding the concept of quantum chaos is pioneered by Eugene Wigner. In a conference at the Oak Ridge National Laboratory in 1957, Wigner wrote down his surmise (guess) for the level-spacing distribution for the spectrum in a nucleus. Such distribution, in a more general form, is the famous Wigner-Dyson distribution

$$p(s) = As^{\beta} \exp(-Bs^2)\,, \tag{1.2}$$

where β, A, and B are constants depending on the type of the “ensemble", and s is the “unfolded" energy level-spacing, meaning the spectrum has been transformed such that the density of levels is unity. For example, $\beta = 1$ for systems with time-reversal symmetry, which guarantees that one can choose a basis such that the Hamiltonian is real-valued. On the other hand, we have $\beta = 2$ for systems without time-reversal symmetry. This surmise is based on the postulate that, in a complicated enough nuclear system, the spectrum will be given as if it is from a random matrix. Based on this random matrix assumption, there are also different properties of spectrum statistics one can derive and compare with the experiment data. (We refer the readers to Ref. [1] for more in depth discussions regarding the random matrix theory.) Later, Bohigas, Giannoni, and Schmit conjectured that for Hamiltonians whose semiclassical counterparts are chaotic, their level-spacing follows the Wigner-Dyson distribution, which is the famous BGS conjecture. On the other hand, it was conjectured that if the Hamiltonian has an integrable classical correspondence, its level-spacing statistics will follow Poisson distribution

$$p(s) = \exp(-s)\,, \tag{1.3}$$

which is called the Berry-Tabor conjecture. As more and more systems have been verified to obey such expectations, Wigner-Dyson level-spacing statistics have become a canonical diagnostic and even the definition for quantum chaos, even when the Hamiltonian does not have a classical counterpart. It is worth mentioning that, under the random matrix theory description, one can also understand the eigenstates, which essentially look like random vectors in the Hilbert space. This also predicts the bipartite entanglement entropy of the eigenstates to scale as the volume law.

Based on the random matrix theory assumption, Srednicki proposed a groundbreaking concept [2], now called the *eigenstate thermalization hypothesis* (ETH). Conceptually, the hypothesis essentially states that closed quantum systems thermalize at the level of individual eigenstates. Mathematically, it predicts the behavior of the eigenstates in a generic chaotic system, generalized from the random matrix theory: for any local observable $\hat{O}$, we have

$$O_{mn} \equiv \langle m|\hat{O}|n\rangle = O(\bar{E})\delta_{mn} + e^{-S(\bar{E})/2} f_O(\bar{E}, \omega) R_{mn}\,, \tag{1.4}$$

where $|m\rangle$ and $|n\rangle$ are the eigenstates with energies E_m and E_n, $\bar{E} = (E_m + E_n)/2$, $\omega = E_n - E_m$, $S(E)$ is the thermodynamic entropy at energy E, and R_{mn} is a random number with zero mean and unit variance. Most importantly, $O(\bar{E})$ and $f_O(\bar{E}, \omega)$ are smooth functions of their arguments. The diagonal-matrix-element part of the hypothesis is sometimes referred to as *diagonal* ETH or simply ETH, while the off-diagonal-matrix-element part is referred as *off-diagonal* ETH. Several numerical works have verified ETH in various many-body systems, and it has become a general belief that eigenstate thermalization is the mechanism which gives rise to the statistical mechanics in quantum systems.

Let us examine some consequences of this hypothesis. Imagine starting with a pure initial state $|\psi\rangle$, evolving under the closed quantum Hamiltonian dynamics $|\psi(t)\rangle \equiv e^{-iHt}|\psi\rangle$. We can write the expectation value of any observable $\hat{O}$ as a function of time as (in units $\hbar = 1$)

$$\langle O\rangle(t) \equiv \langle\psi|e^{iHt}Oe^{-iHt}|\psi\rangle = \sum_m |C_m|^2 O_{mm} + \sum_{m,n\neq m} C_m^* C_n e^{i(E_m-E_n)t} O_{mn}\,, \tag{1.5}$$

where $C_m = \langle m|\psi\rangle$ is the coefficient of the initial state expanded in the energy eigenbasis $|m\rangle$, $H|m\rangle = E_m|m\rangle$. Note that the time dependence is only coming from the off-diagonal matrix elements among the energy eigenstates $O_{m\neq n}$. While the details of the relaxation process depend on the observable and the Hamiltonian, let us assume for a moment that the off-diagonal part decoheres in the long-time. We therefore have, in the long time,

$$\langle O\rangle(t) \approx \sum_m |C_m|^2 O_{mm} = \mathrm{Tr}[\rho_D \hat{O}]\,, \tag{1.6}$$

where $\rho_D \equiv \sum_m |C_m|^2 |m\rangle\langle m|$ is called the diagonal ensemble. Typically, for physical initial states, $|C_m|^2$ will peak at some energy density with convergent energy fluctuation: $\sigma_H^2 \equiv \langle\psi|H^2|\psi\rangle - \langle\psi|H|\psi\rangle^2 \sim O(V)$ and therefore $\sigma_H/V \to 0$ in the thermodynamic limit $V \to \infty$.

The magic from the ETH is that, since O_{mm} is a smooth function depending on the energy, we have

$$\mathrm{Tr}[\rho_D \hat{O}] \approx \mathrm{Tr}[\rho_{\mathrm{MC}} \hat{O}] \approx \mathrm{Tr}[\rho_{\mathrm{Gibbs}} \hat{O}]\,, \tag{1.7}$$

where $\rho_{\mathrm{MC}} = \frac{1}{N}\sum_{m:E_m\in[E-\Delta,E+\Delta]} |m\rangle\langle m|$ is the microcanonical ensemble and $\rho_{\mathrm{Gibbs}} = \frac{1}{Z}\sum_m e^{-\beta E_m}|m\rangle\langle m|$ is the canonical (Gibbs) ensemble. Therefore, statistical mechanics is recovered, meaning the long-time expectation values equal to the thermal values. In fact, any ensemble with the right mean energy and convergent energy fluctuation will give good description for local observables in the thermodynamic limit.

We can also see that the diagonal ensemble depends on the choice of the initial state. If we want *all* initial states to thermalize, then we will need to require that *all* the eigenstates satisfy ETH. One way to see this is to consider an extreme case, where the initial state is an eigenstate. Then for this initial state to thermalize, this eigenstate has to satisfy ETH. This requirement is also called the *strong* ETH, which has been numerically verified in various models [3, 4]. In contrast, the *weak* ETH can allow a vanishing fraction of the eigenstates to not satisfy ETH.

Another important feature about ETH is that it predicts the thermalization in the strong sense (*strong thermalization*), meaning the expectation value is equal to the thermal value at *almost all times*, without needing long-time averaging. On the other hand, in the classical systems, we only expect the thermalization in the weak sense (*weak thermalization*), meaning we only need the long-time average of the expectation values to be equal to the thermal values. Apparently, with only diagonal ETH, weak thermalization holds, since

$$\bar{O} \equiv \lim_{t_0 \to \infty} \frac{1}{t_0} \int_0^{t_0} O(t) = \mathrm{Tr}[\rho_D \hat{O}]\,, \tag{1.8}$$

and the diagonal ETH ensures it to be equal to the thermal value. In fact, conditions on weak thermalization in quantum systems have been discussed by von Neumann. On the other hand, if we also assume off-diagonal ETH, then we have the long-time average of the temporal fluctuation

$$\begin{aligned} &\lim_{t_0 \to \infty} \frac{1}{t_0} \int_0^{t_0} [O(t) - \bar{O}]^2 = \sum_{m,n \neq m} |C_m|^2 |C_n|^2 |O_{mn}|^2 \\ &\leq \max |O_{mn}|^2 \sum_{m,n} |C_m|^2 |C_n|^2 \leq \max |O_{mn}|^2 \propto \exp[-S(\bar{E})]\,, \end{aligned} \tag{1.9}$$

which typically decreases exponentially in system sizes since the density of states $\exp[S(\bar{E})]$ increases exponentially in system sizes at a finite energy density. This in fact implies that, at almost all times, $O(t) = \bar{O}$. From this perspective, ETH provides an even stronger description for the thermalization of a generic closed quantum system. For further reviews on ETH, we refer the reader to Ref. [5].

Having seen what we would expect in the generic chaotic and thermalizing systems, in this thesis, we will explore aspects where some systems show anomalous dynamics or thermalizations which at some level do not seem to be consistent with the ETH while the level-spacing statistics shows the Wigner-Dyson distribution. Furthermore, we will also study a newly proposed diagonostic of quantum chaos — out-of-time-ordered correlators. We will study thier behaviors in several noninteracting integrable models, as a contrast to their behaciors in other chaotic models. In the rest of the introduction, I will give brief descriptions and summaries of the phenomena and the problems addressed and studied in this thesis. More detailed settings and introductions regarding the specific problems will be given in the beginning of each chapter.

Weak Thermalization - Chapter 2

In a seminal paper [6], Bañuls, Hastings, and Cirac used infinite-time-evolved block decimation (iTEBD) method to simulate a quench dynamics in an infinite-sized nonintegrable one-dimensional spin chain, which is the quantum Ising model with a longitudinal field. While the level-spacing statistics of the Hamiltonian shows the Wigner-Dyson distribution, its quench dynamics can show drastically different behaviors depending on the initial states. In particular, when one prepares the initial state as all spins pointing in the y-direction, the dynamics shows expected fast relaxation to the thermal values — the strong thermalization behavior as expected from ETH. (See also Fig. 1.1(a).) However, if one prepares the initial state as all spins pointing in the z-direction, the dynamics shows strong oscillations without relaxing up to the time that can be reliably numerically calculated. It appears that only the time-averaged values approach thermal values slowly — the behavior of weak thermalization. Finally, when the initial state is all spins pointing in the x-direction, the dynamics seems to not relax, or relax to a nonthermal value, a regime called non-thermalization.

Surprisingly, in the weak thermalization region, using exact diagonalization (ED), we are able to reproduce the iTEBD result of the quench dynamics up to a significant portion of the time span. We therefore can try to understand such anomalous dynamics based on the ED data. We discovered that, in the weak thermalization region, the initial state in fact has a relative low (but nonzero) effective temperature. Namely, the initial state has high overlaps with the bottom part of the spectrum. Using the ED spectrum, together with the perturbation theory, we can understand the bottom part of the spectrum as quasiparticles, and the oscillation frequency observed can be understood as the quasiparticle mass gap. We conjecture this description to be valid even in the thermodynamic limit, and hence also the observed dynamics in the iTEBD calculation. Finally, we discuss some possible fates of the oscillation,

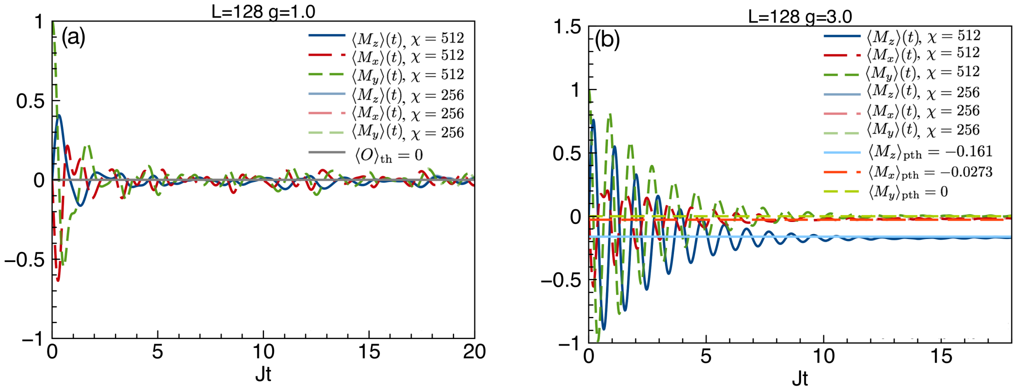

Figure 1.1: (a) A typical strong thermalization behavior in a chaotic system. Here we use a spin-chain dynamics as an example. The magnetizations relax to the thermal values in a short time. (b) Prethermalization in a spin chain. The magnetizations relax to an intermediate almost equilibrium stage instead of the thermal equilibrium. The intermediate almost equilibrium stage is described by the generalized Gibb's ensemble.

and give some estimation of the decay-time of the oscillations based on one possible mechanism: the hard-core repulsion of the quasiparticles.

Prethermalization - Chapter 3

Prethermalization, a term first introduced by Berges et. al. [7], refers to a phenomenon where a system first relaxes to an intermediate almost-equilibrium stage before it reaches the true thermal equilibrium. There are several mechanisms that can make the system show prethermalization, most notably due to the proximity to the integrable point. In this thesis, we will examine prethermalization due to the presence of some emergent almost-conserved quantity coming from some strong coupling limit. Because of the existence of such almost-conserved quantity, one can expect that the relaxation of this quantity will take parametrically longer time than other quantities, resulting in an intermediate almost equilibrium stage. In Fig. 1.1(b), we show an example of the prethermalization in a spin chain, where the magnetization of the system relaxes to an intermediate almost-equilibrium stage which is not described by Gibb's ensemble.

We examine the quantum Ising model with a longitudinal field, which has an approximate spin conservation law at the strong field region. We first use the "slowest operator formalism" [8] to numerically and systematically find the almost-conserved local operator. We then also use perturbation theory to construct the almost-conserved operator and compare it to the numerical finding. The high fidelity between the two results suggests that the numerical finding of the almost-conserved quantity can indeed be understood as the perturbative construction, which can be understood as a “dressed" total spin operator. We also verify that the system does relax to an intermediate almost-equilibrium stage, where the system can be described by the generalized Gibb’s ensemble including this almost-conserved quantity. Finally, we give some mathematical statements regarding the bounds on the perturbation theory and the thermalization time scale.

Out-of-time-ordered commutators/correlators - Chapter 4

While the level-spacing statistics focus on the properties of the spectrum, a new diagnostic has recently emerged as a different diagnostic for quantum chaos: out-of-time-ordered commutators (OTOCs). OTOCs are defined as the following: for operators $W_x(t)$ and $V_y(0)$ sitting on positions x and y and at times t and 0 respectively, we consider

$$C_{WV}(x-y,t) \equiv \langle |[W_x(t), V_y(0)]|^2 \rangle \,, \tag{1.10}$$

where $\langle X \rangle \equiv \mathrm{Tr}[\rho X]$ is the expectation value with respect to some ensemble ρ and we have assumed the translation invariance. If we expand C_{WV}, we have

$$\begin{aligned} C_{WV}(x-y,t) =& \langle V_y^\dagger(0) W_x^\dagger(t) W_x(t) V_y(0) \rangle + \langle W_x^\dagger(t) V_y^\dagger(0) V_y(0) W_x(t) \rangle \\ & - \langle V_y^\dagger(0) W_x^\dagger(t) V_y(0) W_x(t) \rangle - \langle W_x^\dagger(t) V_y^\dagger(0) W_x(t) V_y(0) \rangle \,. \end{aligned} \tag{1.11}$$

Note the last two terms have anomalous time ordering and are therefore also called *out-of-time-ordered correlators* (OTOCs).[1] Such quantities were first examined by Larkin and Ovchinnikov [9]. They recently attracted a great deal of attention due to Kitaev’s study of the blackhole information paradox [10].

As mentioned, one of the motivations to study such quantities is as a diagnostic for the butterfly effect in a quantum system at the initial or intermediate time scale. Recall that, in Eq. (1.1), in order to detect the divergence of the trajectory under some initial perturbation, we need to calculate $\{q(t), p\}_{\mathrm{P.B.}}$. A natural generalization from canonical quantization is by promoting the Poisson bracket to the commutator, obtaining $C(t) = \langle |[\hat{x}(t), \hat{p}]|^2 \rangle \sim e^{2\lambda_{\mathrm{L}} t}$, where using $|A|^2 \equiv A^\dagger A$ removes the effect of phase cancellations when averaging.

OTOCs can also be used to detect *information scrambling* — a process where the quantum information becomes delocalized, and also as a characterization of

---

[1] Here we use the abbreviation OTOC for both out-of-time-ordered commutator and out-of-time-ordered correlator. It should be clear from the context which we are referring to. When there is a possible confusion, we will use the specific name or notation.

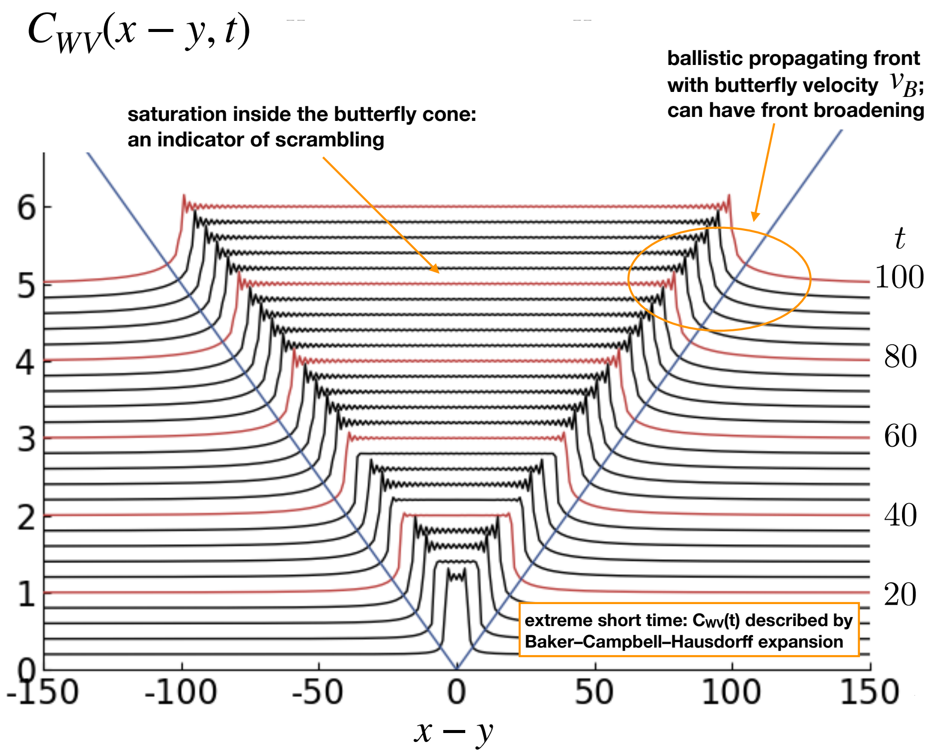

Figure 1.2: An illustration of the behavior of $C_{WV}(x-y,t)$ in a one-dimensional spin system. $C_{WV}(x-y,t)$ spreads with the butterfly velocity v_B, while the front can broaden with time. At extremely short time, $C_{WV}(x-y,t)$ is described by the Baker-Campbell-Hausdorff expansion. The behavior inside the butterfly cone is an indicator for scrambling.

the instability of the so-called thermal field double state. One signature of the scrambling is in fact the saturation or blow-up of $C_{WV}(t)$ (or equivalently, small values of the out-of-time-ordered correlators).

In many-body systems, OTOCs also quantify operator spreading or operator growth. Consider more concretely a spin-$\frac{1}{2}$ system, exapnding the time-evolved operator $W_x(t) = \sum_S a_S(t)S$ in the Heisenberg picture, where S runs over all Pauli-string operators (e.g., $\ldots\sigma_j^z\sigma_{j+1}^x\ldots$). Then V_y serves as a “probe" in Eq. (1.10) to detect how much $W_x(t)$ is not commuting with V_y, therefore profiling a kind of the “shape" of the operator $W_x(t)$.

Initially, when $t \ll |x-y|$, we expect that $W_x(t)$ and V_y almost commute, hence the small $C_{WV}(x-y,t)$. At extremely short time, we can expand $W_x(t)$ via Hausdorff-

Baker-Campbell (HBC) formula

$$W_x(t) = \sum_{n=0}^{\infty} \frac{t^n}{n!} L^n(W_x)\,, \tag{1.12}$$

where $L(W_x) \equiv i[H, W_x]$. The leading short-time behavior is therefore coming from the first nontrivial n such that $[V_y, L^n(W_x)] \neq 0$, which is a pure quantum mechanical effect. Typically, the operator $W_x(t)$ will spread with a ballistic front, with a characteristic speed v_B called the *butterfly velocity*. Around the operator front, $|x-y|/t \sim v_B$, $C_{WV}(x-y,t)$ grows dramatically from some small value to some $O(1)$ value if the operators have bounded spectrum. A manifestation of quantum chaos or quantum butterfly effect is the exponential growth form of $C_{WV}(x-y,t) \sim \exp(-\lambda_L t)$ with fixed $x-y$. On the other hand, recent works have proposed a more universal description for the asymptotic behavior around the front:

$$C(x-y,t) \sim \exp\left[-c\frac{(|x-y|-v_B t)^{1+p}}{t^p}\right] \tag{1.13}$$

from Ref. [11]. Alternatively, if one considers the long-time behavior of $C_{WV}(x,y,t)$ on fixed “rays" $v = \frac{|x-y|}{t}$, one can describe

$$C_{WV}(x-y=vt,t) \sim \exp[-\lambda(v)t]\,, \tag{1.14}$$

where $\lambda(v)$ is dubbed *velocity-dependent Lyapunov exponent* from Ref. [12]. If these two regions connect smoothly, we have $\lambda(v) \sim c(v-v_B)^{1+p}$. The exponent p describes the wavefront broadening as $\sim t^{p/(1+p)}$. Note that it is only when $p = 0$, we have the true position independent exponential growing of $C_{WV}(x,y,t)$, and one can define Lyapunov exponent in this case through OTOCs.

In this thesis, we will examine the behaviors of OTOCs in various one-dimensional integrable spin models which can be mapped to noninteracting fermions, including the quantum Ising model, hard-core boson models, and Luttinger liquid. As we will see, in the short-range models, noninteracting models give $t^{\frac{1}{3}}$ wavefront broadening behavior. However, one can get different wavefront behavior by engineering the quasiparticle dispersion. Finally, we will see that the saturation or non-saturation of $C_{WV}(x-y,t)$ behind the operator front in the studied models depends on the choices of the operators.

Quantum many-body scar states - Chapter 5

Under the assumption of random matrix theory, the Wigner-Dyson distribution is a sharp indicator of quantum chaos. Moreover, the wavefunctions will look essentially “random", and are expected to satisfy ETH if it is a many-body system. However, in some systems, there can be some very special wavefunctions at highly excited energies which do not satisfy the random matrix theory description, while other states do. Such states are called *quantum scar states*.

A prototypical example of scar states in the single-particle quantum mechanics was discovered by Hellar [13] in the stadium billiard. It was shown that the level-spacing statistics of the highly excited states in this system obeys the Wigner-Dyson distribution. When one plots the amplitude of the wavefunctions, most of the states look ergodic, spreading all over the area. However, one can also find some special wavefunctions whose amplitudes are concentrated on some closed orbits in the corresponding classical mechanics. These special wavefunctions are examples of the single-particle scar states.

Can chaotic many-body systems also have scar states? Recently, several works identified some models which host such special non-chaotic or ETH-violating states, now called *quantum many-body scar states*. Examples including the bimagnon states in the Affleck-Kennedy-Lieb-Tasaki model [14, 15] and the η-paring states in the Hubbard model [16]. These states are highly excited states, i.e., having finite energy density, but exhibiting logarithmic bipartite entanglement scaling. Recall the typical random vectors in the Hilbert space have volume-law bipartite entanglement scaling. As a result, these states certainly do not satisfy the random matrix assumption nor ETH. A special construction proposed by Shirashi and Mori [17] describes a procedure to embed nonthermal states into a thermal spectrum.

The interests in scar states surges dramatically by the anomalous dynamics observed in a Rydberg atom experiment [18]. They observe that when one prepares the system with a charge-density-wave initial state, the quench dynamics shows strong oscillations. However, if the initial state is a uniform state, the dynamics shows typical thermalization behavior, despite the fact that it has the same energy density as the charge-density-wave state. It is subsequently pointed out in Refs. [19, 20] with strong numerical evidence that the quantum many-body scar states in the experimentally realized model (now called PXP model) are responsible for the dynamics. The level-spacing statistics of the PXP model show Wigner-Dyson distribution. However, in Fig. 1.3, we can see that there are some very special states having subthermal entanglement entropy scaling in this model, while the majority of the states have volume-law entanglement scaling.

In the very same model, we discover several quantum many-body states that can be

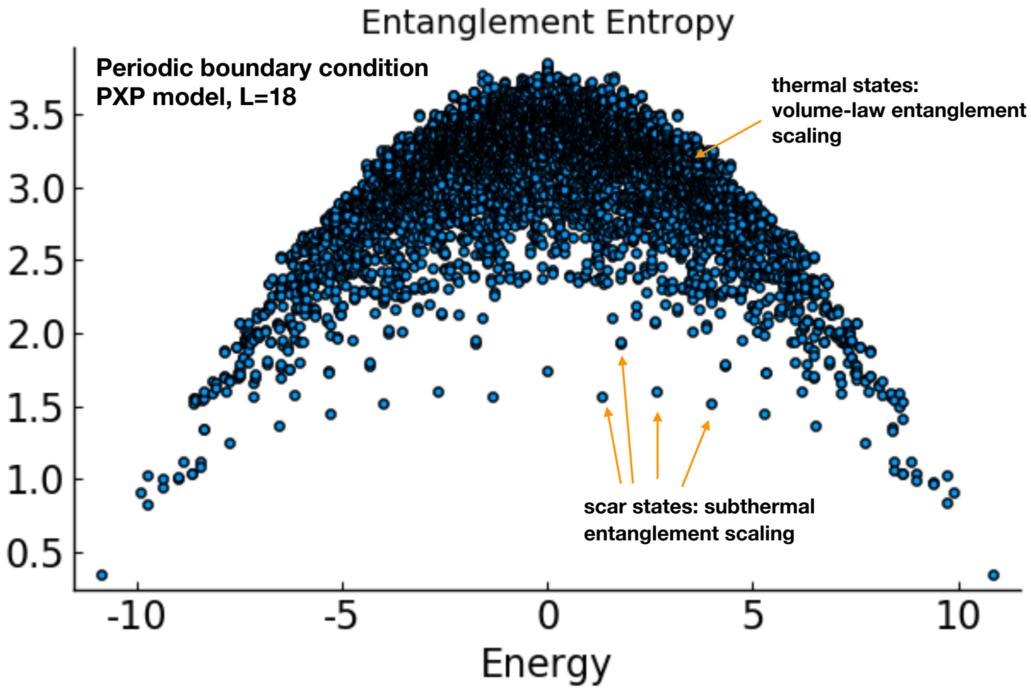

Figure 1.3: Bipartite entanglement entropy of the eigenstates in the PXP model in $L = 18$ and periodic boundary condition. While the majority of the states have high entanglement entropy and in fact volume-law scaling, there are some states have low and subthermal entanglement entropy.

expressed exactly using matrix product states. The existence of these wavefunctions therefore analytically confirms the violation of strong-ETH in this model and provide another example of exact quantum many-body scar states. The most intriguing property of these exact scar states is their translation-symmetry breaking character, which is never possible for a one-dimensional system in the finite temperature thermal ensembles. The translation symmetry breaking is identified by the *valence-bond solid* (VBS) order. Based on the exact scar states we discover, we also construct variational wavefunctions to capture other scar states discovered numerically. In particular, we propose other scar states can be essentially understood as quasiparticle scattering states.

References

[1] M. Mehta, *Random Matrices*, Pure and Applied Mathematics (Elsevier Science, 2004).

[2] M. Srednicki, “Chaos and quantum thermalization”, Phys. Rev. E **50**, 888–901 (1994).

[3] H. Kim, T. N. Ikeda, and D. A. Huse, “Testing whether all eigenstates obey the eigenstate thermalization hypothesis”, Phys. Rev. E **90**, 052105 (2014).

[4] J. R. Garrison, and T. Grover, “Does a Single Eigenstate Encode the Full Hamiltonian?”, Phys. Rev. X **8**, 021026 (2018).

[5] L. D’Alessio, Y. Kafri, A. Polkovnikov, and M. Rigol, “From quantum chaos and eigenstate thermalization to statistical mechanics and thermodynamics”, Adv. Phys. **65**, 239–362 (2016).

[6] M. C. Bañuls, J. I. Cirac, and M. B. Hastings, “Strong and Weak Thermalization of Infinite Nonintegrable Quantum Systems”, Phys. Rev. Lett. **106**, 050405 (2011).

[7] J. Berges, S. Borsányi, and C. Wetterich, “Prethermalization”, Phys. Rev. Lett. **93**, 142002 (2004).

[8] H. Kim, M. C. Bañuls, J. I. Cirac, M. B. Hastings, and D. A. Huse, “Slowest local operators in quantum spin chains”, Phys. Rev. E **92**, 012128 (2015).

[9] A. I. Larkin, and Y. N. Ovchinnikov, “Quasiclassical Method in the Theory of Superconductivity”, Sov. Phys. JETP **28**, 1200–1205 (1969).

[10] A. Kitaev, and S. J. Suh, “The Soft Mode in the Sachdev-Ye-Kitaev Model and Its Gravity Dual”, J. High Energ. Phys. **2018**, 183 (2018).

[11] S. Xu, and B. Swingle, “Accessing Scrambling Using Matrix Product Operators”, arXiv:1802.00801.

[12] V. Khemani, D. A. Huse, and A. Nahum, “Velocity-dependent lyapunov exponents in many-body quantum, semiclassical, and classical chaos”, Phys. Rev. B **98**, 144304 (2018).

[13] E. J. Heller, “Bound-State Eigenfunctions of Classically Chaotic Hamiltonian Systems: Scars of Periodic Orbits”, Phys. Rev. Lett. **53**, 1515–1518 (1984).

[14] S. Moudgalya, S. Rachel, B. A. Bernevig, and N. Regnault, “Exact excited states of nonintegrable models”, Phys. Rev. B **98**, 235155 (2018).

[15] S. Moudgalya, N. Regnault, and B. A. Bernevig, “Entanglement of exact excited states of Affleck-Kennedy-Lieb-Tasaki models: Exact results, many-body scars, and violation of the strong eigenstate thermalization hypothesis”, Phys. Rev. B **98**, 235156 (2018).

[16] O. Vafek, N. Regnault, and B. A. Bernevig, “Entanglement of Exact Excited Eigenstates of the Hubbard Model in Arbitrary Dimension”, SciPost Phys **3**, 043 (2017).

[17] N. Shiraishi, and T. Mori, “Systematic Construction of Counterexamples to the Eigenstate Thermalization Hypothesis”, Phys. Rev. Lett. **119**, 030601 (2017).

[18] H. Bernien, S. Schwartz, A. Keesling, H. Levine, A. Omran, H. Pichler, S. Choi, A. S. Zibrov, M. Endres, M. Greiner, V. Vuletić, and M. D. Lukin, "Probing many-body dynamics on a 51-atom quantum simulator", Nature **551**, 579–584 (2017).

[19] C. J. Turner, A. A. Michailidis, D. A. Abanin, M. Serbyn, and Z. Papić, "Weak ergodicity breaking from quantum many-body scars", Nat. Phys. **14**, 745–749 (2018).

[20] C. J. Turner, A. A. Michailidis, D. A. Abanin, M. Serbyn, and Z. Papić, "Quantum scarred eigenstates in a Rydberg atom chain: Entanglement, breakdown of thermalization, and stability to perturbations", Phys. Rev. B **98**, 155134 (2018).

Chapter 2

WEAK THERMALIZATION

Despite the widely held belief that a non-integrable model will generally thermalize, a seminal numerical work by Bañuls, Cirac, and Hastings [1] observed some unusual and interesting behaviors. The authors used an infinite-matrix-product-state (infinite-MPS) technique [2] to study the following quench problem. Starting from various initial product states, one measures local observables as a function of time evolving under a generic non-integrable quantum spin Hamiltonian

$$H = -J \sum_{j=1}^{L} \sigma_j^z \sigma_{j+1}^z - h \sum_{j=1}^{L} \sigma_j^z - g \sum_{j=1}^{L} \sigma_j^x \ . \tag{2.1}$$

For an initial state where all spins are pointing in the $\hat{y}$ direction, $|Y+\rangle$, the behavior is consistent with the conventional thermalization wisdom. However, there are some initial states that display apparently different behaviors. One type of behavior occurs for initial states with spins pointing close to the $\hat{z}$ direction, $|Z+\rangle$, where observables show strong oscillations without damping for the entire time where the numerical simulation is reliable; since the time-averaged observables apparently approach the thermal values, this behavior was called “weak thermalization.” A subsequent work [3] using an improved “hybrid algorithm” also found similar persistent oscillations starting from a different initial state $|X-\rangle$. On the other hand, another type of behavior occurs for initial states close to $|X+\rangle$, where a local observable σ_j^x apparently does not thermalize, also upon time-averaging.

In this chapter, we provide a simple quasiparticle explanation for the strong oscillation behavior observed in the “weak thermalization” case in Ref. [1]. We focus on the $|Z+\rangle$ initial state and argue that it is actually close to the ground state of the above Hamiltonian, and the oscillation frequency can be essentially understood as the quasiparticle energy above this ground state. This initial state has a finite energy density above the ground state and hence has a finite density of such quasiparticles. However, when the quasiparticle density is small, the quasiparticles are effectively weakly interacting, and the oscillations in the observables can persist to long times. Armed with this quasiparticle description of the origin of oscillations, we can then argue that the interactions among the quasiparticles will make the oscillations decay eventually.

The quasiparticle description developed here also leads us to consider the following quench problem, which is interesting on its own. We argue that the quench problem starting from $|Z+\rangle$ can be viewed approximately as a quench from a Bose-Einstein condensate (BEC) state evolving under a hard-core boson Hamiltonian. The observable of interest can be viewed as a BEC order parameter, which exhibits the strong oscillation.

In fact, the above quench setting is essentially close to a quench from a magnetically ordered state in the quantum Ising chain [4–8], where it has been established that the magnetization order parameter decays exponentially in time. The decoherence time of the order parameter was obtained analytically, and the mechanism for the decoherence can be understood as a destructive interference from Jordan-Wigner fermions with all momenta that are produced by the action of the order parameter field, which is non-local in terms of these fermions.

The BEC quench setting has been studied experimentally [9] and theoretically [10, 11]. The previous studies focused on the evolution of a BEC state with a fixed number of particles, which is natural in experiments but also makes the evolution of the BEC order parameter more challenging to study. Indeed, to study $\langle b_j(t)\rangle$ at time t in this setting, one needs to consider boson correlation $\langle b_j^\dagger(t) b_{j+\ell}(t)\rangle$ in the limit where the separation $\ell \to \infty$ first. More specifically, under hard-core boson Hamiltonian, the correlation function in the Jordan-Wigner fermion representation becomes an infinite-length string operator, which is a formidable calculation without Wick's theorem, as is the case for simple BEC states.

We perform essentially the above correlation function calculation upon using a further trick where we replace the simple product BEC initial state with a different state in the same phase but satisfying Wick's theorem for the Jordan-Wigner fermions. Under these further choices of the initial state and the evolution Hamiltonian, we show that the BEC order parameter $\langle b_j(t)\rangle$ decays exponentially in time. We also study how the decay rate depends on the density of particles in the initial state. From the analogy with the quench in the quantum Ising model, we conjecture that similar expressions as in Refs. [6, 8] for the decoherence time and the oscillation frequency will be applicable to our BEC quench setting. We find that our numerical results are consistent with the conjectured expressions. In particular, we find that the decay rate (i.e., inverse decoherence time) vanishes as $\rho^2 \ln(\frac{1}{\rho})$ at low densities ρ.

We remark that a recent work [12] suggested a possible physics that could dramatically alter the conventional "light-cone" picture of the quench problem. The

Hamiltonian Eq. (2.1) is integrable for vanishing longitudinal field, $h = 0$, and thermalizes readily to the corresponding generalized Gibbs ensemble. When the transverse field is below critical, $|g| < 1$, the propagating quasiparticles can be thought of as individual domain walls in the ferromagnetic order. However, for non-zero longitudional field, $|h| > 0$, these domain walls are confined, which leads to a dramatic suppression of the light-cone propagation and the entanglement entropy growth observed in Ref. [12]. For small h, the true quasiparticles above the ground state can be thought of as "mesons," which are bound (confined) states of two domain walls. Reference [12] calculated masses of stable such mesons for small h, and found that observables show apparently persistent oscillations with frequencies set by these masses. Other authors, Refs. [13, 14], also proposed that oscillation frequencies in quantum quenches in near-critical one-dimensional (1D) systems are determined by quasiparticle masses. In this respect, our quasiparticle explanation of oscillations in the weak thermalization regime is close in spirit to Refs. [12–14]. The microscopic details of the true quasiparticles are different in our regime with fairly large both g and h parameters, but this is a quantitative rather than qualitative difference with Ref. [12]. Our emphasis in this paper is more on the generic statement that the low-energy spectrum can be described in terms of particle-like excitations ("quasiparticles"), whose properties can be extracted, e.g., from ED studies, and that we should always think in terms of such quasiparticles when the initial state has low energy density over the ground state. Our main development is the (approximate) picture of the initial state as a BEC of the quasiparticles and how this system eventually thermalizes (the "condensate" decays), which we argue implies that the physical observables cannot have persistent oscillations at long times.

2.1 Finite-size exact diagonalization comparison and identification of the oscillation frequency

To get some understanding of the observed weak thermalization behavior, we first study the same quench protocol as in Ref. [1] using exact diagonalization (ED). More specifically, we prepare the initial state as a product state where all spins are pointing in the $\hat{z}$ direction, $|Z+\rangle$, and study its evolution under the Hamiltonian Eq. (2.1) with parameters $J = 1$ (taken as the energy unit), $h = 0.5$, and $g = -1.05$. We consider a chain of length L with periodic boundary conditions, $j + L \equiv j$. Throughout, we set $\hbar = 1$.

Figure 2.1 shows comparisons of some local observables with the infinite-system

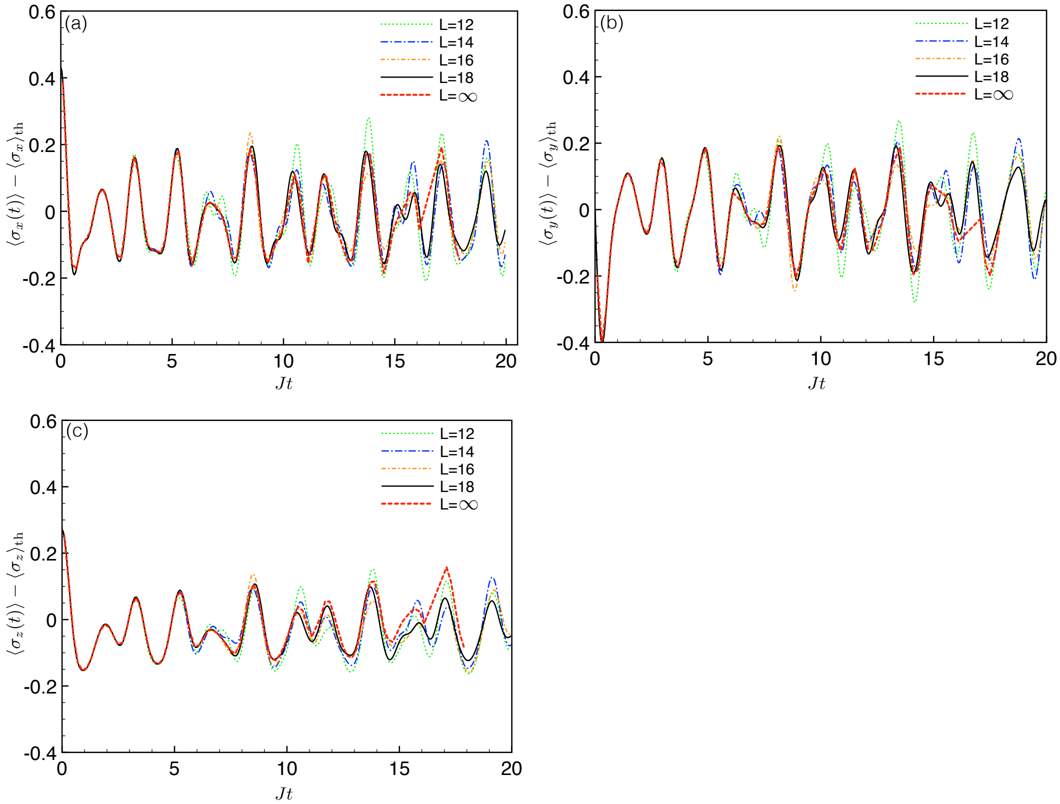

Figure 2.1: (a)-(c) ED calculations of the evolution of some observables for several system sizes compared to infinite-MPS results from Ref. [1] marked as $L = \infty$ (we are grateful to the authors of Ref. [1] for sharing their data with us). For smaller L, visible deviations from the $L = \infty$ results appear at smaller t, which we associate with recurrence phenomenon in finite systems. Close agreement of our ED results with the infinite-MPS results over a large time window allows us to identify the frequency of the oscillations from finite-size spectra, which we argue is essentially the quasiparticle energy at zero momentum.

results from Ref. [1]. Somewhat unexpectedly, our finite-size results for system size $L = 18$ capture the infinite-system results very closely up to time $t \approx 14$, which almost covers the full time window $t \leq 18$ displayed in Ref. [1]. By comparing ED results for a range of sizes between $L = 12$ and $L = 18$, we observe that the time $t_{\rm recurr}(L)$ beyond which the measurements deviate from the infinite-system results increases with the system size. We expect that this time is roughly the time for the information to spread to the whole system, and beyond this time the "recurrence" phenomenon occurs. For our largest size $L = 18$, the recurrence does not happen until $t_{\rm recurr} \approx 14$.

As a result of the close similarity between the ED and infinite-system results, we can

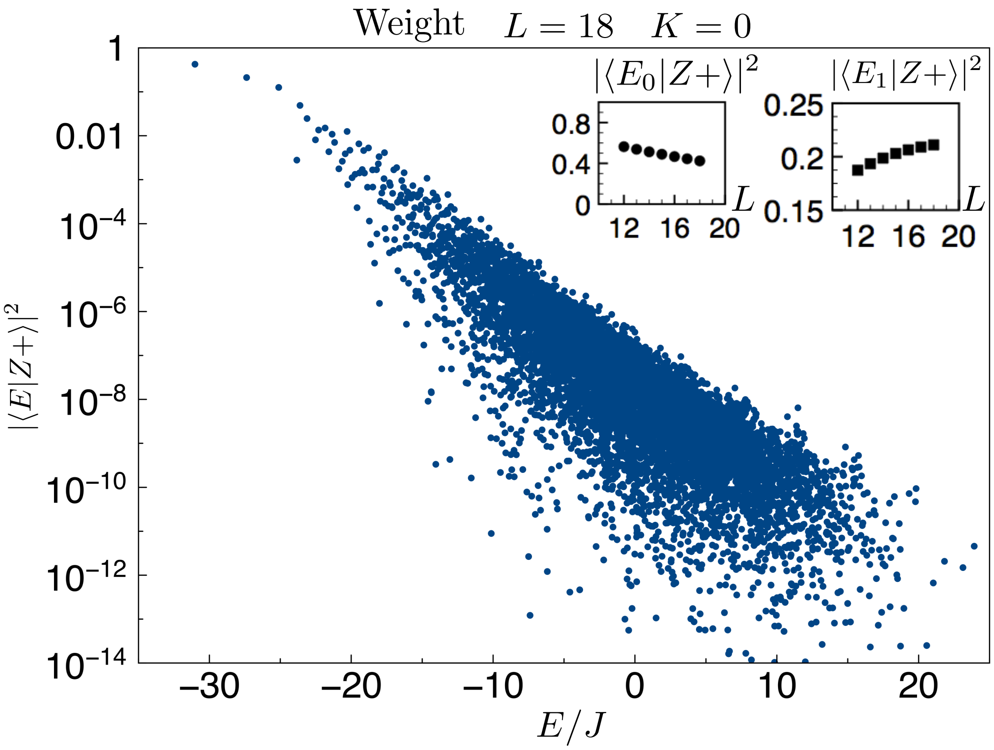

Figure 2.2: Weights of the initial state $|Z{+}\rangle$ on the eigenstates $|E\rangle$ for our largest ED study with $L = 18$. The figure only shows the weights on states with momentum quantum number $K = 0$, since the Hamiltonian is translationally invariant and the initial state has this quantum number (also, only states that are invariant under inversion have non-zero weights). We see that even for our largest size, the majority of the weight is still on the ground state and the first excited state, which is expected since $\langle Z+|H|Z+\rangle = -1.5L = -27$ is close to E_1 for this size. Insets: The system size dependence of the weights on the ground state $|E_0\rangle$ and the first excited state $|E_1\rangle$ from $L = 12$ to $L = 18$. In the thermodynamic limit, the weights on these two states should go to zero, since $|Z{+}\rangle$ has finite energy density above the ground state. Nevertheless, $E_1 - E_0$ is defined in the thermodynamic limit and has a meaning of the quasiparticle gap, controlling oscillations of the observables as in Fig. 2.1 over extended time interval.

understand the oscillation behavior from our ED spectra. First of all, we observe that the oscillation frequency is essentially equal to the energy difference between the ground state and the first excited state. In our calculation with $L = 18$, this energy difference is $\Delta E = E_1 - E_0 \approx 3.6401$. We also note that even in our largest $L = 18$ system, the initial state actually has $|\langle\psi_{\text{ini}}|\psi_0\rangle|^2 \approx 42\%$ weight on the ground state and $|\langle\psi_{\text{ini}}|\psi_1\rangle|^2 \approx 21\%$ weight on the first excited state, as shown in Figure 2.2. Thus, one may think that the finite-size results are mainly determined by these large weights.

On the other hand, in an infinite system, the initial state has a finite energy density above the ground state. The expansion of the initial state in terms of the eigenstates of the infinite system will also be dominated by eigenstates with finite energy density above the ground state. In particular, the weights $|\langle\psi_{\text{ini}}|\psi_0\rangle|^2$ and $|\langle\psi_{\text{ini}}|\psi_1\rangle|^2$ will decay to zero exponentially in system size. However, Ref. [1] still found oscillations with apparently the same frequency in the infinite system. A better picture is that the energy difference $\Delta E = E_1 - E_0$ in the finite-size system can be understood as a quasiparticle energy, which is defined also in the thermodynamic limit (in fact, ΔE is essentially converged to the quoted digits starting from $L = 10$). The ground state is the vacuum of the quasiparticles, while the first excited state has one quasiparticle at momentum $k = 0$. Therefore, the oscillation frequency in the finite-size system can be understood as the creation energy of the $k = 0$ quasiparticle. Note that close to the ground state, any two states that differ by adding one such quasiparticle will have energy difference set by this quasiparticle energy. If the corresponding matrix element for an observable is large and if the amplitudes of these states in $|\psi_{\text{ini}}\rangle$ are significant, they will contribute to the observable with the same oscillation frequency. Thus, this oscillation frequency is more robust than just the energy difference between the ground and first excited states in the finite system. We can therefore infer that the quasiparticle excitation energy is the apparent oscillation frequency of the infinite-system calculation. (As we will see in Sec. 2.3, this is strictly true only in the low quasiparticle density limit, while in general the frequency will obtain density-dependent corrections.)

We can also make a rough estimate of the quasiparticle density in the initial state. The average energy density is $\langle Z+|H|Z+\rangle/L = -J - h = -1.5$. With the quasiparticle energy $\Delta E = 3.6401$ and ground state energy density $E_0/L \approx -1.722$ (estimated from the $L = 18$ ED calculations and essentially converged in L to the quoted digits), we can bound the quasiparticle density as $\rho \lesssim 0.061$. This clearly demonstrates that the initial states in the weak thermalization regime in Ref. [1] are states close to the low-energy part of the spectrum. We can say that in this quasiparticle description, such initial states have low density of quasiparticles. In this case, even though the spin model is a generic non-integrable model, the specific quench puts the system into a regime close to integrability in terms of the low-energy quasiparticles, which we believe is responsible for the observed weak thermalization behavior.

In statistical physics, we routinely calculate properties of many-body systems at low (but finite) temperatures by approximating the low-energy spectrum as a gas of non-interacting quasiparticles. It is natural to ask if this picture can be used for studying quantum dynamics of states at low (but finite) energy density. There is clearly some time scale over which the simple non-interacting picture gives sensible results, while here we want to focus on the asymptotic long-time behavior. A common intuition is that in a generic non-integrable case, the residual interactions of the quasiparticles lead to eventual thermalization in the system, and this approach to thermalization can be studied by some semi-classical kinetic theory for weakly-interacting quasiparticles. Our goal in the remainder of the paper is more modest. We want to show that the oscillations in the above weak thermalization example eventually decay, using as much as possible only precise quantum mechanical arguments. We will still be making some approximations but intuitively only in directions that make thermalization weaker, so our findings of the eventual decay under these approximations should translate to only stronger thermalization without the approximations.

2.2 Perturbative picture of the quasiparticles and truncated Schrieffer-Wolff setup for the entire spectrum and quantum dynamics

Low-energy quasiparticles

To have a more precise formulation of the quasiparticle picture, we use a perturbative local Schrieffer-Wolff transformation [15, 16] near an exactly solvable limit where these quasiparticles are readily identified. The corresponding SW-rotated picture can be viewed as an effective Hamiltonian for the quasiparticles, and we can also study the initial state and its evolution. We take

$$H_0 = -J \sum_{j=1}^{L} \sigma_j^z \sigma_{j+1}^z - h \sum_{j=1}^{L} \sigma_j^z \tag{2.2}$$

as our exactly solvable limit and treat

$$T = -g \sum_{j=1}^{L} \sigma_j^x \tag{2.3}$$

as our perturbation. This is not necessarily the best perturbative starting for our model parameters with sizable g but will suffice for the qualitative picture.

H_0 is diagonal in the σ^z basis. Its energy levels are specified by the number N_{flip} of the spin-down sites, $\sigma_j^z = -1$, and the number N_{dw} of the domain walls, $\sigma_j^z \sigma_{j+1}^z = -1$. The ground state has no spin-down sites and no domain walls, which is the $|Z+\rangle$ state, while a state with $N_{\text{flip}}, N_{\text{dw}}$ has energy $2hN_{\text{flip}} + 2JN_{\text{dw}}$ above the ground state. Note that N_{flip} and N_{dw} are not completely independent. However, what is important later is that the number of different energy "sectors" specified by $N_{\text{flip}}, N_{\text{dw}}$ is bounded by L^2 while the total number of states is growing as 2^L. Many of the sectors are necessarily highly degenerate, particularly in the middle of the spectrum. In cases where the density of spin-flips is small and they are well separated from each other, we can think of an isolated spin-flip as a quasiparticle with energy $2h + 4J$, but there are also quasiparticles with more structure. Abusing the language somewhat, we will refer to the different $N_{\text{flip}}, N_{\text{dw}}$ sectors as having different quasiparticle numbers.

The action of the perturbation term T changes the number of quasiparticle excitations and also introduces their dynamics. The mixture of these effects is what makes the analysis very complicated. To partially simplify the analysis, we find a unitary transformation e^{iS} order by order to eliminate the effect of changing the excitation numbers, which gives us dynamical Hamiltonians that keep the number of quasiparticle excitations fixed (i.e., act within each sector $N_{\text{flip}}, N_{\text{dw}}$). The detailed calculation is presented in Sec. 2.5.

To second order, we obtain the effective Hamiltonian as

$$H' = e^{iS} H e^{-iS} = H_0 + H_{\text{hop}} + H_{\text{config}} + H_{\text{other}} \,, \tag{2.4}$$

with

$$\begin{aligned}
H_{\text{hop}} &= \left(\frac{-g^2}{2h} + \frac{g^2}{2h+4J}\right) \sum_j P^{\uparrow}_{j-1} (\sigma^+_j \sigma^-_{j+1} + \text{H.c.}) P^{\uparrow}_{j+2} \\
&+ \left(\frac{g^2}{2h} - \frac{g^2}{2h-4J}\right) \sum_j P^{\downarrow}_{j-1} (\sigma^+_j \sigma^-_{j+1} + \text{H.c.}) P^{\downarrow}_{j+2} , \\
H_{\text{config}} &= -\frac{g^2}{2h} \sum_j \left(P^{\uparrow}_{j-1} \sigma^z_j P^{\downarrow}_{j+1} + P^{\downarrow}_{j-1} \sigma^z_j P^{\uparrow}_{j+1} \right) \\
&- \frac{g^2}{2h+4J} \sum_j P^{\uparrow}_{j-1} \sigma^z_j P^{\uparrow}_{j+1} - \frac{g^2}{2h-4J} \sum_j P^{\downarrow}_{j-1} \sigma^z_j P^{\downarrow}_{j+1} ,
\end{aligned}$$

where $P^{\uparrow,\downarrow}_j \equiv (1 \pm \sigma^z_j)/2$ are projectors to spin-up and spin-down states respectively and $\sigma^{\pm}_j \equiv (\sigma^x_j \pm i\sigma^y_j)/2$ are raising and lowering operators respectively. The H_{hop} terms can be viewed as correlated hopping for the excitations. As discussed previously, our initial state $|Z+\rangle$ is close to the ground state, i.e., vacuum of quasiparticles. Therefore, we expect the quasiparticles are effectively the down-spins, and the H_{hop} terms move such flipped spins, with additional dependencies on the neighboring spins. The H_{config} terms describe additional contributions to the "classical" energy of the spin configuration, which can be viewed as some density-density-type interactions of the quasiparticles. Note that the quasiparticles also have effective hard-core exclusion interaction. As detailed in Appendix A, H_{other} contains only contributions of order $O(g^3)$, including terms that preserve the excitation numbers and also terms that change the excitation numbers. We will make an approximation where we drop the H_{other} terms (more discussion below) and call the resulting H_{eff} as "effective Hamiltonian," which acts separately in each sector. Thus, by eliminating the leading excitation-number-changing effect in our original Hamiltonian and dropping the H_{other} terms, the dynamics now can be roughly viewed as hard-core bosons with hopping and interaction in the dilute limit, where $\sigma^z_j = -1(+1)$ corresponds to the presence (absence) of bosons.

For excitations that are widely separated spin-flips, we need to consider only the first term in H_{hop} and the first and second terms in H_{config}. The single quasiparticle energy at momentum k is readily evaluated as

$$\epsilon_k = 2h + 4J - \frac{g^2}{h} + \frac{2g^2}{h+2J} - \left(\frac{g^2}{2h} - \frac{g^2}{2h+4J}\right) 2\cos(k) \,. \tag{2.5}$$

The quasiparticle energy at zero momentum, which is relevant for the oscillations

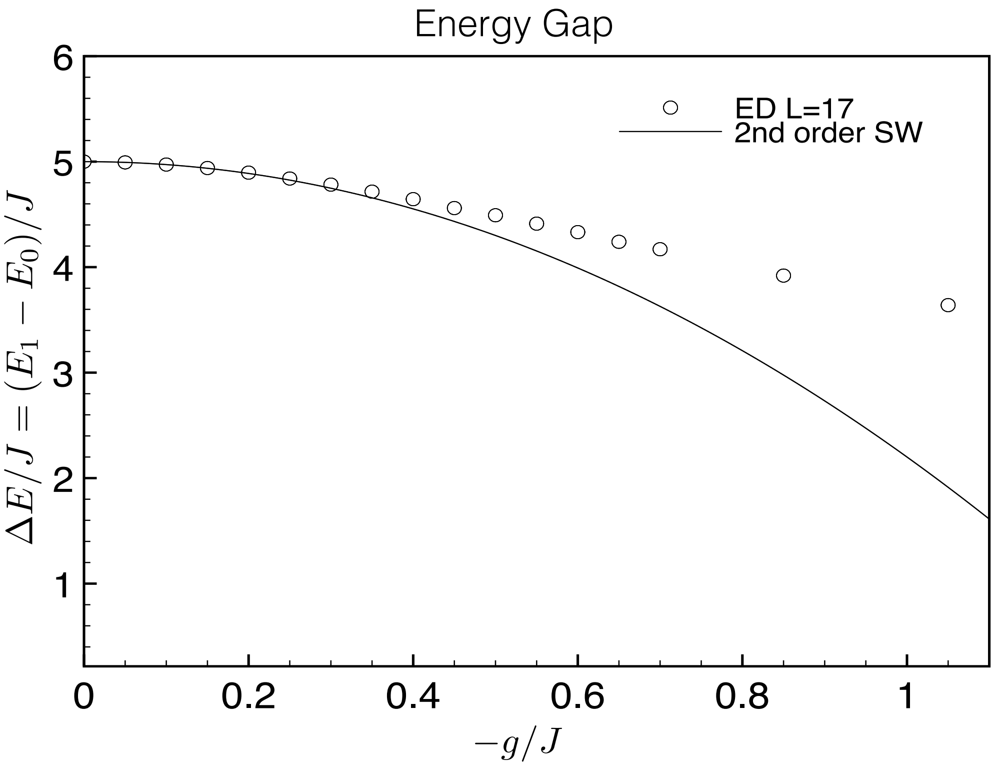

Figure 2.3: The energy difference between the first excited state and the ground state as a function of g. This gap can also be understood as quasiparticle excitation energy. The ED result is from system size $L = 17$ (the ED gap estimates are essentially already converged for $L \gtrsim 10$). We also show perturbative SW result at order $O(g^2)$, Eq. (2.6). The exact and perturbative calculations agree well at small g and deviate more at larger g, but the qualitative picture of the quasiparticle is robust since the gap does not close over the range of g shown.

in the quench problem of interest, is

$$\epsilon_{k=0} = 2h + 4J - \frac{2g^2}{h} + \frac{3g^2}{h + 2J} \; . \tag{2.6}$$

Figure 2.3 shows the excitation energy as a function of g in the range between 0 and -1.05. The perturbative calculation is accurate for small $|g| \lesssim 0.25$ but becomes less accurate at larger $|g|$. In particular, this second-order calculation would give $\epsilon_{k=0} \approx 1.913$ at $g = -1.05$, while the true gap $\Delta E = 3.6401$ is almost two times larger. This quantitative difference is not surprising given that the assumption $g \ll h, J$ is clearly not satisfied in this case (particularly since energy denominators $2h$ appear when treating the sector with one quasiparticle perturbatively in g). However, the true gap remains large in this range of g, and the quasiparticle picture developed perturbatively in g remains qualitatively correct (it can be further improved if needed, but the presented picture is already sufficient for our discussion).

By examining the low-energy ED spectra for $g = -1.05$, we find that the band of states closest to the ground state is well-described by $\epsilon_k = \epsilon_{k=0} + 2J_{\text{eff}}[1 - \cos(k)]$ with $J_{\text{eff}} \approx 0.44$. The effective hopping amplitude again differs quantitatively from the perturbative estimate in Eq. (2.5), but our overall picture of the quasiparticles at low energy is robust.

We finally note that the picture of weakly-interacting spin-flips is not accurate here. Two spin flips can lower their energy by roughly $4J$ if they are next to each other, i.e., there is a significant attractive interaction between them. In the SW perturbative treatment, the next sector in energy after the single-spin-flip sector ($N_{\text{flip}} = 1, N_{\text{dw}} = 2$) has two flipped spins that are next to each other ($N_{\text{flip}} = 2, N_{\text{dw}} = 2$) but otherwise can be anywhere on the chain. The effective Hamiltonian to second order in g gives energy $4h + 4J + 2g^2/(h + 2J)$ and no dispersion for these states, while of course some dispersion will develop at higher order. In fact, by examining the low-energy ED spectra for $g = -1.05$, we find the single-spin-flip band of L states covering energy window $[\Delta E, 5.31]$ above the ground state ($\Delta E = 3.6401$ is the gap), and then another band of L states covering energy $[5.90, 6.84]$ and separated from the next set of states starting at $\approx 2\Delta E = 7.28$. The second band can be viewed as corresponding to a stable bound state of two spin-flips, which is hopping around with an amplitude about two times smaller than the single spin-flip. On the other hand, the states above $2\Delta E$ can be viewed as corresponding to the two-spin-flip continuum with well-separated spin-flips. We can in principle view the bound state as another quasiparticle in the system at low energy and now think about dilute gas of these as well as single-spin-flip quasiparticles, adding more accuracy to the description but also much more complexity. However, we will not use such details below and will proceed with a more crude picture and language of quasiparticles as if they were only single-spin-flips. This is an OK approximation at low energy density but can become quantitatively inaccurate at somewhat higher density.

Truncated Schrieffer-Wolff transformation for dynamics

While our original motivation for using the Schrieffer-Wolff transformations was to understand the low-energy quasiparticles, the transformation as defined acts on the entire Hamiltonian and the entire spectrum. We can boldly try to use the rotated H' with the H_{other} terms omitted and study the quantum dynamics under this "effective Hamiltonian." By doing so, we are essentially postulating an emergent integral of motion, namely the quasiparticle number conservation, or more precisely, preservation of the sector identities. Recent works Refs. [17, 18] conjectured possible emergence of such integrals of motion in translationally invariant systems as a (much weaker) analog of many-body localization physics without underlying disorder. However, this conjecture is far from being established, and we will not try to prove or disprove it here. If such an emergence of the new integral of motion were true, this would likely mean absence of full thermalization in the present context, as one would then expect "equilibration" to an appropriate generalized Gibbs ensemble treating the new integral of motion. Nevertheless, we will see that even in this case the oscillations in the observables still decay, i.e., the weak thermalization turns to a more conventional thermalization at long times. If the conjecture is not true, then our calculations in the truncated SW scheme can be viewed as providing sufficient mechanisms for thermalization, while in the full picture without the new integral of motion the thermalization is likely to proceed only faster.

Keeping the above remarks in mind, we now describe calculations in the truncated SW-rotated picture. The time evolution of an observable $\hat{O}$ becomes

$$\langle\psi_{\rm ini}|e^{iHt}\hat{O}e^{-iHt}|\psi_{\rm ini}\rangle = \langle\psi'_{\rm ini}|e^{iH't}\hat{O}'e^{-iH't}|\psi'_{\rm ini}\rangle\,,$$

where $\hat{O}' = e^{iS}\hat{O}e^{-iS}$ and $|\psi'_{\rm ini}\rangle = e^{iS}|\psi_{\rm ini}\rangle$ are the appropriately rotated operator and initial state.

Consider first observables in the rotated picture. For the observables that we study,

$$\left(\sigma_j^x\right)' \approx \sigma_j^x + O(g)\,, \tag{2.7}$$

$$\left(\sigma_j^y\right)' \approx \sigma_j^y + O(g)\,, \tag{2.8}$$

$$\begin{aligned}\left(\sigma_j^z\right)' \approx\ & \sigma_j^z - \frac{g}{h}\left(P_{j-1}^{\uparrow}\sigma_j^x P_{j+1}^{\downarrow} + P_{j-1}^{\downarrow}\sigma_j^x P_{j+1}^{\uparrow}\right) \\ & -\frac{g}{h+2J}P_{j-1}^{\uparrow}\sigma_j^x P_{j+1}^{\uparrow} - \frac{g}{h-2J}P_{j-1}^{\downarrow}\sigma_j^x P_{j+1}^{\downarrow} + O(g^2).\end{aligned} \tag{2.9}$$

Of course, $\left(\sigma_j^x\right)'$ has an $O(1)$ component onto the operator σ_j^x that changes the quasiparticle number by one and hence "detects" the quasiparticle energy, and similarly for $\left(\sigma_j^y\right)'$. On the other hand, the leading contribution to $\left(\sigma_j^z\right)'$ does not change the quasiparticle number. However, we can see that in the rotated picture at order $O(g)$, this observable also contains σ_j^x, which detects the quasiparticle energy. The above expressions explain why the oscillations in $\langle\sigma_j^x(t)\rangle$ and $\langle\sigma_j^y(t)\rangle$ in Fig. 2.1

have roughly similar amplitudes but are shifted in phase by $\pi/2$, while the oscillation in $\langle\sigma_j^z(t)\rangle$ has a smaller amplitude and is in phase with $\langle\sigma_j^x(t)\rangle$ [indeed, the dominant term in $\left(\sigma_j^z\right)'$ in the regime of low quasiparticle density is $-\frac{g}{h+2J}P_{j-1}^{\uparrow}\sigma_j^x P_{j+1}^{\uparrow}$ and $g < 0$.] Thus, our quasiparticle picture of the origin of oscillations can explain even finer details in the numerical results. Finally, we note that operators $\left(\sigma_j^x\right)'$ and $\left(\sigma_j^y\right)'$ at next order contain contributions that create two spin-flips [see Eq. (2.45) and Eq. (2.46) for explicit formulas]. Hence, when discussing observables in the rotated SW picture, we should also consider operators that change the excitation number by two.

Consider now the initial state in the rotated picture. Since iS is a local operator containing spin-flip terms (see Appendix A for explicit formulas), we can think of $|\psi'_{\text{ini}}\rangle = e^{iS}|\psi_{\text{ini}}\rangle$ roughly as a product state where the spin on each site is rotated a little away from the $\hat{z}$-direction. In terms of hard-core bosons representing the spin-flips (quasiparticles), this state of course has some small density of bosons, since $n_j = (1 - \sigma_j^z)/2$. More crucially, it is actually a Bose-Einstein condensate (BEC) state, since the rotated spin state can be written in the boson language as, approximately, $\prod_j(\alpha + \beta b_j^\dagger)|0\rangle$, where $b_j^\dagger \equiv (\sigma_j^x - i\sigma_j^y)/2$ (denoted σ_j^- earlier and in Appendix A).

To get a more quantitative characterization of the initial state in the rotated picture, we calculated $|\psi'_{\text{ini}}\rangle = e^{iS}|\psi_{\text{ini}}\rangle$ for system sizes $L = 6$ to $L = 13$, using iS calculated to second order in g from Appendix A and applying true unitary e^{iS}. Figure 2.4 shows measurements of the boson density and also of the BEC order parameter as a function of inverse system size $1/L$. The values are essentially converged in the first four non-zero digits. We can see that the density is roughly $\rho \approx 0.05$, consistent with our previous estimate and our picture of diluteness of quasiparticles. Furthermore, the initial state indeed has nonzero BEC order parameter.

To gain some intuition about the truncated SW picture, we performed numerical calculations in the truncated SW picture as follows. For more accuracy, we start with the rotated state $|\psi'_{\text{ini}}\rangle = e^{iS}|\psi_{\text{ini}}\rangle$ and observables $\hat{O}' = e^{iS}\hat{O}e^{-iS}$ using true unitary e^{iS} with $iS = iS^{[1]} + iS^{[2]}$ calculated to second order in g. Note that an exact calculation of e^{iS} is possible on small sizes. However, for the dynamical Hamiltonian, we use the perturbatively developed H' omitting H_{other} terms. Of course, if we used exactly-rotated $H' = e^{iS}He^{-iS}$, everything would be identical to the original calculation with the un-rotated initial state, observables, and Hamiltonian, while the setup where we use the truncated H' allows us to gauge the effect of the truncation.

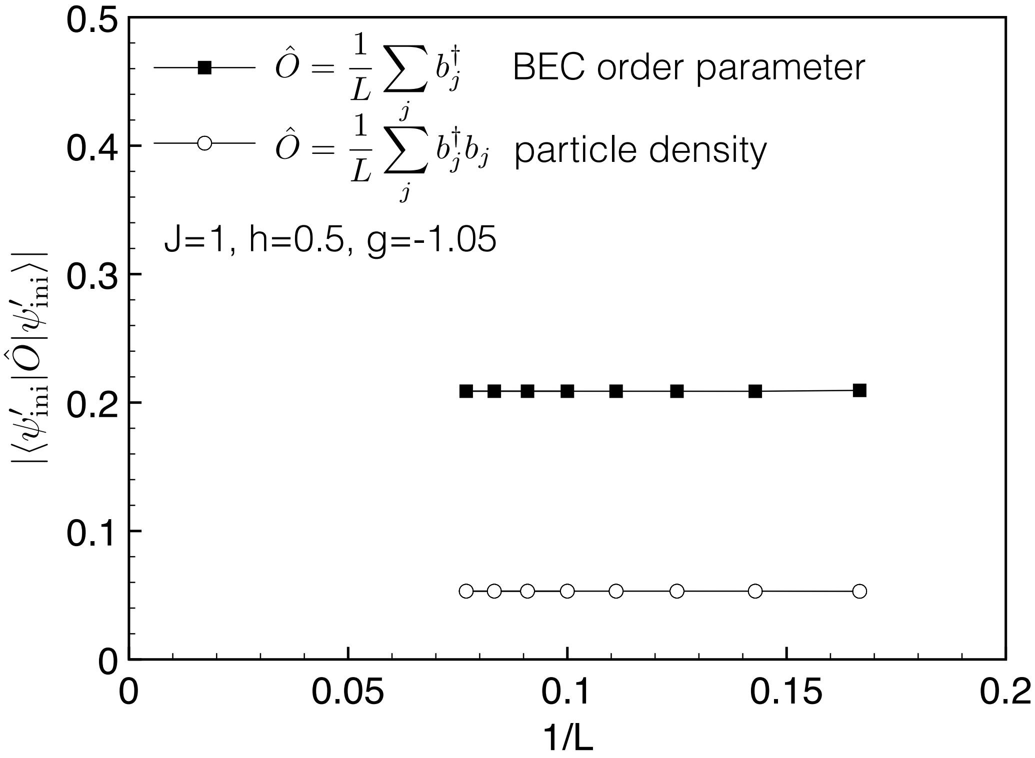

Figure 2.4: Properties of the SW-rotated initial state $|\psi'_{\rm ini}\rangle = e^{iS}|\psi_{\rm ini}\rangle$, with $iS = iS^{[1]} + iS^{[2]}$ calculated to second order in g (see Appendix A for details). The figure shows expectation values of the particle density $b_j^\dagger b_j \equiv (1 - \sigma_j^z)/2$ and BEC order parameter $b_j^\dagger \equiv (\sigma_j^x - i\sigma_j^y)/2$. The particle density $\rho \approx 0.05$ is very low and close to the estimate based on the average energy density in the initial state and the quasiparticle gap.

In principle, the effective Hamiltonian completely separates the different energy scales of the original problem. Thus, the "large" energy scales h and J determine only the spacing between the sectors and would enter only the frequency of the oscillations, while all the processes inside each sector—kinetic energy, effect of hard-core exclusion, and explicit interactions—are now controlled by one energy scale $O(g^2)$ (here for the sake of simplicity we ignore the difference between effects of h and J and imagine them as giving one energy scale).

Figure 2.5 compares the 2nd-order SW calculation described in the previous paragraph with the ED result, for system size $L = 13$ and different parameters. We find persistent oscillations on the time scales similar to those in Fig. 2.1. As shown in the figure, for $g = -0.5$, the perturbative description is still roughly quantitatively ac-

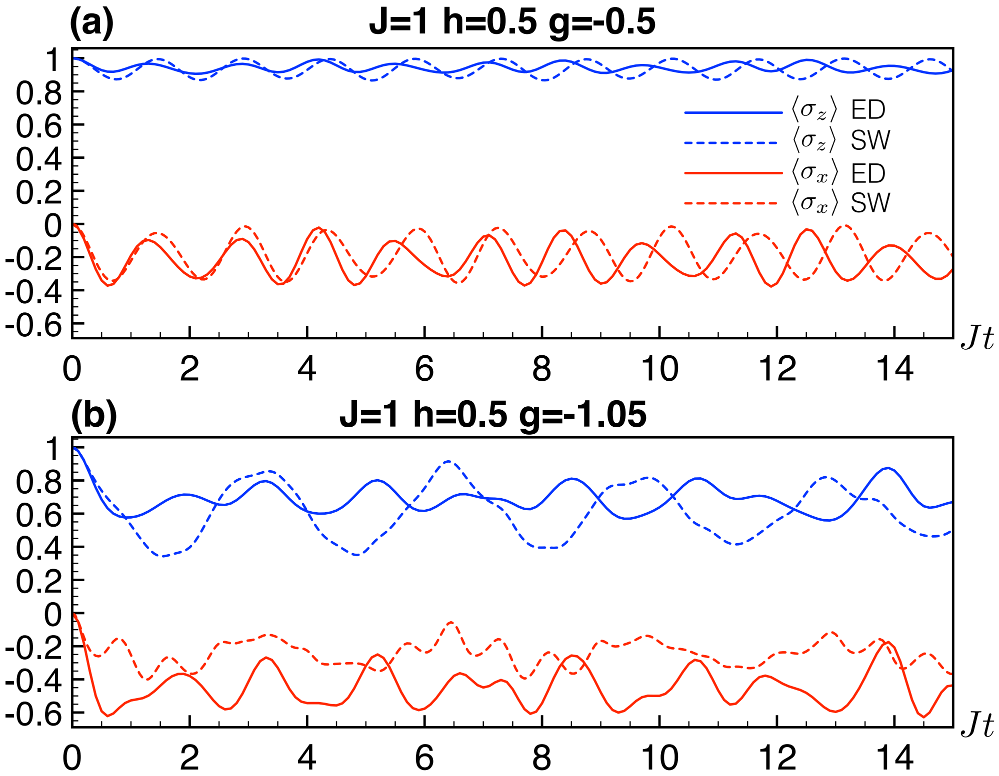

Figure 2.5: Comparisons of the dynamics from ED and 2$^{\text{nd}}$-order SW for two different parameters for system size $L = 13$. (a) $g = -0.5$. The perturbative calculation is still quantitatively accurate at short time. The difference between ED and SW mostly comes from the difference between the exact and perturbative quasiparticle energy gap, resulting in the different oscillation frequencies. (b) $g = -1.05$. The quantitative comparison becomes inaccurate at this parameter. For example, the oscillation frequency in the SW calculation is almost half of the ED calculation. Nevertheless, the SW calculation still captures the qualitative behavior observed in the ED calculation.

curate. The oscillations are somewhat more regular, consistent with the expectation that the truncation reduces decoherence effects. The main difference is due to the frequency difference, as the perturbative calculation of the quasiparticle gap has a small error compare to the ED gap. On the other hand, for $g = -1.05$, the SW calculation deviates significantly from the ED calculation, which is not surprising, since the parameter g is not small anymore. Nevertheless, the ED result of $g = -1.05$ is still qualitatively similar to the ED result of $g = -0.5$, i.e., both have persistent oscillation with frequency given by the quasiparticle energy gap. Moreover, the quasiparticle gap has not closed at $g = -1.05$ as shown in Fig. 2.3. Therefore, we conjecture that the truncated Hamiltonian obtained from SW transformation is still suitable to describe the dynamics, however, with the parameters understood as the renormalized values instead of values calculated from the perturbative formula directly.

To conclude the above discussion, the strong oscillation behavior is mainly coming from the measurement of $\langle\psi'_{\rm ini}|b_j^\dagger(t)|\psi'_{\rm ini}\rangle$ in the boson language. Effectively, this is the evolution of the BEC order parameter with the dynamical Hamiltonian of interacting bosons and the initial BEC state as we discussed. The fate of the oscillations is not an entirely trivial problem, as can be seen from the following considerations. In fact, in the extremely simplified case where the initial state has BEC and the dynamical Hamiltonian is purely boson hopping $H = -J\sum_j(B_j^\dagger B_{j+1} + \text{H.c.}) + W\sum_j N_j = \sum_k[W - 2J\cos(k)]B_k^\dagger B_k$ without interaction and without hard-core constraint, the evolution indeed exhibits undamped oscillation with frequency $\omega = W - 2J$. Note that here B_j are canonical (not hard-core) bosons and $N_j = B_j^\dagger B_j$ (we used capital letters to distinguish from hard-core bosons used in the next section). Furthermore, allowing interactions among quasiparticles of the type typically done in the Landau's Fermi liquid theory, $H_{\rm int} = 1/(2L)\sum_{k,p}V_{k,p}N_kN_p$, leads only to shifting the oscillation frequency by an amount $(1/L)\sum_p V_{0,p}\langle N_p\rangle$, where $\langle N_p\rangle$ is the expectation value in the initial state, but not to decay of the oscillations at long times. Only when we allow more general interactions, we expect that the BEC order parameter will start to damp. In the next section, we will show that already the hard-core exclusion will lead to decrease of the oscillations at long times.

2.3 Quench of BEC state to solvable hard-core boson Hamiltonian

As discussed in the previous section, the dynamics of the quantum spin chain after removing the excitation-changing part can be viewed as an interacting hard-core boson problem. Even though we can obtain the quasiparticle description, the effective problem is still very difficult to analyze due to its non-trivial interactions. Therefore, we further simplify the problem by considering more simple initial states and a solvable effective Hamiltonian.

Specifically, we consider the dynamical Hamiltonian

$$H = W_{\rm eff}\sum_{j=1}^{L} b_j^\dagger b_j - J_{\rm eff}\sum_{j=1}^{L}\left(b_j^\dagger b_{j+1} + \text{H.c.}\right), \tag{2.10}$$

with the hard-core constraint $(b_j^\dagger)^2 = 0$. We also consider periodic boundary conditions $b_{j+L} \equiv b_j$ to be closer to the thermodynamic limit. This Hamiltonian can be viewed as an approximation to the effective Hamiltonian in Eq. (2.4) where we drop H_{other} and two-site and three-site interaction terms. Note that the parameter J_{eff} here is not related to the spin interactions in the original spin chain but should be viewed instead as the effective hopping amplitude of the spin-flips in H_{hop}; this should not cause any confusion since in this section we will focus on the above hard-core boson model. We will show that even dropping these interaction terms, the BEC order parameter will still decay. We would expect that including the dropped terms would allow more channels for thermalization, although details of the interactions can certainly have quantitative effects. We will discuss this approximation and the effects of additional interactions in Sec. 2.3.

The advantage of the above simplified Hamiltonian is that it is exactly solvable. Using Jordan-Wigner (JW) transformation, which transforms the hard-core bosons to fermions,

$$b_j = \left(\prod_{j'=1}^{j-1} e^{i\pi n_{j'}} \right) c_j \, , \tag{2.11}$$

the Hamiltonian can be rewritten in the fermionic representation as

$$\begin{aligned} H &= W_{\mathrm{eff}} \sum_{j=1}^{L} c_j^\dagger c_j - J_{\mathrm{eff}} \sum_{j=1}^{L-1} \left(c_j^\dagger c_{j+1} + \mathrm{H.c.} \right) & (2.12) \\ &- J_{\mathrm{eff}} (-1)^{N_{\mathrm{tot}}+1} \left(c_L^\dagger c_1 + \mathrm{H.c.} \right) \, , & (2.13) \end{aligned}$$

where $N_{\mathrm{tot}} \equiv \sum_{j=1}^{L} n_j$ is the total particle number. As is well-known, in the fermionic representation, for sectors with even N_{tot} we effectively have anti-periodic boundary conditions, while for sectors with odd N_{tot} we have periodic boundary conditions. We can then use Fourier transformation $c_k = (1/\sqrt{L}) \sum_j c_j e^{-ikj}$ to diagonalize the Hamiltonian $H = \sum_k \epsilon_k c_k^\dagger c_k$, where $k = 2\pi(m + 1/2)/L$ for even-particle-number sectors and $k = 2\pi m/L$ for odd-particle-number sectors, with $m = 0, 1, \ldots, L-1$. The single-particle dispersion is $\epsilon_k = W_{\mathrm{eff}} - 2J_{\mathrm{eff}} \cos(k)$.

The difference in the boundary conditions for the even and odd sectors is not important when considering the spectrum and static properties in the thermodynamic limit. However, when considering the dynamics of observables connecting different number-parity sectors, ignoring the boundary conditions and the resulting differences in c_k used to diagonalize the even and odd sectors (ultimately related to the string operator when connecting such sectors), results in an erroneous answer, as we will explicitly show below. This is also the major obstacle to obtaining analytical results for $\langle \psi_{\mathrm{ini}} | b_j^\dagger(t) | \psi_{\mathrm{ini}} \rangle$, with any reasonable initial state $|\psi_{\mathrm{ini}}\rangle$. On the other hand, we can obtain a compact analytical expression for $\langle \psi_{\mathrm{ini}} | b_j^\dagger(t) b_{j+1}^\dagger(t) | \psi_{\mathrm{ini}} \rangle$, which connects sectors with the same number parity. The reason is that the Heisenberg representation of $c_k(t) = c_k e^{-i\epsilon_k t}$ only makes sense when constructing operators that connect sectors with the same number parity.

In the next two subsections, we will consider two different initial states, both with nonzero boson condensation, evolving under Hamiltonian Eq. (2.10). For $W_{\rm eff} > 2J_{\rm eff}$, the ground state of this Hamiltonian in the full Fock space is a trivial Mott insulator. However, this and the value of $W_{\rm eff}$ are actually not important for the relaxation dynamics: one can readily see that $W_{\rm eff}$ only adds to the oscillation frequency for processes connecting sectors with different $N_{\rm tot}$ and not to any relaxation dynamics. The latter is determined by the spectra inside each sector, where $J_{\rm eff}$ is the only energy scale. Of course, the properties of the initial state are also important (e.g., which $N_{\rm tot}$ are present, the energy distribution, etc.). For illustration, we will take $W_{\rm eff} = 5J_{\rm eff}$ to see multiple oscillations before recurrence time. Given our motivation for this model as a simplified effective model for quasiparticles in the original spin problem in the regime of low quasiparticle density, we would like to consider initial states with low average particle density. We will first consider higher densities to better see qualitative behaviors, and afterwards we will return to more appropriate parameters for the original motivation. We will consider quantities $\langle\psi_{\rm ini}|b_j^\dagger(t)|\psi_{\rm ini}\rangle$ (the matter wave or the BEC order parameter) and $\langle\psi_{\rm ini}|b_j^\dagger(t)b_{j+1}^\dagger(t)|\psi_{\rm ini}\rangle$ (pair-boson condensation order parameter). One motivation for considering both single- and pair-boson operators comes from the fact that both these generically contribute to the observables of interest in the rotated SW picture for the original spin problem, see discussion after Eq. (2.9) and Eqs. (2.45)-(2.46) in Appendix A. An even stronger motivation comes from intrinsic interest in the integrable hard-core boson model, as comparing these quantities will illustrate the importance of the boundary conditions on the Jordan-Wigner fermions and ultimately of the string operator when connecting sectors with different number parity.

Initial hard-core boson BEC state as a product state

We first consider our initial state as a hard-core boson coherent state

$$|\psi_{\rm ini,A}\rangle = \prod_{j=1}^{L}(\alpha + \beta b_j^\dagger)|0\rangle\,, \tag{2.14}$$

where $|0\rangle$ is the vacuum of the hard-core bosons. The normalization requires $|\alpha|^2 + |\beta|^2 = 1$. The boson density is $\rho = \langle\psi_{\rm ini,A}|b_j^\dagger b_j|\psi_{\rm ini,A}\rangle = |\beta|^2$, while the BEC order parameter is $\Phi = \langle\psi_{\rm ini,A}|b_j^\dagger|\psi_{\rm ini,A}\rangle = \beta^*\alpha$.

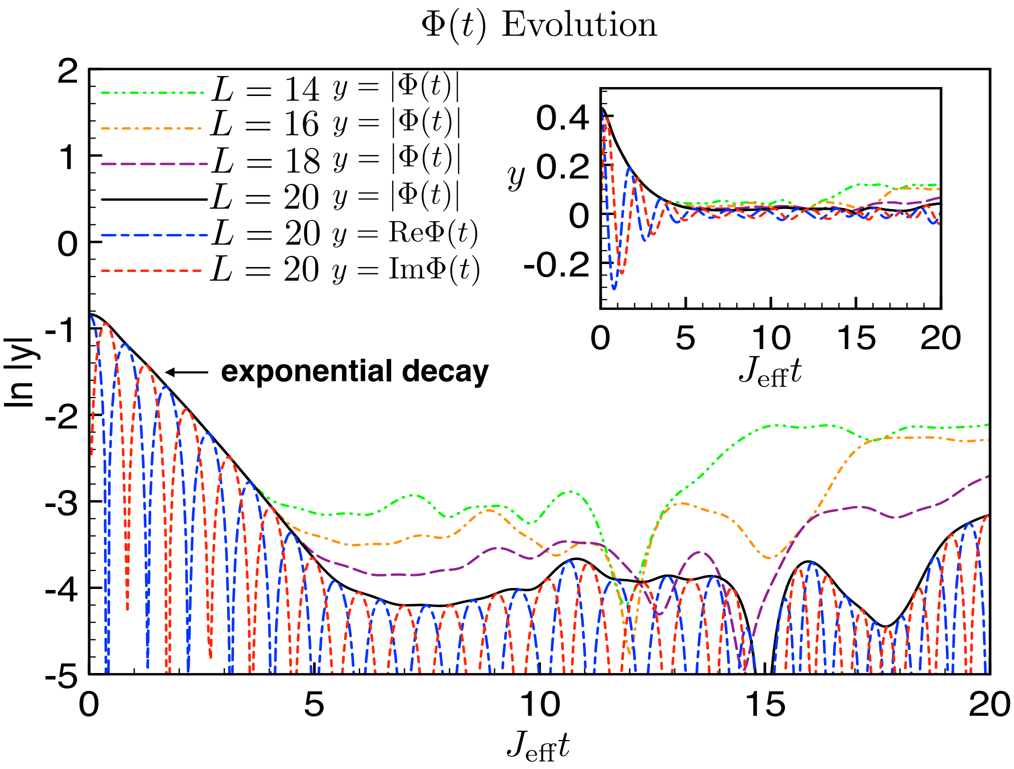

Figure 2.6: (color online) ED results for $\Phi(t) \equiv \langle b_j^\dagger(t) \rangle$ for the hard-core boson model, Eq. (2.10), and the product BEC state, Eq. (2.14), with average boson density $\rho = |\beta|^2 = 0.25$, for system sizes $L = 14, 16, 18, 20$. The parameters of the dynamical Hamiltonian are $J_{\mathrm{eff}} = 1$ and $W_{\mathrm{eff}} = 5J_{\mathrm{eff}}$. Note that the main panel shows $\ln|\Phi(t)|$ vs $J_{\mathrm{eff}}t$, and the results strongly suggest exponential decay in t until recurrence time: as the system size increases, the time interval over which the exponential decay is observed also increases. Inset: linear scale for the observable. The recurrence times where the smaller-size results peel off from the largest-size results are roughly in agreement with those in Fig. 2.7.

Figure 2.6 shows ED results for the evolution of the BEC order parameter

$$\Phi(t) \equiv \langle b_j^\dagger(t) \rangle \equiv \langle \psi_{\mathrm{ini,A}} | b_j^\dagger(t) | \psi_{\mathrm{ini,A}} \rangle \tag{2.15}$$

for the initial state with average density $\rho = 0.25$ and system sizes up to $L = 20$. From the semi-log plot, it is clear that the initial decay is exponential. At later times, the ED results again suffer from the finite-size recurrence effect. However, as the system size increases, we see the exponential decay over a longer time interval. Therefore, we infer that in the thermodynamic limit the BEC order parameter decays exponentially in time even in this integrable system.

We remark that a naive calculation that would ignore the different boundary con-

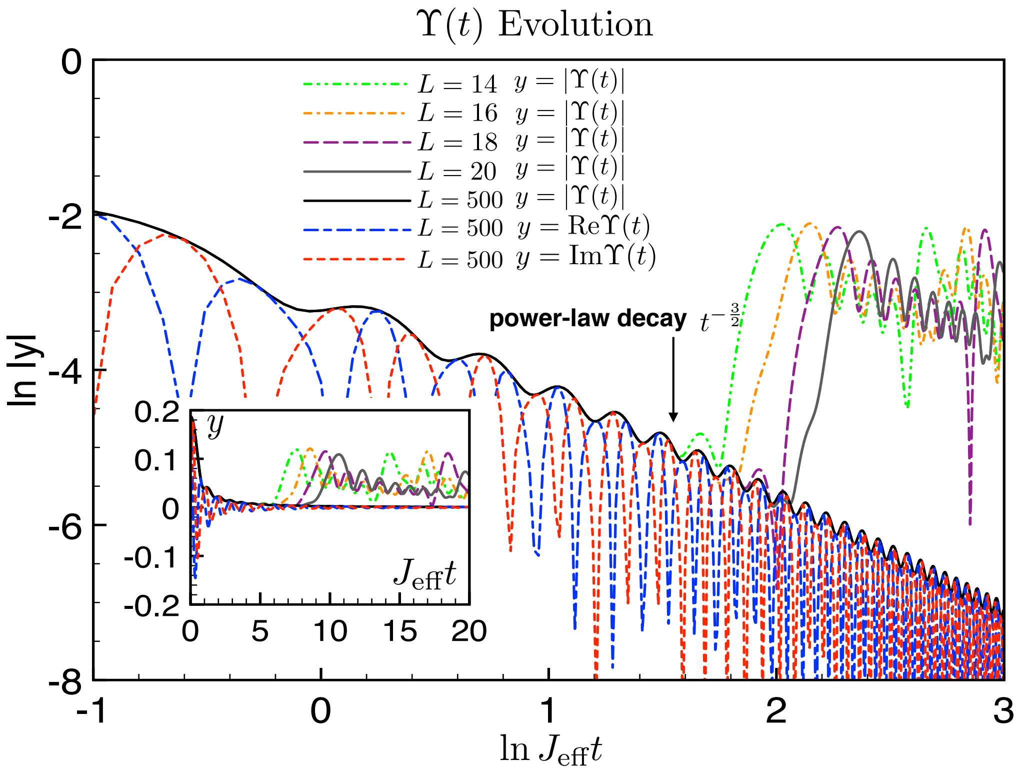

Figure 2.7: (color online) ED results for $\Upsilon(t) \equiv \langle b_j^\dagger(t) b_{j+1}^\dagger(t)\rangle$ for the same systems as in Fig. 2.6 with average density $\rho = 0.25$. This observable can be also calculated analytically using Jordan-Wigner transformation (checked against ED for small L), allowing us to study much larger sizes and times, as illustrated here for $L = 500$. Note that the main panel shows log-log plot, and the long-time behavior in the largest system clearly has a power-law envelope with decay $t^{-3/2}$, in agreement with the analytical calculation in the text. Inset: linear scale for the observable. By comparing data for $L = 14, \ldots, 20$ and much larger $L = 500$, we can also clearly see where the recurrences appear for the smaller sizes.

ditions for the Jordan-Wigner fermions in different number-parity sectors would suggest a different (wrong) result. By translational invariance, the BEC order parameter is just $\langle \psi_{\mathrm{ini,A}} | b_{j=1}^\dagger(t) | \psi_{\mathrm{ini,A}} \rangle$, and one could naively proceed

$$\begin{aligned} \langle \psi_{\mathrm{ini,A}} | b_{j=1}^\dagger(t) | \psi_{\mathrm{ini,A}} \rangle &= \langle \psi_{\mathrm{ini,A}} | c_{j=1}^\dagger(t) | \psi_{\mathrm{ini,A}} \rangle \\ &\overset{\text{!!! wrong !!!}}{=} \frac{1}{\sqrt{L}} \sum_k \langle \psi_{\mathrm{ini,A}} | c_k^\dagger | \psi_{\mathrm{ini,A}} \rangle e^{i\epsilon_k t} e^{-ik} \qquad (2.16) \\ &= \frac{1}{L} \sum_k \sum_j \langle \psi_{\mathrm{ini,A}} | c_j^\dagger | \psi_{\mathrm{ini,A}} \rangle e^{i\epsilon_k t} e^{ikj} e^{-ik} \; . \qquad (2.17) \end{aligned}$$

Expectation values $\langle \psi_{\mathrm{ini,A}} | c_j^\dagger | \psi_{\mathrm{ini,A}} \rangle$ can be easily evaluated in the product BEC state.

From here, the calculation is not sensitive to the details of the sum over k, which can be turned into an integral for large L, and a standard steepest descent analysis of the last equation would give $t^{-\frac{1}{2}}$ decay at large time t. However, this calculation is wrong at the emphasized step, since there is no well-defined fermionic quasiparticle creation operator $c_k^\dagger$ acting between sectors with different parity. Ultimately, this is related to the non-local character of the boson order parameter in terms of the JW fermions, which in the translationally invariant case with periodic boundary conditions for the bosons yields effectively different boundary conditions for the JW fermions in the even and odd sectors. (In the case with open boundary conditions, the above calculation focusing on the site at the left boundary would not be representative of the infinite system, while a valid calculation with a site in the middle of the system would have to time-evolve with the string operator.) In this case, we do not have a simple analytical calculation of the observable even though the model is solvable by JW fermions. A more involved analytical calculation supporting exponential decay of $\Phi(t)$ will be presented in the next subsection.

On the other hand, Fig. 2.7 shows the evolution of

$$\Upsilon(t) \equiv \langle b_j^\dagger(t) b_{j+1}^\dagger(t)\rangle \equiv \langle \psi_{\text{ini,A}}| b_j^\dagger(t) b_{j+1}^\dagger(t) |\psi_{\text{ini,A}}\rangle \ . \tag{2.18}$$

We actually have a full analytical calculation of this observable and a closed-form expression in the thermodynamic limit. Nevertheless, we still show the finite-size ED results (which we also checked against the analytical calculations), as a reference to compare with the results for $\Phi(t)$. We can see that this pair-boson observable decays with a power-law envelope $t^{-3/2}$ until the recurrence phenomenon sets in. Again, as we increase the system size, the recurrence time also increases.

We present the analytical calculation in Appendix B, while here we only show the final result in the thermodynamic limit,

$$\Upsilon(t) = 2(\beta^* \alpha)^2 \int_{-\pi}^{\pi} \frac{dk}{2\pi} \frac{\sin^2(k)}{1+\eta^2 - 2\eta\cos(k)} e^{2i\epsilon_k t} \ , \tag{2.19}$$

where $\eta \equiv |\alpha|^2 - |\beta|^2$. The long-time behavior is controlled by extrema of ϵ_k; these occur at $k = 0$ and $k = \pi$, so we expect oscillations at two frequencies, $2\epsilon_{k=0/\pi} = 2(W \mp 2J)$. Since in the integrand the factor multiplying $e^{2i\epsilon_k t}$ vanishes at both these points, a saddle-point analysis gives power-law envelope $t^{-3/2}$. Both these frequencies and the power-law envelope are indeed observed in the numerical calculations in Fig. 2.7.

Comparing our numerical results for $\Phi(t)$ and $\Upsilon(t)$, we can confidently say that the latter observable decays more slowly, despite being a composite operator in terms of microscopic bosons. On the time scales where the behavior is representative of the thermodynamic limit, the former observable decays faster than power law and is consistent with exponential decay. We will confirm this on yet longer time scales in the next section.

The different behaviors of the above two types of observables are based on the differences when operators change or preserve the number parity. In a very general consideration of a quantum evolution, any observable can be expanded in the eigenstate basis

$$\langle \hat{O}(t) \rangle = \sum_{a,a'} x_a^* O_{a,a'} x_{a'} e^{i(E_a - E_{a'})t} , \tag{2.20}$$

where $x_a = \langle a | \psi_{\text{ini}} \rangle$, $O_{a,a'} = \langle a | \hat{O} | a' \rangle$, and $|a\rangle$ is an eigenstate with energy E_a. When we consider $\hat{O} = (1/L) \sum_j b_j^\dagger b_{j+1}^\dagger = (1/L) \sum_k c_k^\dagger c_{-k}^\dagger e^{ik}$ (appropriate for calculating $\Upsilon(t)$ in translationally invariant setups), it connects states that differ by precisely two quasiparticles with opposite momenta. The energy differences can only be $\epsilon_k + \epsilon_{-k} = 2\epsilon_k$. These are precisely the frequencies that appear in Eq. (2.19) (see also derivation in Appendix B). Note that while the number of states is exponentially large in system size, the number of different frequencies that appear here is only linear in system size, and this is ultimately responsible for the slow power-law “decoherence" in the observable. On the other hand, when we consider $\hat{O} = (1/L) \sum_j b_j^\dagger$, the mismatch between the sectors with different particle number parity (related to $b_j^\dagger$ not being locally represented in terms of the JW fermions) results in a much larger number of different frequencies $E_a - E_{a'}$ that appear with non-zero matrix elements; we believe that this is responsible for the faster decay than power law—exponential decay in this case.

To put these results in perspective, the difference in relaxation dynamics of operators that are non-local (contain string) or local (no string) in terms of the diagonalizing Jordan-Wigner fermions has been known in the context of quenches in the quantum Ising chain, starting from Ref. [4] and very detailed subsequent works Refs. [5–7] (for a recent review, see Ref. [8]). Direct analogs of our $\Phi(t)$ and $\Upsilon(t)$ observables are $\langle \sigma_j^x(t) \rangle$ and $\langle \sigma_j^x(t) \sigma_{j+1}^x(t) \rangle$ in the quantum Ising chain $H = \sum_j (-J\sigma_j^x \sigma_{j+1}^x - h\sigma_j^z)$, which were shown to have exponential and power-law $t^{-3/2}$ envelopes respectively. It has been also anticipated that such difference holds for other models with free-fermion spectrum. To our knowledge, our work is the first explicit study of the exponential decay of the order parameter in the case of the BEC to hard-core boson

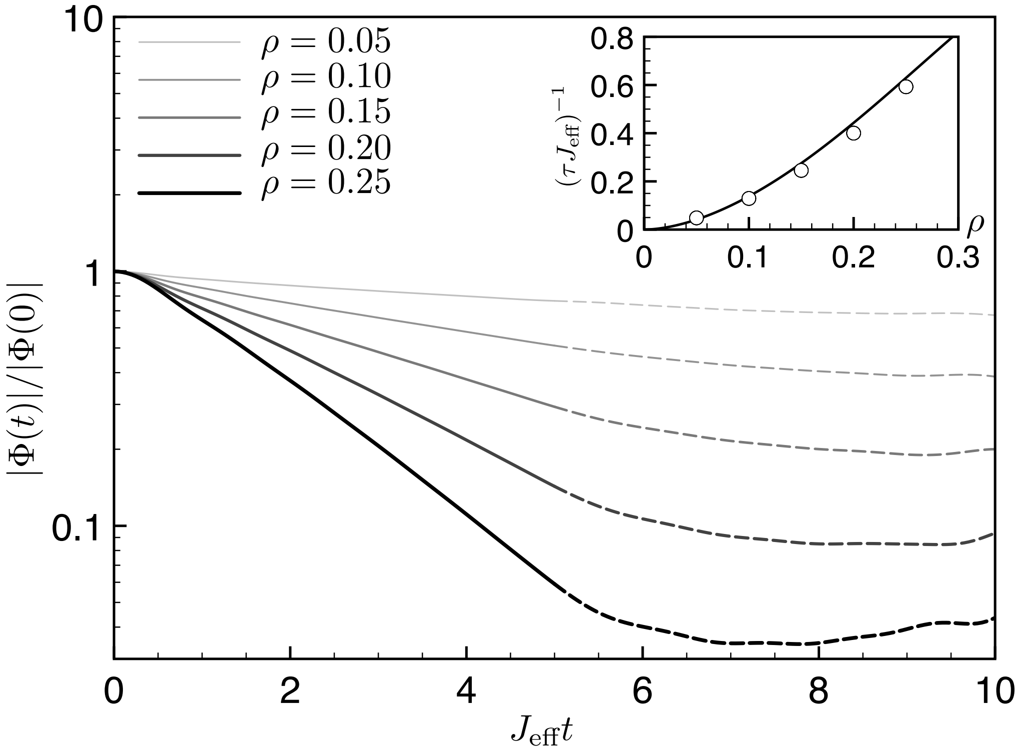

Figure 2.8: Evolution of the absolute value of the BEC order parameter $|\Phi(t)|$ in the same setting as in Fig. 2.6 but for different average boson densities ρ in the initial state and showing only the largest ED size $L = 20$ ($\rho = 0.25$ data is the same as in Fig. 2.6). The measurements are normalized by their initial value in order to compare the decay rates. We clearly see that the decay rate increases as the density increases. The exponential decay ends at roughly $J_{\text{eff}}t \approx 5$, where the finite-size recurrence effect shows up, indicated by the broken line (see also Fig. 2.6). Inset: density dependence of the inverse lifetime $1/J_{\text{eff}}\tau$. The circle symbols are obtained from fitting the exponential decay regime $J_{\text{eff}}t \in [1.5, 4.5]$ to a function $Ae^{-t/\tau}$, while the solid line is calculated from the conjectured Eq. (2.23). The inverse lifetime decreases as density decreases, with a $\rho^2 \log(\frac{1}{\rho})$ dependence at small density.

quench. Our results in the present subsection are numerical, while analytical results for this quench are not available because the time-evolved state here does not have Wick's theorem for the JW fermions, as emphasized in Ref. [10]. We will present (semi)-analytical results on such a quench in the next section by starting with a different initial state which is qualitatively in the same BEC phase but does have Wick's theorem (and will in fact be able to say more about the product BEC states as well).

Having found exponential decay of the BEC order parameter for a sizable (but

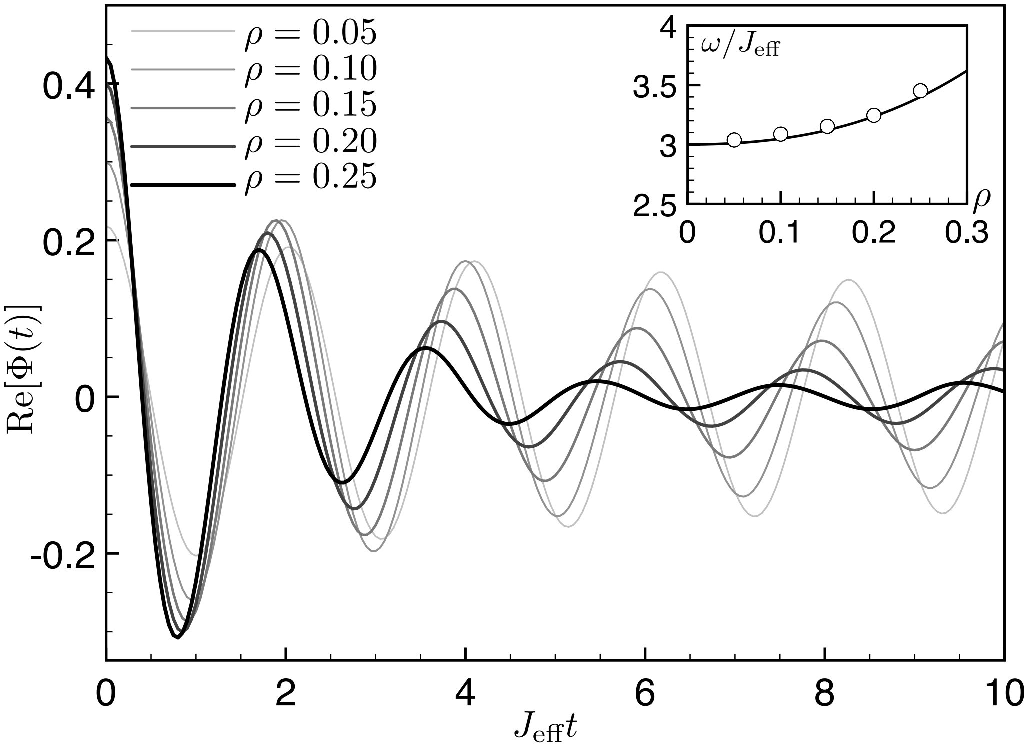

Figure 2.9: Evolution of the real part of the BEC order parameter Re$[\Phi(t)]$ for different average boson densities ρ and showing only the largest ED size $L = 20$; the systems are the same as in Fig. 2.8. Inset: density dependence of the frequency ω obtained from fitting the exponential decay regime $J_{\text{eff}}t \in [1.5, 4.5]$ to a function $Ae^{-t/\tau}\cos(\omega t - \alpha)$, with τ determined from Fig. 2.8. We see that the frequency decreases towards $W_{\text{eff}} - 2J_{\text{eff}} = 3$ as the density decreases to zero. The solid line indicates our conjectured dependence of the oscillation frequency on density, Eq. (2.24).

otherwise generic) average boson density $\rho = 0.25$ in the initial BEC state, we believe that the same qualitative behavior will persist for all densities. We will establish this even more firmly on much larger systems and much longer times in the next subsection using a somewhat different realization of the initial BEC state. Here we would like to study density dependence of the relaxation time moving towards regime of low density, which is of interest in the original spin model. Figure 2.8 shows $|\Phi(t)|$ evolution for varying average boson density in the initial state. In each case, we normalized the observable by its initial value in order to get a better comparison. We can clearly see that the BEC order parameter decays faster with increasing density. Even though we do not have an exact functional form for $|\Phi(t)|$, we still select the exponential decay regime and fit it with $Ae^{-t/\tau}$, where the inverse lifetime τ^{-1} as a function of density is shown in the inset and vanishes at low density. A companion Fig. 2.9 shows the real part $\mathrm{Re}[\Phi(t)]$ for the same systems, where we can see that the frequency of oscillations also depends on the density, approaching the $k = 0$ quasiparticle gap $W_{\text{eff}} - 2J_{\text{eff}}$ in the limit of low density.

The exponential decay of the order parameter was also obtained in earlier studies of the non-equilibrium dynamics of the magnetization in the quantum Ising model [4, 6, 19] (see also Ref. [8] for a recent review). Despite the differences in details between the hard-core boson and Ising models, the exponential decoherence can be attributed to the non-local nature of the observable when expressed in terms of the Jordan-Wigner fermions, which are the non-interacting quasiparticles in both models. The origin of the decoherence of the order parameter is the destructive interference coming from contributions from quasiparticles at all momenta. Ref. [6] obtained analytical formulas for the decay time and the oscillation frequency in the quantum Ising quench from the ferromagnetic phase to the paramagnetic phase. These formulas depend only on the mode occupation numbers of the JW fermions in the initial state and not any other details. We conjecture that the same formulas are valid also for our hard-core boson quench from the BEC state. We propose the inverse decoherence time (inverse lifetime) as

$$\tau^{-1} = \int_{-\pi}^{\pi} \frac{dk}{2\pi} \left| \frac{d\epsilon_k}{dk} \right| \log |1 - 2\langle n_k \rangle| \;, \tag{2.21}$$

where $d\epsilon_k/dk$ is the group velocity of the quasiparticle and $\langle n_k \rangle$ is the mode occupation number in the initial state, $\langle n_k \rangle = \langle \psi_{\text{ini}} | c_k^\dagger c_k | \psi_{\text{ini}} \rangle$. For the initial state $|\psi_{\text{ini}}\rangle = |\psi_{\text{ini, A}}\rangle$, calculations similar to those in Appendix B give in the thermodynamic limit

$$\langle n_k \rangle = \frac{\rho^2 (1 + \cos k)}{\rho^2 + (1-\rho)^2 - (1 - 2\rho)\cos k} \;. \tag{2.22}$$

We can therefore obtain explicit density dependence of the inverse lifetime as

$$(J_{\text{eff}}\tau)^{-1} = \frac{16}{\pi} \frac{\rho^2 (1-\rho)^2}{\rho^2 + (1-\rho)^2} \frac{\log(1-\rho) - \log(\rho)}{1 - 2\rho} \;. \tag{2.23}$$

Note that this expression is symmetric under particle-hole transformation sending $\rho \longrightarrow 1-\rho$, as is expected from simple considerations about this quench. Importantly for our applications to the original spin model, we find that at low density $(J_{\text{eff}}\tau)^{-1} \sim \rho^2 \log(\frac{1}{\rho})$. Inset in Fig. 2.8 compares the inverse lifetime extracted from fits of the time evolution in our ED systems and the conjectured expression Eq. (2.23), denoted by circles and solid line respectively. The fairly good agreement between the two supports our conjecture.

As for the density dependence of the frequency, based on the quantum Ising study in Ref. [6], we can also conjecture that the frequency is given as $\omega = \epsilon_{k_0}$, where k_0 is the wave vector such that $1 - 2\langle n_{k_0}\rangle = 0$. We can then obtain the frequency as a function of density as

$$\omega(\rho) = W_{\text{eff}} - 2J_{\text{eff}}\frac{1-2\rho}{\rho^2 + (1-\rho)^2} \, . \tag{2.24}$$

Inset of Fig. 2.9 compares the fitted frequencies from the ED study (circles) and the above formula (solid line). The close agreement supports our conjecture.

On the other hand, the power-law decay of the pair-boson observable $\Upsilon(t)$ does not depend on the density in the initial state, nor does the oscillation frequency. This is similar to results in the quantum Ising quench for operators that do not change the Ising quantum number [4, 6, 8] and is also another noteworthy point of the differences between the relaxation behaviors of the single- and pair-boson operators.

Initial hard-core boson BEC state realized as a topological superconductor of JW fermions

The initial state used in the previous subsection does not have any special properties like the Wick's theorem that we could utilize to reach larger system sizes when calculating the evolution of the BEC order parameter. In this subsection, we will consider a different initial state which is qualitatively in the same BEC phase but for which Wick's theorem is valid, therefore enabling calculations for much larger system sizes.

Specifically, consider the following hard-core boson Hamiltonian,

$$\begin{aligned} H_{\text{ini}} &= -J_0 \sum_{j=1}^{L} (b_j^\dagger b_{j+1} + \text{H.c.}) \\ &- \Delta_0 \sum_{j=1}^{L} (b_j^\dagger b_{j+1}^\dagger + \text{H.c.}) - \mu_0 \sum_{j=1}^{L} b_j^\dagger b_j \, , \end{aligned} \tag{2.25}$$

with periodic boundary conditions, $b_{j+L} \equiv b_j$. This Hamiltonian preserves particle number parity, with the corresponding ground states in the even and odd parity sectors $|\psi_{\text{g.s., even}}\rangle$ and $|\psi_{\text{g.s., odd}}\rangle$. We will argue below that as long as $|\mu_0| < 2|J_0|$, these ground states have long-range order in the single-boson observable, i.e., $\lim_{|j-j'|\to\infty}\langle b_j^\dagger b_{j'}\rangle \neq 0$. Schematically, we can indicate this long-range order by writing $\langle b_j^\dagger\rangle \neq 0$. In particular, it is actually sensible to consider a superposition of $|\psi_{\text{g.s., even}}\rangle$ and $|\psi_{\text{g.s., odd}}\rangle$ and view it as a BEC of bosons, which contains states with arbitrary particle numbers. For example, we can take $|\psi_{\text{ini}}\rangle = (1/\sqrt{2})(|\psi_{\text{g.s., even}}\rangle + |\psi_{\text{g.s., odd}}\rangle)$, which for $J_0, \Delta_0 > 0$ and appropriate choices of the phases of $|\psi_{\text{g.s., even/odd}}\rangle$ will have positive amplitudes on all states in the boson number basis, similarly to the state Eq. (2.14) with real and positive parameters α and β. However, as will become clear, the details of the superposition are not important.

The above Hamiltonian can be also exactly solved by the Jordan-Wigner transformation Eq. (2.11), which gives

$$\begin{aligned} H_{\text{ini}} &= -J_0 \sum_{j=1}^{L-1} (c_j^\dagger c_{j+1} + \text{H.c.}) - \Delta_0 \sum_{j=1}^{L-1} (c_j^\dagger c_{j+1}^\dagger + \text{H.c.}) \\ &- J_0 (-1)^{N_{\text{tot}}+1} (c_L^\dagger c_1 + \text{H.c.}) \\ &- \Delta_0 (-1)^{N_{\text{tot}}+1} (c_L^\dagger c_1^\dagger + \text{H.c.}) - \mu_0 \sum_{j=1}^{L} c_j^\dagger c_j \ . \end{aligned} \tag{2.26}$$

The fermions effectively have antiperiodic boundary conditions in the even number-parity sector and periodic boundary conditions in the odd number-parity sector. After Fourier transformation with lattice momenta $k = \frac{2\pi}{L}(m + \frac{1}{2})$, $m = 0, 1, \ldots, L-1$ in the even number-parity sector and $k = \frac{2\pi}{L} m$ in the odd number-parity sector, we further apply Bogoliubov transformation to diagonalize the above Hamiltonian. The Bogoliubov quasiparticles are given as $\gamma_k = u_k^* c_k + v_k^* c_{-k}^\dagger$, with $u_k = \cos(\theta_k/2)$, $v_k = \sin(\theta_k/2)$. The parameter θ_k is determined by $\tan(\theta_k) = \frac{-2\Delta_0 \sin(k)}{2J_0 \cos(k) + \mu_0}$. We can readily construct the vacuum of the Bogoliubov quasiparticles in both parity subspaces; e.g., in the even-parity sector we have $|\psi_{\text{g.s., even}}\rangle = |\text{vac}_{\gamma,\text{even}}\rangle = \prod_{k>0} \left(u_k^* - v_k^* c_k^\dagger c_{-k}^\dagger \right) |\text{vac}_c\rangle$, where $|\text{vac}_c\rangle$ is the vacuum for the c fermions and k are chosen appropriately for this number-parity.

The dynamics is governed by the hard-core boson hopping Hamiltonian Eq. (2.10). We are interested in the time evolution of the BEC order parameter $\Phi(t)$ and will calculate its real part, $2\text{Re}[\langle b_j^\dagger(t)\rangle] = \langle b_j^\dagger(t) + b_j(t)\rangle \equiv \langle \Sigma_j(t)\rangle$. The site index j can be arbitrary since the state remains translationally invariant during the evolution. Again, exactly solving the time evolution of Σ_j is very difficult due to the mismatch between the JW fermion boundary conditions in the even and odd sectors. In order to remedy this obstacle, we adopt the factorization trick of McCoy *et. al* [20]. Instead of considering $\langle \Sigma_j(t) \rangle$ directly, we consider

$$\langle \Sigma_j(t)\Sigma_{j+\ell}(t)\rangle \approx \langle \Sigma_j(t)\rangle\langle \Sigma_{j+\ell}(t)\rangle \tag{2.27}$$

for separations $\ell \gg vt$, where v is some characteristic velocity for the spreading of quantum correlations. In this limit, we expect that the above approximation is very accurate based on reasoning similar to Lieb-Robinson bound [21], although we have not tried to prove this rigorously.

Since $\Sigma_j\Sigma_{j+\ell}$ does not mix the even and odd sectors, the above trick enables us to deal separately with the two sectors. Furthermore, it is sufficient to consider the even sector only and calculate the quantity

$$R(\ell, t) \equiv \langle \psi_{\text{ini,B}}|\Sigma_j(t)\Sigma_{j+\ell}(t)|\psi_{\text{ini,B}}\rangle \, , \tag{2.28}$$

where we choose the initial state as $|\psi_{\text{ini,B}}\rangle = |\psi_{\text{g.s.,even}}\rangle$, since we expect the contribution from $|\psi_{\text{g.s.,odd}}\rangle$ will essentially be identical in the thermodynamic limit [6].

In the fermionic representation,

$$R(\ell, t) = \langle \psi_{\text{ini,B}}| \left(\prod_{j'=j}^{j+\ell-1} B_{j'}(t) A_{j'+1}(t) \right) |\psi_{\text{ini,B}}\rangle \, , \tag{2.29}$$

where we defined Majorana fermions $A_j = c_j^\dagger + c_j$ and $B_j = c_j^\dagger - c_j$. It is easy to perform calculations in the Schrodinger picture of the time evolution. Thus,

$$\begin{aligned} |\psi_{\text{ini,B}}(t)\rangle &= e^{-iHt} \prod_{k>0} (u_k^* - v_k^* c_k^\dagger c_{-k}^\dagger) e^{iHt} e^{-iHt} |\text{vac}_c\rangle \\ &= \prod_{k>0} (u_k^* - v_k^* c_k^\dagger c_{-k}^\dagger e^{-i2\epsilon_k t}) |\text{vac}_c\rangle \\ &= \prod_{k>0} [u_k^* - v_k^*(t) c_k^\dagger c_{-k}^\dagger] |\text{vac}_c\rangle \, , \end{aligned} \tag{2.30}$$

where the dynamics can be considered as an evolution of the coherence factor $v_k(t) \equiv v_k e^{2i\epsilon_k t}$.

Since the above state can be viewed as a BCS ground state of a Hamiltonian with the corresponding coherence factors at every instant, the Wick's theorem holds for

$|\psi_{\mathrm{ini,B}}(t)\rangle$ at every time t. In order to apply the Wick's theorem, we need to evaluate the following two-operator correlation functions:

$$\begin{aligned}
\langle A_m A_n\rangle &= \frac{1}{L}\sum_k \left[1-\sin\theta_k \sin(2\epsilon_k t)\right] e^{ik(m-n)}\,,\\
\langle B_m B_n\rangle &= \frac{1}{L}\sum_k \left[-1-\sin\theta_k \sin(2\epsilon_k t)\right] e^{ik(m-n)}\,,\\
\langle A_m B_n\rangle &= \frac{1}{L}\sum_k \left[\cos\theta_k + i\sin\theta_k \cos(2\epsilon_k t)\right] e^{ik(m-n)}\,,\\
\langle B_m A_n\rangle &= \frac{1}{L}\sum_k \left[-\cos\theta_k + i\sin\theta_k \cos(2\epsilon_k t)\right] e^{ik(m-n)}\,.
\end{aligned}$$

For conciseness, we define Toeplitz matrices with elements $[\mathtt{AA}]_{m,n} = \langle A_m A_n\rangle$ when $m \neq n$ and $[\mathtt{AA}]_{m,n} = 0$ when $m = n$; $[\mathtt{BB}]_{m,n} = \langle B_m B_n\rangle$ when $m \neq n$ and $[\mathtt{BB}]_{m,n} = 0$ when $m = n$; $[\mathtt{BA}]_{m,n} = \langle B_m A_{n+1}\rangle$; and $[\mathtt{AB}]_{m,n} = \langle A_{m+1} B_n\rangle$. $[\mathtt{AA}]$ and $[\mathtt{BB}]$ are antisymmetric matrices while $[\mathtt{AB}] = -[\mathtt{BA}]^T$. We then define a $2\ell \times 2\ell$ matrix M as a block Toeplitz matrix with elements

$$\begin{pmatrix} M_{2m-1,2n-1} & M_{2m-1,2n} \\ M_{2m,2n-1} & M_{2m,2n}\end{pmatrix} = \begin{pmatrix} [\mathtt{BB}]_{m,n} & [\mathtt{BA}]_{m,n} \\ [\mathtt{AB}]_{m,n} & [\mathtt{AA}]_{m,n}\end{pmatrix}\,, \tag{2.31}$$

where $m, n = 1, \ldots, \ell$. Note that the matrix M is antisymmetric. Applying Wick's theorem to Eq. (2.29) with $j = 1$, we then have $R(\ell, t) = \mathrm{Pf}(M)$, the Pfaffian of the above matrix M.

Before discussing the time evolution, let us consider properties of the initial state encoded in $R(\ell, t = 0)$, which is a specific boson-boson correlation function in the initial state $|\psi_{\mathrm{ini,B}}\rangle$. This correlation function exhibits two different behaviors depending on the parameters of H_{ini}. At $t = 0$, matrices $[\mathtt{AA}]$ and $[\mathtt{BB}]$ are zero, and by rearranging the columns and rows of the matrix M, we obtain

$$R(\ell, t=0) = (-1)^{\ell(\ell-1)/2}\mathrm{Pf}\begin{pmatrix} 0 & [\mathtt{BA}] \\ -[\mathtt{BA}]^T & 0\end{pmatrix} = \det[\mathtt{BA}]\,,$$

where matrix $[\mathtt{BA}]$ is evaluated at $t = 0$. Thus, $R(\ell, t = 0)$ is equal to the determinant of the Toeplitz matrix $[\mathtt{BA}]$. The asymptotic behavior at large ℓ is given by Szegö's theorem [22],

$$\lim_{\ell\to\infty} R(\ell, t=0) \sim C e^{\lambda_0 \ell}\,, \tag{2.32}$$

where C is a constant and $\lambda_0 = \int_{-\pi}^{\pi} \frac{dk}{2\pi} \log(e^{-i\theta_k} e^{-ik})$. When $\lambda_0 \neq 0$, which occurs for $|\mu_0| > 2|J_0|$, we have exponential decay of the correlation function. On the other hand, when $\lambda_0 = 0$, which occurs for $|\mu_0| < 2|J_0|$, the correlation function approaches a non-zero constant, signaling a long-range order in the boson BEC order parameter. Note that in terms of the Jordan-Wigner fermions, conditions $|\mu_0| > 2|J_0|$ and $|\mu_0| < 2|J_0|$ correspond respectively to the trivial and topological superconductor phase in the one-dimensional spinless superconductor [23, 24] (i.e., strong-coupling and weak-coupling superconducting phases in the sense of Read and Green, Ref. [25]). Thus, we have analytically proven an earlier numerical finding in Ref. [26] that the topological phase of JW fermions corresponds to the single-boson long-range order, while the trivial phase corresponds to short-range order; both phases clearly have long-range order in the pair-boson correlator. We then choose our initial state to be in the regime of the weak-coupling (topological) phase of the JW fermions, which hence has non-vanishing long-range order (BEC) in terms of the original bosons.

After specifying the suitable initial state, we can now discuss the dynamics. Figure 2.10 shows $R(\ell, t)$ calculated for various separations ℓ in a system with total length $L = 400$. We are interested in the regime where $t \ll \ell/v$, where v is some characteristic velocity for the information spreading. We unambiguously see that $R(\ell, t)$ shows an exponential decay over some time interval that increases with increasing separation ℓ. This behavior corresponds to the exponential decay of $\langle \Sigma_j(t) \rangle$ with time, as claimed earlier for the BEC order.

On the other hand, we can also consider $\langle \Sigma_j(t)\Sigma_{j+1}(t) \rangle$, which is similar to the pair-boson observable we considered earlier that does not change the particle number parity. In this case,

$$\begin{aligned} \langle \Sigma_j(t)\Sigma_{j+1}(t) \rangle &= [\mathtt{BA}]_{1,1} = \langle B_1 A_2 \rangle \\ &= \frac{1}{L}\sum_k \left[-\cos\theta_k + i \sin\theta_k \cos(2\epsilon_k t) \right] e^{-ik} \; . \end{aligned} \tag{2.33}$$

At long time, this approaches a constant value given by $\langle b_j^\dagger(t) b_{j+1}(t) \rangle +$ c.c.. The time-dependent part comes from $\langle b_j^\dagger(t) b_{j+1}^\dagger(t) \rangle$+c.c.; upon using the steepest descent analysis, we find oscillations at frequencies $2\epsilon_{k=0/\pi}$ with a power law envelope $t^{-3/2}$, similar to results in the previous subsection for the product BEC initial state. We expect similar behaviors for any fixed ℓ at long times $t \gg \ell/v$: indeed, we expect $\lim_{t\to\infty} \langle b_j^\dagger(t) b_{j+\ell}(t) \rangle = \langle b_j^\dagger b_{j+\ell} \rangle_{\text{therm.}} \equiv C_{\text{therm.}}(\ell) \neq 0$, where $C_{\text{therm.}}(\ell)$ decays exponentially with ℓ. On the other hand, we expect $\lim_{t\to\infty} \langle b_j^\dagger(t) b_{j+\ell}^\dagger(t) \rangle = 0$, where the approach to zero has a power-law envelope $\sim t^{-3/2}$. These predictions are based on our expectations that at long times local observables can be described

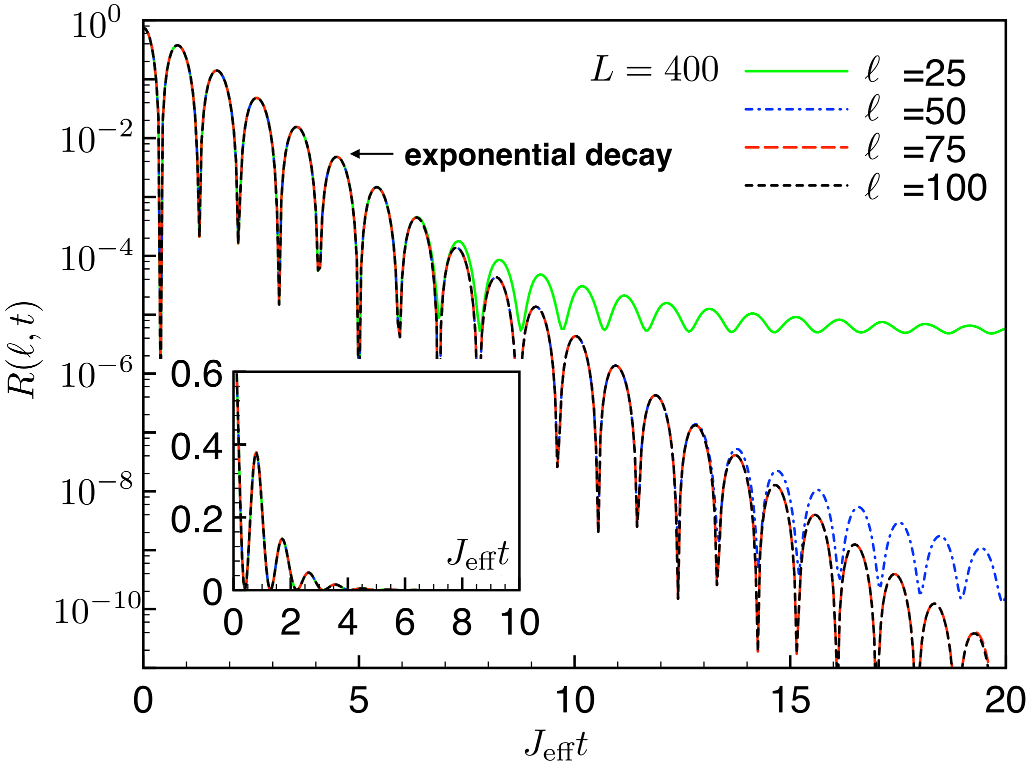

Figure 2.10: (color online) Numerical results for $R(\ell, t)$ obtained using the Pfaffian method; the system size is $L = 400$, and we consider separations $\ell = 25, 50, 75$, and 100. The initial state is the ground state of Eq. (2.25) with parameters $\Delta_0 = 0.60$ and $\mu_0 = -1.60$, corresponding to particle density $\rho = 0.25$. The parameters of the dynamical Hamiltonian are chosen as $J_{\mathrm{eff}} = 1$ and $W_{\mathrm{eff}} = 5$. We are primarily interested in the regime $t \ll \ell/v$, where v is some information-spreading velocity. In this regime, the observable exhibits exponential decay. The time interval over which we see the exponential decay increases as the separation ℓ increases.

using a generalized Gibbs ensemble which is diagonal in the particle number, and that for large $t \gg \ell/v$ the physics of $b_j^\dagger(t) b_{j+\ell}^\dagger(t)$ is that of a local pair-boson creation operator.

We thus see significant care needed when using $R(\ell, t)$ to extract the behavior of the BEC order parameter $\langle b_j^\dagger(t) \rangle$ using Eq. (2.27) which holds only for $t \ll \ell/v$. In Fig. 2.10 we chose to show $\langle \Sigma_j(t) \Sigma_{j+\ell}(t) \rangle$ with $\Sigma_j = b_j^\dagger + b_j$ so that the regime where the sites j and $j + \ell$ start to "feel each other" is manifest by approaching a constant due to $\langle b_j^\dagger(t) b_{j+\ell}(t) \rangle$ + c.c. pieces as discussed above (if we only had $\langle b_j^\dagger(t) b_{j+\ell}^\dagger(t) \rangle$ + c.c. pieces, this time scale would manifest as a crossover from the exponential to $t^{-3/2}$ decay and would be more difficult to detect).

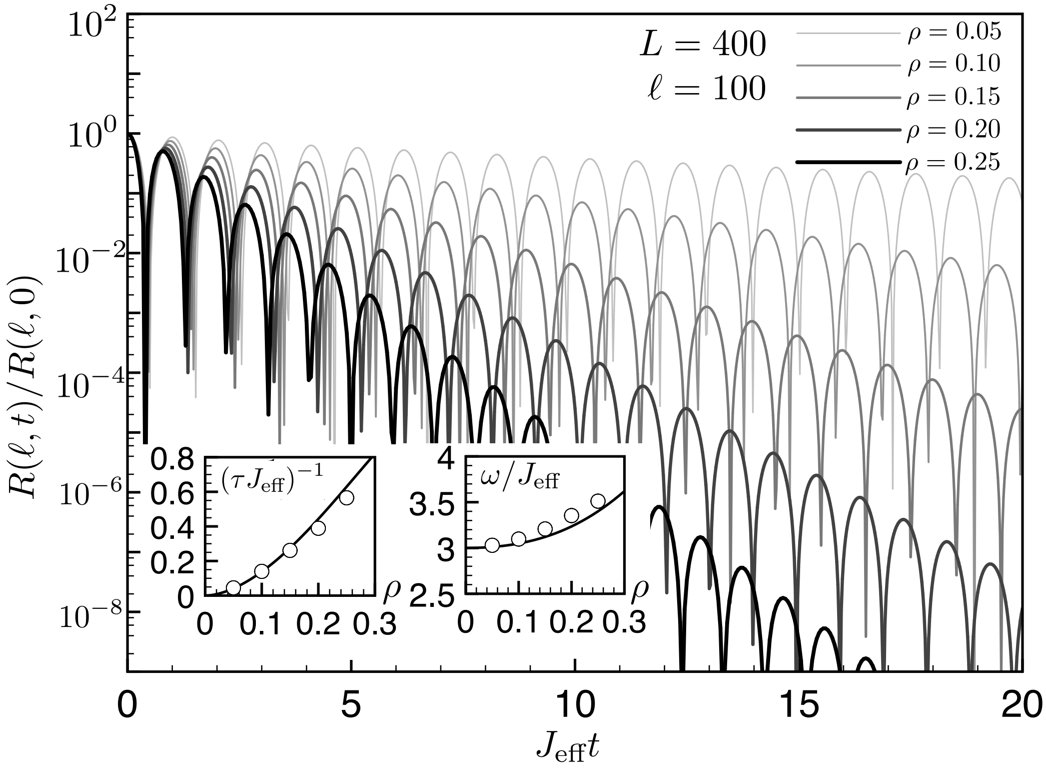

Figure 2.11: $R(\ell, t)$ as in Fig. 2.10 but for different average densities ρ obtained by tuning μ_0 and Δ_0 according to Eq. (2.35) and Eq. (2.36) respectively. We show only the largest separation $\ell = 100$; the full system size is $L = 400$ and is sufficiently large to reflect the thermodynamic limit in L. The values are normalized by the initial value in order to bring out the decay rate, which clearly increases as the density increases. Insets: inverse relaxation time τ^{-1} of the exponential decay and the oscillation frequency ω as a function of density, obtained from fitting the data in the main panel to form $Ae^{-2t/\tau}\cos^2(\omega t - \alpha) + C$. The circle symbols denote the fitted values, while the solid lines denote the conjectured forms Eq. (2.23) and Eq. (2.24) for τ^{-1} and ω respectively (see text for details).

In order to study the density dependence of the decoherence time of the long-range order and compare with the results in the previous subsection, it is tempting to tune the parameters of $|\psi_{\text{ini, B}}\rangle$, μ_0 and Δ_0, such that the density and the energy density are equal to those in $|\psi_{\text{ini, A}}\rangle$. In fact, when trying to achieve this, we found that it is possible to make the JW fermion mode distribution $\langle n_k \rangle$ identical in the two initial states in the thermodynamic limit! The mode occupation number in $|\psi_{\text{ini, B}}\rangle$ is given as $\langle n_k \rangle = |v_k|^2$, or

$$\langle n_k \rangle = \frac{1}{2}\left(1 - \frac{-2J_0\cos(k) - \mu_0}{\sqrt{(2J_0\cos(k) + \mu_0)^2 + [2\Delta\sin(k)]^2}}\right) . \tag{2.34}$$

One can easily verify that if we take

$$\mu_0 = -2\sqrt{J_0^2 - \Delta_0^2} \tag{2.35}$$

and

$$\Delta_0 = J_0\frac{2\rho(1-\rho)}{\rho^2 + (1-\rho)^2} , \tag{2.36}$$

the mode occupation number will become identical to Eq. (2.22). Here we assumed $\rho < 0.5$, while for $\rho > 0.5$ we need to take the opposite sign for μ_0 in Eq. (2.35). In retrospect, by examining the JW fermion pair-function in real-space for the topological superconductor with the condition Eq. (2.35), we can show that the many-body wavefunction $|\psi_{\text{ini, B}}\rangle$ in the boson representation exactly coincides with that of the BEC state Eq. (2.14) when *projected to any sector with fixed particle number*. The relative weights on the different number sectors do not coincide for $|\psi_{\text{ini, A}}\rangle$ and $|\psi_{\text{ini, B}}\rangle$, but this is not important in the thermodynamic limit.

Figure 2.11 shows $R(\ell, t)$ with $\ell = 100$ and system size $L = 400$ for several different densities $\rho = 0.05$ to $\rho = 0.25$, with μ_0 and Δ_0 chosen according to Eq. (2.35) and Eq. (2.36). We use the formula $Ae^{-2t/\tau}\cos^2(\omega t - \alpha) + C$ to fit our numerical data hence obtaining the fitted lifetime τ and frequency ω. The left inset compares the fitted inverse lifetime τ^{-1} denoted by circles and the conjectured inverse lifetime based on Eq. (2.23) denoted by solid line. The agreement between the two is fairly good and therefore supports our conjecture. The right inset compares the fitted frequency (denoted as circles) and the conjectured frequency (solid line) based on Eq. (2.24). The oscillation frequency also agrees with the conjecture quite well.

We hence see that the new choice of the initial state $|\psi_{\text{ini,B}}\rangle$, equipped with Wick's theorem, enables us to calculate the evolution for much larger system size (essentially in the thermodynamic limit). We therefore further confirm the exponential decay of

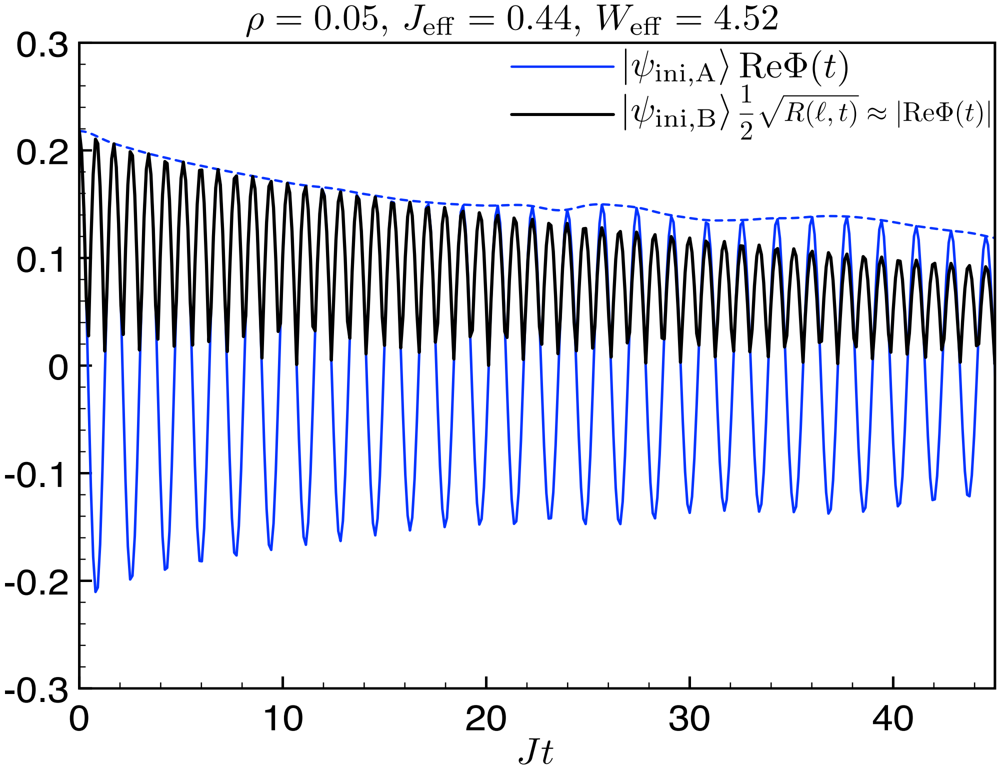

Figure 2.12: (color online) Evolution of $\mathrm{Re}[\Phi(t)]$ for the initial state $|\psi_{\text{ini, A}}\rangle$ and system size $L = 20$ and $|\mathrm{Re}[\Phi(t)]|$ calculated from $\frac{1}{2}\sqrt{R(\ell, t)}$ for the initial state $|\psi_{\text{ini, B}}\rangle$ with separation $\ell = 100$ and system size $L = 400$, both with density $\rho = 0.05$. The dynamical Hamiltonian has $J_{\text{eff}} = 0.44$ and $W_{\text{eff}} = 4.52$, chosen to reproduce the spin-flip quasiparticle dispersion and gap $W_{\text{eff}} - 2J_{\text{eff}} = \Delta E = 3.64$ in the original spin problem. The relaxation times obtained by fitting the exponential decay regime as in Fig. 2.9 and Fig. 2.11 are $\tau_A \approx 46.5$ and $\tau_B \approx 51.0$ respectively. This means that at time $t = 18$—the longest time simulated in the original spin problem—the amplitude will be roughly 0.7 of the initial value.

the BEC order parameter and provide strong numerical evidence for our conjecture of the density dependence of the inverse lifetime and frequency.

Application to the original spin problem

Returning to the original spin problem, in order to make more quantitative comparisons, Fig. 2.12 shows results for the initial states $|\psi_{\text{ini, A}}\rangle$ and $|\psi_{\text{ini, B}}\rangle$ evolving under the hard-core boson Hamiltonian with parameters $J_{\text{eff}} = 0.44$, $W_{\text{eff}} = 4.52$, and density $\rho = 0.05$. These are chosen to be close to the parameters of the spin-flip quasiparticles of the original spin problem, cf. Sec. 2.2. By fitting the exponential decay regime, we obtain the decoherence time $\tau_A \approx 46.5$ and $\tau_B \approx 51.0$, respectively, which are close to an estimate from Eq. (2.23) that gives $\tau \approx 54.7$ for these J_{eff} and ρ. The long lifetime is due to the low density of the quasiparticles (due to low energy density in the initial state), and is the primary reason of the apparent persistent oscillation in the original spin problem. We see that up to time $t = 18$ simulated in the original spin problem in Ref. [1], the amplitude of interest decays to roughly 0.7 of the initial value. The exponential decay is not easily seen in this time range, while it becomes more clear when one goes to longer times. The $L = 20$ ED results in Fig. 2.12 again show recurrence phenomenon starting from about $t \sim 15 - 20$, while the Pfaffian calculation results represent the thermodynamic limit.

We remark that Fig. 2.1 hardly shows any decay while Fig. 2.12 shows some gradual decay already for $t \leq 18$. There could be several reasons for this. The decrease from the initial value in Fig. 2.1 is actually significant, and it could be that the first few oscillations happened to experience stronger decrease due to some microscopics, which then masked the more systematic decay expected at long times. In this respect we remind that the hard-core boson model studied in this section neglected all interactions among the quasiparticles of the spin model other than their hard-core exclusion, see Eq. (2.4) and discussion at the end of Sec. 2.2 (and we also remind that the BEC is only an approximation to the initial state of the quasiparticles). While we would expect that additional interactions generically help the thermalization, we do not know the actual quantitative effect which can depend on details and requires more studies. We also mention that in the truncated Schrieffer-Wolff approach the observables also obtain components on the pair-boson-type operators and hence will have additional power-law-decaying contributions in the hard-core boson model (which should eventually also decay exponentially once integrability-breaking interactions are included). All such unaccounted parts could have enough effect up to $t = 18$ to make the oscillation appear more persistent, while they eventually decay at longer times. We therefore propose that if one can simulate the original spin problem to somewhat longer time, one will eventually observe the decay of the oscillations.

In fact, the Supplemental Material of Ref. [1] also showed a study for parameter $g = -1.5$, where the observables showed visible decays, which we believe can be understood as due to the larger particle density and hence shorter decoherence time. Our ED calculations give energy density in the $|Z+\rangle$ state over the ground state as $(\langle Z+|H|Z+\rangle - E_0)/L = 0.4581$ and the quasiparticle gap as $E_1 - E_0 = 3.2041$, so the quasiparticle density in the ground state is roughly $\rho \approx 0.143$. For this density, Eq. (2.21) gives $J_{\rm eff}\tau \approx 3.935$. From our ED data, we can also extract the quasiparticle hopping amplitude $J_{\rm eff} \approx 0.656$. This gives us $\tau \approx 6$, which was already accessible in the infinite-MPS study in Ref. [1], and our estimates of the oscillation frequency and decay time are in rough agreement with this.

We note another lesson learned from the detailed study of the relaxation of the order parameter in the hard-core boson model. While our original stipulation was that the oscillation frequency is set by the quasiparticle gap, we now see that it is actually a function of the quasiparticle density, see Eq. (2.24). We should indeed expect this generically as the quasiparticle energy is strictly defined only in the limit of vanishing energy density, while here the initial state has a finite energy density (e.g., quasiparticle energies can get renormalized by their residual interactions, etc.). In this respect, the single-boson observable shows more generic behavior even in the integrable hard-core boson model, in contrast to the pair-boson observable whose oscillation frequencies are independent of the density. In any case, the original spin model at $g = -1.05$ is at sufficiently low energy density that the oscillation frequency is very close to the quasiparticle gap, and we did not worry about differentiating between these in the previous sections.

While the above discussions are based on the hard-core boson hopping Hamiltonian, H in Eq. (2.10), we now briefly consider effects of adding more generic interactions. To understand these, we calculated the BEC order parameter $\Phi(t)$ and the pair-boson correlation function $\Upsilon(t)$ evolving under (a) $H_{\rm nn} = H + W_{\rm nn} \sum_j n_j n_{j+1}$; (b) $H_{\rm nnn} = H_{\rm nn} + W_{\rm nnn} \sum_j n_j n_{j+2}$; and (c) $H_{\rm eff}$ from Eq. (2.4) upon dropping $H_{\rm other}$. In each case, the initial state is $|\psi_{\rm ini,A}\rangle$.

Plots Fig. 2.13 (a)-(c) show the corresponding $\Phi(t)$ and $\Upsilon(t)$ results for system size $L = 14$ and particle density $\rho = 0.05$, which is close to the original spin model. On the other hand, plots in Fig. 2.13 (d) shows $\Phi(t)$ and $\Upsilon(t)$ for $\rho = 0.25$ and system size $L = 20$; this is far from the original spin model but allows us to reduce effects due to low particle density and to focus instead on qualitative effects of interactions. We find that the additional interaction terms do not change the qualitative exponential decay behavior of $\Phi(t)$. This is less clear for low density, plots (a1)-(c1), but in these cases, the effect of interactions are also quantitatively small, and we believe the decays are still exponential at long time. On the other hand, the behavior of the pair-boson correlation function $\Upsilon(t)$ changes qualitatively. The power-law decay of $\Upsilon(t)$ in the hard-core boson hopping model is a consequence of the exact solution

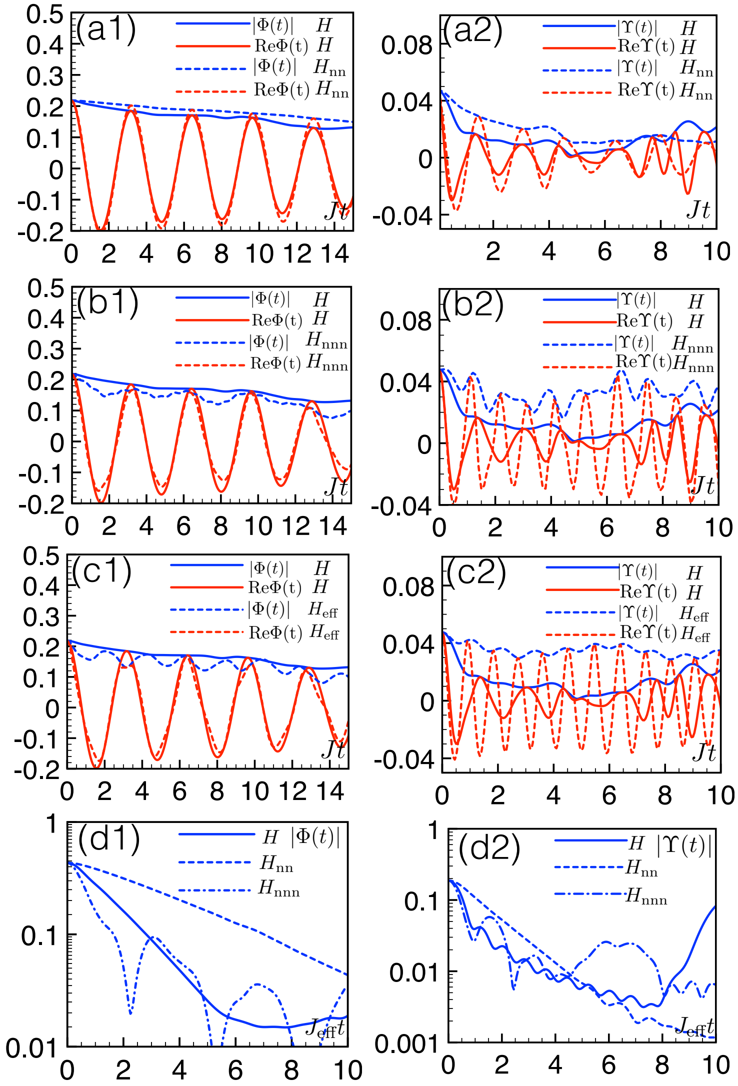

Figure 2.13: (color online) Comparison of the dynamics under the simplified hard-core boson Hamiltonian H in Eq. (2.10) and under various Hamiltonians with different additional interactions. The initial state is $|\psi_{\mathrm{ini,A}}\rangle$. (a)-(c) BEC order parameter (left panels) and pair boson correlation function (right panels) for density $\rho = 0.05$ and system size $L = 14$. The parameters of H_{eff} are obtained from second-order SW for the original spin model, and similar parameters are also used in H, H_{nn}, H_{nnn}: $J_{\mathrm{eff}} = 0.88$, $W_{\mathrm{eff}} = 3.68$, $W_{\mathrm{nn}} = -0.47$, and $W_{\mathrm{nnn}} = 2.35$ (in units of J). The additional interactions basically introduce a small amplitude oscillation in $\Phi(t)$. For the pair boson correlation function, the decay behavior and the oscillation frequencies are affected more strongly (see text for details). (d) BEC order parameter $\Phi(t)$ and pair-boson correlation function $\Upsilon(t)$ for density $\rho = 0.25$, system size $L = 20$ and parameters $J_{\mathrm{eff}} = 1.0$, $W_{\mathrm{eff}} = 1.0$, $W_{\mathrm{nn}} = -0.5$, and $W_{\mathrm{nnn}} = 1.5$ (the results for H are identical as in Fig. 2.6 and 2.7). The additional interaction of the JW fermions in H_{nn} changes the decay in $\Upsilon(t)$ to be faster than the previous power law.

in terms of the non-interacting JW fermions. From Fig. 2.13 (d2), it appears that as we turn on the interaction of the fermions, the power-law decay behavior is destroyed. The addtional interaction in H_{nn} turns $\Upsilon(t)$ into a faster decay; under H_{nnn}, the behavior of $\Upsilon(t)$ is not clear and needs more study. While we would expect exponential decay for generic interactions, this appears to be also true for H_{nn} which is still integrable; we speculate this is because the true excitations are no longer JW fermions.

Finally, we note that for H_{eff}, the behavior of $\Upsilon(t)$ is somewhat special. The reason is that localized bound states of two spin-flip quasiparticles (i.e., two consecutive spin-downs in the background of spin-ups) happen to be exact eigenstates of H_{eff}, since the correlated hopping terms just annihilate these states. Therefore, these bound states are immobile in H_{eff}, which can be detected by $b_j^\dagger b_{j+1}^\dagger$. As a result, the pair-boson correlation function oscillates without decay, which is an artifact of this second-order truncated-SW Hamiltonian. However, if we introduce dynamics for these bound states, for example, considering SW transformation to higher order, we expect the oscillations to damp. The physics of such bound states also manifests itself in short-time enhancement of pair-boson correlations in H_{nn} and H_{nnn}, plots Fig. 2.13 (a2)-(b2), although in these cases the hopping terms in the Hamiltonians do move the bound states, and we expect exponential decays on long time, similar to Fig. 2.13 (d2). Clearly, one has to consider short-distance physics details to understand these results in the pair-boson correlation function quantitatively. Nevertheless, as far as observables discussed in the original spin model, since the pair-boson contributions are sub-dominant to the single-boson contributions, we expect the exponential decay behavior is robust under adding interactions to the simplified hard-core boson hopping Hamiltonian.

2.4 A quick study of “non-thermalizing" initial state $|X+\rangle$

In the same spin model, Ref. [1] also found apparent “non-thermalizing" behavior for the initial state $|X+\rangle$. This case shows much smaller oscillations than the weak thermalization case, but apparently observables approach non-thermal values at the longest simulation times. While we do not have as clear picture of this case compared to the weak thermalization case, we will briefly discuss how far similar physical reasoning can take us in the non-thermalizing case.

First of all, the initial state $|X+\rangle$ lands close to the top of the spectrum of the original Hamiltonian, Eq. (2.1). Equivalently, it is close to the ground state of the

Hamiltonian $\tilde{H} = -H$; this is the language we adopt since we are more used to thinking about ground states and low-energy excitations. Here, we can develop a perturbative treatment starting with $J, h \ll |g|$, where the ground state is guaranteed to be close to $|X+\rangle$. Such a perturbative treatment is, in fact, fairly reasonable for the parameters of interest $J = 1, h = 0.5, g = -1.05$: indeed, h is smaller than g, while for states with aligned spins the $+J\sigma_j^z\sigma_{j+1}^z$ terms in $\tilde{H}$ are frustrated. We find that the $|X+\rangle$ state has weight $|\langle\tilde{E}_0|X+\rangle|^2 \approx 23\%$ on the ground state of $\tilde{H}$ for $L = 18$, which is smaller than in the weak thermalization case but is still a large weight. The average energy density in the initial state is $\langle X+|\tilde{H}|X+\rangle/L - \tilde{E}_0/L \approx 0.28$ is somewhat larger than in the weak thermalization case.

In the perturbative picture, low-energy excitations are spins oriented in the $-\hat{x}$ direction (i.e., flipped compared to the ground state $|X+\rangle$), with dispersion at leading order $\epsilon_k = 2|g| + 2J\cos(k)$. The bottom of the quasiparticle band now lies at $k = \pi$ and can be quite close to the ground state, since $\epsilon_{k=\pi} = 2|g| - 2J$ becomes small for J approaching $|g|$. Our ED results indeed show a fairly small gap at $k = \pi$; the gap is likely smaller than 0.35 in the thermodynamic limit and has strong even-odd effect on L coinciding with whether the mesh of k-points contains π or not. This gap is an order of magnitude smaller than the quasiparticle gap of interest in the weak thermalization case. Of relevance to the study of translationally invariant initial states, the gap to the lowest excitation with momentum $k = 0$ is larger. This gap also has strong even-odd effect on L and is likely smaller than 1.0, which is almost four times smaller than in the weak thermalization case. The lowest $k = 0$ excitation is likely a composite of two quasiparticles near the bottom of the band at momentum π, i.e., it is not simply a single spin-flip of the band $\epsilon_k = 2|g| + 2J\cos(k)$ at $k = 0$. Finally, the apparent velocity for the propagation of quantum correlations is two or more times larger than in the weak thermalization case, as judged from the observed much shorter recurrence times in our finite systems.

All of the above points to a more complex picture in terms of quasiparticles, which are likely moving faster but are also less sharp due to smaller gap and stronger mixing with multi-particle states. Hence, our intuition is that the system should relax faster, which is indeed observed in Ref. [1]. However, we would also naively conclude that the system will approach the "thermalized" state, contrary to what is observed in Ref. [1] on the accessible simulation times. It is possible that the thermalization does eventually happen, but the combined effects of the smallness of the gap and frustrating interactions produce a complex behavior on intermediate time scales. At the same time, the quantum correlations spread more quickly, which limits the accessible simulation times before entanglement increases too much in the infinite-MPS study. A very interesting possibility would be if this system does not thermalize in the conventional sense because of some emergent integral of motion, perhaps of the kind discussed in Refs. [17, 18] and in our discussion of the truncated SW picture earlier. Alternatively, it could be that it thermalizes very slowly because of an approximate integral of motion. Since we are unable to provide a more controlled understanding of the non-thermalizing behavior, we leave this as an interesting open problem.

2.5 Conclusions

We studied the origin and eventual fate of strong oscillations in specific quantum quenches in the non-integrable spin model, where the initial state has low energy density relative to the ground state. By extrapolating our finite-size ED calculations, we were able to interpret the oscillation frequency as the quasiparticle creation energy. We further used SW transformation to derive the effective Hamiltonian to have a better description of the quasiparticles at finite density. The time evolution problem can be viewed as a quench from a dilute BEC state to an interacting hard-core boson Hamiltonian. The oscillation signal mainly comes from the observables changing the particle number by one.

Inspired by the finite-size ED and perturbative SW calculations, we further simplified the problem by considering two specific BEC initial states and the hard-core boson Hamiltonian with hopping only. This problem is interesting on its own even without the context of the spin problem we discussed. We considered first the initial state as a simple product state analogous to the boson coherent state but under hard-core constraint. The other initial state was prepared as a topological superconductor in the Jordan-Wigner fermionic representation, which we argued has long range order in the bosonic representation and is qualitatively in the same BEC phase as the first state. Furthermore, Wick's theorem is valid for this state, allowing us to obtain results for much larger systems and longer times via the Pfaffian method.

Incidentally, we discovered that under the condition Eq. (2.35), the topological superconductor wave function, when written in terms of bosons and projected into a sector with a fixed particle number, has amplitudes independent of the positions of the particles, thus becoming the initial BEC state studied in Refs. [10] and [11]. Since the restriction to fixed particle number is not important in the thermodynamic limit, in principle, one can study essentially the same quench problems but with the advantage of Wick's theorem. The bosonic two-point correlation function hence reduces to an evaluation of a block Toeplitz determinant with 2×2 blocks. Such block Toeplitz determinants are not as well studied, and we have not been able to obtain an analytical expression in our case (e.g., some of the calculation tricks in Ref. [6] were not directly applicable to our problem). Finding such a compact expression for the correlation functions remains an interesting outstanding problem.

Our numerical calculations strongly suggest that the BEC order parameter $\langle b_j^\dagger(t) \rangle$ decays exponentially with time. Both the decay rate and the oscillation frequency depend on the boson density. We believe that the exponential decay originates from the non-local nature of the boson creation operator in terms of the JW fermions. The non-locality of the operator excites quasiparticles at all momenta, whose interferences produce the exponential decay. Using analogy with quenches from the ferromagnetic state in the quantum Ising chain [6, 8], we conjectured the inverse lifetime as Eq. (2.21), and hence obtained explicit density dependence of the lifetime. We also conjectured that the oscillation frequency depends on the density as Eq. (2.24). On the other hand, the pair-boson observable $\langle b_j^\dagger(t) b_{j+1}^\dagger(t) \rangle$ also has oscillations but with a $t^{-3/2}$ power-law decay, and the oscillation frequencies and power-law decay behavior are independent of the density in the initial state.

As an open problem for quenches from the BEC state, it will be interesting to study the validity of our conjectures for the decoherence time and oscillation frequency in the specific hard-core boson hopping model. Our calculation of the different decaying behaviors for single- and pair-boson observables can in principle be distinguished and verified in cold atom experiments such as the setting in Ref. [9], with non-zero hopping and much stronger on-site interaction. It will also be interesting to add integrability-preserving and integrability-breaking interactions to the hard-core boson hopping model and study how these affect the described behaviors.

Returning to the original spin system exhibiting weak thermalization, we made several approximations and simplifications when mapping this to the BEC quench problem. In particular, we implicitly introduced an additional conserved quantity in our SW treatment by dropping H_{other} terms that connect different sectors. Specifically, our truncated-SW Hamiltonian conserves the sector identity, or equivalently the total quasiparticle number. An interesting possibility would be that such successive SW transformations developed to higher orders converge, implying true emergence of such integrals of motions in the translationally invariant system, in the spirit of Refs. [17, 18]. One can also view this SW transformation as a kind of renormalization, which pushes the effect of changing the excitation numbers to lower energy in the effective Hamiltonian, but at the expense of making the original observables more complex. However, at present we do not know how to address this interesting possibility in thermodynamically large systems.

Fairly conservatively, we would expect that the dropped terms in the Hamiltonian would lead to improved thermalization, in the sense that the system is more generic and likely to thermalize at long times. Since even without those dropped terms and with the simplified initial state structure, we showed that the oscillation signal still decays, we expect in the full problem the oscillations will decay in the long time limit. Nevertheless, the decay becomes slower as we decrease the quasiparticle density and can be particularly slow at small density. Therefore, we boldly conclude that the oscillation will decay eventually in the weak thermalization regime, and the apparently persistent oscillation is due to its slow decay rate as a result of the low density of the quasiparticles.

We would also like to mention a puzzling problem regarding the $|X-\rangle$ initial state studied in Ref. [3], which also shows the persistent oscillation behavior up to time $t = 20$. This state is also on the lower end of the spectrum, but with three times higher energy density than the $|Z+\rangle$ state. Our naive estimation using the hard-core boson hopping model would give us a much shorter decoherence time disagreeing with the infinite-MPS simulation. We suspect that to get a more quantitative agreement, we need to incorporate further details about the quasiparticle interactions, such as those discussed at the end of Sec. 2.2. We will leave this for the future work.

Appendix A: Local Schrieffer-Wolf Transformation

We consider H_0, Eq. (2.2), as our basic solvable Hamiltonian and treat T, Eq. (2.3), as our perturbation. The latter can be decomposed as

$$T = T_{1,2} + T_{-1,-2} + T_{1,0} + T_{-1,0} + T_{1,-2} + T_{-1,2} \,, \tag{2.37}$$

with

$$\begin{aligned} T_{1,2} &= -g \sum_j P^{\uparrow}_{j-1} \sigma^-_j P^{\uparrow}_{j+1}\,, \\ T_{-1,-2} &= -g \sum_j P^{\uparrow}_{j-1} \sigma^+_j P^{\uparrow}_{j+1}\,, \\ T_{1,0} &= -g \sum_j \left(P^{\uparrow}_{j-1} \sigma^-_j P^{\downarrow}_{j+1} + P^{\downarrow}_{j-1} \sigma^-_j P^{\uparrow}_{j+1} \right)\,, \\ T_{-1,0} &= -g \sum_j \left(P^{\uparrow}_{j-1} \sigma^+_j P^{\downarrow}_{j+1} + P^{\downarrow}_{j-1} \sigma^+_j P^{\uparrow}_{j+1} \right)\,, \\ T_{1,-2} &= -g \sum_j P^{\downarrow}_{j-1} \sigma^-_j P^{\downarrow}_{j+1}\,, \\ T_{-1,2} &= -g \sum_j P^{\downarrow}_{j-1} \sigma^+_j P^{\downarrow}_{j+1}\,. \end{aligned}$$

Each $T_{m,n}$ satisfies $[H_0, T_{m,n}] = 2(mh + nJ)T_{m,n}$ and works like a generalized ladder operator on the energy levels of H_0. Furthermore, $T_{-m,-n} = T^{\dagger}_{m,n}$.

We develop a perturbative local Schieffer-Wolff approach following Ref. [15]. Consider a unitary transformation e^{iS} with the generator

$$iS = iS^{[1]} + iS^{[2]} + \dots\,, \tag{2.38}$$

where $iS^{[k]}$ is of order $O(g^k)$. We can expand the rotated Hamiltonian as

$$\begin{aligned} H' &\equiv e^{iS} H e^{-iS} = H_0 + T + [iS^{[1]}, H_0] \\ &+ [iS^{[1]}, T] + [iS^2, H_0] + \frac{1}{2}[iS^{[1]}, [iS^{[1]}, H_0]] + O(g^3)\,. \end{aligned}$$

The generators $iS^{[k]}$ are chosen order by order so as to eliminate the excitation-number-changing part of the previous order. Specifically, we choose $iS^{[1]}$ such that

$$T + [iS^{[1]}, H_0] = 0\,, \tag{2.39}$$

with the solution

$$iS^{[1]} = \frac{T_{1,2} - T_{-1,-2}}{2h + 4J} + \frac{T_{1,0} - T_{-1,0}}{2h} + \frac{T_{1,-2} - T_{-1,2}}{2h - 4J}\,. \tag{2.40}$$

To this order,

$$H' = H_0 + \frac{1}{2}[iS^{[1]}, T] + [iS^{[2]}, H_0] + O(g^3)\,, \tag{2.41}$$

where the second term contains both excitation-number-preserving terms (i.e., sector-diagonal terms) and excitation-number-changing terms (i.e., sector-off-diagonal terms), now in second order. To eliminate the excitation-number-changing-terms to this order, we choose $iS^{[2]}$ such that

$$\left(\frac{1}{2}[iS^{[1]}, T]\right)_{\text{sector-off-diag}} + [iS^{[2]}, H_0] = 0\,, \tag{2.42}$$

giving us

$$H' = H_0 + \left(\frac{1}{2}[iS^{[1]}, T]\right)_{\text{sector-diag}} + O(g^3)\,. \tag{2.43}$$

This is the Hamiltonian quoted in the main text, Eq. (2.4), with H_{other} containing terms of order $O(g^3)$.

While we do not need explicit $iS^{[2]}$ to determine the effective Hamiltonian to this order, we do use it when rotating the operators and the initial state in Sec. 2.2 in calculations leading to Fig. 2.4. Hence we quote the solution to Eq. (2.42):

$$\begin{aligned}
iS^{[2]} \;=\;& \left(\frac{1}{4h} - \frac{1}{8J-4h}\right)\frac{[T_{1,0}, T_{-1,2}] - \text{H.c.}}{4J}\\
&+ \left(\frac{1}{8J-4h} + \frac{1}{4h}\right)\frac{[T_{1,-2}, T_{1,0}] - \text{H.c.}}{4J-4h}\\
&+ \left(\frac{1}{4h} - \frac{1}{8J+4h}\right)\frac{[T_{1,0}, T_{1,2}] - \text{H.c.}}{4J+4h}\\
&+ \left(\frac{1}{4h} + \frac{1}{8J+4h}\right)\frac{[T_{-1,-2}, T_{1,0}] - \text{H.c.}}{4J}\\
&+ \left(\frac{1}{8J-4h} - \frac{1}{8J+4h}\right)\frac{[T_{-1,2}, T_{1,2}] - \text{H.c.}}{8J}\\
&+ \left(\frac{1}{8J+4h} + \frac{1}{8J-4h}\right)\frac{[T_{-1,-2}, T_{-1,2}] - \text{H.c.}}{4h}\,.
\end{aligned} \tag{2.44}$$

While in principle we can continue to obtain higher order effective Hamiltonians, the form of the previous order will not be changed. Note that in the main text, for the purpose of demonstrating the SW picture, we used the perturbatively truncated H', while we rotated the operators and the initial state using $\exp(iS^{[1]} + iS^{[2]})$ (i.e., without further expansion of the exponential). This was actually easier to implement and also guarantees that the operators and initial state are rotated by a unitary and will agree with perturbative treatment to this order (when studying dynamics, this also assumes appropriately small elapsed time). We did not use exact unitary rotation of the Hamiltonian since then the rotated problem would be unitarily equivalent to the original problem, with no new information. We expect that using truncated Hamiltonian, which in addition conserves excitation number, should make it only more difficult to thermalize, and we indeed do not observe any faster thermalization.

For completeness, we also present below the effective observables to first order, even though we did not explicitly use them in the main text. To obtain the observables in the rotated picture, we use the formula $\hat{O}' = e^{iS}\hat{O}e^{-iS} = \hat{O} + [iS^{[1]}, \hat{O}] + O(g^2)$. With $\hat{O} = \sigma_j^x, \sigma_j^y$ and, σ_j^z, we have

$$\begin{aligned}
(\sigma_j^x)' &\approx \sigma_j^x + \frac{g}{2h}(\sigma_{j-2}^z\sigma_{j-1}^y\sigma_j^y + \sigma_j^y\sigma_{j+1}^y\sigma_{j+2}^z + 2P_{j-1}^{\uparrow}\sigma_j^z P_{j+1}^{\downarrow} + 2P_{j-1}^{\downarrow}\sigma_j^z P_{j+1}^{\uparrow}) \\
&- \frac{g}{4J-2h}(P_{j-2}^{\downarrow}\sigma_{j-1}^y\sigma_j^y + \sigma_j^y\sigma_{j+1}^y P_{j+2}^{\downarrow} + 2P_{j-1}^{\downarrow}\sigma_j^z p_{j+1}^{\downarrow}) \\
&+ \frac{g}{4J+2h}(P_{j-2}^{\uparrow}\sigma_{j-1}^y\sigma_j^y + \sigma_j^y\sigma_{j+1}^y P_{j+2}^{\uparrow} - 2P_{j-1}^{\uparrow}\sigma_j^z P_{j+1}^{\uparrow}) \qquad (2.45) \\
(\sigma_j^y)' &\approx \sigma_j^y - \frac{g}{2h}(\sigma_{j-2}^z\sigma_{j-1}^y\sigma_j^x + \sigma_j^x\sigma_{j+1}^y\sigma_{j+2}^z) \\
&+ \frac{g}{4J-2h}(P_{j-2}^{\downarrow}\sigma_{j-1}^y\sigma_j^x + \sigma_j^x\sigma_{j+1}^y P_{j+2}^{\downarrow}) \qquad (2.46) \\
&- \frac{g}{4J+2h}(P_{j-2}^{\uparrow}\sigma_{j-1}^y\sigma_j^x + \sigma_{j+1}^y P_{j+2}^{\uparrow})\,,
\end{aligned}$$

and $(\sigma_j^z)'$ as in Eq. (2.9).

Appendix B: Calculation of $\langle b_j^\dagger(t) b_{j+1}^\dagger(t)\rangle$, Eq. (2.19).

In this Appendix, we present details of the calculation of $\Upsilon(t) \equiv \langle b_j^\dagger(t) b_{j+1}^\dagger(t)\rangle$ for the initial product BEC state. We first obtain a closed-form expression for the observable in a finite system of length L and then derive the thermodynamic limit Eq. (2.19). Since the Jordan-Wigner fermions have different boundary conditions in the even- and odd-number-parity sectors, when calculating the time evolution we split

$$\begin{aligned}
\Upsilon(t) &= \Upsilon_{\text{even}}(t) + \Upsilon_{\text{odd}}(t)\,, \qquad (2.47) \\
\Upsilon_{\text{even (odd)}}(t) &\equiv \langle P_{\text{even (odd)}} b_j^\dagger(t) b_{j+1}^\dagger(t) P_{\text{even (odd)}}\rangle\,, \\
& \qquad (2.48)
\end{aligned}$$

where $P_{\text{even (odd)}}$ is the projector to the even- (odd-)number-parity sector.

We can use translational invariance to consider instead $\langle \sum_j b_j^\dagger(t) b_{j+1}^\dagger(t)\rangle / L$. Keeping in mind implicit surrounding sector projectors, we can express

$$\frac{1}{L}\sum_j b_j^\dagger(t) b_{j+1}^\dagger(t) = \frac{1}{L}\sum_k c_k^\dagger c_{-k}^\dagger e^{ik} e^{i2\epsilon_k t} \tag{2.49}$$

$$= \frac{1}{L^2}\sum_k e^{ik} e^{i2\epsilon_k t} \sum_{j,j'} c_j^\dagger c_{j'}^\dagger e^{ik(j-j')} \tag{2.50}$$

$$= \frac{2}{L^2}\sum_k \sin(k) e^{i2\epsilon_k t} \sum_{j<j'} \sin[k(j'-j)] c_j^\dagger c_{j'}^\dagger \,, \tag{2.51}$$

where momenta k should be taken appropriately for each number-parity sector. We also used $\epsilon_{-k} = \epsilon_k$ and kept only the surviving total even part in k in the last line.

Restoring the sector projectors, we now need to evaluate $\langle P_{\text{even (odd)}} c_j^\dagger c_{j'}^\dagger P_{\text{even (odd)}}\rangle$ in the initial product BEC state Eq. (2.14). We can express the projectors as $P_{\text{even (odd)}} = (1 \pm e^{i\pi N_{\text{tot}}})/2$. Writing the fermionic operators in terms of the bosonic operators gives $c_j^\dagger c_{j'}^\dagger = b_j^\dagger \left(\prod_{s=j+1}^{j'-1} e^{i\pi n_s}\right) b_{j'}^\dagger$, where we assumed $j < j'$. We can easily evaluate expectation values in the product BEC state and obtain

$$\langle P_{\text{even (odd)}} c_j^\dagger c_{j'}^\dagger P_{\text{even (odd)}}\rangle = (\beta^* \alpha)^2 \frac{\eta^{j'-j-1} \pm \eta^{L-(j'-j+1)}}{2},$$

where we defined $\eta \equiv \langle e^{i\pi n_s}\rangle = |\alpha|^2 - |\beta|^2$.

When calculating the expectation value of Eq. (2.51), the summation over $j < j'$ actually contains only a function of $j' - j$. For each separation $\ell = j' - j$, there are $L - \ell$ identical terms to be summed. Therefore, we now need to calculate

$$\sum_{\ell=1}^{L-1} (L-\ell)\sin(k\ell)(\eta^{\ell-1} \pm \eta^{L-\ell-1})$$
$$= \pm \sum_{s=1}^{L-1} s \sin(ks)(\eta^{L-s-1} \pm \eta^{s-1})$$
$$= \sum_{s=1}^{L-1} \operatorname{Im}\left[s e^{iks}(\pm\eta^{L-s-1} + \eta^{s-1})\right] \,, \tag{2.52}$$

where in the second line we changed the summation variable to $s \equiv L - \ell$ and also used that $kL = 2\pi m + \pi$ or $kL = 2\pi m$, $m \in \mathbb{Z}$, in the even- or odd-parity sectors respectively (upper and lower signs respectively).

The summation can be done exactly using the formula

$$\sum_{s=1}^{L-1} s a^s = a\frac{\partial}{\partial a}\sum_{s=1}^{L-1} a^s = \frac{a(1-a^L)}{(1-a)^2} - \frac{La^L}{1-a} \,, \tag{2.53}$$

applying it with $a = e^{ik}\eta^{-1}$ and $a = e^{ik}\eta$ for the first and second parts respectively. Putting everything together, we find

$$\Upsilon_{\text{even (odd)}}(t) = (\beta^*\alpha)^2 \frac{1}{L^2} \sum_k \sin(k) e^{i2\epsilon_k t}$$
$$\text{Im}\left[\frac{e^{ik}(1 \pm \eta^L)}{(\eta - e^{ik})^2} + \frac{L}{\eta - e^{ik}} + \frac{e^{ik}(1 \pm \eta^L)}{(1 - e^{ik}\eta)^2} \pm \frac{L\eta^{L-1}}{1 - e^{ik}\eta}\right],$$

where we again used $e^{ikL} = \mp$ in the even (odd) sectors respectively. The finite-site result can be easily summed numerically at this point for any L, which is how we obtained the corresponding data in the main text. We can also easily take the thermodynamic limit, remembering that $|\eta| < 1$. In particular, we see that in the thermodynamic limit, the contributions from the even- and odd-number-parity sectors are the same, and we obtain Eq. (2.19) in the main text.

References

[1] M. C. Bañuls, J. I. Cirac, and M. B. Hastings, "Strong and Weak Thermalization of Infinite Nonintegrable Quantum Systems", Phys. Rev. Lett. **106**, 050405 (2011).

[2] M. C. Bañuls, M. B. Hastings, F. Verstraete, and J. I. Cirac, "Matrix Product States for Dynamical Simulation of Infinite Chains", Phys. Rev. Lett. **102**, 240603 (2009).

[3] M. B. Hastings, and R. Mahajan, "Connecting entanglement in time and space: Improving the folding algorithm", Phys. Rev. A **91**, 032306 (2015).

[4] D. Rossini, S. Suzuki, G. Mussardo, G. E. Santoro, and A. Silva, "Long time dynamics following a quench in an integrable quantum spin chain: Local versus nonlocal operators and effective thermal behavior", Phys. Rev. B **82**, 144302 (2010).

[5] P. Calabrese, F. H. L. Essler, and M. Fagotti, "Quantum Quench in the Transverse-Field Ising Chain", Phys. Rev. Lett. **106**, 227203 (2011).

[6] P. Calabrese, F. H. L. Essler, and M. Fagotti, "Quantum quench in the transverse field Ising chain: I. Time evolution of order parameter correlators", J. Stat. Mech. **2012**, P07016 (2012).

[7] P. Calabrese, F. H. L. Essler, and M. Fagotti, "Quantum quenches in the transverse field Ising chain: II. Stationary state properties", J. Stat. Mech. **2012**, P07022 (2012).

[8] F. H. L. Essler, and M. Fagotti, "Quench dynamics and relaxation in isolated integrable quantum spin chains", J. Stat. Mech. **2016**, 064002 (2016).

[9] M. Greiner, O. Mandel, T. W. Hänsch, and I. Bloch, “Collapse and revival of the matter wave field of a Bose-Einstein condensate.”, Nature **419**, 51–54 (2002).

[10] M. Kormos, M. Collura, and P. Calabrese, “Analytic results for a quantum quench from free to hard-core one-dimensional bosons”, Phys. Rev. A **89**, 013609 (2014).

[11] P. P. Mazza, M. Collura, M. Kormos, and P. Calabrese, “Interaction quench in a trapped 1D Bose gas”, J. Stat. Mech. **2014**, P11016 (2014).

[12] M. Kormos, M. Collura, G. Takács, and P. Calabrese, “Real-time confinement following a quantum quench to a non-integrable model”, Nat. Phys. **13**, 246 (2016).

[13] G. Delfino, “Quantum quenches with integrable pre-quench dynamics”, J. Phys. Math. Theo. **47**, 402001 (2014).

[14] G. Delfino, and J. Viti, “On the theory of quantum quenches in near-critical systems”, J. Phys. Math. Theo. **50**, 084004 (2017).

[15] A. H. MacDonald, S. M. Girvin, and D. Yoshioka, “t/u expansion for the Hubbard model”, Phys. Rev. B **37**, 9753–9756 (1988).

[16] S. Bravyi, D. P. DiVincenzo, and D. Loss, “Schrieffer–Wolff transformation for quantum many-body systems”, Ann. Phys. **326**, 2793–2826 (2011).

[17] T. Grover, and M. P. A. Fisher, “Quantum disentangled liquids”, J. Stat. Mech. **2014**, P10010 (2014).

[18] J. R. Garrison, R. V. Mishmash, and M. P. A. Fisher, “Partial breakdown of quantum thermalization in a hubbard-like model”, Phys. Rev. B **95**, 054204 (2017).

[19] S. Sachdev, and A. P. Young, “Low Temperature Relaxational Dynamics of the Ising Chain in a Transverse Field”, Phys. Rev. Lett. **78**, 2220–2223 (1997).

[20] B. M. McCoy, E. Barouch, and D. B. Abraham, “Statistical mechanics of the XY model. IV. Time-dependent spin-correlation functions”, Phys. Rev. A **4**, 2331–2341 (1971).

[21] M. B. Hastings, “Locality in Quantum and Markov Dynamics on Lattices and Networks”, Phys. Rev. Lett. **93**, 140402 (2004).

[22] B. M. McCoy, and T. T. Wu, *The Two-Dimensional Ising Model* (Harvard University Press Cambridge, MA, 1973).

[23] A. Y. Kitaev, “Unpaired Majorana fermions in quantum wires”, Phys.-Uspekhi **44**, 131–136 (2001).

[24] O. Motrunich, K. Damle, and D. A. Huse, “Griffiths effects and quantum critical points in dirty superconductors without spin-rotation invariance: One-dimensional examples”, Phys. Rev. B **63**, 224204 (2001).

[25] N. Read, and D. Green, “Paired states of fermions in two dimensions with breaking of parity and time-reversal symmetries and the fractional quantum Hall effect”, Phys. Rev. B **61**, 10267–10297 (2000).

[26] O. Motrunich, “Single-particle off-diagonal long range order in |Pf| wave function for topological superconductors”, in Proceedings of APS March Meeting (Feb. 2012).

Chapter 3

PRETHERMALIZATION

Prethermalization refers to a system equilibrates to a state which is described by a Gibbs ensemble controlled by some effective Hamiltonian (instead of the original Hamiltonian) at some intermediate time, and truly thermalizes only at much later time. Prethermalization has been observed and studied in many different systems. In particular, various works showed that systems with weak integrability breaking exhibit this phenomenon [1–3]. In addition, prethermalization has been shown rigorously to exist in periodically driven many-body systems under strong driving frequencies using the Floquet-Magnus expansion [4, 5] and renormalization technique [6, 7]. The latter also applies to time-independent many-body systems, and in particular can be used to prove rigorously the presence of exponentially long relaxation times of "particles" such as doublons in the Hubbard model in the strong coupling limit [8–10]. There are also very recent proposals utilizing the prethermalization to protect the edge modes in the topological superconductor [11, 12].

In fact, we can view most of the aforementioned prethermalization systems as having quantities with hierarchically different thermalization time scales or having different rates of dynamics. Upon time evolution, the fast degrees of freedom relax very quickly, while the slow degrees of freedom evolve slowly during this initial period. This results in the apparent prethermalization stage, where the slow degrees of freedom appear to be frozen. These quantities with slow dynamics can be viewed as *quasi-conserved* [13, 14]. Emergence of such a quasi-conserved quantity is what accounts for the prethermalization stage. If such a quantity could develop an exact conservation law, this would extend the prethermalization to infinitely long time and would correspond to partial breakdown of the ETH, as envisioned, e.g., in Refs. [15, 16].

Motivated by this point of view, in this paper we numerically systematically search for such hidden quasi-conserved quantities which cannot be directly identified from the Hamiltonian itself. Following the "slowest operator formalism" introduced in Ref. [17], we numerically construct the quasi-conserved local operator for the non-integrable spin model

$$H = \sum_{j=-\infty}^{\infty} \left(J Z_j Z_{j+1} + h Z_j + g X_j \right) , \tag{3.1}$$

where X_j, Y_j, and Z_j denote Pauli matrices operating on site j of the one-dimensional chain. We constrain our slowest operator to be translationally invariant and represented as a sum of local terms. We find that, in the large g limit, there exists a quasi-conserved operator whose thermalization time scale increases exponentially as one increases its maximum range up to some point. Furthermore, the operator can be understood as a dressed "total spin-z operator" (for appropriately chosen spin axes). This operator has a very slow dynamics compared to other quantities. We also simulate the dynamics of the quantum spin chain following a quench and confirm that this quasi-conserved quantity has a non-trivial effect. Specifically, at intermediate times, the system equilibrates to a state which can be described by a generalized Gibbs ensemble (GGE) that includes such a quantity as an "integral of motion." While our study cannot reach infinite maximum range, we find that the rate of decrease of the slowest operator with the maximum range becomes weaker beyond some point and starts resembling behavior observed in regimes of good thermalization. A conservative interpretation of this behavior is that our system shows only prethermalization with very long time scale. Nevertheless, the available data does not rule out a more exotic possibility that the slowest operator converges and becomes exactly conserved in the thermodynamic limit, which would indicate breakdown of the ETH.

3.1 Method of the slowest operator

Our motivation is to numerically search for the operator that "best-commutes" with the Hamiltonian. We focus on translationally-invariant Hermitian operators obtained as sums of local terms and adopt the formalism of Ref. [17]. We restate this approach as a problem in the operator Hilbert space as follows.

We consider traceless, and translationally-invariant operators with maximum range M,

$$Q^{(M)} = \sum_{j=-\infty}^{\infty} q_j^{(M)} , \tag{3.2}$$

where $q_j^{(M)}$ is an operator with support on a region extending from site j to site $j + M - 1$. We denote the space of traceless translationally-invariant operators with maximum range M as $\mathcal{T}_M$. The operator space $\mathcal{T}_M$ is a vector space, as one can easily verify. A natural basis for $q_j^{(M)}$ is provided by "Pauli string operators," i.e., operators of the form $\prod_{k=j}^{j+M-1} A_k$ where A_k can be I, X, Y, or Z acting on site k, and A_k are independent for different k. However, there is a "gauge degree of freedom" for the representation of $q_j^{(M)}$. For instance, we can write $H = \sum_j q_j \in \mathcal{T}_2$ using $q_j = JZ_jZ_{j+1} + hZ_jI_{j+1} + gX_jI_{j+1}$ or $q_j = JZ_jZ_{j+1} + hI_jZ_{j+1} + gI_jX_{j+1}$, etc. We fix the gauge by requiring the operator A_k on the first site, $k = j$, to be non-identity in every Pauli string basis vector, i.e., A_j can only be X, Y, or Z, while $A_{k>j}$ can be I, X, Y, or Z. This also automatically satisfies the tracelessness condition. The Hermiticity condition of an operator just corresponds to the condition of real coefficients in this basis. It is now easy to see that the dimension of $\mathcal{T}_M$ is $\dim(\mathcal{T}_M) = 3 \cdot 4^{M-1}$.

We define the Frobenius inner product (also know as Hilbert-Schmidt inner product) on the operator space $\mathcal{T}_M$ as

$$\langle Q, Q' \rangle = \frac{\mathrm{Tr}[q_j^\dagger q_j']}{\mathrm{Tr}[I^{\otimes M}]}\,, \tag{3.3}$$

where q_j, q_j' are understood in the above gauge acting on M sites only and $I^{\otimes M}$ is the identity operator also acting on M sites. One can easily see that the aforementioned Pauli-string operators are advantageous as they form an orthonormal basis under this inner product. The above inner product defines the norm $\|Q\|_\mathrm{F} \equiv \sqrt{\langle Q, Q \rangle}$, which we can view as an "intensive Frobenius norm" (see below). For example, $\|H\|_\mathrm{F} = \sqrt{J^2 + g^2 + h^2}$. Note that instead of the conventional definition of the operator inner product, here we only take the local piece q_j in the trace calculation after the gauge fixing. This definition has the advantage that the norm is "intensive," compared to the conventional definition of Frobenius norm that would increase with the system size. In fact, if we consider a chain of length L with periodic boundary conditions and operators $Q^{(M)} = \sum_{j=1}^{L} q_j$ (assuming $M < L$), we can easily verify that the above inner product is simply appropriately scaled conventional Frobenius inner product:

$$\langle Q, Q' \rangle = \mathrm{Tr}[Q^\dagger Q']/(L\,\mathrm{Tr}[I^{\otimes L}])\,. \tag{3.4}$$

In other words, Eq. (3.3) is obtained from Eq. (3.4) when applied to this "gauge-fixing" writing of the translationally-invariant operators. If one does not use the gauge-fixing, one should use Eq. (3.4) to calculate the inner product. In what follows, we will always use only the intensive Frobenius norm, often dropping the descriptor "intensive" for brevity.

A natural embedding $\mathcal{T}_M \subset \mathcal{T}_N$ for $M < N$ is obtained by the tensor product with the identities, $q_j^{(N)} = q_j^{(M)} \otimes I_{j+M} \otimes \cdots \otimes I_{j+N-1}$, where $\sum_j q_j^{(M)} \in \mathcal{T}_M$ and $\sum_j q_j^{(N)} \in \mathcal{T}_N$. We will not emphasize the difference between $\sum_j q_j^{(M)}$ and $\sum_j q_j^{(N)}$, since it only depends on what operator space one is considering, while the inner product in Eq. (3.3) is independent of the embedding. We can further consider the norm closure $\overline{\bigcup_{M\in\mathbb{N}} \mathcal{T}_M}$, which is a mathematically well-defined Hilbert space.

The commutator with a fixed operator can be viewed as a linear map between the operator spaces. We define the superoperator

$$\mathrm{ad}_A(O) \equiv [A, O] \, . \tag{3.5}$$

Clearly, ad_H is a linear map from the operator space $\mathcal{T}_M$ to space $\mathcal{T}_{M+1}$, since $H \in \mathcal{T}_2$. In fact, for any operator $A \in \mathcal{T}_r$ and $O \in \mathcal{T}_s$, we have $\mathrm{ad}_A(O) \in \mathcal{T}_{r+s-1}$. Using the Pauli string basis, we can write down the matrix representation $\mathbf{B}$ for ad_H, which in general will be a $3 \cdot 4^M \times 3 \cdot 4^{M-1}$ matrix. We want to find an operator in $\mathcal{T}_M$ that "best commutes" with the Hamiltonian, which we define as minimizing the *residual norm* $\|\mathrm{ad}_H(Q^{(M)})\|_\mathrm{F}$ under the constraint $\|Q^{(M)}\|_\mathrm{F} = 1$. This corresponds to finding the smallest singular value σ_0 of $\mathbf{B}$, or the smallest eigenvalue λ_0 of $\mathbf{C} \equiv \mathbf{B}^\dagger\mathbf{B}$, where $\lambda_0 = \sigma_0^2$. The corresponding eigenoperator is the sought-for *slowest operator*; we will denote this operator as $Q_0^{(M)}$ and the corresponding eigenvalue as $\lambda_0(M)$, which will be the squared residual norm of the slowest operator. To avoid the trivial zero-eigenvalue solution given by the Hamiltonian itself, we add $\lambda_h |H\rangle\langle H|$ to $\mathbf{C}$, with large enough λ_h such that the slowest operator is nontrivial. Thus found operator $Q_0^{(M)}$ is orthogonal to H in the Frobenius inner product.

Note that in the I-X-Y-Z Pauli-string basis, $\mathbf{C}$ is always a symmetric matrix with real coefficients. This guarantees the eigenvalues to be real, and the eigenvectors can be chosen with real amplitudes in the I-X-Y-Z Pauli-string basis. This means that the slowest operator $Q_0^{(M)}$ can always be chosen to be Hermitian. In other words, we fix the overall phase of the eigenoperator by requiring the Hermicity of the operator, up to a minus sign.

We can argue that this defines a procedure to find a translationally invariant (quasi)-local conserved quantity in the thermodynamic limit. Indeed, consider the limit $\lambda_0(\infty) = \lim_{M\to\infty} \lambda_0(M)$. Since $\lambda_0(M)$ is a decreasing function of M bounded from below by 0, $\lambda_0(\infty)$ exists. If $\lambda_0(\infty) = 0$ and $\lim_{M\to\infty} \frac{Q_0^{(M)}}{\|Q_0^{(M)}\|_\mathrm{F}}$ exists, then we have a normalizable operator [hence quasilocal or local if $\lambda_0(M) = 0$ for some finite M already] which commutes with the Hamiltonian. If such (quasi)local conserved quantity does exist, a suitable thermal equilibrium description should include this quantity in the GGE. On the other hand, even though an arbitrary linear combination of eigenstate projectors $\hat{A} = \sum_E a_E |E\rangle\langle E|$ commutes with the Hamiltonian, $\hat{A}$ can be non-normalizable under our definition of the Frobenius norm. It is therefore not guaranteed that $\lambda_0(\infty) = 0$. Furthermore, even if $\lambda_0(\infty) = 0$, we cannot guarantee that the limit $\lim_{M\to\infty} \frac{Q_0^{(M)}}{\|Q_0^{(M)}\|_{\mathrm{F}}}$ exists. In practice, one can only find Q_0^M with M finite, but we can try to explore these questions by studying behaviors for increasing M.

Simplifications due to symmetries

The size of the matrix $\mathbf{C}$ can be further reduced by using time-reversal and parity symmetries. The time-reversal operation U_T corresponds to the complex conjugation in the Z basis; this maps $Y_j \longrightarrow U_T^{-1} Y_j U_T = -Y_j$, while leaving the other Pauli operators unchanged. Therefore, the time-reversal-even (-odd) sector corresponds to even (odd) number of Pauli Y operators in the Pauli string basis respectively.

The matrix $\mathbf{C}$ can be further simplified by utilizing the parity (i.e., mirror) symmetry with respect to the origin. To illustrate how the parity operation U_P acts on the I-X-Y-Z Pauli-string basis, we consider an example of $S = \sum_j X_j Y_{j+1} Z_{j+2} I_{j+3} \in \mathcal{T}_4$. Upon parity operation, $S' = U_P^{-1} S U_P = \sum_j X_{-j} Y_{-j-1} Z_{-j-2} = \sum_j Z_j Y_{j+1} X_{j+2}$, where in the last equality we gauge-fixed the writing of S'. We see that the parity operation U_P acts on the operators in $\mathcal{T}_M$ by reversing the order of operators in each of the Pauli-string basis vector and gauge-fixing the expression. More specifically, if $S = \sum_j \sigma_j^{\mu_1} \cdots \sigma_{j+r_0-1}^{\mu_{r_0}} I_{j+r_0} \cdots I_{j+r-1} \in \mathcal{T}_r$, where $\sigma_j^{\mu_1}$ and $\sigma_{j+r_0-1}^{\mu_{r_0}}$ can only be X, Y, or Z, then $U_P^{-1} S U_P = \sum_j \sigma_j^{\mu_{r_0}} \sigma_{j+1}^{\mu_{r_0-1}} \cdots \sigma_{j+r_0-1}^{\mu_1} I_{j+r_0} \cdots I_{r-1} \in \mathcal{T}_r$. We can therefore easily form the parity-even and -odd subspaces by forming $O \pm U_P^{-1} O U_P$ basis vectors.

Algorithm

For small maximum range $M \leq 8$, we exactly diagonalize the matrix $\mathbf{C}$ to find the lowest eigenvalue and the slowest operator. For larger maximum range $M \geq 9$, iterative methods are preferred since one can construct $\mathbf{C}$ as a sparse matrix. While Lanczos method is one of the standard iterative algorithms to find the lowest eigenpair, the smallness of the relevant eigenvalues in the large g regime makes the convergence extremely slow. Fortunately, the positive-definite character of the matrix $\mathbf{C}$ enables us to adapt a conjugate-gradient-based algorithm. Here, we use the "locally optimal block preconditioned conjugate gradient method" from Ref. [18]

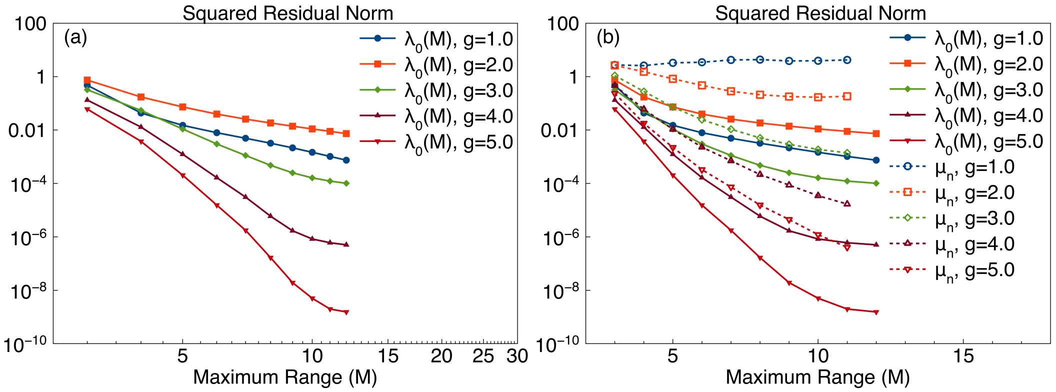

Figure 3.1: (color online) Behavior of the squared residual norm $\lambda_0(M)$ (in units of J^2) vs maximum range M on (a) log-log plot and (b) semi-log plot, for model parameters $J = 1.0$, $h = 1.5$, and varying g. For small g, $\lambda_0(M)$ decays as power-law in M. For large g, it first decays exponentially as one increases M, and then turns into a slower trend at larger M. Panel (b) shows additional data from the Schrieffer-Wolff construction of quasi-conserved quantity (see Sec. 3.3 for details), which can be viewed as a variational bound. The residual norm μ_n from the SW construction of order n, which corresponds to $M = n+1$ maximum range, shows a classic asymptotic expansion behavior for the smaller g values, where it starts to increase at large order. While this behavior is not manifest yet for the larger g values, from the observed trends we suspect that μ_n will also start to increase eventually beyond some order.

to find the lowest eigenpair.

3.2 Scaling of the squared residual norm

Figure 3.1 shows the M-dependence of the squared residual norm $\lambda_0(M)$ on a log-log plot and a semilogrithmic plot. For small g, the dependence is roughly a power law, which is consistent with the result in Ref. [17] in the regime where the system has good ergodic behavior. On the other hand, for large g, $\lambda_0(M)$ first decays exponentially with M but then turns into a slower decay at larger M. The exponential decay was also observed in the case of such "slowest operator" construction in the many-body localization [19]. This exponential behavior differentiates the speed of the dynamics of this operator compared to other quantities. As one increases the maximum range, one can optimize the residual norm exponentially better, which also indicates longer thermalization time scale, since the residual norm is related to the speed of the dynamics of the operator (see Sec. 3.2 below). We therefore expect this quantity to be quasi-conserved, which can affect the thermalization of the system.

Interestingly, the exponential decay of $\lambda_0(M)$ for the slowest operator does not continue to larger M. Instead, the decay trend seems to turn into a power law at larger M. As discussed in the previous section, even though the scaling trend turns into a slower decay at large M, one always gets an equal or smaller residual norm as one increases M. If the residual norm goes to zero as $M \to \infty$ and $\lim_{M\to\infty} \frac{Q_0^{(M)}}{\|Q_0^{(M)}\|_{\mathrm{F}}}$ exists, then we would indeed obtain a conserved quasilocal operator. However, due to limits on our numerical calculations, we cannot reach larger maximum range and cannot be conclusive about the behavior of $\lambda_0(M)$ at large M. The eventual turn to a slower decay (similar to behavior in the good ergodic regime $g \leq 2$) may be signaling that beyond some time the operator will thermalize. Hence, it may well be that the observed behavior corresponds to a prethermalization phenomenon on some intermediate time scales, where the time scale can be parametrically large.

Next-slowest operators

While the exponential scaling of the slowest operator for large g suggests that it is quasi-conserved, one may wonder how many quasi-conserved quantities exist. To answer this question, we further study the scaling of the squared residual norm $\lambda(M)$ of the first five slowest operators in the time-reversal and parity even (odd) sector, denoted as "TePe" ("ToPo") in Fig. 3.2. The operators in the "TePo" and "ToPe" sectors have higher squared residual norms than the ones shown in the figure and are hence less interesting and not included. Here we only show results that are accessible using the exact diagonalization of the matrix $\mathbf{C}$, or $M \leq 8$.

Figure 3.2(a) shows the scaling of $\lambda(M)$ for $g = 1.0$. Note that the slowest operator in this case has a similar scaling trend compared to other operators. Therefore the speed of the dynamics is not hierarchically slower than for other degrees of freedom.

On the other hand, in panels Figs. 3.2(b) and 3.2(c), the slowest operator clearly has faster scaling than the next-slowest operators. This is another feature suggesting that for large g, the speed of the dynamics of the slowest operator is hierarchically slower than other operators, resulting in apparent freezing of its dynamics and hence the prethermalization phenomenon. We conclude that in these particular cases, there is only one quasi-conserved quantity. This differs from the proposal in Ref. [7] that there may be two independent quasi-conserved quantities (excluding the energy itself) in the strong coupling regime. We suspect that this difference comes from our separation of operators into independent ones using the orthogonality in the Frobenius inner product.

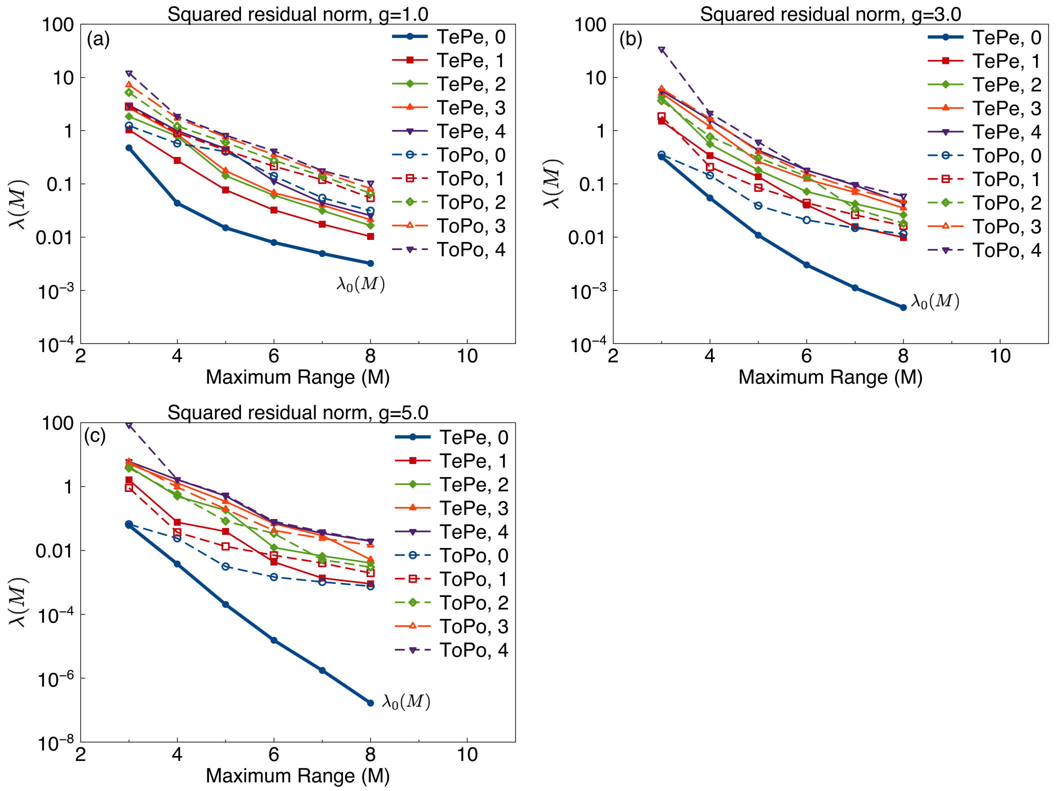

Figure 3.2: Behavior of the squared residual norm $\lambda(M)$ for the first five slowest operators in the "TePe" and "ToPo" sectors. (a) For $g = 1.0$, the slowest operator in the "TePe" sector shows similar dependence on M as the other nearby slow operators; no particularly slow degrees of freedom exist in this case. On the other hand, in panels (b) for $g = 3.0$ and (c) for $g = 5.0$, the slowest operator has exponential dependence on M up to some range, while the other operators decrease more slowly throughout, which suggests that the slowest operator has parametrically more slow dynamics compared to other degrees of freedom.

Relation to operator norm and thermalization time scale

Minimizing the commutator $[H, Q]$ with respect to the Frobenius norm is advantageous because it can be relatively easily calculated numerically and is independent of the system size. On the other hand, to relate the smallness of the commutator to the dynamics, it is more appropriate to use the conventional operator norm. Indeed, following Ref. [17], let us consider a quench setting where we start from some initial state $|\psi_{\text{ini}}\rangle$. Using the Heisenberg representation of observables, $Q_H(t) \equiv e^{iHt} Q e^{-iHt}$, and denoting the expectation value of the operator $\langle Q_H(t)\rangle \equiv \langle\psi_{\text{ini}}|Q_H(t)|\psi_{\text{ini}}\rangle$, the deviation of the expectation value from its initial

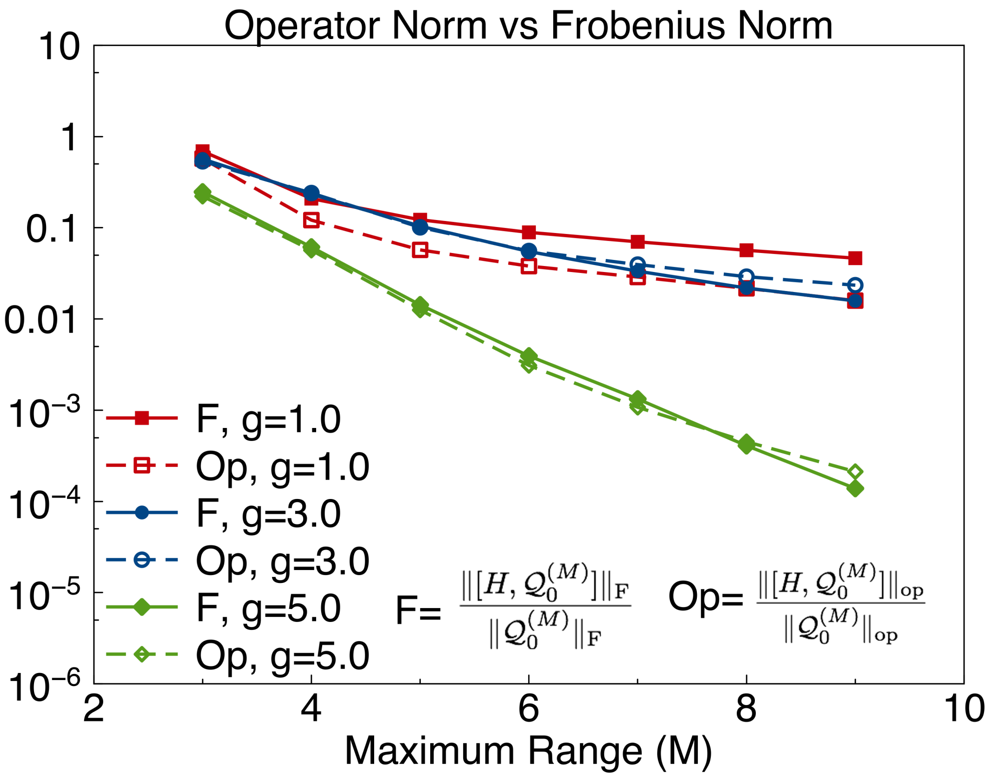

Figure 3.3: (color online) Comparison between the residual Frobenius norm and operator norm measures of the slowest operator $Q_0^{(M)}$; the operator is obtained from the minimization of the residual Frobenius norm as described in Sec. 3.1. The inverse of $\frac{\|[H,Q_0^{(M)}]\|_{\mathrm{op}}}{\|Q_0^{(M)}\|_{\mathrm{op}}}$ gives the thermalization time scale of $Q_0^{(M)}$. For large coupling, cases $g = 3.0$ and $g = 5.0$, we find that the numerical values of the residual Frobenius and operator norm measures are close to each other up to some M and then start deviating (see text for some discussion).

value can be estimated as

$$\begin{aligned} |\langle Q_H(t)\rangle - \langle Q\rangle| &= \left|\left\langle \int_0^t d\tau \frac{dQ_H}{d\tau}(\tau)\right\rangle\right| \\ &\leq \int_0^t d\tau \left|\left\langle \frac{dQ_H}{d\tau}(\tau)\right\rangle\right| \\ &\leq \int_0^t d\tau \|[H, Q_H(\tau)]\|_{\mathrm{op}} = t\|[H, Q]\|_{\mathrm{op}}\,, \end{aligned} \tag{3.6}$$

where we have used $\|[H, Q_H(\tau)]\|_{\mathrm{op}} = \|[H, Q]\|_{\mathrm{op}}$ for arbitrary τ, and the above inequality holds for any initial state. If we assume that Q has unit operator norm, we see that for $\langle Q_H(t)\rangle$ to deviate from its initial value by an order-one number, the time scale is $t_* \sim (\|[H, Q]\|_{\mathrm{op}})^{-1}$. For a general not normalized Q, including the suitable normalization gives the time scale $t_* \sim \left(\frac{\|[H,Q]\|_{\mathrm{op}}}{\|Q\|_{\mathrm{op}}}\right)^{-1}$.

Figure 3.3 demonstrates the comparison between the Frobenius norm measure and the operator norm measure of the smallness of the commutator $[H, Q_0^{(M)}]$, where the slowest operator $Q_0^{(M)}$ is as before obtained by minimizing the residual Frobenius norm for given M. Note that the operator norm per site of a translationally invariant operator like $\sum_{j=1}^{L} q_j^{(M)}$, unlike the intensive Frobenius norm defined earlier, depends on the system size L and should be obtained in the thermodynamic limit (a familiar example is the ground-state energy per site of a translationally invariant Hamiltonian). However, we expect the size dependence to diminish for increasing L. We confirmed this by calculating the operator norms by diagonalizing the corresponding operators on finite systems up to size $L = 16$, and Fig. 3.3 shows our results for the largest L; we were able to go only up to $M = 9$ because the calculations became prohibitively expensive for larger M. Unlike the residual Frobenius norm, the residual operator norm $\frac{\|[H,Q_0^{(M)}]\|_{\text{op}}}{\|Q_0^{(M)}\|_{\text{op}}}$ can increase with M since the minimization procedure is not with respect to the operator norm. This can also potentially serve as a criterion for picking an "optimal" quasi-conserved operator $Q_0^{(M_*)}$ for some $M = M_*$ that gives the minimum residual operator norm measure. However, we do not observe a clear minimum of the residual operator norm measure for the accessible M. Nevertheless, we can already bound t_* from below from the $M=9$ data. Thus, for $g = 5.0$, we can bound $t_* > 5 \cdot 10^3$ which is already very long; while for $g = 3.0$, we can bound t_* from below by approximately $t_* > 30$.

While here we were able to calculate the operator norm explicitly numerically, it is instructive to consider the following crude bound for the prethermalization condition obtained from the scaling of the residual Frobenius norm. First, we note that we can write $[H, Q_0^{(M)}] = \sum_j \eta_j$, where η_j has maximum range $M + 1$. We then have $\|[H, Q_0^{(M)}]\|_{\text{op}} \leq \sum_j \|\eta_j\|_{\text{op}} = L\|\eta_j\|_{\text{op}} \leq L\, 2^{(M+1)/2}\|[H, Q_0^{(M)}]\|_{\text{F}}$ (recall that here and below we use the intensive Frobenius norm). On the other hand, for $Q_0^{(M)} = \sum_j q_j$, heuristically we can estimate $\|Q_0^{(M)}\|_{\text{op}} \approx \sum_j \|q_j^{(M)}\|_{\text{op}} = L\|q_j^{(M)}\|_{\text{op}}$, and we also have exact bound $\|q_j^{(M)}\|_{\text{op}} \geq \|Q_0^{(M)}\|_{\text{F}}$. We therefore obtain

$$\frac{\|[H, Q_0^{(M)}]\|_{\text{op}}}{\|Q_0^{(M)}\|_{\text{op}}} \leq 2^{\frac{M+1}{2}} \frac{\|[H, Q_0^{(M)}]\|_{\text{F}}}{\|Q_0^{(M)}\|_{\text{F}}} = 2^{\frac{M+1}{2}} \sqrt{\lambda_0(M)}\,, \tag{3.7}$$

(which is nonrigorous bound). To maximize the thermalization time scale, we find $\bar{M}_*$ by minimizing the right-hand side and obtain a crude criterion

$$\frac{d \log_{10} \lambda_0(M)}{dM}\Big|_{M=\bar{M}_*} = -\log_{10} 2\,. \tag{3.8}$$

Thus, the optimal $\bar{M}_*$ from this heuristic bound is determined as the point where the magnitude of the slope of $\log_{10} \lambda_0(M)$ vs M drops below value $\log_{10} 2$ (assuming that the magnitude of the slope is decreasing with M, as observed in Fig. 3.1). We expect $\bar{M}_* \leq M_*$ (the latter defined from the true operator-norm minimization).

The above arguments also show how one may reconcile the fact that while the Frobenius norm measure $\lambda_0(M)$ is always decreasing with M, the thermalization time scale could still be finite. The actual data for the operator norm vs Frobenius norm in Fig. 3.3 shows that the operator norm measure is numerically close to the Frobenius norm over the available maximum range M, particularly for large g. That is, the factor of $2^{\frac{M+1}{2}}$ in the heuristic bound Eq. (3.7) between the two measures is an overestimate, and at least over this range of M the Frobenius norm measure can be used to bound the speed of the dynamics.

We can understand the rough agreement between the Frobenius and operator norm measures if the operators $Q_0^{(M)}$ and $[H, Q_0^{(M)}]$ have roughly similar "profiles" in the operator space. Indeed, in this case, the numerators on both sides of the inequality in Eq. (3.7) and the denominators should have similar relations, which would cancel out in the ratio (while the overestimating factor $2^{\frac{M+1}{2}}$ arose from using different limits of the relations between the Frobenius and operator norms for the denominator and numerator). We expect this to be particularly true when $Q_0^{(M)}$ is "localized" in real space, which we indeed find in the strong coupling regime at least for the available M—see our understanding of the slowest operator from the perturbative SW picture in Sec. 3.3 and direct measurements of its profile in Sec. 3.4. We do start observing some deviations between the Frobenius and operator norm measures for larger M, which could be indicating changing localization properties; however, the differences are still small to reach definite conclusions.

Examining carefully all data in Fig. 3.3, we would like to point out that even though for $g = 1.0$ the operator norm measure is smaller than the one for $g = 3.0$, it does not imply that the system with $g = 1.0$ will exhibit prethermalization. For a fair comparison of the dynamics, one also needs to compare the thermalization time scale of $Q_0^{(M)}$ to other degrees of freedom in the same system. We indeed know from the previous section, cf. Fig. 3.2, that for $g = 1.0$, the next-slowest operators have comparable relaxation times to $Q_0^{(M)}$ and the prethermalization phenomenon is less likely than for $g = 3.0$, where the slowest operator is more separated from the rest. This could explain our findings in Sec. 3.5 of clear prethermalization at $g = 3.0$ and no prethermalization at $g = 1.0$.

While the residual norm provides us some bound on the thermalization time scale, it is also important to obtain the physical meaning of the slowest operator. In the system in the good ergodic regime studied in Ref. [17], in the nontranslationally invariant setting, the slowest operator can be understood as dressed energy density modulation operator. On the other hand, in the translationally invariant setting, the slowest operator does not have simple connection to the energy density modulation and its physical meaning remains an open question. In the MBL system, Ref. [19] used this approach to explicitly construct the approximately conserved operators as local integrals of motion. As we will show in the next Sec. 3.3, the slowest operator we found in the large g regime can be understood as a dressed total spin-z operator, coming from the solvable limit $H_0 = \sum_j (gX_j + hZ_j)$, which can be viewed as a quasi-local integral of motion.

3.3 Schrieffer-Wolff Construction of Quasi-Conserved Quantity

Reference [7] used a renormalization scheme to construct an effective Hamiltonian which commutes with H_0 up to some order in small parameter, which can then be used to describe the prethermalization dynamics. Here, we use an approach with similar spirit but based on the *l*ocal Schrieffer-Wolff (SW) transformation [20, 21] to construct a quasi-conserved operator perturbatively. The term “local” is stressed since the generators are solved in the form of sum of local terms, in contrast with the “global” SW transformation, where the generators are solved using projectors of the H_0 eigenspaces [21]. The locality in particular allows us to construct the quasi-conserved quantity numerically to high order and measure its properties exactly, in contrast to the more abstract construction in Ref. [7]. A popular variant of a local SW transformation was in fact proposed in Ref. [22] as a perturbative treatment of the Hubbard model in the large U limit; this reference used generalized “ladder” operators connecting different Hubbard sectors, and we discuss the relation to our approach in Appendix A. Before proceeding, we briefly point some differences with Ref. [21]. First, our setup works in the thermodynamic limit $L \to \infty$ from the start. More importantly, we choose the solution of Eq. (3.12) for the generator that eliminates the off-diagonal part of V_m among all the sectors, while in Ref. [21] one is only focusing on the off-diagonal part between the ground-state sector and other sectors.

We first describe the specific SW transformation used here and how we numerically construct a perturbation series for a quasi-conserved operator $\tilde{I}^{(n)}$ to n-th order. We then calculate the squared residual norm of $\tilde{I}^{(n)}$ and the overlap between $Q_0^{(M)}$ and

$\tilde{I}^{(n)}$ to demonstrate the similarity between the two operators. We will see that the slowest operator $Q_0^{(M)}$ in the large g regime can be understood—at least up to the maximum range accessible in our work—as $\tilde{I}^{(n)}$, which is essentially dressed "total spin-z operator."

Procedure of SW transformation

In the large-g limit, we can decompose $H = H_0 + \epsilon T$, with $H_0 = \sum_j (gX_j + hZ_j)$ being our solvable limit and $\epsilon T = J \sum_j Z_j Z_{j+1}$ treated as perturbation with small parameter ϵ. [For example, we can define $\epsilon \equiv J/\sqrt{g^2 + h^2}$ so that for convenience $\|T\|_F = \|H_0\|_F$ in the intensive Frobenius norm, but the specific choice is not important.] We construct a unitary transformation $U = e^{-i\epsilon S_1} e^{-i\epsilon^2 S_2} \dots e^{-i\epsilon^n S_n}$, with S_m being Hermitian and ϵ-independent, such that the rotated Hamiltonian $H' \equiv U^\dagger (H_0 + \epsilon T) U$ commutes with H_0 up to order n in the formal expansion in ϵ. Stated another way, the eigenvalues of H_0 define the corresponding unperturbed sectors, and we want H' to have only sector-diagonal terms up to order n in ϵ, while sector-off-diagonal terms are present only in higher order. If we then undo the rotation on H_0 back to the original picture, i.e., perform the inverse rotation to define $I \equiv U H_0 U^\dagger$, we obtain an operator that commutes with H up to order n by construction.

To be more specific, we follow Ref. [20] and consider an expansion of H' in powers of ϵ:

$$H' = H_0 + \sum_{m=1}^{n} \epsilon^m [i\mathrm{ad}_{S_m}(H_0) + V_m] + H_{>n}\,, \tag{3.9}$$

where $V_1 \equiv T$ and

$$\begin{aligned} V_m &= \sum_{p=2}^{m} \sum_{[k_1,\dots,k_p]=m} \mathfrak{f}(k_1,\dots,k_p)\, i\mathrm{ad}_{S_{k_p}} \dots i\mathrm{ad}_{S_{k_1}}(H_0) \\ &+ \sum_{p=1}^{m-1} \sum_{[k_1,\dots,k_p]=m-1} \mathfrak{f}(k_1,\dots,k_p)\, i\mathrm{ad}_{S_{k_p}} \dots i\mathrm{ad}_{S_{k_1}}(T) \end{aligned} \tag{3.10}$$

for $m \geq 2$. Here we have used the notation "$[k_1, \dots, k_p] = m$" to mean the summation conditions $1 \leq k_i \leq n$ for $i = 1, \dots, p$ and $k_1 + \dots + k_p = m$, while the function $\mathfrak{f}(k_1, \dots, k_p) = \Theta(1 \leq k_1 \leq \dots \leq k_p \leq n)/[\prod_{l=1}^{n} \mathrm{card}(l)!]$, where $\Theta(\bullet) = 1$ if the condition in the argument is true and $\Theta(\bullet) = 0$ otherwise, and $\mathrm{card}(l)$ counts the number of elements in $\{k_1, \dots, k_p\}$ that are equal to l. By construction, each V_m is ϵ-independent; it enters with a coefficient ϵ^m and is part of the m-th term in

Eq. (3.9) for $m = 1, \ldots, n$. Furthermore, $H_{>n} = \sum_{m=n+1}^{\infty} \epsilon^m V_m$ collects all the terms with ϵ powers higher than n.

The generators of the SW transformation are solved order by order by finding iS_m such that

$$i\mathrm{ad}_{S_m}(H_0) + V_m = V_m^{\mathrm{diag}}\,, \tag{3.11}$$

where we have defined O^{diag} as a part of an operator O that is "diagonal" in the H_0 sector label; i.e., O^{diag} is the component of the operator that commutes with H_0. Equivalently, O^{diag} is the component of O in the kernel (nullspace) of ad_{H_0}. The remainder $O^{\text{off-diag}} \equiv O - O^{\mathrm{diag}}$ is the "off-diagonal" part of the operator, and can be also viewed as a component of O orthogonal to the kernel of ad_{H_0} in the Frobenius inner product [20]. We can solve for the generator

$$iS_m = [\mathrm{ad}_{H_0}]^{-1} V_m^{\text{off-diag}}\,, \tag{3.12}$$

where $[\mathrm{ad}_{H_0}]^{-1}$ is the *pseudoinverse* of ad_{H_0}. Note that iS_m solving Eq. (3.11) is determined only up to a component in the kernel of ad_{H_0}, and we make a choice here where such component is zero, i.e., iS_m is composed of only sector-off-diagonal operators; this is common choice in the SW approach, cf. Refs. [20–22]. The described procedure generates an effective Hamiltonian which commutes with H_0 up to order n by truncating out $H_{>n}$, obtaining $H_{\mathrm{eff}}^{(n)} = H_0 + \sum_{m=1}^{n} \epsilon^m V_m^{\mathrm{diag}}$.

An important property of the above SW transformation is its locality, which ensures the representability of S_m and V_m in finite-dimensional operator spaces, making the SW procedure programmable as operations of matrices and vectors. In fact, one can show that for $H_0 \in \mathcal{T}_1$ and $T \in \mathcal{T}_2$ we have $V_m \in \mathcal{T}_{m+1}$ and $S_m \in \mathcal{T}_{m+1}$, see Ref. [21] and Proposition 3.6.1 in Appendix B.

We remark that the SW transformation generally does not converge when one takes the $n \longrightarrow \infty$ limit. There are rigorous results for the convergence of the ground state energy estimates for gapped Hamiltonians [20, 21] but no known results for the ability of the SW procedure to capture the entire spectrum of interest here. Nevertheless, the SW transformation is well-defined for any finite n and can be used to obtain rigorous bounds on the dynamics in the spirit of Refs. [4, 5, 7]. Thus, one can show that, for small enough ϵ, $\|H_{>n}\|_{\mathrm{F}} < O(n^{2n+2}\epsilon^{n+1})$, see Ref. [21] and Theorem 3.6.1 in Appendix B. The dynamics described by $H' = H_{\mathrm{eff}}^{(n)} + H_{>n}$ in the rotated picture does not truly conserve H_0 but only approximately. In other words, while $H_{\mathrm{eff}}^{(n)}$ conserves H_0, the "remainder" $H_{>n}$ does not and is responsible for the eventual thermalization of the dynamics, which can be very slow if ϵ is small.

We can thus intuitively understand the prethermalization via this perturbative SW construction [4, 5, 7, 12]. The solvable limit H_0 defines different sectors labeled by different integers, which can be viewed as counting the number (up to some off-set) of some emergent "particles." (see also Appendix A). The perturbation term ϵT introduces interactions within the sectors and transitions between the sectors. The interactions within the sectors are indeed the "diagonal" part of T. At m-th order, the coefficient ϵ^m in the SW perturbation theory basically describes the transition amplitude of any process with m inter-sector transitions. The generator iS_m is set to rotate the picture such that these processes are eliminated. The remaining part V_m^{diag} basically describes the processes which start and end in the same sector connected by m times of the inter-sector transitions. The perturbation series would be convergent for small enough ϵ if there were at most $O(e^{cm})$ of such processes. However, generically, in a translationally invariant system, there are order $O(m^{\gamma m})$ such processes coming from combinatorial factorials in m. The exponential suppression of the transition amplitude is then not enough to suppress the factorial factor. Therefore, even though at high order of n, the transition amplitude is perturbatively small $O(\epsilon^n)$, manifesting slowness of individual processes, there are, however, too many ways of the transitions $O(n^{\gamma n})$ such that the system will eventually thermalize.

Quasi-conserved quantity by SW transformation

Once we have obtained the generators for the SW transformation, we can rotate H_0 back to the original picture and obtain the quasi-conserved operator. Consider

$$I \equiv U H_0 U^\dagger = H_0 + \sum_{m=1}^{n} \epsilon^m I_m + I_{>n} \,, \tag{3.13}$$

where

$$I_m = \sum_{p=1}^{m} \sum_{[k_1,\ldots,k_p]=m} (-1)^p\, \mathfrak{f}(k_1,\ldots,k_p)\, i\mathrm{ad}_{S_{k_1}} \ldots i\mathrm{ad}_{S_{k_p}}(H_0) \tag{3.14}$$

and $I_{>n} = \sum_{m=n+1}^{\infty} \epsilon^m I_m$ collects all the higher-power in ϵ terms. We then obtain the quasi-conserved operator $I^{(n)} = H_0 + \sum_{m=1}^{n} \epsilon^m I_m$. In Appendix B, we show that $I^{(n)} \in \mathcal{T}_{n+1}$. To compare with the slowest operator, we remove the part of $I^{(n)}$ that is parallel to H and normalize the resulting operator:

$$I^{(n)\perp} = I^{(n)} - H \frac{\langle H, I^{(n)} \rangle}{\|H\|_{\mathrm{F}}^2} \,, \tag{3.15}$$

$$\tilde{I}^{(n)} = \frac{I^{(n)\perp}}{\|I^{(n)\perp}\|_{\mathrm{F}}} \,. \tag{3.16}$$

For small enough ϵ, we can bound the squared residual norm as

$$\mu_n \equiv \|\mathrm{ad}_H(\tilde{I}^{(n)})\|_{\mathrm{F}}^2 \leq \mathcal{O}(n^{4n}\epsilon^{2n}) \,. \tag{3.17}$$

The proof of this bound and a more precise statement is in Appendix C.

Applying the previous heuristic argument for the thermalization time scale, Eq. (3.7), we get $t_*^{-1} \sim \mathcal{O}((2\epsilon)^n n^{2n})$. If we treat the perturbation strength ϵ as given, and the SW order n as an optimization parameter, then we can find that the residual operator norm is minimized at $n = n_* = 1/(e\sqrt{2\epsilon})$. The thermalization time scale is therefore maximized as $t_* = \mathcal{O}(\exp(\frac{\sqrt{2}}{e\sqrt{\epsilon}}))$. Note that unlike Refs. [4–7], where the heating rate is proven to be $\mathcal{O}(\exp(\frac{A}{\epsilon}))$, we only obtain $\mathcal{O}(\exp(\frac{A'}{\sqrt{\epsilon}}))$. This can be traced back to the estimation of the convergence radius in Appendices B and C to be $\rho_n \sim 1/n^2$, and hence the squared residual norm $\mu_n \sim \mathcal{O}(n^{4n}\epsilon^{2n})$. We suspect that a tighter convergence radius $\rho_n \sim 1/n$ is possible (see Appendix D); hence the bound on the thermalization time-scale could be improved to $\mathcal{O}(\exp(\frac{A}{\epsilon}))$. Without pursuing this tighter bound further, we leave this for future studies.

As mentioned earlier, the locality of iS_m and V_m allows us to formulate this procedure in finite-dimensional operator Hilbert spaces amenable to numerical calculations. Figure 3.1(b) shows the squared residual norm calculated from such SW construction of the quasi-conserved operator for several values of parameter g. Note that at order n, the constructed operator has maximum range $M = n + 1$. The trend of μ_n at large g more or less follows the trend of $\lambda_0(M)$, where the residual norm drops almost exponentially in low order, and turns into a slower trend, which is possibly a manifestation of the combinatorial factor $\mathcal{O}(n^{\gamma n})$. While not appearing in the figure yet for large g, we expect μ_n will eventually start increasing at high enough order n; this is because in generic systems the combinatorial factors (like the ones appearing in the previous paragraph) will win over the exponential suppression at large enough n; such behavior of μ_n is observed in the $g = 1$ and $g = 2$ cases. Nevertheless, noting that the above arguments are based on the “worst-case-scenario” analytical bounds on the perturbatively-constructed operators, our numerical results for μ_n in the larger g cases do not rule out the possibility that $\mu_n \to 0$. On the other hand, unlike the perturbative construction, the numerical minimization for the slowest operator is guaranteed to get an equal or smaller residual norm when increasing M.

Figure 3.4(a) shows the overlap between the slowest operator $Q_0^{(M)}$ with maximum range $M = 11$ and the SW construction $\tilde{I}^{(n)}$ with order n up to 10. The overlap at large g is almost 100%! Accordingly, we can understand the slowest operator we

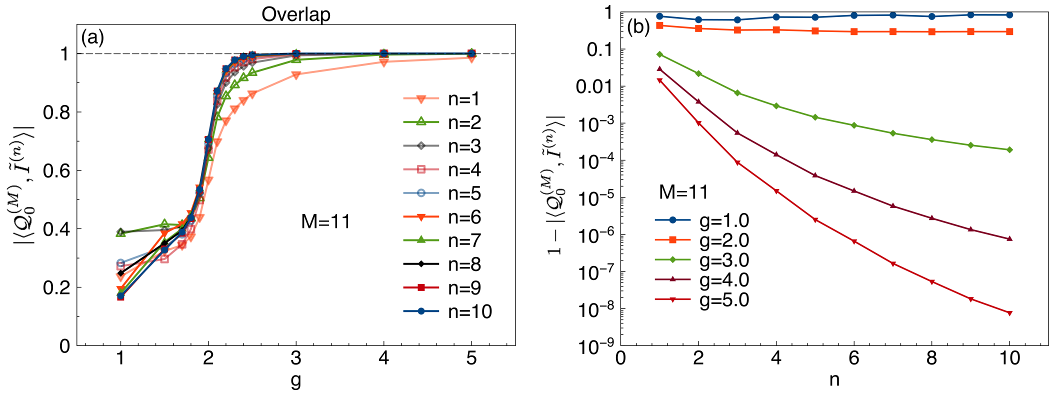

Figure 3.4: (color online) (a) The overlap between the full numerical optimization $Q_0^{(M)}$ with $M = 11$ and the perturbative SW construction $\tilde{I}^{(n)}$ with order $n = 1$ to 10. (b) One minus the overlap on the log-linear plot. At large g, the overlap between the two operators is almost 100%, which means that the slowest operator we found is essentially the dressed spin operator coming from the solvable limit H_0. On the other hand, for small g, the slowest operator does not look like the perturbative SW construction operator anymore. Interestingly, there is apparently a strong change in behavior around $g_c \approx 2$; however, we do not know if there is a true transition.

found in the large g limit as the translationally invariant sum of the dressed spin-z operator, or the dressed H_0. Interestingly, there appears to be a strong change in behavior at $g_c \approx 2$. For $g > g_c$, the slowest operator looks like the dressed spin-z operator, with an exponential scaling of the residual norm for small M; on the other hand, for $g < g_c$, the slowest operator does not look like the dressed spin-z operator, and its residual norm has a power-law scaling.

Note that despite the fact that the SW construction $\tilde{I}^{(n)}$ and the slowest operator $Q_0^{(M)}$ have very high overlap $1-\alpha$, where α can be a very small number as shown in Fig. 3.4(b), the difference between their squared residual norms can still be sizable. Indeed, consider $\tilde{I}^{(n)} = (1-\alpha)Q_0^{(M)} + \beta\eta$, where $\|Q_0^{(M)}\|_{\mathrm{F}} = \|\eta\|_{\mathrm{F}} = 1$ and η is some operator perpendicular to $Q_0^{(M)}$ in the Frobenius inner product. The normalization condition of $\tilde{I}^{(n)}$ gives $\beta^2 = 2\alpha - \alpha^2$, hence $\beta = O(\sqrt{\alpha})$. The squared residual norm of $\tilde{I}^{(n)}$ is $\|\mathrm{ad}_H(\tilde{I}^{(n)})\|_{\mathrm{F}}^2 = (1-\alpha)^2\|\mathrm{ad}_H(Q_0^{(M)})\|_{\mathrm{F}}^2 + \beta^2\|\mathrm{ad}_H(\eta)\|_{\mathrm{F}}^2 + 2\beta(1-\alpha)\mathrm{Re}[\langle \mathrm{ad}_H(Q_0^{(M)}), \mathrm{ad}_H(\eta)\rangle]$. We can thus see that

$$
\begin{aligned}
&\|\mathrm{ad}_H(\tilde{I}^{(n)})\|_{\mathrm{F}}^2 - \|\mathrm{ad}_H(Q_0^{(M)})\|_{\mathrm{F}}^2 \approx \\
&\approx 2\alpha\|\mathrm{ad}_H(\eta)\|_{\mathrm{F}}^2 + 2\sqrt{2\alpha}\,\mathrm{Re}[\langle \mathrm{ad}_H(Q_0^{(M)}), \mathrm{ad}_H(\eta)\rangle]\,,
\end{aligned}
$$

where we expressed everything in terms of the small number α and kept only terms that are expected to dominate. Note that while $\|\mathrm{ad}_H(Q_0^{(M)})\|_{\mathrm{F}}$ is a small number, no such smallness is expected for $\|\mathrm{ad}_H(\eta)\|_\mathrm{F}$ since the deviation direction η is not special in any way. Since $\|\eta\|_\mathrm{F} = 1$, we expect that $\|\mathrm{ad}_H(\eta)\|_\mathrm{F}$ is a number of order 1 in the energy units of H (and could be larger depending on the range of typical terms in η), which could be sufficient to explain the visible difference between the two residual norms in Fig. 3.1(b) despite the high overlap between $\tilde{I}^{(n)}$ and $Q_0^{(M)}$.

3.4 Characterizing the Slowest Operators

In this section, we analyze some properties of the quasi-conserved operators that we found in Sec. 3.1. We measure their "locality" in the operator space and in the real space, to contrast different behaviors of the slowest operators between small g and large g regimes.

Operator inverse participation ratio

From the previous section, we expect that for large g the quasi-conserved operator looks like a dressed spin operator. It is therefore reasonable to expect that $Q_0^{(M)}$ should be a sum of a small number of Pauli string operators, analogous to the local integrals of motion in MBL studies [19]. Using the Pauli string basis I, X, Y, Z (without forming the parity-invariant basis), we measure the operator inverse participation ratio (OIPR) [1] defined as

$$\mathrm{OIPR}(Q_0^{(M)}) = \left(\sum_{i=1}^{3\cdot 4^{M-1}} |a_i|^4 \right)^{-1} , \tag{3.18}$$

where a_i's are the amplitude of the I-X-Y-Z Pauli-string basis and we assumed normalization $\sum_{i=1}^{3\cdot 4^{M-1}} |a_i|^2 = 1$. The OIPR is bounded from below by 1.

Figure 3.5 shows the OIPR of the slowest operator $Q_0^{(M)}$ for different g. Interestingly, for larger $g \gtrsim 2$, the OIPR seems to converge to a finite value at large enough M. This behavior is consistent with our expectation that the quasi-conserved operator is a dressed total spin operator. The convergence of the OIPR indicates locality in the operator space. On the other hand, for small $g \lesssim 2$, the OIPR does not saturate but instead grows strongly with M. This suggests that the slowest operators we found in the ergodic regime are composed of an extensive number of the Pauli string basis states; hence they are "delocalized" in the operator space.

---

[1] Here we call the quantity in Eq. (3.18) "operator inverse participation ratio" so that it is consistent with usual definition, e.g., as used in single-particle localization problems where for a normalized wavefunction $\psi(x)$ the inverse participation ratio is $1/\sum_x |\psi(x)|^4$; this convention is different from that in Ref. [19].

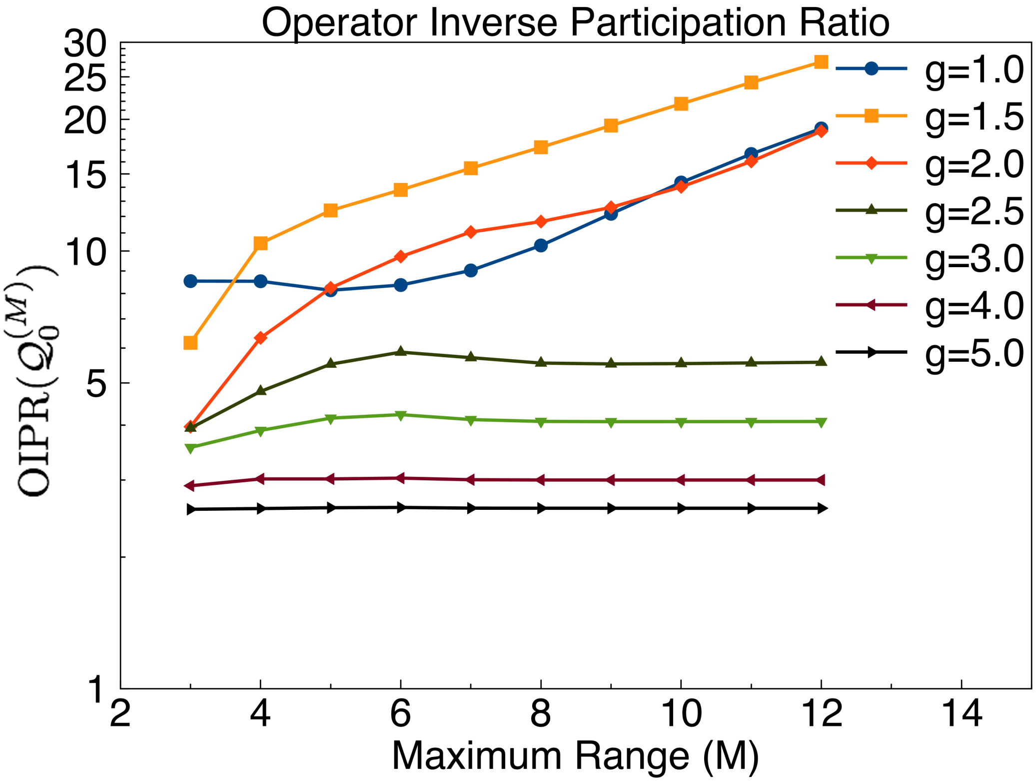

Figure 3.5: (color online) Operator inverse participation ratio of the slowest operator vs maximum range M for different g. For large $g \gtrsim 2$, the OIPR appears to converge to a finite value, which suggests its locality in the operator space. On the other hand, in the ergodic regime, $g \lesssim 2$, the OIPR does not converge and instead grows strongly with M (the behavior on the linear-log plot suggests exponential growth).

Real-space profile of the slowest operator

In this subsection, we examine the real-space shape of the slowest operator more closely. We define W_r as the weight of $Q_0^{(M)}$ on range-r operators. In other words, we can decompose $Q_0^{(M)} = \sum_{r=1}^{M} O_r$, with O_r being an operator with range exactly equal to r, and define $W_r = \|O_r\|_{\mathrm{F}}^2$. The normalization condition ensures that $\sum_r W_r = \sum_r \|O_r\|_{\mathrm{F}}^2 = \|Q_0^{(M)}\|_{\mathrm{F}}^2 = 1$. Figure 3.6(a) shows the weights W_r measured for the slowest operator $Q_0^{(M)}$ with $M = 12$.

For large $g \gtrsim 2$, the weight has an almost-exponential decay at small r. Figures 3.6(b)-(e) show the weights W_r for $Q_0^{(M)}$ at fixed g when increasing M from $M = 6$ to $M = 12$. From the plots, we can see that for large g, the weight of the profile is peaked on 2-local operators, which we can understand already from the leading order SW construction, see Eq. (3.34) in Appendix A. We also see that the exponentially decaying part of W_r at short distances is essentially converged, or

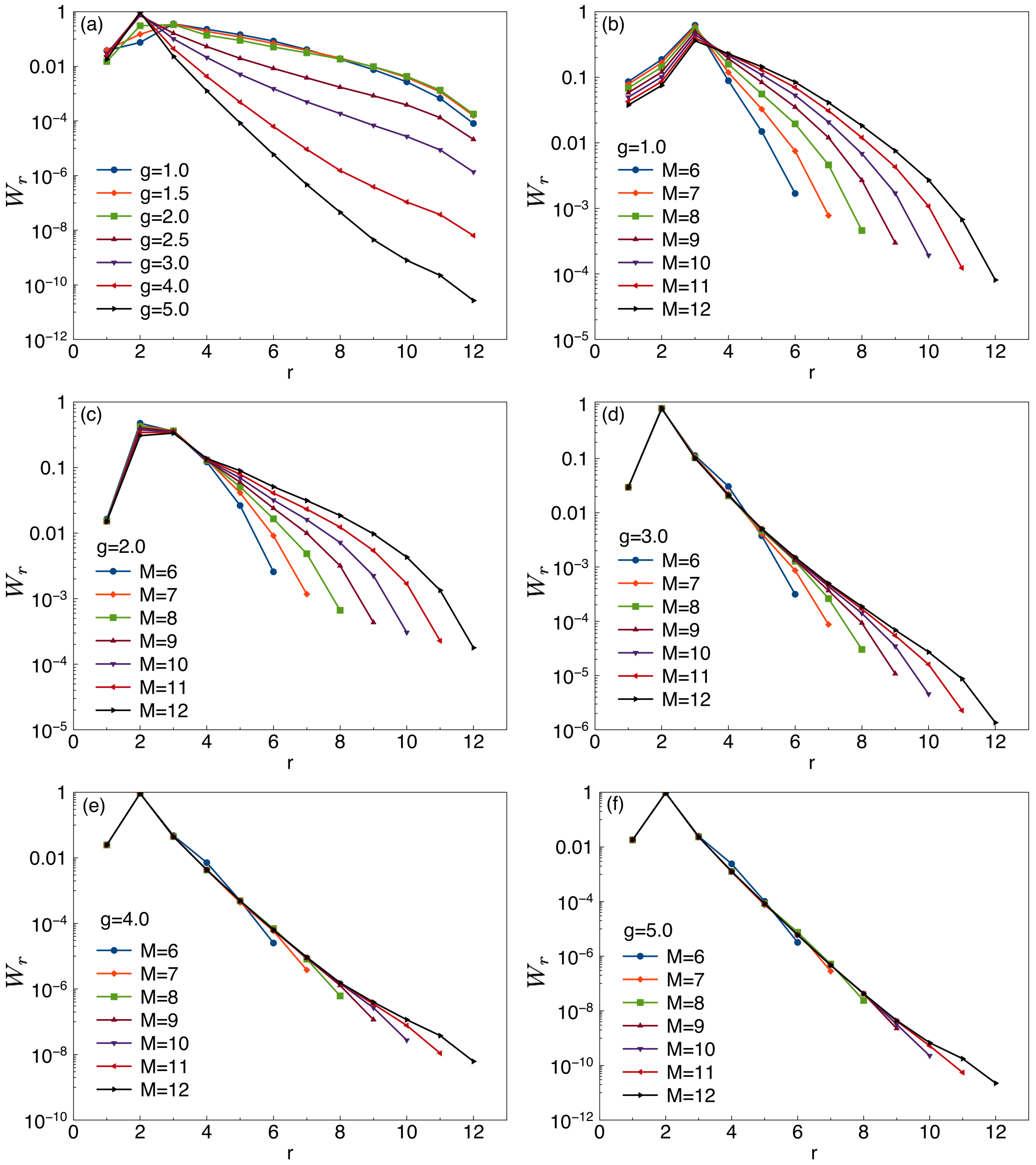

Figure 3.6: (color online) (a) The weight W_r of range-r operators contained in $Q_0^{(M)}$ with maximum range $M = 12$ for various g. For large $g \gtrsim 2$, the weight W_r decays exponentially at short distance r. The decay length grows as g decreases. For small $g \lesssim 2$, the decay of W_r is naively better described by a Gaussian, with the curves almost independent of g. (b)-(f) The weight W_r of range-r operators in $Q_0^{(M)}$ when varying M from $M = 6$ to $M = 12$ for fixed g indicated in each panel. For large g, the exponentially decaying part at short distances is essentially converged in M; however, the long-distance behavior is not clear. For small g, the weight distribution is pushed to larger r and shows significantly slower decay as a function of r when one increases M; this suggests that these operators are not normalizable in the large M limit.

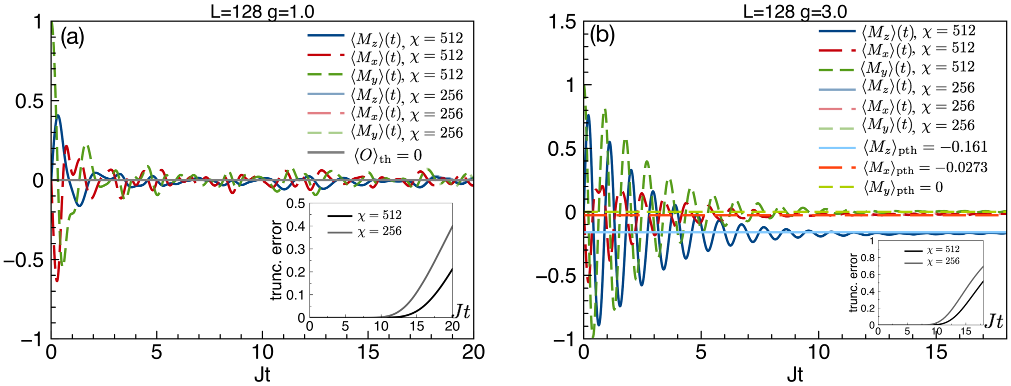

Figure 3.7: (color online) TEBD simulations with bond dimensions $\chi = 256$ and $\chi = 512$ of the evolution of various “magnetizations” $\langle M_{x,y,z}\rangle$ upon quench from the initial state $|Y+\rangle$. The Hamiltonian is given by Eq. (3.1) with parameters $J = 1.0$, $h = 1.5$, and different g indicated in each panel. (a) Evolution of the magnetizations for $g = 1$. The magnetizations appear to approach the thermal value $\langle O\rangle_{\rm th} = 0$ expected for any traceless observable O. (b) Evolution of the magnetizations for $g = 3$. The magnetizations are approaching values described by the generalized Gibbs ensemble that includes also the quasi-conserved operator (see text for details); the expected prethermalized values are marked with subscript “pth.” Insets in both panels show truncation error $1 - \langle\psi(t)|\psi(t)\rangle$ of the matrix-product states. We set the cut-off for the $\chi = 256$ simulation as $\mathfrak{s}_0 = 10^{-6}$, while for the $\chi = 512$ simulation the cut-off is $\mathfrak{s}_0 = 10^{-8}$.

independent of M. However, the “shape” of the operator at long distances is not yet converged and is hence undetermined. Despite the fact that we can not determine the long-distance behavior for the slowest operators due to computational limitations, it is clear that the short-distance decay becomes slower when one decreases g.

On the other hand, for small $g \lesssim 2$, there is no clear exponential decay even at short distance. In fact, for fixed g and M, the weights appear to decay faster than exponentially (with a Gaussian-like profile). However, the overall curve shifts to larger r as one increases M, with no apparent convergence to some fixed curve independent of M. This suggests the non-normalizability for the $\lim_{M\to\infty} Q_0^{(M)}$ operators in the small g regime and is also consistent with the result of increasing OIPR as one increases M, since there are more Pauli string operators involved in $Q_0^{(M)}$.

3.5 Dynamical Simulation

In order to demonstrate the effect of the quasi-conserved operator that we found in the large g limit, we perform a quench dynamics calculation and observe an intermediate prethermalization state. We explicitly show that to describe the prethermalization state, one needs to include the slowest operator in the generalized Gibbs ensemble (GGE). We prepare the initial state as a product state with all spins pointing in the positive-y direction, $|\psi\rangle = |Y+\rangle$ at time $t = 0$. We evolve the state under the Hamiltonian Eq. (3.1) as $|\psi(t)\rangle = e^{-iHt}|\psi\rangle$ and measure the evolution of the magnetizations $\langle M_\mu\rangle(t) \equiv \frac{1}{L}\sum_{j=1}^{L}\langle\psi(t)|\sigma_j^\mu|\psi(t)\rangle/\langle\psi(t)|\psi(t)\rangle$, where $\mu = x, y, z$. We use time-evolved block-decimation (TEBD) method [23] to simulate the quench dynamics in a system of length $L = 128$ with open boundary conditions. We use second-order Trotter-Suzuki decomposition with Trotter step $\delta t = 0.02$, which is sufficiently small to achieve the desired accuracy. We control truncations of the MPS using "cut-off" $\mathfrak{s}_0$, which means that we discard singular values smaller than $\mathfrak{s}_0$. We also use "bond dimension" χ, which means that we keep at most χ singular values. Two different sets of truncation parameters are used and compared against each other in order to estimate the effect of truncations on the MPS: $\mathfrak{s}_0 = 10^{-6}$, $\chi = 256$ and $\mathfrak{s}_0 = 10^{-8}$, $\chi = 512$. Figure 3.7 shows the results of the TEBD calculations. The loss of norm (truncation error) seen in the insets is due to various truncations and provides some measure of the accuracy of the time evolution (note that it is roughly compensated in the magnetization measurements by normalizing at each t, so the exhibited magnetizations are still reasonably accurate over the time range shown).

The effective inverse temperature β for any initial state $|\psi\rangle$ is determined by finding the parameter β such that equation $\langle\psi|H|\psi\rangle = \frac{1}{Z}\mathrm{Tr}[e^{-\beta H}H]$ is satisfied, where $Z = \mathrm{Tr}[e^{-\beta H}]$. The thermal value is defined as $\langle\ldots\rangle_{\mathrm{th}} = \frac{1}{Z}\mathrm{Tr}[\rho_{\mathrm{th}}\ldots]$, where $\rho_{\mathrm{th}} = e^{-\beta H}$ is the associated Gibbs ensemble. Since $\langle Y + |H|Y+\rangle = 0$, it is easy to verify that the effective inverse temperature $\beta = 0$ for this initial state. As a result, for any traceless observable O, the thermal value $\langle O\rangle_{\mathrm{th}} = 0$. Hence, if the system thermalizes, the magnetizations $\langle M_\mu\rangle(t)$ should approach zero.

Figure 3.7 shows the dynamical evolution of the magnetizations for parameters $g = 1$ and $g = 3$ for system size $L = 128$. For $g = 1$, even though the magnetizations have not fully equilibrated yet on our simulation times, we can see that they are fluctuating around zero, which is the expected thermal value. It is therefore reasonable to assume that the magnetizations are equilibrating toward zero, and the system thermalizes, without any prethermalization stage. On the other hand, for $g = 3$, it is visually clear that $\langle M_z\rangle(t)$ is approaching a sizable nonzero value. $\langle M_x\rangle(t)$ is also approaching a small nonzero value, even though it is less clear visually. The prethermalization stage persists over our simulation time, which is consistent with our bound on t_* in

Sec. 3.2.

Crude features in the dynamics for $g = 3$ can in fact be understood easily as the precession of the spins. If $J = 0$, the spins, which are pointing along y+ direction initially, will precess under H_0 persistently. The $T = J\sum_j Z_j Z_{j+1}$ term introduces interactions among the spins, resulting in the decay of the precession, therefore the damping of the magnetization oscillation. There is a simple quasiparticle description to understand the oscillation and the decay [24]. Viewing H_0 as the "total particle number," part of the T term introduces "hopping" of the "particles." The oscillation frequency can essentially be understood as the quasiparticle excitation energy. Even if we modeled the quasiparticles using an integrable hard-core boson Hamiltonian, the oscillations will damp eventually. However, the equilibrium value (at least at this intermediate stage) is not described by the Gibbs ensemble.

Here we verify the conjecture that, to describe these intermediate equilibrium values, one needs to include the quasi-conserved quantity into a generalized Gibbs ensemble (GGE). The GGE in this case is $\rho_{\text{pth}} \equiv e^{-\alpha H} e^{-\mu Q_0^{(M)}}/Z_{\text{pth}}$, and $Z_{\text{pth}} \equiv \text{Tr}[e^{-\alpha H} e^{-\mu Q_0^{(M)}}]$. [Here we used the above form for the GGE rather than $e^{-\alpha H - \mu Q_0^{(M)}}$, since the former is easier to evaluate numerically where one only needs to diagonalize $Q_0^{(M)}$ once, instead of diagonalizing $\alpha H + \mu Q_0^{(M)}$ for each pair of (α, μ). Furthermore, since $Q_0^{(M)}$ and H almost commute, we expect the two expressions are approximately the same.] The parameters (α, μ) are determined by finding the values satisfying the following equations

$$\langle\psi|H|\psi\rangle = \frac{1}{Z_{\text{pth}}}\text{Tr}[H\rho_{\text{pth}}]\,, \tag{3.19}$$

$$\langle\psi|Q_0^{(M)}|\psi\rangle = \frac{1}{Z_{\text{pth}}}\text{Tr}[Q_0^{(M)}\rho_{\text{pth}}]\,. \tag{3.20}$$

For the initial state $|Y+\rangle$, $\langle Y+|H|Y+\rangle = 0$; while $\frac{1}{L}\langle Y+|Q_0^{(M)}|Y+\rangle = 0.63889$ using $Q_0^{(M=12)}$. In fact, the "particle densities" in the initial state, $\frac{1}{L}\langle Y+|Q_0^{(M)}|Y+\rangle$, measured from $M = 8$ to $M = 11$ are within approximately 1% from the $M = 12$ result. Note also that since the initial state is a product state, the particle density in a finite system of size L will be independent of L as long as $L \geq M$. We then solve for (α, μ) on the right-hand side using Newton's method, while ρ_{pth} is evaluated by the exact diagonalization of H and $Q_0^{(M)}$ for system size $L = 16$ and $M = 8$ (the largest L and M accessible with our computation resources), under periodic boundary condition; we find $(\alpha, \mu) = (-0.05155, -1.4417)$. We then calculate the prethermalized GGE values as $\langle M_z\rangle_{\text{pth}} = -0.161045$, $\langle M_x\rangle_{\text{pth}} = -0.0273397$, and $\langle M_y \rangle_{\text{pth}} = 0$ (by time-reversal symmetry in the effective Hamiltonian for the prethermalized state), where $\langle \dots \rangle_{\text{pth}} = \frac{1}{Z_{\text{pth}}}\text{Tr}[\rho_{\text{pth}} \dots]$. Figure 3.7(b) shows a fair agreement between the observed prethermal equilibrium values $\langle M_\mu \rangle(t)$ and the GGE estimates $\langle M_\mu \rangle_{\text{pth}}$.

We have thus explicitly verified that the quasi-conserved operator in the large g regime has nontrivial effects on the relaxation of the system. Furthermore, to describe the equilibrium values at the intermediate prethermalization stage, one needs to include this quasi-conserved operator in the generalized Gibbs ensemble.

3.6 Discussion

We numerically construct the slowest operator that is translationally invariant with maximum range M. In the small coupling regime, the norm of the commutator of the slowest operator with the Hamiltonian has a power-law dependence on M. On the other hand, in the strong coupling regime, we find exponential decay at least at small M, identifying the slowest operator as quasi-conserved operator. At larger M, however, the decay becomes slower, possibly a power law. This may be related to the eventual thermalization of the system, after a prethermalization stage with a parametrically long time scale. The true behavior at large M is not certain due to the limitations of our numerical calculations, constrained by the exponentially large operator Hilbert space. However, from the analysis of the OIPR, it appears that the quasi-conserved operator resides only on a very small fraction of states in the total Hilbert space. It may therefore be possible to reduce the relevant operator Hilbert space dimension by identifying the property of this space and by restricting studies to only such an ansatz, which could potentially allow reaching larger maximum range; we leave this idea for future studies.

Our TEBD calculation of the dynamics after a quench explicitly confirms the existence of the prethermalization stage for large g and further supports the GGE construction that includes the quasi-conserved operator. From the residual Frobenius norm of the quasi-conserved operator $\sqrt{\lambda_0(M)}$, we can heuristically provide a lower bound on the thermalization time scale as $t_* \sim 2^{-\frac{M+1}{2}} \lambda_0(M)^{-1/2}$; we can also bound the thermalization time more accurately by measuring the conventional operator norm, $t_* \sim (\|[H, Q_0^{(M)}]\|_{\text{op}} / \|Q_0^{(M)}\|_{\text{op}})^{-1}$. However, we cannot determine the time scale of the prethermalization stage from the TEBD calculations due to the limited accessible simulation time. Even if we could extend the TEBD calculation to longer times, we may have to consider a different truncation scheme [25] to get more accurate results. A straightforward truncation of small singular values in the MPS state does not necessary conserve the quasi-conserved quantity, and hence may artificially decrease the prethermalization time. It would be interesting to extract the prethermalization time scale directly from simulations or even from experiments to compare with our heuristic argument.

Another interesting observation which we still do not fully understand is the apparent "transition" between the prethermalization and ergodic behaviors. While it is not clear what defines the prethermalization "phase," it appears that the different scaling behavior of the residual norm can serve as an indicator. Furthermore, the OIPR seems to provide a stronger signature: the OIPR of the slowest operator appears to converge with M in the large coupling regime $g \geq 2.5$, while the OIPR diverges in the ergodic regime. Also, the operator profile appears to converge with increasing M for $g \geq 3$ while it does not converge for $g \leq 2$. The persistence of this sharp distinction between the prethermalization and ergodic behaviors to larger M or even $M \to \infty$ deserves more study.

An exciting possibility which may be suggested by our results for $g \geq 3$ is the existence of the truly conserved quasi-local quantity [13, 15, 16], or the convergence of the SW transformation in the $n \to \infty$ limit. While the theoretical upper bounds on the norms in the SW series do not prove the convergence, they do not disprove it either. In fact, from our numerical calculations in Appendix E, the convergence of the SW transformation might even be possible. This would imply that we can find a (quasi-local) unitary transformation U such that $U^\dagger H U$ commutes with H_0. A partial breakdown of ETH would be possible due to the existence of this emergent "particle conservation" in the entire spectrum. In fact, the quantum Ising model $H = \sum_j X_j + \epsilon \sum_j Z_j Z_{j+1}$ provides an example where the SW procedure converges [12, 26]. In this case, instead of one (or few) conserved quantity, there is a macroscopic number of conservation laws due to the model's integrability. Nevertheless, the SW procedure "does not know" the free fermion solution but still converges and finds a conserved quantity, which happens to be the total number of the Bogoliubov quasi-particles. Our intriguing results in the nonintegrable model thus warrant further detailed studies of the convergence of the SW transformation.

In conclusion, by numerically searching for the slowest operator, we identified the quasi-conserved operator at large coupling, which we believe is responsible for the prethermalization behavior. The residual norm of the quasi-conserved operator has exponential decay with its maximum range up to some point; the OIPR and real-space profile show that it is localized in the operator Hilbert space and real space. By comparing with the perturbative SW construction, we concluded that the quasi-conserved quantity is essentially the dressed total spin-z operator. Finally, by simulating the quench dynamics, we verified the conjecture that the quasi-conserved quantity leads to prethermalization behavior. Furthermore, the apparent equilibrium values at the prethermalization stage can be described by including the quasi-conserved quantity in the GGE.

Appendix A: Generalized Ladder Algebra Formalism

In Ref. [22], MacDonald *et. al.* proposed a perturbative expansion for the electronic Hubbard model in the large U limit using generalized ladder algebra formalism. In fact, their transformation is a variant of a local SW transformation [20, 21]. A small difference from the SW transformation used in the present work is that Ref. [22] constructs a unitary transformation of the form $\exp(i\epsilon S_1 + i\epsilon^2 S_2 + \cdots + i\epsilon^n S_n)$ rather than $\exp(i\epsilon S_1)\exp(i\epsilon^2 S_2)\ldots\exp(i\epsilon^n S_n)$. This modifies Eq. (3.10) by replacing $\mathfrak{f}(k_1,\ldots,k_p)$ to $\frac{1}{p!}$, see Ref. [20]. The variant in the present paper is slightly easier to use in numerical calculations because there are fewer terms in the series.

For our spin Hamiltonian, the spectrum of the solvable limit H_0 is composed of different sectors labeled by different "particle" numbers. To be concrete, consider

$$H_0 = \Gamma \sum_j Z_j \,, \tag{3.21}$$

where we have rotated $gX_j + hZ_j$ to the new z-direction and $\Gamma = \sqrt{g^2 + h^2}$. The (rotated) perturbation T can be decomposed into $T = \sum_{\ell=-2}^{2} T_\ell$, where T_ℓ-s are called generalized ladder operators, with the property that $[H_0, T_\ell] = 2\Gamma\ell T_\ell$. More explicitly, defining $P_j, M_j = \frac{1}{2}(X_j \pm iY_j)$, we have

$$T_{+2} = t_2 \sum_j P_j P_{j+1} \,, \tag{3.22}$$

$$T_{-2} = t_2 \sum_j M_j M_{j+1} = T_{+2}^\dagger \,, \tag{3.23}$$

$$T_{+1} = t_1 \sum_j (P_j Z_{j+1} + Z_j P_{j+1}) \,, \tag{3.24}$$

$$T_{-1} = t_1 \sum_j (M_j Z_{j+1} + Z_j M_{j+1}) = T_{+1}^\dagger \,, \tag{3.25}$$

$$T_0 = u_0 \sum_j Z_j Z_{j+1} + w_0 \sum_j (P_j M_{j+1} + M_j P_{j+1}) \,, \tag{3.26}$$

where $t_1 = -\frac{Jgh}{\Gamma^2}$, $t_2 = \frac{Jg^2}{\Gamma^2}$, $u_0 = \frac{Jh^2}{\Gamma^2}$, and $w_0 = t_2$.

Let us further define

$$T^{(k)}(\ell_1, \dots, \ell_k) \equiv T^{(k)}[\ell] = T_{\ell_1} \dots T_{\ell_k} \,. \tag{3.27}$$

One can easily verify that these operators are also generalized ladder operators: $[H_0, T^{(k)}[\ell]] = 2\Gamma M^{(k)}[\ell] T^{(k)}[\ell]$, where $M^{(k)}[\ell] \equiv \sum_{i=1}^{k} \ell_i$. In particular, if $M^{(k)}[\ell] = 0$, then $T^{(k)}[\ell]$ is in the nullspace of ad_{H_0}.

It is easy to argue that V_m can all be expressed as nested commutators of T_ℓ-s by mathematical induction from Eq. (3.10) and Eq. (3.12), given that iS_k and V_k are all composed of nested commutators of T_ℓ-s for $k < m$. Assuming $V_m = (2\Gamma)^{1-m} \sum_{\{\ell\}} C^{(m)}[\ell] T^{(m)}[\ell]$, where coefficients $C^{(m)}[\ell]$ have special structure such that V_m is composed of nested commutators of T_ℓ-s, Eq. (3.12) gives

$$iS_m = (2\Gamma)^{-m} \sum_{\{\ell\}, M^{(m)}[\ell] \neq 0} \frac{C^{(m)}[\ell] T^{(m)}[\ell]}{M^{(m)}[\ell]} \,. \tag{3.28}$$

One can therefore see that it is a special type of the local SW where everything is expressed by the generalized ladder algebra.

As an example, we work out the effective Hamiltonian and the quasi-conserved operator to second-order. At first order, $V_1 = T$, so we want to find iS_1 such that $i\mathrm{ad}_{S_1}(H_0) + T = T_0$. The solution is

$$iS_1 = \frac{1}{4\Gamma}(T_{+2} - T_{-2}) + \frac{1}{2\Gamma}(T_{+1} - T_{-1}) \,. \tag{3.29}$$

We therefore obtain

$$\begin{aligned} V_2 &= \frac{1}{2} i\mathrm{ad}_{S_1} i\mathrm{ad}_{S_1}(H_0) + i\mathrm{ad}_{S_1}(T) = \frac{1}{2} i\mathrm{ad}_{S_1}(T_0 + T) \\ &= \frac{1}{8\Gamma}\Big(2[T_{+2}, T_0] - 2[T_{-2}, T_0] + 4[T_{+1}, T_0] - 4[T_{-1}, T_0] \\ &- [T_{+2}, T_{+1}] + [T_{-2}, T_{-1}] + 3[T_{+2}, T_{-1}] - 3[T_{-2}, T_{+1}] \\ &+ 2[T_{+2}, T_{-2}] + 4[T_{+1}, T_{-1}]\Big) \,. \end{aligned} \tag{3.30}$$

The last line is the diagonal part of V_2 while the rest is the off-diagonal part. At second order, we solve for iS_2 such that $i\mathrm{ad}_{S_2}(H_0) + V_2 = V_2^{\mathrm{diag}}$; the solution is

$$\begin{aligned} iS_2 &= \frac{1}{48\Gamma^2}\Big(3[T_{+2}, T_0] + 3[T_{-2}, T_0] + 12[T_{+1}, T_0] \\ &+ 12[T_{-1}, T_0] - [T_{+2}, T_{+1}] - [T_{-2}, T_{-1}] \\ &+ 9[T_{+2}, T_{-1}] + 9[T_{-2}, T_{+1}]\Big) \,. \end{aligned} \tag{3.31}$$

We can now obtain contributions to the quasi-conserved operator as

$$\begin{aligned} I_1 &= T - T_0 = T_{+2} + T_{-2} + T_{+1} + T_{-1}\ , \qquad (3.32) \\ I_2 &= -V_2^{\text{diag}} + i\text{ad}_{S_1}(T_0) = \frac{1}{4\Gamma}\Big(- [T_{+2}, T_{-2}] - 2[T_{+1}, T_{-1}] \\ &+ [T_{+2} - T_{-2}, T_0] + 2[T_{+1} - T_{-1}, T_0]\Big)\ . \qquad (3.33) \end{aligned}$$

To compare with the slowest operator approach, we calculate the component perpendicular to H, which can be obtained via Eq. (3.15). For example, we find for the leading-order SW construction,

$$I_1^{\perp} = I_1 - \frac{J^2 g^2 (g^2 + 4h^2)}{2(J^2 + g^2 + h^2)^2 (g^2 + h^2)} H\ . \qquad (3.34)$$

This can be used to understand the 1-local and 2-local content of the slowest operator for large g, see Fig. 3.6.

Appendix B: Bound on $H_{>n}$

In this Appendix, we prove the bound on $\|H_{>n}\|_{\text{F}}$ quoted in the main text. We set the norm of H_0 as the energy unit, $\|H_0\|_{\text{F}} = \Gamma$, and the norm of the perturbation term as $\epsilon\|T\|_{\text{F}} = \epsilon\Gamma$, where ϵ is the strength of the perturbation and is used to organize the perturbative expansion. We also assume that $H_0 \in \mathcal{T}_1$ and $T \in \mathcal{T}_2$. Without loss of generality, we assume working in the basis such that $H_0 = \Gamma \sum_j Z_j$, since for any general $H_0 \in \mathcal{T}_1$ one can always rotate the basis to achieve this. The results in this appendix are parallel to the results obtained in Ref. [21] but are tailored to our definitions of norms for translationally-invariant operators and the specific SW procedure used; furthermore, our results are not restricted to effective Hamiltonians in the lowest-energy sector but are valid for the entire spectrum.

We first prove the locality of the operators S_m and V_m in the SW transformation procedure, Sec. 3.3, and of the operators I_m in the quasi-conserved quantity obtained by SW transformation, Sec. 3.3.

Proposition 3.6.1. *$V_m \in \mathcal{T}_{m+1}$, $S_m \in \mathcal{T}_{m+1}$, and $I_m \in \mathcal{T}_{m+1}$.*

Proof. By assumption, $H_0 \in \mathcal{T}_1$, hence ad_{H_0} maps $\mathcal{T}_m$ to $\mathcal{T}_m$. The pseudo-inverse $[\text{ad}_{H_0}]^{-1}$ thus also maps from $\mathcal{T}_m$ to $\mathcal{T}_m$. Therefore, from Eq. (3.12) it follows that if $V_m \in \mathcal{T}_{m+1}$ then $S_m \in \mathcal{T}_{m+1}$. Initially, $V_1 = T \in \mathcal{T}_2$ and hence $S_1 \in \mathcal{T}_2$. Assume $V_k \in \mathcal{T}_{k+1}$ and $S_k \in \mathcal{T}_{k+1}$ hold for $k \leq m-1$. Now consider the first term in V_m in Eq. (3.10); we see that $i\text{ad}_{S_{k_p}} \dots i\text{ad}_{S_{k_1}}(H_0) \in \mathcal{T}_{m+1}$ since $k_1 + \cdots + k_p = m$. The second term in V_m is also in $\mathcal{T}_{m+1}$, by noticing that $k_1 + \cdots + k_p = m - 1$ and $T \in \mathcal{T}_2$ in $i\mathrm{ad}_{S_{k_p}} \ldots i\mathrm{ad}_{S_{k_1}}(T)$. By similar argument applied to Eq. (3.14), we have $I_m \in \mathcal{T}_{m+1}$. The proposition is proved by mathematical induction. $\square$

Here we introduce a different norm on the operator Hilbert space $\mathcal{T}_k$ which will be technically useful in the future proofs. Consider any operator $O \in \mathcal{T}_k$ written in the Pauli-string basis composed of I, $P \equiv \frac{1}{2}(X + iY)$, $M \equiv \frac{1}{2}(X - iY)$, and Z: $O = \sum_j \sum_{\mathbf{a}} o_{\mathbf{a}} Q^{\mathbf{a}}_{j;k}$, where $Q^{\mathbf{a}}_{j;k} = \sigma^{a_1}_j \ldots \sigma^{a_k}_{j+k-1}$ denotes the "I-P-M-Z" string with support on sites j to $j + k - 1$ with non-identity on the site j. That is, σ on each site other than j can be one of the four operators I, P, M, or Z, while it can be only P, M, or Z on the site j (recall that $\mathcal{T}_k$ consists of traceless operators, and this "gauge" choice for writing local operators is similar to the one in the main text).

Definition 3.6.1. *For $O = \sum_j \sum_{\mathbf{a}} o_{\mathbf{a}} Q^{\mathbf{a}}_{j;k} \in \mathcal{T}_k$, the one-norm is defined as $\|O\|_1 = \sum_{\mathbf{a}} |o_{\mathbf{a}}|$.*

Such a definition of the one-norm is in fact basis-dependent, so it is crucial that our one-norm is understood in the basis such that $H_0 = \Gamma \sum_j Z_j$ and operators are expanded in the I-P-M-Z strings. These particular I-P-M-Z strings are orthogonal but not normalized with the respect to the Frobernius inner product in $\mathcal{T}_k$. In fact, $\|Q^{\mathbf{a}}_{j;k}\|^2_{\mathrm{F}} = 2^{-N_{\mathbf{a}}}$, where $N_{\mathbf{a}}$ is the number of P and M letters in $Q^{\mathbf{a}}_{j;k}$.

Our one-norm can be used to bound the Frobenius norm discussed in the main text:

Proposition 3.6.2. *For $O \in \mathcal{T}_k$, we have $\|O\|_F \leq \|O\|_1 \leq \sqrt{5 \cdot 6^{k-1}}\|O\|_F$.*

Proof. Indeed, writing O in the I-P-M-Z strings as $O = \sum_j \sum_{\mathbf{a}} o_{\mathbf{a}} Q^{\mathbf{a}}_{j;k}$, we have

$$\|O\|^2_{\mathrm{F}} = \sum_{\mathbf{a}} |o_{\mathbf{a}}|^2 2^{-N_{\mathbf{a}}} \leq \sum_{\mathbf{a}} |o_{\mathbf{a}}|^2 \leq \left(\sum_{\mathbf{a}} |o_{\mathbf{a}}| \right)^2 = \|O\|^2_1 .$$

The last inequality follows from the fact that there are more non-negative terms on the right-hand side.

For the bound on the one-norm, using Cauchy-Schwartz inequality, we have

$$\sum_{\mathbf{a}} \left(|o_{\mathbf{a}}| \, 2^{-\frac{N_{\mathbf{a}}}{2}} \right) \left(2^{\frac{N_{\mathbf{a}}}{2}} \right) \leq \sqrt{\sum_{\mathbf{a}} \left(|o_{\mathbf{a}}| \, 2^{-\frac{N_{\mathbf{a}}}{2}} \right)^2} \sqrt{\sum_{\mathbf{a}} \left(2^{\frac{N_{\mathbf{a}}}{2}} \right)^2} ,$$

or

$$\|O\|_1 \leq \|O\|_{\mathrm{F}} \sqrt{\sum_{\mathbf{a}} 2^{N_{\mathbf{a}}}} . \tag{3.35}$$

Remembering that the first site can only be P, M, or Z, a simple combinatorial exercise gives $\sum_{\mathbf{a}} 2^{N_{\mathbf{a}}} = 5 \cdot 6^{k-1}$. ☐

We now present two propositions describing key properties of our one-norm that will be used in the proof of the main bounds.

Proposition 3.6.3. *If $U \in \mathcal{T}_r$ and $W \in \mathcal{T}_s$, then $\|ad_U(W)\|_1 \leq 2(r+s-1)\|U\|_1\|W\|_1$.*

Proof. By writing out $U = \sum_j \sum_{\mathbf{a}} u_{\mathbf{a}} Q^{\mathbf{a}}_{j;r}$ and $W = \sum_k \sum_{\mathbf{b}} w_{\mathbf{b}} Q^{\mathbf{b}}_{k;s}$ in the I-P-M-Z strings, we have

$$\|\mathrm{ad}_U(W)\|_1 = \| \sum_k \sum_{j=k-r+1}^{k+s-1} \sum_{\mathbf{a},\mathbf{b}} u_{\mathbf{a}} w_{\mathbf{b}} [Q^{\mathbf{a}}_{j;r}, Q^{\mathbf{b}}_{k;s}] \|_1 \ . \tag{3.36}$$

Let us first consider the product $Q^{\mathbf{a}}_{j;r} Q^{\mathbf{b}}_{k;s}$ for a particular j and strings $\mathbf{a}$ and $\mathbf{b}$. By the multiplication rules among I, P, M, and Z, we note that $Q^{\mathbf{a}}_{j;r} Q^{\mathbf{b}}_{k;s}$ will "split" into $2^{N_{\mathbf{a},\mathbf{b}}}$ new I-P-M-Z strings, where $N_{\mathbf{a},\mathbf{b}}$ is the number of the positions that the letter P in $Q^{\mathbf{a}}_{j;r}$ collides with M in $Q^{\mathbf{b}}_{k;s}$ or M in $Q^{\mathbf{a}}_{j;r}$ collides with P in $Q^{\mathbf{b}}_{k;s}$, since $PM = \frac{1}{2}(I+Z)$ and $MP = \frac{1}{2}(I-Z)$. However, each such new string will carry a factor $2^{-N_{\mathbf{a},\mathbf{b}}}$, with a plus or minus sign. Therefore, $Q^{\mathbf{a}}_{j;r} Q^{\mathbf{b}}_{k;s}$ will generate $2^{N_{\mathbf{a},\mathbf{b}}}$ new strings carrying coefficients $\pm u_{\mathbf{a}} w_{\mathbf{b}} 2^{-N_{\mathbf{a},\mathbf{b}}}$, and likewise for $Q^{\mathbf{b}}_{k;s} Q^{\mathbf{a}}_{j;r}$. Upon summing over k, each new string should be understood as "gauge-fixed" by shifting the position such that the first non-trivial letter is at position k.

Now we consider writing out the full $\mathrm{ad}_U(W)$ in Eq. (3.36) in the I-P-M-Z strings. Coefficient for each basis string will be some collection of the contributions described above from different j, $\mathbf{a}$, and $\mathbf{b}$. Applying the triangle inequality $|x+y+\cdots+z| \leq |x|+|y|+\cdots+|z|$ for each such coefficient, we then have

$$\begin{aligned} \|\mathrm{ad}_U(W)\|_1 &\leq 2 \sum_{j=k-r+1}^{k+s-1} \sum_{\mathbf{a},\mathbf{b}} |u_{\mathbf{a}} w_{\mathbf{b}} 2^{-N_{\mathbf{a},\mathbf{b}}}| 2^{N_{\mathbf{a},\mathbf{b}}} \\ &= 2(r+s-1)\|U\|_1\|W\|_1 \ , \end{aligned} \tag{3.37}$$

where the first factor of 2 accounts for $Q^{\mathbf{a}}_{j;r} Q^{\mathbf{b}}_{k;s}$ and $Q^{\mathbf{b}}_{k;s} Q^{\mathbf{a}}_{j;r}$, and the factor of $r+s-1$ comes from the counts of j. ☐

Equation (3.12) establishes the relation between S_m and V_m, from which we deduce the following Proposition:

Proposition 3.6.4. $\|S_m\|_1 \leq \frac{\|V_m\|_1}{2\Gamma}$.

Proof. First, we note that since $[\mathrm{ad}_{H_0}]^{-1}$ is the pseudoinverse of ad_{H_0}, it is customary to rewrite Eq. (3.12) as $iS_m = [\mathrm{ad}_{H_0}]^{-1}V_m$. The pseudoinverse of ad_{H_0} in fact can be easily obtained as follows. To be specific, let us consider ad_{H_0} as a map from $\mathcal{T}_{m+1}$ to $\mathcal{T}_{m+1}$, since iS_m and V_m belong to $\mathcal{T}_{m+1}$. Also recall that we have rotated the Pauli basis such that $H_0 = \Gamma \sum_j Z_j$ in order to define the one-norm. The I-P-M-Z strings are in fact (non-normalized) eigenvectors of ad_{H_0} with eigenvalues $2(N_P - N_M)\Gamma$, where N_P (N_M) is the number of P (M) in the I-P-M-Z string. The pseudoinverse $[\mathrm{ad}_{H_0}]^{-1}$ is thus diagonal with eigenvalues $\frac{1}{2(N_P-N_M)\Gamma}$ if $N_P - N_M \neq 0$ and zero if $N_P - N_M = 0$. Therefore, assuming $V_m = \sum_j \sum_{\mathbf{a}} v_{\mathbf{a}} Q^{\mathbf{a}}_{j;m+1}$ in the I-P-M-Z strings, we have

$$\begin{aligned} \|S_m\|_1 &= \sum_{\mathbf{a}:N_P-N_M\neq 0} \left| \frac{v_{\mathbf{a}}}{2(N_P-N_M)\Gamma} \right| \\ &\leq \sum_{\mathbf{a}} \frac{|v_{\mathbf{a}}|}{2\Gamma} = \frac{\|V_m\|_1}{2\Gamma} . \end{aligned} \tag{3.38}$$

□

We are now ready to consider the SW-rotated Hamiltonian, Eq. (3.9). To remind readers, H' is obtained by an exact unitary rotation using generators $iS_1, \ldots, iS_n$, which we call n-th order SW, with specific rules for finding these generators. Equation (3.9) represents a formal expansion of H' in powers of ϵ. The "potentials" V_m in Eq. (3.10) for $m \leq n$ (actually, even $m \leq n+1$) are already representative of the infinite-order SW series and do not depend on n, while the potentials for $m > n$ that contribute to the "remainder" $H_{>n}$ actually depend on n. Not to overburden the notation, we consider n as fixed and do not put extra label on such V_m. Below, we focus on convergence properties of the formal expansion in ϵ of $H_{>n}$, which will also provide a bound on its norm and inform us about locality properties of H'.

To obtain an upper bound on the norm of $H_{>n}$, we need some control over the V_m terms, especially for $m > n$. This is provided by the following Lemma.

Lemma 3.6.1. *In the SW construction to the n-th order, for $m > n$, $\|V_m\|_F \leq \Gamma(\rho_n)^{-m}$, where $\rho_n \equiv \frac{1}{263n^2}$.*

Proof. It is convenient to define $v_m \equiv \|V_m\|_1$ and $s_m \equiv \|S_m\|_1$. From Eq. (3.10), abbreviating $A_{k_p\ldots k_1} \equiv i\mathrm{ad}_{S_{k_p}} \ldots i\mathrm{ad}_{S_{k_1}}(H_0)$ and $B_{k_p\ldots k_1} \equiv i\mathrm{ad}_{S_{k_p}} \ldots i\mathrm{ad}_{S_{k_1}}(T)$ and using triangle inequality, we have

$$\begin{aligned}\|V_m\|_{\mathrm{F}} &\leq v_m \leq \sum_{p=2}^{m} \sum_{[k_1,\ldots,k_p]=m} \mathfrak{f}(k_1,\ldots,k_p) \| A_{k_p\ldots k_1} \|_1 \\ &+ \sum_{p=1}^{m-1} \sum_{[k_1,\ldots,k_p]=m-1} \mathfrak{f}(k_1,\ldots,k_p) \| B_{k_p\ldots k_1} \|_1 \ .\end{aligned}$$

Using Proposition (3.6.3) and the fact that $S_{k_\ell} \in \mathcal{T}_{k_\ell+1}$ and $k_\ell \leq n$, we have

$$\begin{aligned}\|A_{k_p\ldots k_1}\|_1 &\leq 2^p(k_p+\cdots+k_1+1)\ldots(k_1+1) \\ &\times s_{k_p}\ldots s_{k_1}\|H_0\|_1 \\ &\leq 2^p\left[\prod_{\ell=1}^{p}(\ell n+1)\right]\times s_{k_p}\ldots s_{k_1}\|H_0\|_1 \\ &\leq p!\left(\frac{n+1}{\Gamma}\right)^p v_{k_p}\ldots v_{k_1}\|H_0\|_1 \\ &< p!\left(\frac{n+2}{\Gamma}\right)^p v_{k_p}\ldots v_{k_1}\|H_0\|_1 \ , \end{aligned} \tag{3.39}$$

where the last inequality is taken solely to simplify later calculations. Similarly, we have

$$\begin{aligned}\|B_{k_p\ldots k_1}\|_1 &\leq 2^p(k_p+\cdots+k_1+2)\ldots(k_1+2) \\ &\times s_{k_p}\ldots s_{k_1}\|T\|_1 \\ &\leq p!\left(\frac{n+2}{\Gamma}\right)^p v_{k_p}\ldots v_{k_1}\|T\|_1 \ .\end{aligned}$$

Next, we use the relation $\sum_{[k_1,\ldots,k_p]=m}\mathfrak{f}(k_1,\ldots,k_p)\,(\bullet) = \frac{1}{p!}\sum_{[k_1,\ldots,k_p]=m}(\bullet)$, where $(\bullet)$ is any summand symmetric under permutation of indices $k_1,\ldots,k_p$. We therefore obtain

$$\begin{aligned}v_m &\leq \|H_0\|_1\sum_{p=2}^{m}c^p\sum_{[k_1,\ldots,k_p]=m}v_{k_1}\ldots v_{k_p} \\ &+ \|T\|_1\sum_{p=1}^{m-1}c^p\sum_{[k_1,\ldots,k_p]=m-1}v_{k_1}\ldots v_{k_p} \ , \end{aligned} \tag{3.40}$$

where $c \equiv \frac{n+2}{\Gamma}$.

It is convenient to iteratively define another set of numbers, μ_m, starting with $\mu_1 \equiv v_1$, and

$$\begin{aligned} \mu_m &\equiv \|H_0\|_1 \sum_{p=2}^{m} c^p \sum_{k_1+\cdots+k_p=m} \mu_{k_1}\ldots\mu_{k_p} \\ &+ \|T\|_1 \sum_{p=1}^{m-1} c^p \sum_{k_1+\cdots+k_p=m-1} \mu_{k_1}\ldots\mu_{k_p} \,, \end{aligned} \tag{3.41}$$

for $m \geq 2$. Note that in the summation, the condition $k_\ell \leq n$ for $\ell = 1,\ldots,p$ is omitted compared to Eq. (3.40) but we are still requiring $1 \leq k_\ell$. It is easy to show inductively that $v_m \leq \mu_m$ for all m.

We can now obtain bounds on the iteratively defined μ_m using auxiliary Taylor series $\mu(z) \equiv \sum_{m=1}^{\infty} \mu_m z^m$. It is easy to verify that $\mu(z)$ satisfies equation

$$\begin{aligned} \mu &= \|H_0\|_1 \left(\frac{1}{1-c\mu} - 1 - c\mu\right) \\ &+ \|T\|_1\, z \left(\frac{1}{1-c\mu} - 1\right) + v_1\, z \,. \end{aligned} \tag{3.42}$$

Indeed, by expanding the right-hand-side in powers of μ, plugging in $\mu(z)$ series, and matching the coefficients of z^m on both sides, we reproduce the iterative definition of μ_m. Solving for μ as a function of z and noting $v_1 = \|T\|_1$, we have

$$\mu(z) = \frac{1 - \sqrt{1 - 4\|T\|_1(c + \|H_0\|_1 c^2)z}}{2(c + \|H_0\|_1 c^2)}\,,$$

where we have chosen the solution such that $\mu(0) = 0$. Clearly, $\mu(z)$ is analytic in the disk $|z| \leq z_0$, where

$$z_0 \equiv \frac{1}{4\|T\|_1(c + \|H_0\|_1 c^2)} \geq \frac{1}{263n^2} \equiv \rho_n \,. \tag{3.43}$$

Here the number 263 is just a conservative estimation with no special meaning other than that the inequality holds for any $n \geq 1$, and we have used the fact that $\|H_0\|_1 = \Gamma$ and $\|T\|_1 \leq \sqrt{30}\|T\|_F = \sqrt{30}\Gamma$ from Prop. 3.6.2.

Furthermore, inside the disk, $|\mu(z)|$ is bounded by

$$|\mu(z)| \leq \frac{1}{2(c + \|H_0\|_1 c^2)} < \Gamma \,, \tag{3.44}$$

where we have made a crude bound dropping any n dependence since it will not affect considerations of the convergence of series in m below. By Cauchy's theorem,

$$\begin{aligned} \mu_m &= \frac{1}{2\pi i}\oint_{|z|=\rho_n} \frac{\mu(z)}{z^{m+1}} dz \leq \frac{1}{2\pi i}\oint_{|z|=\rho_n} \left|\frac{\mu(z)}{z^{m+1}}\right| dz \\ &\leq \Gamma(\rho_n)^{-m} \,. \end{aligned} \tag{3.45}$$

It follows that $\|V_m\|_F \leq v_m \leq \mu_m \leq \Gamma(\rho_n)^{-m}$. □

It is now easy to obtain the main bound:

Theorem 3.6.1. *If* $\frac{\epsilon}{\rho_n} \leq \frac{1}{2}$, *then* $\|H_{>n}\|_F \leq 2\Gamma\left(\frac{\epsilon}{\rho_n}\right)^{n+1} = O\left(n^2\epsilon\right)^{n+1}$.

Proof. We have

$$\begin{aligned} \|H_{>n}\|_{\mathrm{F}} &\leq \sum_{m=n+1}^{\infty} \epsilon^m \|V_m\|_{\mathrm{F}} \leq \Gamma\frac{(\epsilon/\rho_n)^{n+1}}{1-\epsilon/\rho_n} \\ &\leq 2\Gamma\left(\frac{\epsilon}{\rho_n}\right)^{n+1} = O\left(n^2\epsilon\right)^{n+1} . \end{aligned} \tag{3.46}$$

□

This theorem also implies that for a fixed n, for small enough $\epsilon < \rho_n$ the local SW transformation has convergent expansion in ϵ. Since the expansion in ϵ is closely related to expansion in maximum range, we thus have such a convergent expansion in maximum range for the full SW-rotated Hamiltonian (at fixed n) in our definition of the $\|\bullet\|_{\mathrm{F}}$ norm, or simply $U^\dagger H U$ belongs to the norm closure $\overline{\bigcup_{M\in\mathbb{N}}\mathcal{T}_M}$.

It is important that n is understood as fixed since the available lower bound ρ_n on the convergence radius goes to zero when $n \longrightarrow \infty$. Thus, even though we can formally define SW series developed to arbitrary order, their convergence as $n \longrightarrow \infty$ is not guaranteed even for very small perturbation. Nevertheless, bounds obtained at finite n allow us to make rigorous lower bounds on the thermalization time as discussed in the main text. We remark that while our bounds here are sufficient for a general nonquantitative discussion of prethermalization in the perturbative SW picture, we suspect that they are gross overestimates even in the spirit of such bounds. Thus a numerical evaluation of such bounds in Appendix D suggests qualitatively tighter bounds $1/\rho_n \sim O(n)$ and $\|H_{>n}\| \leq O(n^n\epsilon^n)$, which would lead to a parametrically different thermalization time. In any case, we emphasize that all numerical calculations with the SW construction of the quasi-conserved quantity in the main text are exact and do not employ any such bounds (see also Appendix E).

Appendix C: Bound on $\mathrm{ad}_H(\tilde{I}^{(n)})$

In this appendix, we give an upper bound on the squared residual norm of $\tilde{I}^{(n)}$, or $\|\mathrm{ad}_H(\tilde{I}^{(n)})\|_{\mathrm{F}}^2$. For the sake of simplicity, we further assume $\langle H_0, T\rangle = 0$ from now on. Again, to bound $I_{>n}$, we need some control over the I_m terms.

Lemma 3.6.2. $\|I_m\|_F \le \Gamma(\rho_n)^{-m}$, *where* $\rho_n = \frac{1}{263n^2}$.

Proof. Analogous to Lemma 3.6.1, we have

$$\begin{aligned} \|I_m\|_1 &\le \|H_0\|_1 \sum_{p=1}^{m} c^p \sum_{[k_1,\dots,k_p]=m} \nu_{k_1}\dots\nu_{k_p} \\ &\le \|H_0\|_1 \sum_{p=1}^{m} c^p \sum_{k_1+\dots+k_p=m} \mu_{k_1}\dots\mu_{k_p} \equiv \chi_m \,. \end{aligned} \tag{3.47}$$

Consider the auxiliary Taylor series $\chi(z) \equiv \sum_{m=1}^{\infty} \chi_m z^m$. It is easy to verify that

$$\chi(z) = \|H_0\|_1 \left[\frac{1}{1 - c\mu(z)} - 1\right] . \tag{3.48}$$

$\chi(z)$ is analytic in the same domain as $\mu(z)$, i.e., in the disk $|z| < z_0$. Inside the disk, $c|\mu(z)| \le 1/2$ and $|\chi(z)| \le \|H_0\|_1 = \Gamma$. By Cauchy's theorem,

$$\chi_m = \frac{1}{2\pi i} \oint_{|z|=\rho_n} \frac{\chi(z)}{z^{m+1}} dz \le \Gamma(\rho_n)^{-m} . \tag{3.49}$$

It follows that $\|I_m\|_\mathrm{F} \le \|I_m\|_1 \le \chi_m \le \Gamma(\rho_n)^{-m}$. □

We can now find a bound on $I_{>n}$:

Theorem 3.6.2. *If* $\frac{\epsilon}{\rho_n} \le \frac{1}{2}$, *then* $\|I_{>n}\|_F \le 2\Gamma\left(\frac{\epsilon}{\rho_n}\right)^{n+1}$.

Proof. Similarly to Theorem 3.6.1, we have

$$\|I_{>n}\|_\mathrm{F} \le \sum_{m=n+1}^{\infty} \epsilon^m \|I_m\|_\mathrm{F} \le 2\Gamma\left(\frac{\epsilon}{\rho_n}\right)^{n+1} , \tag{3.50}$$

provided $\epsilon/\rho_n \le 1/2$. □

This theorem also assures that for fixed n and small enough ϵ, we have $\|I\|_\mathrm{F} < \infty$; thus $I \in \overline{\bigcup_{M\in\mathbb{N}} \mathcal{T}_M}$ under the norm $\|\bullet\|_\mathrm{F}$. Stated another way, for fixed n, the expansion in ϵ converges for small enough ϵ; since this is essentially an expansion in the maximum range, the produced full I is quasi-local.

We now turn to the truncation $I^{(n)}$ and its component $I^{(n)\perp}$ perpendicular to H in the Frobenius inner product. Since we want a normalized $\tilde{I}^{(n)}$, we first prove a lower bound on the norm of $I^{(n)\perp}$.

Lemma 3.6.3. $\|I^{(n)\perp}\|_F^2 \ge \alpha\epsilon^2\Gamma^2 + \Gamma^2 O(n^6\epsilon^3)$, *where* $\alpha > 0$ *if* $T^{diag} \neq 0$.

Proof. From Eq. (3.15), we have

$$\|I^{(n)\perp}\|_{\mathrm{F}}^2 = \|I^{(n)}\|_{\mathrm{F}}^2 - \frac{|\langle H, I^{(n)}\rangle|^2}{\|H\|_{\mathrm{F}}^2} \,. \tag{3.51}$$

Consider

$$\begin{aligned} \left|\langle I^{(n)}, H\rangle\right| &= \left|\langle H_0, H\rangle + \sum_{m=1}^{n}\left(\epsilon^m\langle I_m, H_0\rangle + \epsilon^{m+1}\langle I_m, T\rangle\right)\right| \\ &\leq \left|\Gamma^2 + \epsilon\langle I_1, H_0\rangle + \epsilon^2(\langle I_2, H_0\rangle + \langle I_1, T\rangle)\right| \\ &+ \sum_{m=3}^{n}\epsilon^m\|I_m\|_{\mathrm{F}}\|H_0\|_{\mathrm{F}} + \sum_{m=2}^{n}\epsilon^{m+1}\|I_m\|_{\mathrm{F}}\|T\|_{\mathrm{F}}\,, \end{aligned}$$

where we have used $\langle H_0, T\rangle = 0$.

The overlap between $I^{(n)}$ and H can be calculated explicitly to $O(\epsilon^2)$ as follows. First, notice that $I_1 = -i\mathrm{ad}_{S_1}(H_0) = T - T^{\text{diag}} = T^{\text{off-diag}}$. Therefore we have $\langle I_1, H_0\rangle = 0$. On the other hand, $\langle I_1, T\rangle = \|T^{\text{off-diag}}\|_{\mathrm{F}}^2$.

Consider now $I_2 = \frac{1}{2}i\mathrm{ad}_{S_1}i\mathrm{ad}_{S_1}(H_0) - i\mathrm{ad}_{S_2}(H_0)$. Since $i\mathrm{ad}_{S_2}(H_0) = V_2^{\text{diag}} - V_2 = -V_2^{\text{off-diag}}$, we have $\langle i\mathrm{ad}_{S_2}(H_0), H_0\rangle = 0$. Hence $\langle I_2, H_0\rangle = -\frac{1}{2}\langle \mathrm{ad}_{S_1}\mathrm{ad}_{S_1}(H_0), H_0\rangle = -\frac{1}{2}\langle \mathrm{ad}_{S_1}(H_0), \mathrm{ad}_{S_1}(H_0)\rangle = -\frac{1}{2}\|I_1\|_{\mathrm{F}}^2 = -\frac{1}{2}\|T^{\text{off-diag}}\|_{\mathrm{F}}^2$, where we have used $\langle \mathrm{ad}_{S_m}(A), B\rangle = \langle A, \mathrm{ad}_{S_m}(B)\rangle$ (which follows from hermiticity of S_m).

Combining the above calculations, we have

$$\begin{aligned} \left|\langle I^{(n)}, H\rangle\right| &\leq \Gamma^2\left(1 + \epsilon^2\frac{\|T^{\text{off-diag}}\|_{\mathrm{F}}^2}{2\Gamma^2}\right) \\ &+ \Gamma\sum_{m=3}^{\infty}\epsilon^m(\|I_m\|_{\mathrm{F}} + \|I_{m-1}\|_{\mathrm{F}}) \\ &\leq \Gamma^2\left[1 + \epsilon^2\frac{\|T^{\text{off-diag}}\|_{\mathrm{F}}^2}{2\Gamma^2} + 2\sum_{m=3}^{\infty}\left(\frac{\epsilon}{\rho_n}\right)^m\right] \\ &\leq \Gamma^2\left[1 + \epsilon^2\frac{\|T^{\text{off-diag}}\|_{\mathrm{F}}^2}{2\Gamma^2} + 4\left(\frac{\epsilon}{\rho_n}\right)^3\right]\,, \end{aligned} \tag{3.52}$$

where we have used $\rho_n < 1$ and assumed $\frac{\epsilon}{\rho_n} \leq \frac{1}{2}$.

We know $\|H\|_{\mathrm{F}}^2 = \Gamma^2(1+\epsilon^2)$, since $\langle H_0, T\rangle = 0$. Hence

$$\begin{aligned} \frac{|\langle I^{(n)}, H\rangle|^2}{\|H\|_{\mathrm{F}}^2} &\leq \Gamma^2\frac{\left[1 + \epsilon^2\frac{\|T^{\text{off-diag}}\|_{\mathrm{F}}^2}{2\Gamma^2} + 4\left(\frac{\epsilon}{\rho_n}\right)^3\right]^2}{1+\epsilon^2} \\ &= \Gamma^2\left[1 - \alpha\epsilon^2 + O(n^6\epsilon^3)\right]\,, \end{aligned} \tag{3.53}$$

where $\alpha \equiv 1 - \frac{\|T^{\text{off-diag}}\|_{\mathrm{F}}^2}{\Gamma^2} > 0$ if $T^{\text{diag}} \neq 0$. If $T^{\text{diag}} = 0$ so that $\alpha = 0$, one has to verify the negativity of the coefficient of the next order ϵ^3. While we expect this to be true, to simplify the discussion we made the assumption that $T^{\text{diag}} \neq 0$.

Finally, we have

$$\begin{aligned} \|I^{(n)}\|_{\mathrm{F}} &= \|UH_0U^\dagger - I_{>n}\|_{\mathrm{F}} \geq \|H_0\|_{\mathrm{F}} - \|I_{>n}\|_{\mathrm{F}} \\ &\geq \Gamma\left[1 - 2\left(\frac{\epsilon}{\rho_n}\right)^{n+1}\right] . \end{aligned} \tag{3.54}$$

We can therefore obtain

$$\begin{aligned} \|I^{(n)\perp}\|_{\mathrm{F}}^2 &\geq \Gamma^2\left[1 + O(n^2\epsilon)^{n+1}\right]^2 - \Gamma^2\left[1 - \alpha\epsilon^2 + O(n^6\epsilon^3)\right] \\ &= \alpha\epsilon^2\Gamma^2 + \Gamma^2 O(n^6\epsilon^3) . \end{aligned} \tag{3.55}$$

□

We now have the ingredients for bounding $\mathrm{ad}_H(\tilde{I}^{(n)})$ and can prove the following theorem:

Theorem 3.6.3. $\|ad_H(\tilde{I}^{(n)})\|_F^2 = \frac{\|ad_H(I^{(n)\perp})\|_F^2}{\|I^{(n)\perp}\|_F^2} \leq O\left(n^{4n+6}\epsilon^{2n}\right)$.

Proof. First, we note that

$$\begin{aligned} \|\mathrm{ad}_H(I^{(n)\perp})\|_{\mathrm{F}} &= \|\mathrm{ad}_H(I^{(n)})\|_{\mathrm{F}} = \|\mathrm{ad}_H(I) - \mathrm{ad}_H(I_{>n})\|_{\mathrm{F}} \\ &\leq \|\mathrm{ad}_H(I)\|_{\mathrm{F}} + \|\mathrm{ad}_H(I_{>n})\|_{\mathrm{F}} . \end{aligned} \tag{3.56}$$

The first term can be bounded by

$$\begin{aligned} \|\mathrm{ad}_H(I)\|_{\mathrm{F}} &= \|[H, UH_0U^\dagger]\|_{\mathrm{F}} = \|[U^\dagger HU, H_0]\|_{\mathrm{F}} \\ &= \|[H_{>n}, H_0]\|_{\mathrm{F}} \leq \|[H_{>n}, H_0]\|_1 \\ &\leq \sum_{m=n+1}^{\infty} \epsilon^m \|[V_m, H_0]\|_1 \\ &\leq \sum_{m=n+1}^{\infty} \epsilon^m 2(m+1)v_m\|H_0\|_1 \\ &\leq 2\Gamma^2 \sum_{m=n+1}^{\infty} (m+1)\left(\frac{\epsilon}{\rho_n}\right)^m \\ &= 2\Gamma^2\frac{(n+2)\beta^{n+1}}{(1-\beta)^2}\left(1 - \beta\frac{n+1}{n+2}\right) \\ &\leq 8\Gamma^2(n+2)\beta^{n+1} , \end{aligned} \tag{3.57}$$

where we have defined $\beta \equiv \frac{\epsilon}{\rho_n}$ and used $\beta \leq 1/2$.

The second term in Eq. (3.56) can be bounded as

$$\begin{aligned}
\|\mathrm{ad}_H(I_{>n})\|_{\mathrm{F}} &\leq \sum_{m=n+1}^{\infty} \epsilon^m \|\mathrm{ad}_H(I_m)\|_1 \\
&\leq \sum_{m=n+1}^{\infty} \epsilon^m 2(m+2)\|H\|_1\|I_m\|_1 \\
&\leq \sum_{m=n+1}^{\infty} \epsilon^m 2(m+2)\sqrt{30}\sqrt{1+\epsilon^2}\Gamma\|I_m\|_1 \\
&\leq 4\sqrt{15}\Gamma^2 \sum_{m=n+1}^{\infty} (m+2)\left(\frac{\epsilon}{\rho_n}\right)^m \\
&= 4\sqrt{15}\Gamma^2 \frac{(n+3)\beta^{n+1}}{(1-\beta)^2}\left(1-\beta\frac{n+2}{n+3}\right) \\
&\leq 16\sqrt{15}\Gamma^2(n+3)\beta^{n+1}\,, \qquad (3.58)
\end{aligned}$$

where we have used $\|H\|_1 \leq \sqrt{30}\|H\|_{\mathrm{F}} = \sqrt{30}\Gamma\sqrt{1+\epsilon^2}$ and $\sqrt{1+\epsilon^2} < \sqrt{2}$.

Combining the above two bounds and Lemma 3.6.3, we have

$$\begin{aligned}
\frac{\|\mathrm{ad}_H(I^{(n)\perp})\|_{\mathrm{F}}^2}{\|I^{(n)\perp}\|_{\mathrm{F}}^2} &\leq \frac{\left[\Gamma^2(an+b)\left(\frac{\epsilon}{\rho_n}\right)^{n+1}\right]^2}{\alpha\epsilon^2\Gamma^2+\Gamma^2 O(n^6\epsilon^3)} \\
&= \Gamma^2 O\left(n^{4n+6}\epsilon^{2n}\right)\,, \qquad (3.59)
\end{aligned}$$

where $a = 8 + 16\sqrt{15}$, $b = 16 + 48\sqrt{15}$. □

Appendix D: Better bounds on $\|V_m\|$ and the convergence radius using numerical experiments

In Appendix B, we estimated the convergence radius $\rho_n \sim 1/n^2$, which is a lower bound. This would give the thermalization time scale to be $O(\exp(A/\sqrt{\epsilon}))$, where ϵ is the perturbation strength. In this Appendix, we demonstrate a numerical experiment to support the conjecture that a tighter bound $\rho_n \sim 1/n$ is possible.

Recall that when bounding v_m, following Ref. [21], we used a very crude bound of $(k_p + \ldots k_1 + 1)\ldots(k_1+1) \leq p!(n+1)^p$, see Eq. (3.39). We suspect that this approximation, which allowed an analytical calculation of the numbers μ_m which bound v_m, Eq. (3.41), is however too crude and changes the leading behavior of the convergence radius ρ_n. If we do not make this approximation, we can define another

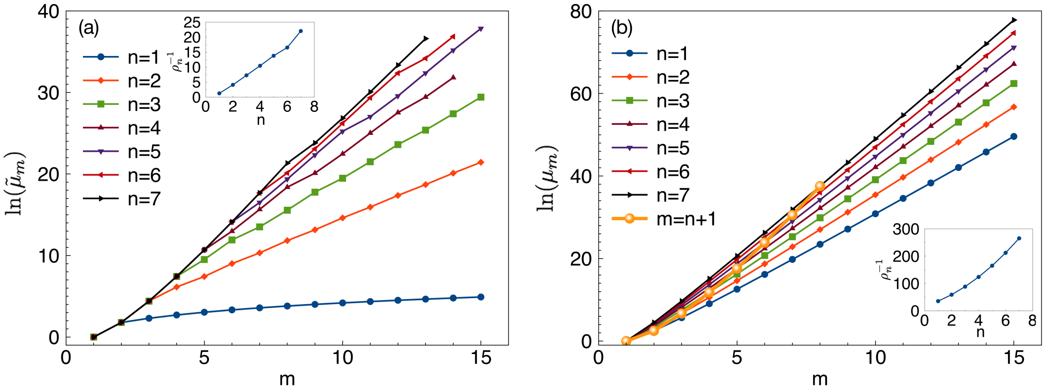

Figure 3.8: (color online) Numerical calculations of the iterative bounds on $\|V_m\|_1$: (a) $\tilde{\mu}_m$ generated by Eq. (3.60) and (b) μ_m generated by Eq. (3.41), for different SW order n. For convenience, the one-norms of $\|H_0\|_1$ and $\|T\|_1$ are taken to be one, which does not affect the functional dependence of the convergence radius ρ_n on n. The curve $m = n+1$ in (b) denotes the bound on the infinite-SW $\|V_m\|_1$ since V_m does not depend on n once $n \geq m-1$. Insets: the inverse convergence radius ρ_n^{-1} as a function of n. By assuming $\tilde{\mu}_m = A_n(\rho_n)^{-m}$, or $\ln(\tilde{\mu}_m) = \ln A_n - m\ln(\rho_n)$ for $m > n$, we can extract $\ln(1/\rho_n)$ from the slope of $\ln(\tilde{\mu}_m)$ vs m and plot ρ_n^{-1} in the inset. For ρ_n extracted from $\tilde{\mu}_m$, we suspect $\rho_n^{-1} \sim n$; while for μ_m, we observe $\rho_n^{-1} \sim n^2$ as expected.

set of numbers $\tilde{\mu}_m$ which bound v_m:

$$\begin{aligned}\tilde{\mu}_m \equiv & \sum_{p=2}^{m} \sum_{[k_1,\ldots,k_p]=m} \mathfrak{f}(k_1,\ldots,k_p) \\ & \times (k_p + \cdots + k_1 + 1)\ldots(k_1+1)\,\tilde{\mu}_{k_1}\ldots\tilde{\mu}_{k_p} \\ & + \sum_{p=1}^{m-1} \sum_{[k_1,\ldots,k_p]=m-1} \mathfrak{f}(k_1,\ldots,k_p) \\ & \times (k_p + \cdots + k_1 + 2)\ldots(k_1+2)\,\tilde{\mu}_{k_1}\ldots\tilde{\mu}_{k_p}\,, \end{aligned} \tag{3.60}$$

where we have assumed $\|H_0\|_1 = \|T\|_1 = \Gamma = 1$, without loss of generality.

Starting with $\tilde{\mu}_1 \equiv v_1 = 1$, we can iteratively calculate $\tilde{\mu}_m$ for a given n. The results are shown in Fig. 3.8(a). Recall that V_m for $m \leq n+1$ are already independent of n (and can be viewed as representative of the infinite-order SW procedure), while V_m for $m > n+1$ describe formal expansion in powers of ϵ at fixed n and form the "remainder" $H_{>n}$. The same property is shared by $\tilde{\mu}_m$, i.e., $\tilde{\mu}_m$ for $m \leq n+1$ are independent of n and appear as the limiting curve in Fig. 3.8(a), while the data for $m > n$ determine convergence properties of the remainder $H_{>n}$. For easy reference, we quote several numbers on the limiting curve, which are "universal" numbers under this bounding procedure: $\tilde{\mu}_2 = 6, \tilde{\mu}_3 = 82, \tilde{\mu}_4 = 1695, \tilde{\mu}_5 = 43995$, etc. Focusing now on the remainder terms and assuming behavior $\tilde{\mu}_m = A_n(\rho_n)^{-m}$ for $m > n$, we can extract the convergence radius from the slope of $\ln(\tilde{\mu}_m) = \ln(A_n) - m\ln(\rho_n)$ vs m. The inset shows the n dependence of the inverse convergence radius $(\rho_n)^{-1}$, which in fact suggests $\rho_n^{-1} \sim n$.

As a comparison, in Fig. 3.8(b) we also show the same procedure applied to μ_m, Eq. (3.41), with the same normalization $\|H_0\|_1 = \|T\|_1 = \Gamma = 1$. In this case, the inverse convergence radius ρ_n^{-1} shows n^2 behavior, as expected from the analysis in Appendix B. Note that in this case we did not treat separately $m \leq n + 1$ and $m > n + 1$, since we used the same n-dependent c in the iteration equation for all m. Of course, we know that v_m no longer depends on n for $m \leq n + 1$, and for each m we could use μ_m from the smallest SW order n satisfying this condition to bound such infinite-SW-order v_m; these are indicated as "$m = n + 1$" curve in Fig. 3.8(b), and we expect such procedure to bound v_m by m^{2m}.

To conclude, we thus suspect that the lower bound on the convergence radius can be possibly tighter than in Appendix B and is tentatively $\rho_n \sim 1/n$, though we do not have a rigorous mathematical proof. Related to this, the behavior of $\tilde{\mu}_m$ for $m \leq n + 1$, which bounds the infinite-SW-order v_m, appears to be $\ln(\tilde{\mu}_m) = m\ln(m)$ up to subdominant contributions, compared to $\ln(\mu_m) = 2m\ln(m)$ [this could be crudely seen by noting that the vertical range in panel (a) in Fig. 3.9 is two times smaller than in panel (b)].

Appendix E: Numerical results for $\|V_m\|$ in a generic model

In Sec. 3.3, we defined the local SW procedure to produce an effective Hamiltonian that commutes with H_0 up to order n. The procedure gives "potentials" V_m and the generator iS_m is chosen to eliminate the off-diagonal part of V_m for $m \leq n$. In Appendix B, we provided an analytical bound $\|V_m\|_{\mathrm{F}} \leq \|V_m\|_1 \leq \Gamma(\rho_n)^{-m}$, where the inverse convergence radius grows as $1/\rho_n \sim n^2$. These are bounds valid for all m but are particularly used for $m > n$ bounding the terms in the remainder $H_{>n}$, while for $m \leq n$ where V_m are already independent of n we can bound $\|V_m\|_1 \leq \Gamma(\rho_m)^{-m}$. From numerical experiments in Appendix D with more accurate bounds, we see that the bounds in Appendix B are too crude and better bounds are possible, tentatively with $1/\rho_n \sim n$.

In this appendix, we directly calculate $\|V_m\|_{\mathrm{F}}$ and $\|V_m\|_1$, with no approximations, in a generic model to compare with these theoretical bounds. All numerical results

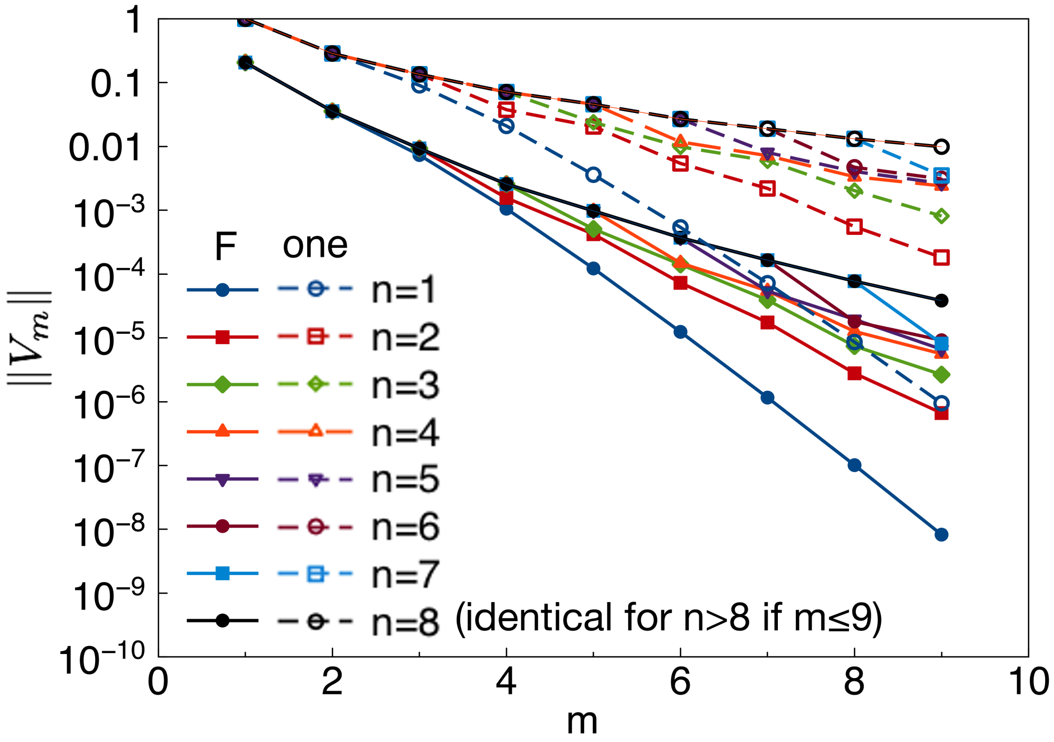

Figure 3.9: (color online) Actual Frobenius norms and one-norms (denoted by "F" and "one" respectively) of operators V_m that appear in the SW transformation, to be compared with bounds in Fig. 3.8. The model is defined using H_0 in Eq. (3.21) with $\Gamma = 1$ and T in Eqs. (3.22)-(3.26) with $t_1 = -12/121$, $t_2 = 16/121$, $u_0 = 9/121$, and $w_0 = t_2$. The parameters are chosen such that $\|H_0\|_1 = \|T\|_1 = 1$ and the ratios among t_1, t_2, w_0, u_0 corresponding to the case with $h = 1.5$ and $g = 2.0$ in the main text. Note that the actual $\|V_m\|_\mathrm{F}$ and $\|V_m\|_1$ are still decreasing for the accessible m, in stark contrast with the bounds that show very fast increase (at least m^m) starting already at $m = 1$.

on the SW-generated quasi-conserved operators in the main text are also obtained with no approximations but contain all terms including all factors of ϵ^m summed up, while the purpose of this appendix is to measure individual V_m terms for direct comparisons with theoretical bounds. Since S_m is determined from V_m by a relatively simple local rule and the structure of I_m is similar to V_m, we expect the results for all these operators to be qualitatively similar and will focus on the potentials V_m. Figure 3.9 shows the numerical values of $\|V_m\|_\mathrm{F}$ and $\|V_m\|_1$, calculated for the SW-generated potentials for the model in Appendix A taking H_0 in Eq. (3.21) with $\Gamma = 1$ and T in Eqs. (3.22)-(3.26) with $t_1 = -12/121$, $t_2 = 16/121$, $u_0 = 9/121$, and $w_0 = t_2$. The parameters are chosen such that $\|H_0\|_1 = \|T\|_1 = 1$, while the ratios among t_1, t_2, w_0, u_0 are such that they correspond to the case with $J = 1$, $h = 1.5$, and $g = 2$ in the main text rotated to the new basis as described in Appendix A; to directly connect with this data point in the main text, the appropriate ϵ is approximately 1.936.

Recall that the V_m generated by the SW procedure are independent of the perturbation parameter ϵ but contain all information needed for evaluating series for any ϵ. The above normalization of H_0 and T is chosen such that we can directly compare with the numbers in Appendix D. The best bounds in Appendix D are very quickly increasing already starting with $m = 1$, reaching values $e^{21} \sim 10^9$ already for $m = 8$, see top panel in Fig. 3.9 remembering that it plots logarithms of the bounds on $||V_m||_1$. On the other hand, the actual values of $||V_m||_1$ are decreasing with m for accessible m. This suggests that even the best theoretical upper bound on $||V_m||_1$ is a vast overestimation. In fact, taken at face value, the numerical results in Fig. 3.9 might even suggests the possibility of convergence of the SW procedure in some models. A more conservative view is that the actual $||V_m||_1$ will eventually start increasing for large enough m, and the initial decrease is due to the chosen normalization $||H_0||_1 = ||T||_1 = 1$ where the one-norm measure is somehow less fair between the 1-local and 2-local terms. However, we emphasize that the bounds in Appendix D are obtained for exactly the same normalization and the comparison with the bounds in Fig. 3.9 is fair. (We needed to use the one-norm in the theoretical bounds because we were not able to prove analogs of Props. 3.6.3 and 3.6.4 for the Frobenius norm.) The large difference between the actual norm and the theoretical bound starts already at $m = 2$, where we have verified by direct analytical calculation of the potential V_2 in Eq. (3.30) that $||V_2||_1 \approx 0.286$ while the bound $\tilde{\mu}_2 = 6$.

One likely source of the overestimation is that the theoretical bounds always replace the norm of a sum of a large number of terms by the sum of norms of the terms, while there can be many cancellations among the terms. More specifically, we can trace the faster-than-exponential growth of the bounds $\tilde{\mu}_m$ to factors $(k_p + \dots k_1 + 1) \dots (k_1 + 1)$ in the second line of Eq. (3.60) and $(k_p + \dots k_1 + 2) \dots (k_1 + 2)$ in the fourth line of Eq. (3.60), which in turn originate from the factor $r + s - 1$ in the bound in Prop. 3.6.3 for a commutator of an operator in $\mathcal{T}_r$ and an operator in $\mathcal{T}_s$. Examining Eq. (3.36) and how it is used in the proof of Prop. 3.6.3, we see that there are $2(r+s-1) \cdot 3 \cdot 4^{r-1} \cdot 3 \cdot 4^{s-1}$ terms that are being collected, while the number of basis states for writing out $\mathrm{ad}_U(W) \in \mathcal{T}_{r+s-1}$ is $3 \cdot 4^{r+s-2}$. (Here for simplicity we ignore generation of multiple strings from products $Q^{\mathbf{a}}_{j;r} Q^{\mathbf{b}}_{k;s}$.) Thus, an amplitude for each basis state will have roughly $6(r+s-1)$ contributions. If these contributions all came with the same sign, we would indeed obtain the bound in Prop. 3.6.3. However, different contributions can come with different signs depending on details of various commutators. If these signs were uncorrelated, it would be natural to replace $6(r+s-1)$ by $\sqrt{6(r+s-1)}$ when estimating a typical amplitude in the operator string basis, and such a replacement could potentially bring the bound on the growth of $\|V_m\|_1$ from m^m to a much slower $m^{m/2}$. Thus, such cancellations, while still not preventing eventual thermalization, could potentially lead to parametrically longer relaxation times as a function of ϵ.[2]

Interestingly, there can be additional suppression of the growth of the bounds $\tilde{\mu}_m$ when we consider more carefully the bound in Prop. 3.6.4. Indeed, the denominator in Prop. 3.6.4 represents the smallest possible energy difference between the energy sectors of H_0. However, at m-th order, V_m consists of pieces that have m of elementary (i.e., from the bare perturbation T) raising or lowering steps on the H_0 sector label. We may then guess that a typical term in V_m would be raising or lowering the H_0 sector label by roughly $\sqrt{m}$, so for estimating a typical contribution we could replace the denominator 2Γ in Prop. 3.6.4 with $2\Gamma\sqrt{m}$. However, we caution that the discussed cancellations and suppressions compared to the earlier bounds implicitly assume lack of structure among the various complicated terms, hence random-walk-type estimates. If there is a structure that would lead to some sign or magnitude bias among the terms, this could possibly arrest the discussed suppressions. Our numerical experiment in Fig. 3.9 where we have not seen faster-than-exponential growth yet, together with the speculative arguments above, suggest that the convergence of the SW procedure is an open question worth further explorations. Even if eventually the convergence radius vanishes, we clearly expect strong quantitative and perhaps qualitative modifications of how this happens, which would also have implications for estimates of the relaxation times.

References

[1] F. H. L. Essler, S. Kehrein, S. R. Manmana, and N. J. Robinson, "Quench dynamics in a model with tuneable integrability breaking", Phys. Rev. B **89**, 165104 (2014).

[2] B. Bertini, F. H. L. Essler, S. Groha, and N. J. Robinson, "Thermalization and light cones in a model with weak integrability breaking", Phys. Rev. B **94**, 245117 (2016).

---

[2] Starting with $t_n^{-1} \sim \epsilon^n n^{\gamma n}$, finding optimal n_* gives optimal $t_*^{-1} \sim \exp\left(-\frac{\gamma}{e\epsilon^{1/\gamma}}\right)$

[3] T. Langen, T. Gasenzer, and J. Schmiedmayer, “Prethermalization and universal dynamics in near-integrable quantum systems”, J. Stat. Mech. **2016**, 064009 (2016).

[4] T. Kuwahara, T. Mori, and K. Saito, “Floquet-Magnus Theory and Generic Transient Dynamics in Periodically Driven Many-Body Quantum Systems”, Ann. Phys. **367**, 96–124 (2016).

[5] T. Mori, T. Kuwahara, and K. Saito, “Rigorous Bound on Energy Absorption and Generic Relaxation in Periodically Driven Quantum Systems”, Phys. Rev. Lett. **116**, 120401 (2016).

[6] D. A. Abanin, W. De Roeck, W. W. Ho, and F. Huveneers, “Effective Hamiltonians, prethermalization, and slow energy absorption in periodically driven many-body systems”, Phys. Rev. B **95**, 014112 (2017).

[7] D. A. Abanin, W. De Roeck, W. W. Ho, and F. Huveneers, “A Rigorous Theory of Many-Body Prethermalization for Periodically Driven and Closed Quantum Systems”, Commun. Math. Phys. **354**, 809–827 (2017).

[8] M. Bukov, S. Gopalakrishnan, M. Knap, and E. Demler, “Prethermal Floquet Steady States and Instabilities in the Periodically Driven, Weakly Interacting Bose-Hubbard Model”, Phys. Rev. Lett. **115**, 205301 (2015).

[9] R. Sensarma, D. Pekker, E. Altman, E. Demler, N. Strohmaier, D. Greif, R. Jördens, L. Tarruell, H. Moritz, and T. Esslinger, “Lifetime of double occupancies in the Fermi-Hubbard model”, Phys. Rev. B **82**, 224302 (2010).

[10] N. Strohmaier, D. Greif, R. Jördens, L. Tarruell, H. Moritz, T. Esslinger, R. Sensarma, D. Pekker, E. Altman, and E. Demler, “Observation of Elastic Doublon Decay in the Fermi-Hubbard Model”, Phys. Rev. Lett. **104**, 080401 (2010).

[11] J. Kemp, N. Y. Yao, C. R. Laumann, and P. Fendley, “Long coherence times for edge spins”, J. Stat. Mech. **2017**, 063105 (2017).

[12] D. V. Else, P. Fendley, J. Kemp, and C. Nayak, “Prethermal strong zero modes and topological qubits”, Phys. Rev. X **7**, 041062 (2017).

[13] M. Fagotti, “Conservation laws for a class of generic hamiltonians”, arXiv:1408.1950.

[14] M. Mierzejewski, T. Prosen, and P. Prelovšek, “Approximate conservation laws in perturbed integrable lattice models”, Phys. Rev. B **92**, 195121 (2015).

[15] T. Grover, and M. P. A. Fisher, “Quantum disentangled liquids”, J. Stat. Mech. **2014**, P10010 (2014).

[16] J. R. Garrison, R. V. Mishmash, and M. P. A. Fisher, “Partial breakdown of quantum thermalization in a Hubbard-like model”, Phys. Rev. B **95**, 054204 (2017).

[17] H. Kim, M. C. Bañuls, J. I. Cirac, M. B. Hastings, and D. A. Huse, "Slowest local operators in quantum spin chains", Phys. Rev. E **92**, 012128 (2015).

[18] A. Knyazev, "Toward the Optimal Preconditioned Eigensolver: Locally Optimal Block Preconditioned Conjugate Gradient Method", SIAM J. Sci. Comput. **23**, 517–541 (2001).

[19] T. E. O'Brien, D. A. Abanin, G. Vidal, and Z. Papić, "Explicit construction of local conserved operators in disordered many-body systems", Phys. Rev. B **94**, 144208 (2016).

[20] N. Datta, J. Frohlich, L. Rey-Bellet, and R. Fernández, "Low-temperature phase diagrams of quantum lattice systems. II. Convergent perturbation expansions and stability in systems with infinite degeneracy", Helvetica Phys. Acta. **69**, 752–820 (1996).

[21] S. Bravyi, D. P. DiVincenzo, and D. Loss, "Schrieffer–Wolff transformation for quantum many-body systems", Ann. Phys. **326**, 2793–2826 (2011).

[22] A. H. MacDonald, S. M. Girvin, and D. Yoshioka, "t/u expansion for the Hubbard model", Phys. Rev. B **37**, 9753–9756 (1988).

[23] G. Vidal, "Efficient Classical Simulation of Slightly Entangled Quantum Computations", Phys. Rev. Lett. **91**, 147902 (2003).

[24] C.-J. Lin, and O. I. Motrunich, "Quasiparticle Explanation of the Weak-Thermalization Regime under Quench in a Nonintegrable Quantum Spin Chain", Phys. Rev. A **95**, 023621 (2017),

[25] C. D. White, M. Zaletel, R. S. K. Mong, and G. Refael, "Quantum dynamics of thermalizing systems", Phys. Rev. B **97**, 035127 (2018).

[26] C.-J. Lin, and O. I. Motrunich, (unpublished).

Chapter 4

OUT-OF-TIME ORDERED CORRELATORS IN THE NONINTERACTING INTEGRABLE MODELS

First discussed by Larkin and Ovchinnikov [1] and recently revived by Kitaev [2, 3], the out-of-time-ordered commutator/correlator (OTOC) has attracted a lot of attention in the physics community across many different fields, including quantum information, high-energy physics, and condensed matter physics. Consider

$$\begin{aligned} C_{WV}(t) &\equiv \frac{1}{2}\langle [W(t),V]^\dagger [W(t),V]\rangle \\ &= \frac{1}{2}\left[\langle V^\dagger W(t)^\dagger W(t)V\rangle + \langle W(t)^\dagger V^\dagger V W(t)\rangle \right.\\ &\qquad \left. -\langle W(t)^\dagger V^\dagger W(t) V\rangle - \langle V^\dagger W(t)^\dagger V W(t)\rangle\right] , \end{aligned}$$

where $\langle O\rangle \equiv \mathrm{Tr}[e^{-\beta H}O]/\mathrm{Tr}[e^{-\beta H}]$ denotes the thermal average and $W(t) \equiv e^{iHt}We^{-iHt}$ is the Heisenberg evolution of the operator W. We see that the last line involves operators with unusual time ordering, hence the name "OTOC." In particular, if W and V are Hermitian and unitary (e.g., Pauli matrices), then $C_{WV}(t) = 1 - \mathrm{Re}F_{WV}(t)$, where $F_{WV}(t) \equiv \langle W(t)VW(t)V\rangle$.

There are several aspects about this object which make it interesting to study. First of all, such $C(t)$ is a possible diagnostic for quantum chaos. In classical physics, one hallmark of chaos is that a small difference in the initial condition results in an exponential deviation of the trajectory—the famous "butterfly effect." Denoting q as the generalized coordinate of the classical system in the language of Hamiltonian dynamics, the butterfly effect can be diagnosed from the behavior $|\frac{\partial q(t)}{\partial q(0)}| \sim e^{\lambda_\mathrm{L} t}$, where λ_L is the Lyapunov exponent. The object $\frac{\partial q(t)}{\partial q(0)}$ can be calculated from the Poisson bracket $\{q(t), p\}_{\mathrm{P.B.}}$ [4, 5]. A natural generalization of this diagnostic to quantum systems is by promoting the Poisson bracket to a commutator. Therefore, the behavior of the object $C(t) = \langle |[x(t), p]|^2\rangle \sim e^{2\lambda_\mathrm{L} t}$ is an immediate generalization of the classical chaos to quantum systems, where using $|A|^2 \equiv A^\dagger A$ removes the effect of phase cancellations when averaging. Unlike classical systems where λ_L can be arbitrarily large, in quantum systems it was argued [4, 6] that under some natural assumptions λ_L is bounded by $2\pi/\beta$ (assuming the unit $\hbar = 1$), where β is the inverse temperature of the system.

Several works have used this diagnostic to argue for the existence of quantum butterfly effect [7–10] and extract the Lyapunov exponent, with examples including the $O(N)$ model [11], fermionic models with critical Fermi surface [12], and weakly diffusive metals [13]. On the other hand, some systems, for example Luttinger liquids [14] and many-body localized systems [15–19], do not show the exponential growth and are hence characterized as less chaotic or as slow scramblers. Also, some works have shown that in certain Hamiltonians, the exponent extracted from OTOC does not match the classical counterpart of the semiclassical limit [20, 21]. For systems with bounded local Hilbert space and Hamiltonians with local interactions, a work [22] proposed that the density-OTOC is a more suitable diagnostic.

Another perspective on the OTOC is that it demonstrates the instability of the "thermal field double state" and the scrambling of information [4, 23, 24]. It is expected that if $F(t)$ is small [or $C(t)$ is large] in the long-time limit, the system is scrambled; while large $F(t)$ [small $C(t)$] signals absence of scrambling. This also leads to a more sophisticated quantum information-theoretical definition of scrambling [25]. There are also some considerations regarding the quasiprobability behind the OTOC [26, 27]. Several works used holographic description to show the nontriviality of the OTOC [23, 28]. A conformal field theory calculation showed agreement with the holographic calculations [24].

From the operator point of view, $C(t)$ is a measure of operator spreading. Let us consider a 1d quantum spin-1/2 chain for concreteness, and assume W operates on site i (denoted as W_i) while V operates on site j (denoted as V_j) which we will treat as a "probe" and will vary its position. The Heisenberg-evolved operator $W_i(t)$ can be written in the basis of Pauli-string operators, $W_i(t) = \sum_S a_S(t) S$, where S runs over all Pauli-strings (e.g., $\dots \sigma_0^x \sigma_1^z \sigma_2^z \dots$) and $a_S(t)$ denotes the corresponding amplitudes. Then, at infinite temperature, $C(t) = 2 \sum_S' |a_S(t)|^2$, where the primed summation is over the Pauli-strings with nontrivial commutation with V_j, or $[S, V_j] \neq 0$, and for concreteness we assumed that such $[S, V_j]$ is a Pauli string itself (times 2), as is the case where the "probing" V_j is a single-site Pauli operator. Therefore, by examining V_j at different positions, one can quantify to some degree how $W_i(t)$ is spread over the space. Recent calculations in the case of the time evolution given by local random quantum gates show nontrivial operator spreading and OTOC growth [29–34].

For systems whose evolution is described by a local Hamiltonian dynamics or a local quantum circuit, a description has recently emerged that operators spread with a front ballistically, with a velocity v_B dubbed "butterfly velocity." For systems governed by a local Hamiltonian, outside the light cone, at very short time, the commutator function exhibits a position-dependent power-law growth in time, which can be understood using Baker-Campbell-Hausdorff expansion of the Heisenberg evolution of operators [35–38].

While operators spread with a ballistic velocity, the front itself can broaden. It has been proposed recently [38] that the functional form of the wavefront has a universal description

$$C(\ell, t) \sim \exp\left[-c\frac{(\ell - v_B t)^{1+p}}{t^p}\right] . \tag{4.1}$$

(One has to also carefully specify the window around the wavefront where such a description is valid.) Another characterization is to examine long-time behavior along fixed-velocity rays [39]. For systems governed by local Hamiltonians, outside the light cone, $v > v_B$, one expects

$$C(\ell = vt, t) \sim \exp[-\lambda(v)t] , \tag{4.2}$$

where $\lambda(v)$ is dubbed a "velocity-dependent" Lyapunov exponent.

Note that strictly speaking, the above two proposals, Eqs. (4.1) and (4.2), are describing different asymptotic regimes. However, if the two descriptions can be connected smoothly, then one obtains $\lambda(v) = c(v - v_B)^{1+p}$. The exponent p describes wavefront broadening as $\sim t^{p/(1+p)}$ [39]. For example, for the random circuit model [29, 31], we have $p = 1$ corresponding to $\sim t^{1/2}$ spreading. For models with a noninteracting fermionic quasiparticle description [37–39], we have $p = 1/2$ and $\sim t^{1/3}$ spreading. Finally, for one-dimensional (1D) chains of coupled Sachdev-Ye-Kitaev quantum dots and models with a large-N limit, $p = 0$ and the wavefront does not broaden but shows an exponential growth at fixed ℓ and increasing t, which is reminiscent of the classical chaos—the butterfly effect [38–43]. While the existence of a well-defined exponential growth regime for local Hamiltonians with bounded local Hilbert spaces is still an outstanding question (with emerging thinking that there is probably no such regime), a recent work [44] has reported an exponential growth near the wavefront in spin models with long-range interactions.

While most of the works focus on the OTOC diagnosing scrambling in chaotic systems, it is also interesting to consider its behavior in nonchaotic or integrable systems. From the operator spreading and information scrambling point of view, the OTOC in integrable systems could still be interesting and reveal some nontrivial aspects. We therefore study in detail the OTOCs in the quantum Ising chain, hard-core boson models with short-range and long-range hoppings and Luttinger liquid model.

4.1 Quantum Ising model

Here we study the OTOCs in the quantum Ising chain

$$H = -\frac{J}{2}\left(\sum_{j=0}^{L-1} \sigma_j^z \sigma_{j+1}^z + g \sum_{j=0}^{L-1} \sigma_j^x\right), \tag{4.3}$$

with periodic boundary condition. The specific choice of couplings is such that at the $T = 0$ quantum critical point, $g = 1$, the maximal quasiparticle velocity is $v_B = J$, which is also the butterfly velocity and we will also set $J = 1$. We will focus on the case where W and V are single-site Pauli matrices whose positions we can vary. We will be interested in the quantities

$$C_{\mu\nu}(\ell, t) \equiv \frac{1}{2}\langle |[\sigma_\ell^\mu(t), \sigma_0^\nu]|^2\rangle = 1 - \mathrm{Re} F_{\mu\nu}(\ell, t), \tag{4.4}$$

where $\mu, \nu = x, y, z$, and $F_{\mu\nu}(\ell, t) = \langle \sigma_\ell^\mu(t)\sigma_0^\nu\sigma_\ell^\mu(t)\sigma_0^\nu\rangle$. Using lattice translation and mirror (i.e., $j \to -j$) symmetries, one can easily show that $C_{\mu\nu}(\ell, t) = \frac{1}{2}\langle |[\sigma_0^\mu(t), \sigma_\ell^\nu]|^2\rangle$. In some occasions, it is more natural to consider the latter expression.

In particular, we will focus on $F_{xx}(\ell, t)$, $F_{zz}(\ell, t)$, and $F_{zx}(\ell, t)$, as they represent three different types of behavior of the OTOC in the quantum Ising chain. The model is solved using Jordan-Wigner (JW) fermions. In terms of these, some spin operators are local and some become nonlocal (i.e., contain string operator), and the three OTOCs correspond to different combinations of local and nonlocal operators. Previous studies [45] have shown that there is a qualitative distinction between the dynamical correlation functions in the two cases. For operators that are local in terms of the JW fermions, the correlations show power-law decay in time *at any temperature*. On the other hand, correlations of nonlocal operators decay exponentially in time. Thus, the nonlocal operators exhibit behavior that is closer to generic (i.e., nonintegrable) "thermal" behavior, in contrast to the local operators. Similar distinction has also been observed in quench settings [46–48], where operators that are local in the JW fermions approach their limiting values in a power-law fashion ("slow thermalization"), while for the nonlocal operators the approach is exponential in time ("fast thermalization"); in both cases, the limiting values are described by a generalized Gibbs ensemble appropriate for this integrable model. It is therefore interesting to see if such qualitatively different behavior has any nontrivial correspondence in the OTOC calculations. Indeed, we observe that the OTOC composed with local operators shows no sign of scrambling, namely $\lim_{t\to\infty} F_{xx}(\ell,t) = 1$ (which is the same as the value at $t = 0$) and the approach is t^{-1} power law. On the other hand, the OTOC composed with nonlocal operators shows the signature of scrambling, $\lim_{t\to\infty} F_{zz}(\ell,t) \to 0$. However, we find that the long-time behavior of $F_{zz}(\ell,t)$ is a very slow $t^{-1/4}$ power law; this is a departure from the exponential decays found in the dynamical correlation and quench settings described above and shows that the OTOC encodes some different aspects; the very slow decay is also highly unusual and not fully understood.

We consider the quantum Ising model, Eq. (4.3), on a finite chain with periodic boundary conditions used to minimize boundary effects. We diagonalize the model via Jordan-Wigner transformation and subsequent Bogoliubov transformation [45]. In the fermionic representation, the spin operators are written as $\sigma_j^x = 1 - 2c_j^\dagger c_j$ and $\sigma_j^z = -\prod_{j'<j}(1-2c_{j'}^\dagger c_{j'})(c_j + c_j^\dagger)$. We therefore obtain

$$H = H_{\rm NS}P_+ + H_{\rm R}P_- \,, \tag{4.5}$$

$$H_{\rm NS/R} = -\frac{J}{2}\sum_{j=0}^{L-1}\left(c_j^\dagger c_{j+1} + c_{j+1}^\dagger c_j + c_j^\dagger c_{j+1}^\dagger + c_{j+1}c_j - 2g c_j^\dagger c_j + g\right) \,, \tag{4.6}$$

where $P_\pm = [1 \pm (-1)^{N_{\rm tot}}]/2$ are the projectors to even/odd fermion number parity sectors, with $N_{\rm tot} = \sum_{j=0}^{L-1} c_j^\dagger c_j$ the total fermion number; $H_{\rm NS}$ is understood with $c_{j+L} = -c_j$ boundary conditions (Neveu-Schwarz boundary conditions), while in $H_{\rm R}$ we have $c_{j+L} = c_j$ (Ramond boundary conditions). We then use appropriate Fourier transform $c_k = \frac{1}{\sqrt{L}}\sum_j c_j e^{-ikj}$ for each Hamiltonian $H_{\rm NS/R}$ and Bogoliubov transformation $\gamma_k = u_k c_k - i w_k c_{-k}^\dagger$, diagonalizing $H_{\rm NS/R} = \sum_{k\in K_{\rm NS/R}} \epsilon_k(\gamma_k^\dagger\gamma_k - \frac{1}{2})$, where $K_{\rm NS} = \{\frac{(2n+1)\pi}{L} | n = 0,\ldots,(L-1)\}$ and $K_{\rm R} = \{\frac{2n\pi}{L} | n = 0,\ldots,(L-1)\}$; the quasiparticle dispersion is $\epsilon_k = J(1+g^2-2g\cos k)^{1/2}$. This diagonalization is achieved by choosing the coherence factors as $u_k = \cos(\theta_k/2)$ and $w_k = \sin(\theta_k/2)$, where $\tan(\theta_k) = \sin(k)/[g - \cos(k)]$.

When making connections with the spin model, particularly when dealing with the string operators, it will be convenient to use Majorana representation. We will follow Ref. [45] and introduce Majorana fermions $A_j \equiv c_j^\dagger + c_j$ and $B_j = c_j^\dagger - c_j$.

The OTOCs can thus be expressed as fermionic correlation functions. The thermal ensemble grants the Wick's theorem, which allows us to express all the correlation functions using two-point correlation functions. However, the different fermion boundary conditions in the different fermion-number-parity sectors result in some complications in the calculation of dynamical correlation functions, and a more sophisticated treatment is needed. We will carefully state the procedure below and in the subsequent sections for the specific OTOCs. To prepare for such discussion, we here introduce some notations which will be useful later.

To enable free-fermion calculations, we introduce thermal ensembles corresponding to the two types of boundary conditions, $Z_{\text{NS/R}} \equiv \text{Tr}(e^{-\beta H_{\text{NS/R}}})$ and $\langle O \rangle_{\text{NS/R}} \equiv \text{Tr}(e^{-\beta H_{\text{NS/R}}} O)/Z_{\text{NS/R}}$. Note that the trace in each case is defined over the full Fock space, i.e., including both parity sectors, even though $H_{\text{NS/R}}$ originally arose in the even/odd parity sectors. These ensembles are introduced because the Wick's theorem only holds for an ensemble defined with respect to a quadratic Hamiltonian that is fixed over the full Fock space. To evaluate the thermal average with respect to the spin Hamiltonian H, we recall Eq. (4.5) and use

$$\langle O \rangle = \frac{Z_{\text{NS}}}{Z} \langle O P_+ \rangle_{\text{NS}} + \frac{Z_{\text{R}}}{Z} \langle O P_- \rangle_{\text{R}} \,. \tag{4.7}$$

Since $P_\pm = [1 \pm (-1)^{N_{\text{tot}}}]/2$, we will have to calculate $\langle O \rangle_{\text{NS/R}}$ and $\langle O(-1)^{N_{\text{tot}}} \rangle_{\text{NS/R}}$.

We are interested in situations where O in Eq. (4.7) is composed of several time evolved operators, $O = Q_1(t_1) Q_2(t_2) \dots$, where $Q(t) = e^{iHt} Q e^{-iHt}$. To be able to use free-fermion calculations and Wick's theorem, it is crucial to require that each $Q_1, Q_2, \dots$, does not change the fermion parity. In this case, considering, e.g., the operator in the first term in Eq. (4.7), we have: $O P_+ = Q_1(t_1) Q_2(t_2) \dots P_+ = Q_1^{\text{NS}}(t_1) Q_2^{\text{NS}}(t_2) \dots P_+$, where $Q^{\text{NS}}(t) \equiv e^{iH_{\text{NS}}t} Q e^{-iH_{\text{NS}}t}$. At this point, we can evaluate

$$\begin{aligned} \langle O P_+ \rangle_{\text{NS}} &= \langle Q_1^{\text{NS}}(t_1) Q_2^{\text{NS}}(t_2) \dots P_+ \rangle_{\text{NS}} \\ &= [\langle Q_1^{\text{NS}}(t_1) Q_2^{\text{NS}}(t_2) \dots \rangle_{\text{NS}} + \langle Q_1^{\text{NS}}(t_1) Q_2^{\text{NS}}(t_2) \dots (-1)^{N_{\text{tot}}} \rangle_{\text{NS}}]/2 \,. \end{aligned} \tag{4.8}$$

For each term in the last expression, both the the density matrix and the time evolution are determined by H_{NS} viewed over the full Fock space (i.e., including both parity sectors), thus enabling free-fermion calculations. Similar considerations apply to the calculation of $\langle O P_- \rangle_{\text{R}}$, which can be expressed entirely in terms of free fermions with Hamiltonian H_{R} over the full Fock space. We will often abuse the notation by dropping the labels "NS" or "R" in $Q^{\text{NS}}(t)$ or $Q^{\text{R}}(t)$ for brevity where the precise meaning can be recovered from the context.

In the thermodynamic limit, one in fact expects $\langle O(-1)^{N_{\text{tot}}} \rangle_{\text{NS/R}} \to 0$ and $\langle O \rangle_{\text{NS}} = \langle O \rangle_{\text{R}} = \langle O \rangle$. While for all the calculations one can in principle just evaluate $\langle O \rangle_{\text{NS}}$

or $\langle O\rangle_{\mathrm{R}}$ and take the thermodynamical limit, in this paper we calculate exact finite-size $F_{\mu\nu}(\ell,t)$ [and hence $C_{\mu\nu}(\ell,t)$] using Eq. (4.7) so that we can compare the results against exact diagonalization of the spin system at small system sizes to ensure the correctness.

To study the behavior of $C_{\mu\nu}(\ell,t)$ around the wavefront in more detail, or more specifically, to examine if the wavefront has the functional form $C_{\mu\nu}(\ell,t)\sim e^{-\lambda(\ell-ct)}$, we will also study the function $G_{\mu\nu}(\ell,t)=\partial\ln C_{\mu\nu}(\ell,t)/\partial t$, which characterizes the onset of the scrambling [40] if there is one and the spreading of the operator wavefront [29, 31, 49]. When discussing the analytical results and the calculation of $G_{\mu\nu}(\ell,t)$, we consider only the part $\langle O\rangle_{\mathrm{NS}}$.

The crucial ingredients to obtain all the correlation functions are the two-point Majorana correlation functions, which we list in Appendix A. In all the calculations of the OTOC, we will need to use the numerical values of Z, Z_{NS}, and Z_{R}. The partition sums Z_{NS} and Z_{R} can be calculated easily by $Z_{\mathrm{NS/R}}=\sum_{E_{\mathrm{NS/R}}}e^{-\beta E_{\mathrm{NS/R}}}$, where $E_{\mathrm{NS/R}}$ denotes the eigenenergies of $H_{\mathrm{NS/R}}$. Note again that here we consider H_{NS} acting on the full fermion Fock space including both even and odd parity sectors and performs free-fermion calculation of Z_{NS}, and similarly treats H_{R} to calculate Z_{R}. On the other hand, the calculation of Z is nontrivial as it involves the projectors to the different sectors, and its details are presented in Appendix A.

4.2 Quantum Ising Model: XX OTOC

First, we discuss the commutator function $C_{xx}(\ell,t)=1-\mathrm{Re}F_{xx}(\ell,t)$. In the fermionic representation, $\sigma^x_\ell=A_\ell B_\ell$. Therefore we have

$$F_{xx}(\ell,t)=\langle A_\ell(t)B_\ell(t)A_0B_0A_\ell(t)B_\ell(t)A_0B_0\rangle\ . \tag{4.9}$$

Note that we need to use Eq. (4.7) and evaluate both $\langle OP_+\rangle_{\mathrm{NS}}$ and $\langle OP_-\rangle_{\mathrm{R}}$. While these expectation values can be evaluated using Wick's theorem, the calculation is simplified when cast in the form of Pfaffians of anitsymmetric matrices. We present details in Appendix B.

Figure 4.1 shows the numerical results for $C_{xx}(\ell,t)$ at various time slices. We can immediately identify the velocity of the wavefront as $c=1$, which is the maximum of the quasiparticle group velocity $v_k=\partial\epsilon_k/\partial k$ and is also the butterfly velocity $v_B=c$. In the present case, the OTOC function is "shell-like." That is, inside the timelike region, in the long-time limit, $C_{xx}(\ell,t)\to 0$, indicating no scrambling. More precisely, as far as characterizing the operator spreading of $\sigma^x(t)$, the vanishing

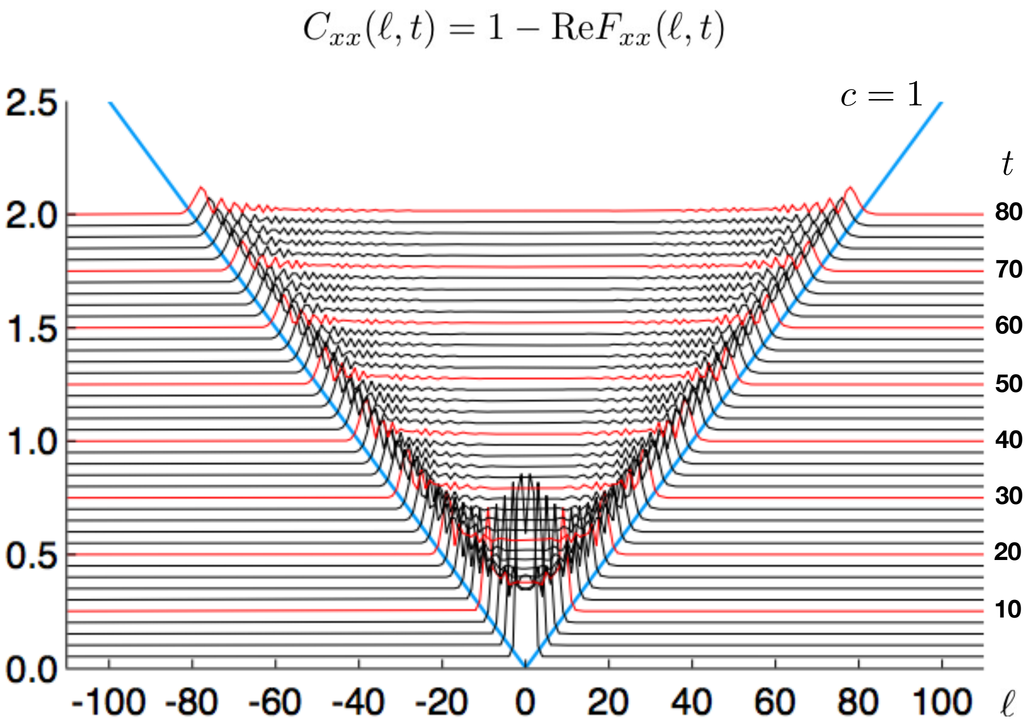

Figure 4.1: (color online) The function $C_{xx}(\ell,t)$ for the quantum Ising chain at the critical point, $g = 1$, at infinite temperature (inverse temperature $\beta = 0$); the system size is $L = 512$. We show data as a function of ℓ at fixed time t, for t in steps of $\Delta t = 2$ marked along the right border; here and in all figures, the energy unit J in Eq. (4.3) is set to 1. The traces at fixed t are shifted in the y direction by $0.025t$ thus offering three-dimensional-like visualization. For every t that is a multiple of 10, we mark the trace with red color for easier reading of the data. The light cone can be readily identified and corresponds to the maximal quasiparticle group velocity $c = \max_k \frac{d\epsilon_k}{dk} = J = 1$. In the timelike region, $C_{xx}(\ell,t)$ approaches zero in the long-time limit, indicating the absence of "scrambling."

of the C_{xx} OTOC in the long-time limit suggests that expansion of $\sigma^x(t)$ in terms of Pauli strings does not contain many σ^y or σ^z operators "in the middle" of the strings. This can be indeed seen from the explicit expressions for $\sigma^x(t)$ in Appendix E.

"Universal" early-time growth with separation-dependent power law

Before the light cone reaches, we can argue that there is a "universal" power-law growth of $C_{xx}(\ell,t) \sim t^{2(2\ell-1)}$. Indeed, consider $W = \sigma_0^x$ and $V = \sigma_\ell^x$. The Heisenberg evolution $W(t)$ at short time can be expanded via Hausdorff-Baker-

Campbell (HBC) formula

$$W(t) = \sum_{n=0}^{\infty} \frac{t^n}{n!} L^n(W) \,, \tag{4.10}$$

where $L(W) \equiv i[H, W]$. It is easy to check that for these W and V, the smallest n such that $[L^n(W), V] \neq 0$ is $n = 2\ell - 1$, and the nonzero contribution to the commutator comes from the piece in $L^n(W)$ that reaches site ℓ, namely $J^{2\ell-1} g^{\ell-1} \sigma_0^y \sigma_1^x \ldots \sigma_{\ell-1}^x \sigma_\ell^z$. Therefore, the leading order behavior is

$$C_{xx}(\ell, t) \approx \frac{2(Jt)^{4\ell-2} g^{2\ell-2}}{[(2\ell-1)!]^2} \,, \tag{4.11}$$

which is also shown in Fig. 4.2 and captures well the exact calculation in this regime. We expect that such an argument based on the HBC formula is in fact very general and not related to any integrability of the model [14, 50, 51]. We thus expect such power-law growth with position-dependent power to be "universal," present also in nonintegrable systems, as long as one is considering systems with bounded on-site Hilbert spaces and Hamiltonians with local interactions. Such a power-law growth is indeed also observed in the XXZ model [14]. However, we emphasize that this is just a quantum mechanical effect before the light cone reaches and should not be identified as a signature of scrambling or lack of it.

Lastly, we note that if we fix time t and take the separation ℓ to large values, the commutator function $C_{xx}(\ell, t)$ decays faster than the exponential function in ℓ, namely $C_{xx}(\ell, t) \sim \exp[a(t)\ell - 4\ell \ln \ell]$, where $a(t)$ is some number that depends on t.

Behavior around the wavefront

To examine the behavior of $C_{xx}(\ell, t)$ around the wavefront more closely, we study the function

$$G_{xx}(\ell, t) \equiv \frac{\partial \ln C_{xx}(\ell, t)}{\partial t} \,. \tag{4.12}$$

We can calculate this in a way that avoids numerical differentiation (see Appendix B for details) and present the results in Fig. 4.3. We see that before the oscillation sets in, $G_{xx}(\ell, t)$ shows very strong ℓ dependence. On the other hand, the inset in Fig. 4.3 demonstrates that $G_{xx}(\ell, t)$ shows essentially no temperature dependence. We conclude that the behavior near this wavefront does not show the "exponential divergence" that could be associated with the "butterfly effect," and we can exclude the possibility of any temperature-dependent description of the wavefront. Thinking

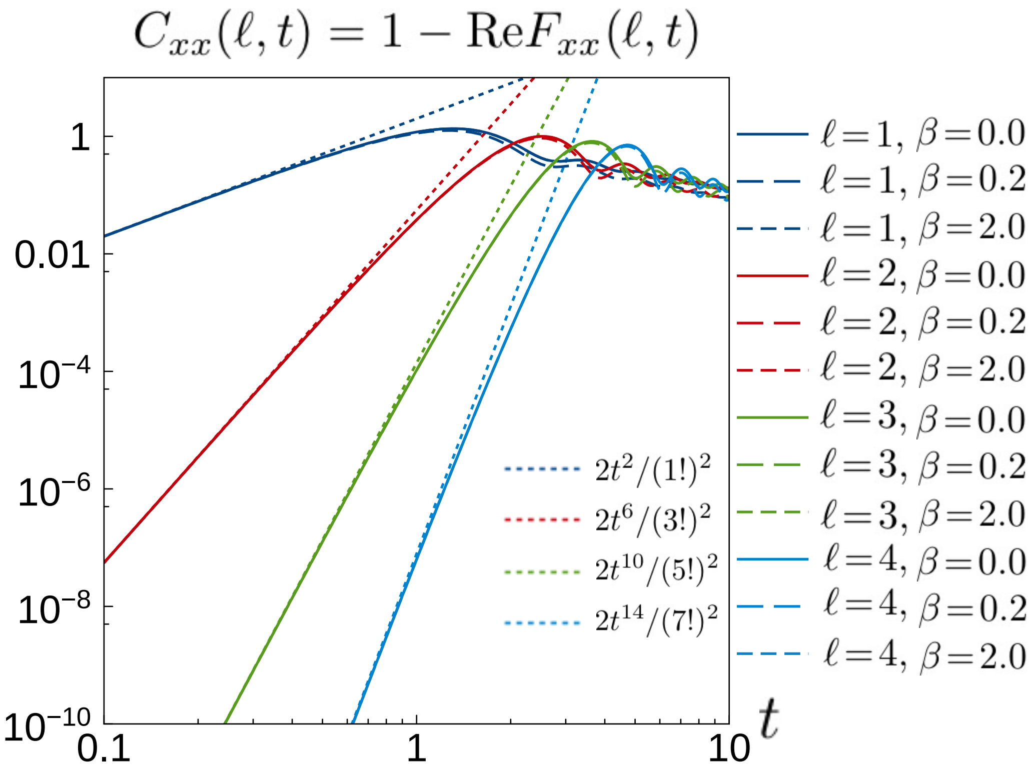

Figure 4.2: (color online) The function $C_{xx}(\ell,t)$ for several fixed separations ℓ at short time before the light cone reaches (i.e., spacelike separation between the operators). The growth of the commutator is compared to the "universal" power-law behavior given by $\approx 2t^{2(2\ell-1)}/[(2\ell–1)!]^2$; note that there is essentially no temperature dependence in this regime.

about possible other descriptions of the wavefront, we do not clearly see a parametrically large time window where we could sharply distinguish this transition region behavior from the short-time and long-time behaviors. While we see that the onset of oscillations (more precisely, onset of nonmonotonic behavior) happens at larger $t - \ell/c$ when ℓ is increased, at present we do not know if there is any asymptotic functional form in a well-defined window to describe the wavefront. Thus we also note that the frequency of oscillations vanishes as one approaches the $\ell/t = c$ ray, so the later "onset" of oscillations for larger ℓ could be related to this. In any case, we can definitely tell that any "universal" description needs to be essentially temperature-independent.

Note added: After the publication of this result, two papers [38, 39] appeared that proposed a universal functional form for the OTOC around the wavefront. We verify that the proposed wavefront description [39] indeed holds for $F_{xx}(\ell,t)$ in Fig. 4.4.

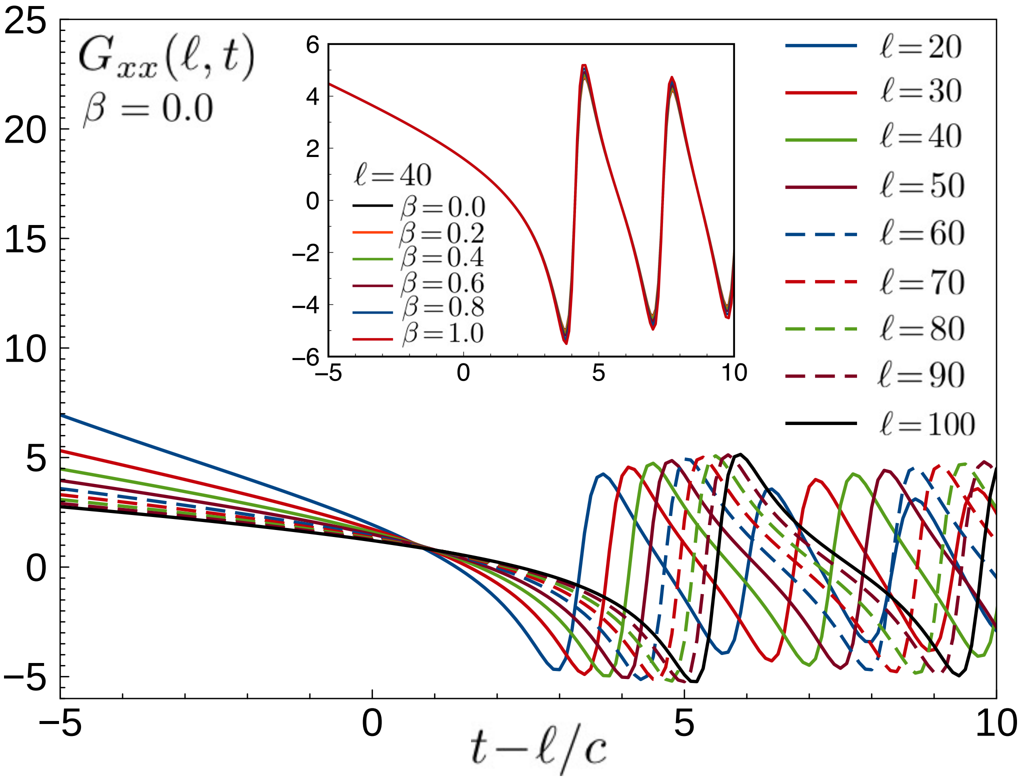

Figure 4.3: The derivative function $G_{xx}(\ell, t) \equiv \partial \ln C_{xx}(\ell, t)/\partial t$ around the wavefront. Before the oscillation sets in, $G_{xx}(\ell, t)$ has very strong ℓ dependence, for which we do not know any universal description. Inset: $G_{xx}(\ell, t)$ for fixed $\ell = 40$ and several different inverse temperatures β, illustrating that there is basically no temperature dependence around the wavefront.

Specifically, on rays with fixed velocity outside the light cone, $(x = vt, t)$ with $v > c$, we have verified that the OTOC has exponential decay $\sim \exp[-\lambda(v)t]$ at long times, with $\lambda(v)$ vanishing as $(v - c)^{3/2}$ as $v \to c$. Furthermore, the broadening we observed near the wavefront (seen, e.g., in the movement of the first oscillation feature inside the light cone for increasing ℓ in Figs. 4.3.

Universal long-time decay with t^{-1} power law

The limiting value of $F_{xx}(\ell, t)$ for fixed ℓ but $t \to \infty$ can be easily shown to be one. Indeed, considering all the Wick contractions in Eq. (4.9), we see that if the contraction has any nonequal time correlation function, this term will be zero since all the fermionic correlation functions go to zero in the $t \to \infty$ limit. We therefore

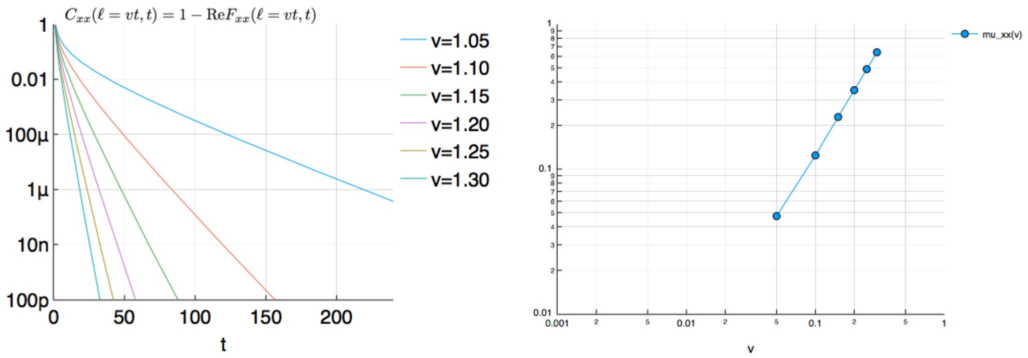

Figure 4.4: The behavior of the commutator function $C_{xx}(\ell, t) = 1 - \mathrm{Re}F_{xx}(\ell, t)$ along the ray $\ell = vt$. (Recall σ^x is *local* in JW fermions.) The parameters are $g = 1$, $\beta = 0$ and $L = 512$. The function displays a exponential decay at the long times. The short-time behavior in the log-linear plot maybe a manifestation of some power-law factor. For the figure at the right-hand side, I fit $C_{xx}(\ell, t)$ to $Ce^{-\mu_{xx}(v)t}$ at the long-time region where it looks a straight line in the log-linear plot. The behavior of $\mu_{xx}(v) \sim (v - c)^{\frac{3}{2}}$.

have

$$\begin{aligned} F_{xx}(\ell, \infty) &= \langle A_\ell(\infty) B_\ell(\infty) A_\ell(\infty) B_\ell(\infty)\rangle \langle A_0 B_0 A_0 B_0\rangle \\ &= \Big(\langle A_0 B_0\rangle^2 + 1 + \langle A_0 B_0\rangle\langle B_0 A_0\rangle\Big)^2 = 1 \ . \end{aligned}$$

We conclude that $C_{xx}(\ell, \infty) = 0$, which is a signature of no scrambling.

The long time behavior of $C_{xx}(\ell, t)$ is shown in Fig. 4.5 for different separations ℓ and different inverse temperatures β. The data suggests universal t^{-1} behavior independent of ℓ and β. We can indeed understand this from the stationary phase approximation for the fermionic correlation functions. The standard stationary phase approximation applied to the fermionic correlation functions gives $t^{-1/2}$ decay at long times. The full Wick contraction for Eq. (4.9) is complicated but can be obtained by simplifying the calculation of the Pfaffian, see Appendix B for details. From this, we can identify the dominant behavior at fixed ℓ and long time:

$$C_{zz}(\ell, t) \sim \Big(1 - \langle A_0 B_0\rangle^2\Big) \frac{2}{\pi |\epsilon''_\pi| t} \ , \tag{4.13}$$

where ϵ''_k is the second derivative of ϵ_k with respect to k (for $g = 1$ considered here, $|\epsilon''_\pi| = J/2 = 1/2$). Note that in this expression the temperature dependence enters only in the expectation value $\langle A_0 B_0\rangle = \langle\sigma^x_0\rangle$, which is zero at infinite temperature and approaches value 0.7698 at zero temperature (so that the coefficient of the t^{-1} decay is always nonzero). We can recognize that the t^{-1} decay comes from two pairs

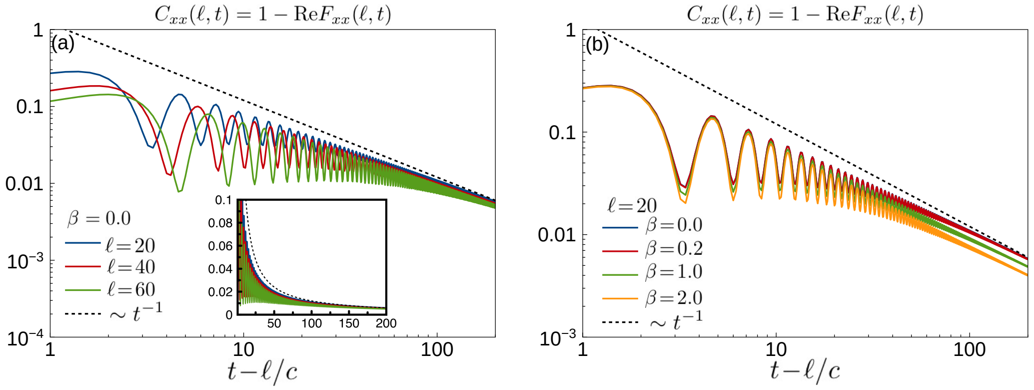

Figure 4.5: Long-time behavior of $C_{xx}(\ell, t)$ in the timelike region; note the log-log scale. The data is shown as a function of t at fixed ℓ, where on the horizontal axis we show the time elapsed after the wavefront passes. Panel (a) shows several different separations ℓ and is at infinite temperature; the inset shows the same data on the linear-linear scale. Panel (b) shows several different temperatures at fixed separation $\ell = 20$. In all cases, we observe power-law decay t^{-1}, which can be understood from the long-time behavior of the fermion correlation functions.

of unequal-time contractions and two pairs of equal-time contractions. Appendix E provides qualitative understanding of this long-time behavior directly from the operator spreading picture. We also note that the above calculations and qualitative results hold for all g and nonzero temperatures.

It is interesting to compare the OTOC behavior with results for dynamical correlation functions as well as for thermalization of such spin observable in quench settings. The dynamical correlation function $\langle \sigma^x_\ell(t)\sigma^x_0\rangle = \langle A_\ell(t)B_\ell(t)A_0B_0\rangle$ approaches $\langle\sigma^x_0\rangle^2$ in the long-time with t^{-1} power-law. Indeed, this power law comes from simple calculation, $\langle \sigma^x_\ell(t)\sigma^x_0\rangle - \langle\sigma^x_0\rangle^2 = \langle A_\ell(t)B_0\rangle\langle B_\ell(t)A_0\rangle - \langle A_\ell(t)A_0\rangle\langle B_\ell(t)B_0\rangle$, and is ultimately related to the long-time behavior of the fermion dynamical correlation function. However, we note that details of the contraction pieces (i.e., how "fractions" of the spin operator get contracted) is different here compared to the OTOC calculation, even though the long-time t^{-1} power law is similar. Let us now consider quench setting where one starts with some initial state $|\psi_{\mathrm{ini}}\rangle$ (e.g., a product state or a ground state at some other parameter $g' \neq g$) and then evolves under the present Hamiltonian. Here one finds that $\langle\psi_{\mathrm{ini}}|\sigma^x_0(t)|\psi_{\mathrm{ini}}\rangle$ decays as $t^{-3/2}$ to its equilibrium value in the long-time limit [48]. Generally, it is clear that the OTOC, dynamical correlation function, and behavior under quench, probe different aspects of the Heisenberg-evolved operator $\sigma^x_0(t)$ (see also Appendix E).

4.3 Quantum Ising Model: ZZ OTOC

In this section, we discuss the commutator function $C_{zz}(\ell, t) = 1 - \mathrm{Re} F_{zz}(\ell, t)$. The new feature here is that σ^z_ℓ is nonlocal in terms of the JW fermions and furthermore changes the fermion parity. While one can write $\sigma^z_\ell = -(\prod_{j<\ell} A_j B_j) A_\ell$, its Heisenberg evolution $\sigma^z_\ell(t)$ cannot be obtained from the simple free-fermion Heisenberg evolution of the fermions $A_j(t)$ and $B_j(t)$. The reason is that the original spin Hamiltonian in the fermionic language is in fact composed of projections into two different fermion-parity sectors, with different free-fermion Hamiltonian used in each sector. The operator σ^z_ℓ, however, changes the fermion-parity, while the Heisenberg evolution of the fermion operators are simple only when working with a fixed free-fermion Hamiltonian over the full Fock space. Therefore, we need a more sophisticated treatment when calculating the dynamical quantities.

Following McCoy and Abraham [52], we "double" the OTOC and consider the following quantity

$$\Gamma_{zz}(\ell, t; L) \equiv \langle \sigma^z_{\frac{L}{2}}(t) \sigma^z_{L-\ell}(t) \sigma^z_0 \sigma^z_{\frac{L}{2}-\ell} \sigma^z_{\frac{L}{2}}(t) \sigma^z_{L-\ell}(t) \sigma^z_0 \sigma^z_{\frac{L}{2}-\ell} \rangle \,, \tag{4.14}$$

where by periodic boundary conditions site $L - \ell \equiv -\ell$ will be "close" to site 0 (and site $L/2 - \ell$ will be "close" to site $L/2$). Consider large enough L such that $L/2 \gg \ell$ and $L/2 \gg vt$ for some characteristic velocity v (here $v \leq c = 1$). Invoking the Lieb-Robinson bound and the cluster property [52], we have

$$\begin{aligned} \Gamma_{zz}(\ell, t; L) &\approx \langle \sigma^z_{\frac{L}{2}}(t) \sigma^z_{\frac{L}{2}-\ell} \sigma^z_{\frac{L}{2}}(t) \sigma^z_{\frac{L}{2}-\ell} \rangle \langle \sigma^z_{L-\ell}(t) \sigma^z_0 \sigma^z_{L-\ell}(t) \sigma^z_0 \rangle \\ &= F_{zz}(\ell, t) F_{zz}(-\ell, t) = F^2_{zz}(\ell, t) \,, \end{aligned} \tag{4.15}$$

where we have used the mirror symmetry $F_{zz}(-\ell, t) = F_{zz}(\ell, t)$. The advantage of introducing the function $\Gamma_{zz}(\ell, t; L)$ is that $\sigma^z(t)$ operators come in pairs that do not change the fermion parity, which allows expressing the evolution using fixed free-fermion Hamiltonians, so the full function can be calculated via Wick's theorem in terms of the JW fermions. Again, the evaluations of the Wick's theorem can be conveniently formulated as Pfaffians of appropriate antisymmetric matrices. We present the details in Appendix C.

Figure 4.6 shows $C_{zz}(\ell, t)$ at $g = 1.0$, $\beta = 0$, calculated using the above procedure on a system of size $L = 512$. Note that since we can only calculate $F^2_{zz}(\ell, t)$, we recover the sign of $\mathrm{Re} F_{zz}(\ell, t)$ by requiring "continuity" of the "derivative" $D_\ell F_{zz}(\ell, t) \equiv F_{zz}(\ell + 1, t) - F_{zz}(\ell, t)$ and the known value of $\mathrm{Re} F_{zz}(\ell, t) \approx 1$ in the spacelike region $\ell \gg ct$. We have verified such recovery of the sign also by examining continuity of $\partial_t F_{zz}(\ell, t)$ as we vary t. As in our study of $C_{xx}(\ell, t)$ in Fig. 4.1, we can immediately identify the light cone velocity as the maximal group velocity of the quasiparticles. On the other hand, we also observe that $C_{zz}(\ell, t)$ approaches a nonzero value inside the light cone at long times. In fact, in the inset of Fig. 4.10(a), we can see that $\mathrm{Re}F_{zz}(\ell, t)$ approaches zero in the long-time limit, and hence $C_{zz}(\ell, t)$ approaches 1. Thus $C_{zz}(\ell, t)$ has a "ball-like" structure, in contrast to the "shell-like" $C_{xx}(\ell, t)$. We interpret this property of $C_{zz}(\ell, t)$ as a signature of some scrambling of the information in the system. From the operator spreading point of view, this behavior corresponds to $\sigma_0^z(t)$ having a lot of weight on Pauli-strings with "random" σ_ℓ^μ in the middle of the strings; more precisely, the infinite-temperature $C_{zz}(\ell, t)$ approaching 1 corresponds to the weight of the strings that have $\sigma_\ell^\mu = \sigma^x$ or σ^y approaching 1/2 of the total weight, a kind of "scrambling."

Early-time behavior of $C_{zz}(\ell, t)$

The early-time growth of $C_{zz}(\ell, t)$ can be also understood by the argument employing the HBC expansion, Eq. (4.10). In this case, for $W = \sigma_0^z$ and $V = \sigma_\ell^z$, the smallest n such that $[L^n(W), V] \neq 0$ is $n = 2\ell + 1$; the corresponding piece in $L^n[W]$ is $-J^{2\ell+1} g^{\ell+1} \sigma_0^x \sigma_1^x \ldots \sigma_{\ell-1}^x \sigma_\ell^y$. This gives us

$$C_{zz}(\ell, t) \approx 2 \frac{(Jt)^{2(2\ell+1)} g^{2(\ell+1)}}{[(2\ell + 1)!]^2} . \tag{4.16}$$

In Fig. 4.7, we compare the above formula and the numerical results for $C_{zz}(\ell, t)$. We see that the short-time behavior is well captured by this argument.

Behavior of $C_{zz}(\ell, t)$ around the wavefront

Here we investigate the behavior of $C_{zz}(\ell, t)$ around the wavefront. Again, we study the derivative function

$$G_{zz}(\ell, t) \equiv \frac{\partial \ln C_{zz}(\ell, t)}{\partial t} . \tag{4.17}$$

Details of the calculation that avoids numerical differentiation are presented in Appendix C. In principle, if $C_{zz}(\ell, t)$ has the Lyapunov behavior, namely the exponential growth around the wavefront, we should be able to extract this from $G_{zz}(\ell, t = t_0)$, where $t_0 = \ell/c$ is the characteristic wavefront passage time defined using analytically known maximal group velocity $c = 1$. In Fig. 4.8, we see that $G_{zz}(\ell, t)$ is well described by a linear function $\lambda_0 + \lambda_1(t - \ell/c)$ around the wave front. However, the parameters $\lambda_0(\ell)$ and $\lambda_1(\ell)$ have a strong dependence on ℓ but very weak dependence on β. It is therefore not clear if we should view this functional form as a well defined

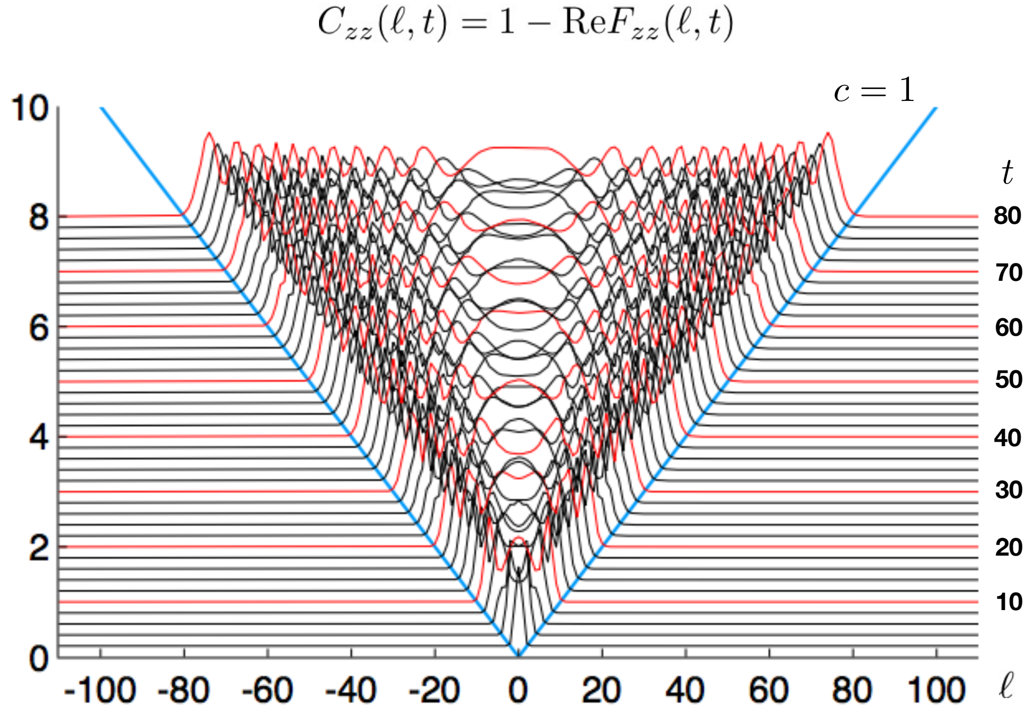

Figure 4.6: (color online) The function $C_{zz}(\ell, t) = 1 - \mathrm{Re}F_{zz}(\ell, t)$ for the critical Ising chain ($g = 1$) at infinite temperature ($\beta = 0$), evaluated using the "doubling trick," Eq. (4.15), on a periodic chain of length $L = 512$. Here we restore the sign of $\mathrm{Re}F_{zz}(\ell, t)$ from $\mathrm{Re}\sqrt{\Gamma_{zz}(\ell, t; L)}$ by requiring "continuity" of the "derivative" $D_\ell \mathrm{Re}F_{zz}(\ell, t) = \mathrm{Re}F_{zz}(\ell + 1, t) - \mathrm{Re}F_{zz}(\ell, t)$ (see text for details). We show data as a function of ℓ at fixed t, with time steps $\Delta t = 2$. The traces at fixed t are shifted by $0.1t$ in the y-direction for 3D-like visualization; every t that is multiple of 10 is marked with red color for easier tracing. Similarly to $C_{xx}(\ell, t)$ in Fig. 4.1, we can readily identify the light cone and associate it with the maximal quasiparticle velocity $c = 1$. Unlike $C_{xx}(\ell, t)$, in the timelike region $C_{zz}(\ell, t)$ approaches a nonzero value close to 1 at long times. In other words, $F_{zz}(\ell, t)$ approaches value close to zero, which suggests scrambling of the information.

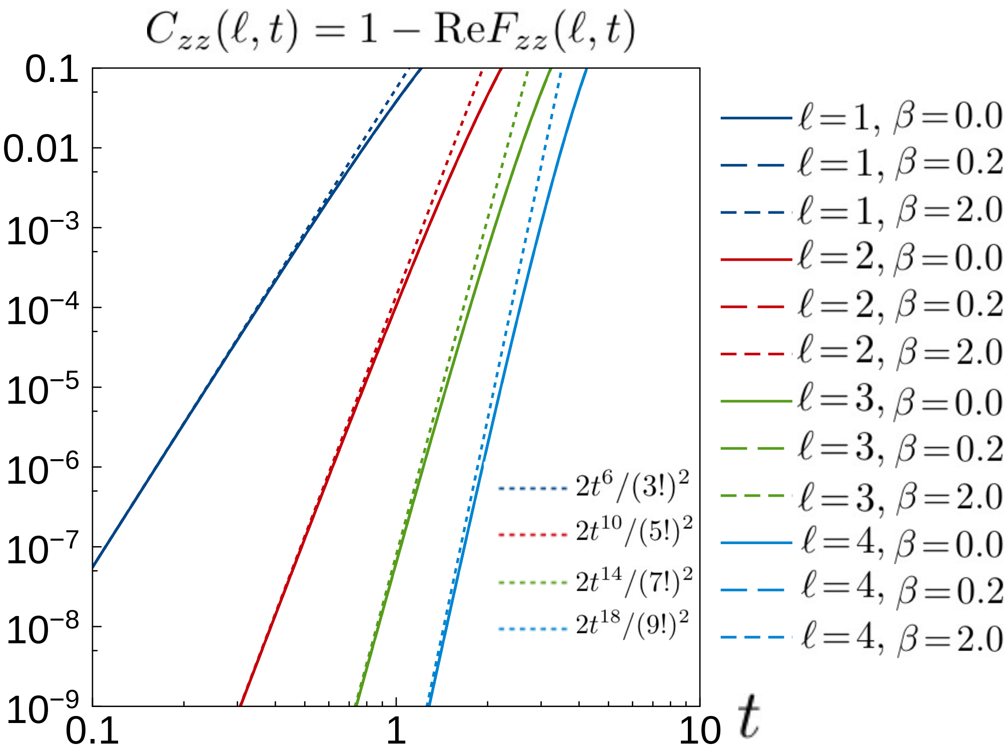

Figure 4.7: (color online) The short-time behavior of $C_{zz}(\ell,t)$ examined for several separations ℓ and different inverse temperatures β; the system is the same as in Fig. 4.6. The early-time growth of $C_{zz}(\ell,t)$ is well described by the "universal" power-law given by $\approx 2t^{4\ell+2}/[(2\ell+1)!]^2$.

asymptotic description and identify λ_0 as the Lyapunov exponent. One possibility is that when ℓ is large, λ_0 approaches a finite value while λ_1 approaches zero, therefore it is well-defined when $\ell \to \infty$ with $\ell/t \sim c$ fixed. In this case, around the wavefront, we could say that $C_{zz}(\ell,t) \sim \exp[\lambda_0(t-\ell/c)]$. However, we do not seem to have a parametrically large window exhibiting such behavior that could be clearly separated from the short-time and long-time regimes. Furthermore, any such Lyapunov exponent extracted from our data would be essentially temperature-independent, which would not be consistent with existing proposals. We do see that the onset of oscillations (which in our mind cuts off any asymptotic description of the wavefront behavior) is pushed to larger $t-\ell/c$ for larger ℓ, but we do not know if there is any asymptotic functional description to this. If there is, then similarly to the C_{xx} wavefront in Fig. 4.3, the description should be essentially temperature independent.

Following the proposals in Refs. [38, 39], we verify the wavefront broadening

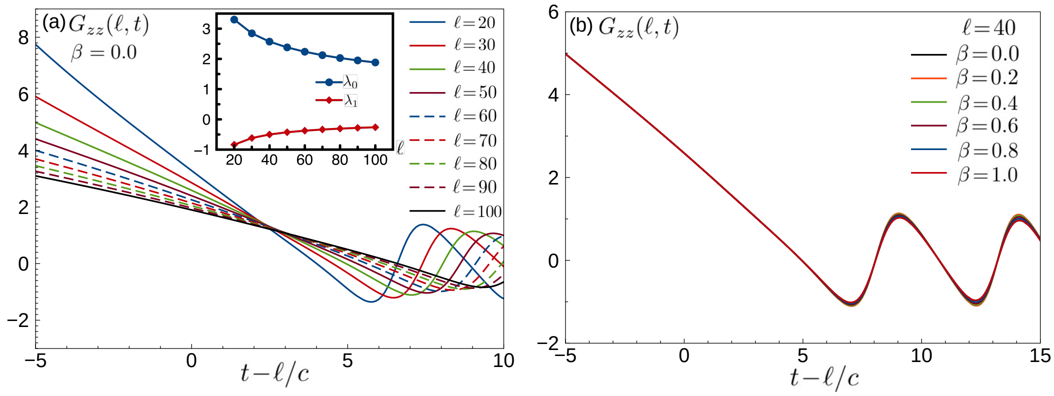

Figure 4.8: The derivative function $G_{zz}(\ell,t) \equiv \partial \ln C_{zz}(\ell,t)/\partial t$ around the wavefront. (a) $G_{zz}(\ell,t)$ as a function of time for several different separations ℓ, where the horizontal axis shows time measured relative to the "exact" wavefront passage time defined from the known maximal group velocity $c = 1$; this data shows shows strong ℓ dependence. Around $t-\ell/c = 0$, the behavior of $G_{zz}(\ell,t)$ is well approximated by a linear function. We fit $G_{zz}(\ell,t)$ to $\lambda_0 + \lambda_1(t-\ell/c)$ in the region $t-\ell/c \in [-3,3]$ and show the resulting parameters g_0 and g_1 for different ℓ in the inset. (b) $G_{zz}(\ell,t)$ for fixed $\ell = 40$ at different inverse temperatures β; we see that such wavefront characterization does not show strong temperature dependence.

functional form of $C_{zz}(\ell,t)$ in Fig. 4.9. The OTOC $C_{zz}(\ell,t)$ again has exponential decay $\sim \exp[-\lambda(v)t]$ at long times, with $\lambda(v)$ vanishing as $(v-c)^{3/2}$ as $v \to c$. The broadening we observed near the wavefront is consistent with the proposed broadening $\sim t^{1/3} \sim \ell^{1/3}$.

Unusual slow $t^{-1/4}$ power-law at long time

An analytical treatment of $C_{zz}(\ell,t)$ is very difficult since it involves analyzing the Pfaffian of a large matrix with essentially infinite dimension in the thermodynamic limit $L \to \infty$. Here, we analyze it by examining the numerical results in Fig. 4.10. As before, the data is for the critical Ising chain coupling, $g = 1$, and the calculations are done for system size $L = 512$. The horizontal axis shows $t{-}\ell/c$. We focus on the long-time behavior of the OTOC $F_{zz}(\ell,t)$ after the wavefront passes. We discover that, while $F_{zz}(\ell,t)$ approaches zero in the long-time limit, the approach is described by an oscillating function with a slow power-law envelope $t^{-1/4}$. This long-time power-law behavior is independent of the separation ℓ or the inverse temperature β. It is worth mentioning that the finite-temperature calculation for the Ising conformal field theory [24] gives the same limiting value as our lattice calculation. However, our $t^{-1/4}$ power-law approach behavior is not described by the conformal field theory.

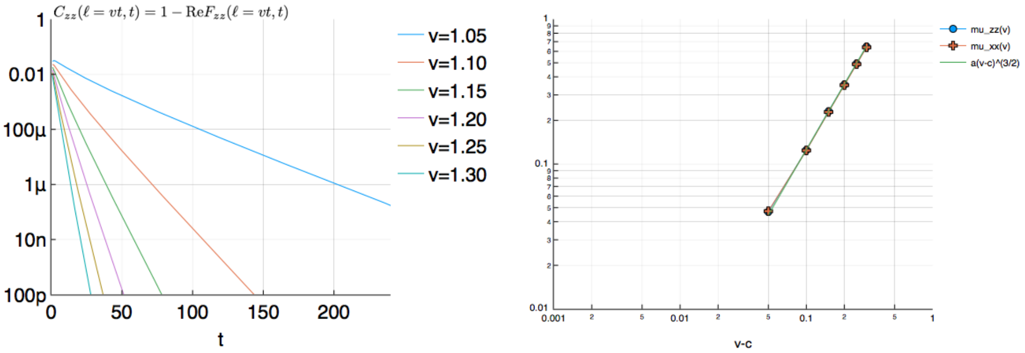

Figure 4.9: The behavior of the commutator function $C_{zz}(\ell, t) = 1 - \mathrm{Re}F_{zz}(\ell, t)$ along the ray $\ell = vt$. (Recall σ^z is *nonlocal* in JW fermions.) The parameters are $g = 1$, $\beta = 0$ and $L = 512$. The function displays a exponential decay at the long times. The short-time behavior is different from C_{xx}. For the figure at the right-hand side, $C_{zz}(\ell, t)$ is fitted to $Ce^{-\mu_{zz}(v)t}$ at the long-time region. The behavior of $\mu_{zz}(v) \sim (v - c)^{\frac{3}{2}}$. Surprisingly, the long-time behavior of C_{zz} is very similar to C_{xx}. The numerical values of $\mu_{zz}(v)$ and $\mu_{xx}(v)$ are very close.

We can further examine the oscillations by following a specific ray $t = \ell/v$ for varying v. We show this in Fig. 4.10(c), where we find a single oscillation frequency for each such ray and show its dependence on v in the inset. We conjecture that the frequency is determined by some "stationary phase" approximation on a propagation factor $\exp(ik\ell - i\epsilon_k t)$. This would give the oscillation frequency as $\omega(v) = \epsilon_{k_0} - k_0 v$, where k_0 is the momentum such that the quasiparticle group velocity $\partial\epsilon_k/\partial k|_{k=k_0} = v$. For $v = 0$, this gives $\omega(v = 0) = \epsilon_{k=\pi} = 2$, which is the frequency where the quasiparticle group velocity is zero. The oscillations in panels Fig. 4.10(a) and 4.10(b), where we analyze the limit $t \longrightarrow \infty$ at fixed ℓ which corresponds to $v = 0$, indeed appear to approach this frequency. However, at present we do not have an analytical understanding of this "stationary phase" conjecture and of the observed $t^{-1/4}$ power law. We leave this most interesting and mysterious observation as an open question.

In contrast, the dynamical correlation function $\langle\sigma^z_\ell(t)\sigma^z_0\rangle$ decays exponentially in t and ℓ as long as the temperature is nonzero [45, 53–57]. The decay length and coherence time depend on the parameter regime (g and β). At infinite temperature, the correlation function has a singular behavior $\langle\sigma^z_\ell(t)\sigma^z_0\rangle = \delta_{\ell,0}e^{-t^2}$ [58], consistent with vanishing correlation length and coherence time. Similarly, calculations in quench settings found that $\langle\psi_{\mathrm{ini}}|\sigma^z_0(t)|\psi_{\mathrm{ini}}\rangle$ decays exponentially as well [47, 48]. We thus see that there is a qualitative difference between the long-time behaviors of the OTOC and of the dynamical correlations as well as thermalization of the

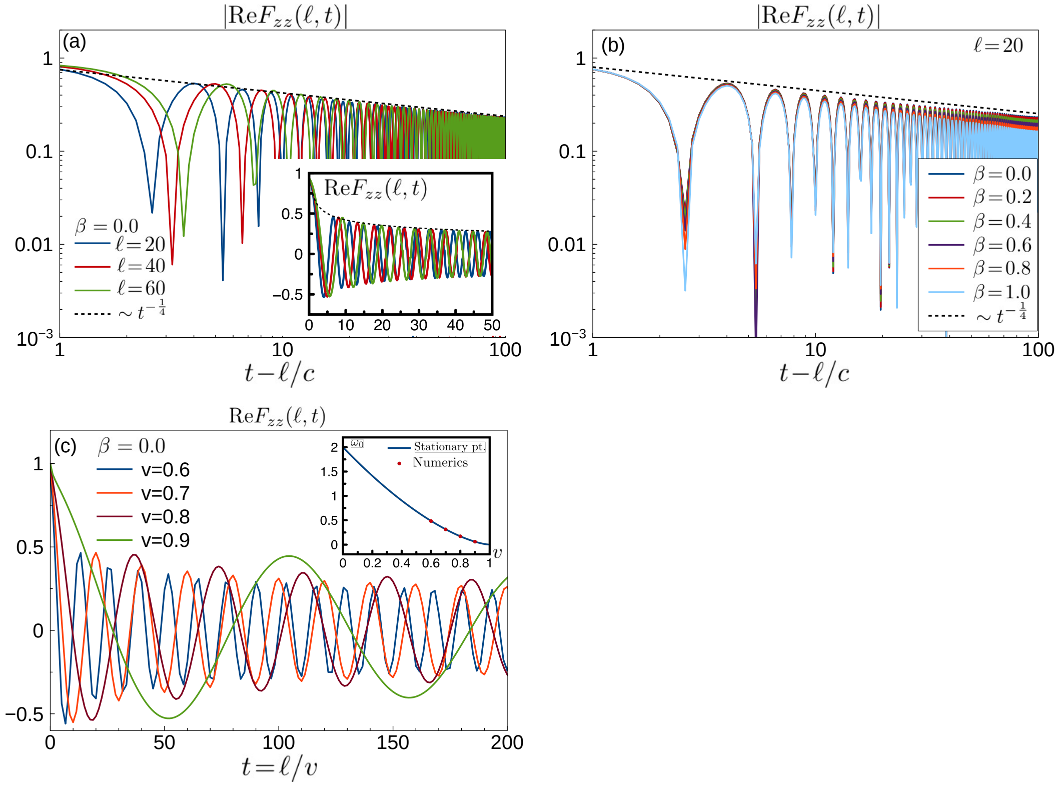

Figure 4.10: (color online) Long-time behavior of $|\mathrm{Re}F_{zz}(\ell,t)|$ in the timelike region (i.e., after the wavefront passes) at (a) different separations and (b) different inverse temperatures. (a) For different separations and $\beta = 0$, in the long-time limit, $|\mathrm{Re}F_{zz}(\ell,t)|$ shows $t^{-\frac{1}{4}}$ decay. Inset: Linear plot of $\mathrm{Re}F_{zz}(\ell,t)$, where we fixed the sign by requiring continuity of the derivative $D_t F_{zz}(\ell,t) \equiv F_{zz}(\ell,t+\Delta t) - F_{zz}(\ell,t)$, where Δt is the time step in the numerical calculation. (b) The temperature only affects the coefficient of the power-law decay; in the long-time limit, the decay is still $t^{-1/4}$. (c) $\mathrm{Re}F_{zz}(\ell,t)$ along several different rays $\ell/t = v =$ const inside the timelike region, where for each v we observe single oscillation frequency that depends on v. Inset: Comparison of the frequency fitted from from the numerical calculations (red dots) and from the "stationary phase" conjecture (blue line) $\omega(v) = \epsilon_{k_0} - k_0 v$, $\partial_k \epsilon|_{k_0} = v$, described in the main text.

σ^z operator. This indicates that the OTOC captures some different aspects of the physics, and this finding deserved further understanding.

4.4 Quantum Ising Model: ZX OTOC

Lastly, we discuss the function $C_{zx}(\ell,t)$. In the JW fermion language, here we have both a nonlocal operator and a local operator. As in the case of $C_{zz}(\ell,t)$, σ^z changes the fermion parity sector. Therefore, we need to use the "doubling trick." We consider the following function:

$$\Gamma_{zx}(\ell, t; L) \equiv \langle \sigma^z_{\frac{L}{2}}(t)\sigma^z_{L-\ell}(t)\sigma^x_0\sigma^x_{\frac{L}{2}-\ell}\sigma^z_{\frac{L}{2}}(t)\sigma^z_{L-\ell}(t)\sigma^x_0\sigma^x_{\frac{L}{2}-\ell}\rangle \; .$$

For large enough system size such that $L/2 \gg \ell$, $L/2 \gg ct$, and using the cluster property and invoking the Lieb-Robinson bound, we have

$$\begin{aligned} \Gamma_{zx}(\ell, t; L) &\approx \langle \sigma^z_{\frac{L}{2}}(t)\sigma^x_{\frac{L}{2}-\ell}\sigma^z_{\frac{L}{2}}(t)\sigma^x_{\frac{L}{2}-\ell}\rangle\langle \sigma^z_{L-\ell}(t)\sigma^x_0\sigma^z_{L-\ell}(t)\sigma^x_0\rangle \\ &= F_{zx}(\ell, t)F_{zx}(-\ell, t) = F^2_{zx}(\ell, t) \; . \end{aligned} \tag{4.18}$$

In the last line, we have used translational invariance and the mirror symmetry which gives $F_{zx}(-\ell, t) = F_{zx}(\ell, t)$. We can now express $\Gamma_{zx}(\ell, t; L)$ in terms of the JW fermions evolving under fixed free-fermion Hamiltonians and reduce the calculations to Pfaffians as detailed in Appendix D.

Figure 4.11 shows $C_{zx}(\ell, t)$ at $g = 1.0$, $\beta = 0$, calculated using system size $L = 512$. After the wavefront passes, $C_{zx}(\ell, t)$ approaches a nonzero value in the long-time limit. In fact, Re$F_{zx}(\ell, t)$ approaches a negative value. We identify this behavior as some "partial scrambling," since ReF_{zx} does not approach 1 ("absence of scrambling") or 0 ("total scrambling").

Early-time behavior of $C_{zx}(\ell, t)$

The short-time behavior of $C_{zx}(\ell, t)$ before the wavefront reaches is again described by the "universal" power law with position-dependent exponent. In this case with $W = \sigma^x_0$ and $V = \sigma^z_\ell$, the smallest n such that $[L^n(W), V] \neq 0$ is $n = 2\ell$, and the corresponding term in $L^n[W]$ is $-J^{2\ell}g^\ell\sigma^y_0\sigma^x_1 \dots \sigma^x_{\ell-1}\sigma^y_\ell$. We thus have the leading behavior

$$C_{zx}(\ell, t) \approx \frac{2(Jt)^{4\ell}g^{2\ell}}{[(2\ell)!]^2} \; . \tag{4.19}$$

In Fig. 4.12, we compare the exact numerical results with this leading-order prediction at short time and find good agreement.

Behavior of $C_{zx}(\ell, t)$ around the wavefront

Here we also investigate the behavior of $C_{zx}(\ell, t)$ around the wavefront. We study the derivative function

$$G_{zx}(\ell, t) \equiv \frac{\partial \ln C_{zx}(\ell, t)}{\partial t} \; ; \tag{4.20}$$

the details of the calculation are presented in Appendix D. Figure 4.13 shows the results around the wavefront defined by $c = 1$. Similarly to our earlier findings for

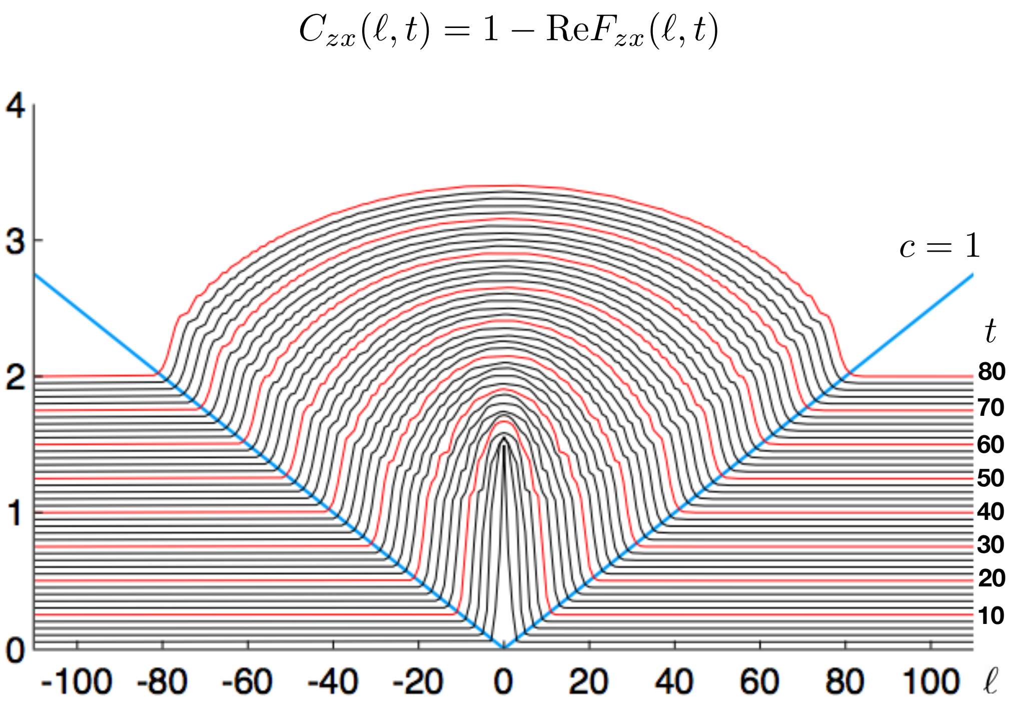

Figure 4.11: (color online) The function $C_{zx}(\ell, t)$ for the same critical Ising chain as in Figs. 4.1 and 4.6. The traces at fixed t are shifted by $0.025t$ in the y-direction for 3D-like visualization; every t that is a multiple of 10 is marked with red color for easier tracing. We can readily indentify the light cone and the corresponding velocity $c = 1$. In the timelike region, $C_{zx}(\ell, t)$ approaches a nonzero value larger than 1 in the long-time limit, i.e., $F_{zx}(\ell, t)$ approaches a negative value.

$G_{xx}(\ell, t)$ and $G_{zz}(\ell, t)$, we see that $G_{zx}(\ell, t)$ has strong ℓ dependence but essentially no β dependence. Again, we do not seem to have a parametrically large window around the wavefront that can be sharply separated from the short-time and long-time behaviors, and we definitely do not have any temperature-dependent asymptotic functional description.

Long-time behavior of $C_{zx}(\ell, t)$

Figure 4.14 shows the long-time behavior of the OTOC $F_{zx}(\ell, t)$. We can see that F_{zx} approaches some nonzero value. Unlike our results for F_{xx} or F_{zz}, the approach of the F_{zx} to the limiting value has a very strong ℓ dependence, and we have not been able to identify a "universal" long-time description of this behavior. Furthermore, the limiting value of $F_{zx}(\ell, t)$ when $t \to \infty$ appears to have strong β dependence,

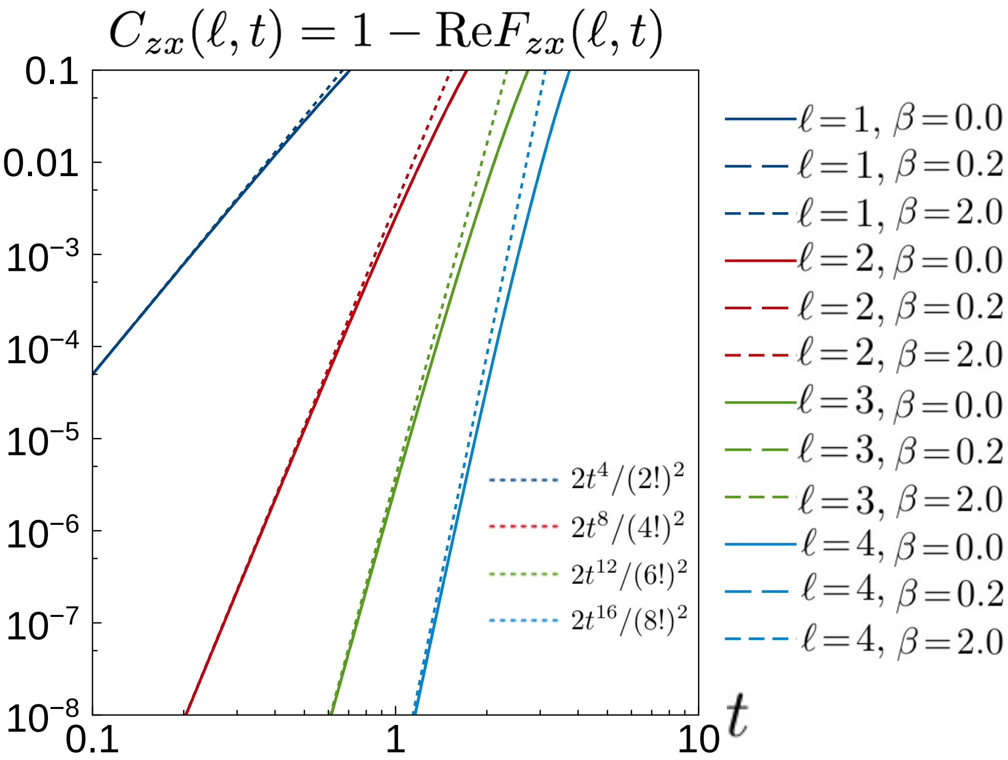

Figure 4.12: (color online) The short-time behavior of $C_{zx}(\ell,t)$ for several separations ℓ and different inverse temperatures β; the system is the same as in Fig. 4.11. The early-time growth of $C_{zx}(\ell,t)$ is well described by the "universal" power law $\approx 2t^{4\ell}/[(2\ell)!]^2$.

contributing to our difficulty of finding universal description.

4.5 Discussions of the results in the quantum Ising model

In this paper, we studied the behavior of the OTOC in the integrable quantum Ising model. We focused on three different OTOCs, which are representative of different combinations of two different types of operators in terms of the JW fermions. In all cases, we can clearly identify the light cone velocity, which is given by the maximum group velocity of the quasiparticles. We also argued that before the wavefront reaches, the OTOCs have "universal" power-law growth with position-dependent power. This can be understood from the Hausdorff-Baker-Campbell expansion of the Heisenberg evolution of the operators. We expect that such early-time power-law growth should also hold in nonintegrable models, as long as one has bounded local Hilbert space and local Hamiltonian.

On the other hand, the long-time behaviors are different for the different OTOC

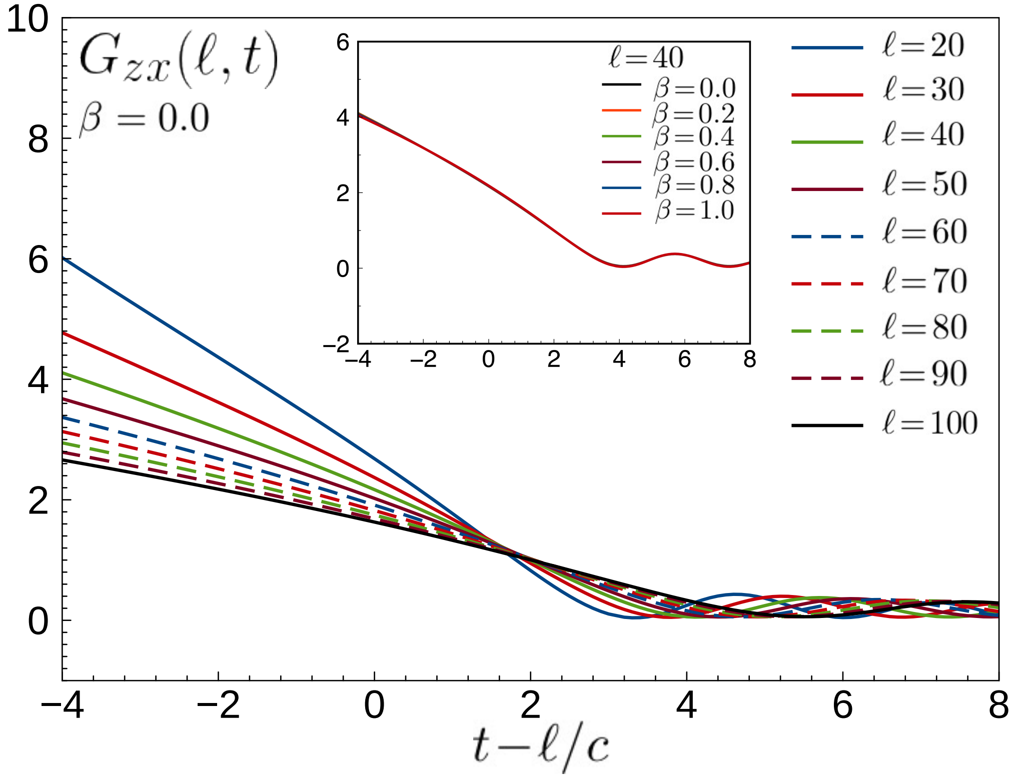

Figure 4.13: The derivative function $G_{zx}(\ell,t) \equiv \partial \ln C_{zx}(\ell,t)/\partial t$ around the wavefront. $G_{zx}(\ell,t)$ has very strong ℓ dependence and no apparent universal description. Inset: $G_{zx}(\ell,t)$ for fixed $\ell = 40$ and several inverse temperatures β; there is essentially no temperature dependence.

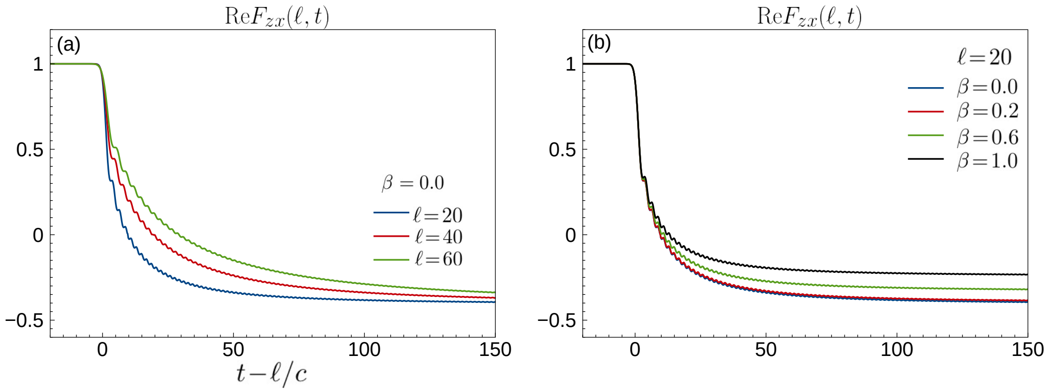

Figure 4.14: (color online) Long-time behavior of $\mathrm{Re}F_{zx}(\ell,t)$ after the wavefront passes. (a) For different separations ℓ at $\beta = 0$, the limiting value as $t \longrightarrow \infty$ appears to be the same, but the approach behavior has a strong ℓ dependence becoming more slow for larger ℓ. (b) For different inverse temperatures β at fixed $\ell = 20$, we see that both the limiting value and the approach behavior have significant temperature dependence.

types. The first type is represented by $C_{xx}(\ell, t)$, which involves only operators that are local in terms of the JW fermions. The OTOC can be calculated using a finite number of Wick contractions in the fermionic language. The limiting value of $C_{xx}(\ell, t)$ is zero when $t \to \infty$, which is a hallmark of absence of information scrambling. The approach is given by t^{-1} power-law at long time, which can be understood from the stationary phase approximation for the fermion correlation function. This power law persists at any temperature and also at any parameter g of the Ising model. We expect that OTOCs composed of operators that are local in JW fermions will have similar behavior.

The second type is represented by $C_{zz}(\ell, t)$, which involves only operators that are nonlocal in terms of the JW fermions (these operators contain "string" operator when fermionizing the spin model). Due to this nonlocal character, the OTOC calculation involves $O(L)$ Wick contractions. In the long-time limit, $F_{zz}(\ell, t)$ approaches zero [$C_{zz}(\ell, t)$ approaches 1], which is a signature of scrambling. Interestingly, the approach is a very slow power-law $t^{-1/4}$. While we can tentatively identify the frequency of oscillations that are present in the long-time behavior as coming from the stationary phase approximation, it is not clear how the $t^{-1/4}$ arises.

The aforementioned $t^{-1/4}$ behavior of $F_{zz}(\ell, t)$ is found at $g = 1$ and any β. One immediate question is whether this behavior depends on g. We performed such studies, although the results are not easy to interpret with available system sizes. For $g > 1$, $F_{zz}(\ell, t)$ appears to approach zero with a faster decay than $t^{-1/4}$. We observe oscillations with multiple frequencies, which makes it difficult to identify the precise power-law decay. On the other hand, for $g < 1$, the decay has both oscillating and nonoscillating components, which makes the identification of the long-time behavior even more difficult, but the decay appears to be also faster than $t^{-1/4}$. Thus, for both $g > 1$ and $g < 1$ we seem to find power-law decay faster than for the "critical" coupling $g = 1$. At present, we do not understand the origin of this qualitative difference, which persists all the way to infinite temperature. We can only speculate that the full many-body spectrum of the $g = 1$ Ising chain has something special about it compared to $g \neq 1$, even though the thermodynamic phase transition occurs only at zero temperature.

The last type of the OTOC behavior is represented by $C_{zx}(\ell, t)$ and involves both local and nonlocal operators in terms of the JW fermions. However, the long-time behavior of $C_{zx}(\ell, t)$ has a very strong ℓ dependence, while the limiting value also has a β dependence. Because of this, we have not been able to find a "universal"

(ℓ-independent) description for $C_{zx}(\ell, t)$ in the long-time limit.

For each of the three types of OTOCs, we tried to study the behavior around the wavefront by considering the time derivative of the logarithm of the corresponding $C_{\mu\nu}(\ell, t)$ function. In all cases, we found a strong ℓ dependence and very weak β dependence. Incidentally, such derivative $G_{zz}(\ell, t)$ can be well described by a linear function around the wavefront, but we do not know if there is some significance to this. However, we cannot find any parametrically large time window that would enable the exponential-growth description of the wavefront, and we can confidently exclude possibility of any temperature-dependent asymptotic description.

We conclude with some open questions and future directions. The main unresolved issue in the present paper is finding better physical understanding of the long-time behavior of the $C_{zz}(\ell, t)$ commutator function. Recent studies [32] argued that OTOCs in random quantum circuit models with a conserved charge have a power-law approach in the long-time limit due to a diffusive charge spreading. Our quantum Ising chain, besides the global Z_2 symmetry, is also integrable and has many integrals of motion, and it would be interesting to understand if there is a more direct relation between the long-time OTOC behaviors and the integrals of motion. We would also like to study OTOCs in other spin models that map to free fermions, in particular, with $U(1)$ global symmetry [59]. More generally, we would like to understand OTOCs in other integrable models that do not map to free fermions, and also effects of weak integrability breaking. Another interesting direction is to study integrable models with long-range interactions. The model in this paper is short-ranged and does not show any Lyapunov growth behavior near the wavefront. There appears to be mounting evidence that even nonintegrable models but with local interactions and bounded on-site Hilbert spaces do not have a precisely-defined exponential Lyapunov growth regime near the wavefront. A very recent study [51] proposed that such an exponential growth behavior can be found in nonintegrable models with long-range interactions. It would be interesting to explore if integrable models with long-range couplings may also exhibit the exponential growth regime.

Appendix A: Majorana two-point functions and partition sum of the spin model

Before we proceed, we remind the reader that in this appendix and in Appendices B, C, and D, the time-dependent operators are understood as evolved under the corresponding free-fermion Hamiltonians $H_{\mathrm{NS/R}}$ as explained in the main text after Eq. (4.7) and determined by the label of the ensemble used, $\langle \dots \rangle_{\mathrm{NS/R}}$.

We now list the Majorana two-point correlation functions, which are ingredients in the applications of the Wick's theorem:

$$\begin{aligned}
\langle A_m(t)A_n\rangle_{\mathrm{NS/R}} &= \frac{1}{L}\sum_{k\in K_{\mathrm{NS/R}}} e^{-ik(m-n)} \\
&\quad \left[\cos(\epsilon_k t) - i\sin(\epsilon_k t)\tanh\left(\frac{\beta\epsilon_k}{2}\right)\right], \\
\langle A_m(t)B_n\rangle_{\mathrm{NS/R}} &= \frac{1}{L}\sum_{k\in K_{\mathrm{NS/R}}} e^{-ik(m-n)}e^{-i\theta_k} \\
&\quad \left[\cos(\epsilon_k t)\tanh\left(\frac{\beta\epsilon_k}{2}\right) - i\sin(\epsilon_k t)\right], \\
\langle B_m(t)A_n\rangle_{\mathrm{NS/R}} &= \frac{-1}{L}\sum_{k\in K_{\mathrm{NS/R}}} e^{-ik(m-n)}e^{i\theta_k} \\
&\quad \left[\cos(\epsilon_k t)\tanh\left(\frac{\beta\epsilon_k}{2}\right) - i\sin(\epsilon_k t)\right], \\
\langle B_m(t)B_n\rangle_{\mathrm{NS/R}} &= \frac{-1}{L}\sum_{k\in K_{\mathrm{NS/R}}} e^{-ik(m-n)} \\
&\quad \left[\cos(\epsilon_k t) - i\sin(\epsilon_k t)\tanh\left(\frac{\beta\epsilon_k}{2}\right)\right].
\end{aligned}$$

The equal-time correlations are thus $\langle A_m A_n\rangle_{\mathrm{NS/R}} = -\langle B_m B_n\rangle_{\mathrm{NS/R}} = \delta_{mn}$, $\langle A_m B_n\rangle_{\mathrm{NS/R}} = \frac{1}{L}\sum_{k\in K_{\mathrm{NS/R}}} e^{-ik(m-n)}e^{-i\theta_k}\tanh(\beta\epsilon_k/2)$, and $\langle B_m A_n\rangle_{\mathrm{NS/R}} = -\langle A_n B_m\rangle_{\mathrm{NS/R}}$.

We define matrices $[\mathtt{AA}_{\mathrm{NS/R}}](t)$ with matrix elements $[\mathtt{AA}_{\mathrm{NS/R}}]^m_n(t) \equiv \langle A_m(t)A_n\rangle_{\mathrm{NS/R}}$ and analogously for $[\mathtt{AB}_{\mathrm{NS/R}}]^m_n(t)$, $[\mathtt{BA}_{\mathrm{NS/R}}]^m_n(t)$ and $[\mathtt{BB}_{\mathrm{NS/R}}]^m_n(t)$. We also use $[\mathtt{I}]$ and $[\mathtt{0}]$ to denote identity and zero matrices. For simplicity, the equal-time correlators are denoted by omitting the time argument. We also use $[\mathtt{AA}_{\mathrm{NS/R}}]^{m=i:j}_{n=k:l}(t)$ to represent the submatrix of $[\mathtt{AA}_{\mathrm{NS/R}}](t)$ with row index from i to j and column index from k to l. We will frequently omit NS/R in $[\mathtt{AA}_{\mathrm{NS/R}}](t)$ and other matrices since it will be clear from the context which matrix is used.

As we mentioned in the main text, the calculation of the partition function Z of the spin model is less straightforward as it involves the projectors. Specifically, we have

$$Z = \mathrm{Tr}(e^{-\beta H_{\mathrm{NS}}}P_+) + \mathrm{Tr}(e^{-\beta H_{\mathrm{R}}}P_-)\,, \tag{4.21}$$

where $P_\pm = [1 \pm (-1)^{N_{\mathrm{tot}}}]/2$. We therefore have

$$Z = Z_{\mathrm{NS}}\frac{1+\langle(-1)^{N_{\mathrm{tot}}}\rangle_{\mathrm{NS}}}{2} + Z_{\mathrm{R}}\frac{1-\langle(-1)^{N_{\mathrm{tot}}}\rangle_{\mathrm{R}}}{2}\,. \tag{4.22}$$

In the Majorana fermion language,

$$(-1)^{N_{\text{tot}}} = (-1)^{L(L-1)/2} \prod_{j=0}^{L-1} A_j \prod_{j=0}^{L-1} B_j \ . \tag{4.23}$$

Defining $D_{\text{NS/R}} = [\texttt{AB}_{\text{NS/R}}]_{n=0:L-1}^{m=0:L-1}$ and

$$F_{\text{NS/R}} = \begin{pmatrix} 0 & D_{\text{NS/R}} \\ -D_{\text{NS/R}}^{\text{T}} & 0 \end{pmatrix} , \tag{4.24}$$

we have by Wick's theorem (recalling that equal-time contractions $\langle A_m A_n \rangle_{\text{NS/R}}$ and $\langle B_m B_n \rangle_{\text{NS/R}}$ vanish for $m \neq n$):

$$\begin{aligned} \langle (-1)^{N_{\text{tot}}} \rangle_{\text{NS/R}} &= (-1)^{L(L-1)/2} \text{Pf}(F_{\text{NS/R}}) \\ &= \det(D_{\text{NS/R}}) \ . \end{aligned} \tag{4.25}$$

Appendix B: Pfaffian calculation of $F_{xx}(\ell, t)$

In this appendix, we present details of the calculation of $F_{xx}(\ell, t)$ for the spin chain with periodic boundary conditions using the Pfaffian method. We define 2 × 2 matrices

$$\begin{aligned} R_{\text{NS/R}}^{xx} &= \begin{pmatrix} 0 & [\texttt{AB}]_0^0 \\ -[\texttt{AB}]_0^0 & 0 \end{pmatrix} , \\ S_{\text{NS/R}}^{xx} &= \begin{pmatrix} [\texttt{AA}]_0^\ell(t) & [\texttt{AB}]_0^\ell(t) \\ [\texttt{BA}]_0^\ell(t) & [\texttt{BB}]_0^\ell(t) \end{pmatrix} , \\ U_{\text{NS/R}}^{xx} &= \begin{pmatrix} [\texttt{AA}]_\ell^0(-t) & [\texttt{BA}]_\ell^0(-t) \\ [\texttt{AB}]_\ell^0(-t) & [\texttt{BB}]_\ell^0(-t) \end{pmatrix} , \\ J^{xx} &= \begin{pmatrix} 1 & 0 \\ 0 & -1 \end{pmatrix} ; \end{aligned}$$

4 × 4 matrices

$$\begin{aligned} M_{\text{NS/R}}^{xx} &= \begin{pmatrix} R_{\text{NS/R}}^{xx} & S_{\text{NS/R}}^{xx} \\ -(S_{\text{NS/R}}^{xx})^{\text{T}} & R_{\text{NS/R}}^{xx} \end{pmatrix} , \\ N_{\text{NS/R}}^{xx} &= \begin{pmatrix} J^{xx} + R_{\text{NS/R}}^{xx} & S_{\text{NS/R}}^{xx} \\ (U_{\text{NS/R}}^{xx})^{\text{T}} & J^{xx} + R_{\text{NS/R}}^{xx} \end{pmatrix} ; \end{aligned}$$

8 × 8 matrix

$$\Phi_{\text{NS/R}}^{xx} = \begin{pmatrix} M_{\text{NS/R}}^{xx} & N_{\text{NS/R}}^{xx} \\ -(N_{\text{NS/R}}^{xx})^{\text{T}} & M_{\text{NS/R}}^{xx} \end{pmatrix} ;$$

and $4 \times 2L$ matrix

$$Q^{xx}_{\mathrm{NS/R}} = \begin{pmatrix} \mathtt{[AA]}^{\ell}_{n=0:L-1}(t) & \mathtt{[AB]}^{\ell}_{n=0:L-1}(t) \\ \mathtt{[BA]}^{\ell}_{n=0:L-1}(t) & \mathtt{[BB]}^{\ell}_{n=0:L-1}(t) \\ \mathtt{[I]}^{0}_{n=0:L-1} & \mathtt{[0]}^{0}_{n=0:L-1} \\ \mathtt{[0]}^{0}_{n=0:L-1} & -\mathtt{[I]}^{0}_{n=0:L-1} \end{pmatrix} .$$

Applying Wick's theorem, we have

$$\begin{aligned} &\langle \sigma^x_\ell(t)\sigma^x_0\sigma^x_\ell(t)\sigma^x_0\rangle_{\mathrm{NS/R}} = \mathrm{Pf}(\Phi^{xx}_{\mathrm{NS/R}}) , \\ &\langle \sigma^x_\ell(t)\sigma^x_0\sigma^x_\ell(t)\sigma^x_0(-1)^{N_{\mathrm{tot}}}\rangle_{\mathrm{NS/R}} \\ &= (-1)^{\frac{L(L-1)}{2}} \mathrm{Pf}\begin{pmatrix} M^{xx}_{\mathrm{NS/R}} & N^{xx}_{\mathrm{NS/R}} & Q^{xx}_{\mathrm{NS/R}} \\ -(N^{xx}_{\mathrm{NS/R}})^{\mathrm{T}} & M^{xx}_{\mathrm{NS/R}} & Q^{xx}_{\mathrm{NS/R}} \\ -(Q^{xx}_{\mathrm{NS/R}})^{\mathrm{T}} & -(Q^{xx}_{\mathrm{NS/R}})^{\mathrm{T}} & F_{\mathrm{NS/R}} \end{pmatrix} . \end{aligned}$$

In the thermodynamic limit, we expect $\langle \sigma^x_\ell(t)\sigma^x_0\sigma^x_\ell(t)\sigma^x_0\rangle = \langle \sigma^x_\ell(t)\sigma^x_0\sigma^x_\ell(t)\sigma^x_0\rangle_{\mathrm{NS/R}}$.

To obtain a compact analytical result, we focus on $\langle \sigma^x_\ell(t)\sigma^x_0\sigma^x_\ell(t)\sigma^x_0\rangle_{\mathrm{NS}}$. The Pfaffian can be simplified as follows (we omit the labels "xx" and "NS" for brevity):

$$\begin{aligned} &\mathrm{Pf}\begin{pmatrix} R & S & J+R & S \\ -S^{\mathrm{T}} & R & U^{\mathrm{T}} & J+R \\ -J+R & -U & R & S \\ -S^{\mathrm{T}} & -J+R & -S^{\mathrm{T}} & R \end{pmatrix} \\ &= \mathrm{Pf}\begin{pmatrix} R & S & J+R & 0 \\ -S^{\mathrm{T}} & R & U^{\mathrm{T}} & J \\ -J+R & -U & R & S+U \\ 0 & -J & -(S^{\mathrm{T}}+U^{\mathrm{T}}) & 0 \end{pmatrix} \\ &= \mathrm{Pf}\begin{pmatrix} R & S & J & 0 \\ -S^{\mathrm{T}} & R & S^{\mathrm{T}}+U^{\mathrm{T}} & J \\ -J & -(S+U) & 0 & S+U \\ 0 & -J & -(S^{\mathrm{T}}+U^{\mathrm{T}}) & 0 \end{pmatrix} \\ &= \mathrm{Pf}\begin{pmatrix} R & S & J & 0 \\ -S^{\mathrm{T}} & R & 0 & J \\ -J & 0 & 0 & S+U \\ 0 & -J & -(S^{\mathrm{T}}+U^{\mathrm{T}}) & 0 \end{pmatrix} . \end{aligned}$$

The matrix $S + U$ is

$$S + U = 2\begin{pmatrix} \mathrm{Re}\langle A_\ell(t)A_0\rangle & i\,\mathrm{Im}\langle A_\ell(t)B_0\rangle \\ i\,\mathrm{Im}\langle B_\ell(t)A_0\rangle & \mathrm{Re}\langle B_\ell(t)B_0\rangle \end{pmatrix} ,$$

and we therefore obtain

$$
\begin{aligned}
F_{xx}(\ell,t) &= 1 + 2i\,\langle B_\ell(t)A_0\rangle\,\mathrm{Im}\langle B_\ell(t)A_0\rangle\\
&+ 2i\,\langle A_\ell(t)B_0\rangle\,\mathrm{Im}\langle A_\ell(t)B_0\rangle\\
&- 2\langle A_\ell(t)A_0\rangle\,\mathrm{Re}\langle A_\ell(t)A_0\rangle\\
&- 2\langle B_\ell(t)B_0\rangle\,\mathrm{Re}\langle B_\ell(t)B_0\rangle\\
&- 4\langle A_0B_0\rangle^2\,\mathrm{Re}\langle A_\ell(t)A_0\rangle\,\mathrm{Re}\langle B_\ell(t)B_0\rangle\\
&+ 4\langle A_\ell(t)A_0\rangle\,\langle B_\ell(t)B_0\rangle\,\mathrm{Im}\langle A_\ell(t)B_0\rangle\,\mathrm{Im}\langle B_\ell(t)A_0\rangle\\
&+ 4\langle A_\ell(t)A_0\rangle\,\langle B_\ell(t)B_0\rangle\,\mathrm{Re}\langle A_\ell(t)A_0\rangle\,\mathrm{Re}\langle B_\ell(t)B_0\rangle\\
&- 4\langle A_\ell(t)B_0\rangle\,\langle B_\ell(t)A_0\rangle\,\mathrm{Im}\langle A_\ell(t)B_0\rangle\,\mathrm{Im}\langle B_\ell(t)A_0\rangle\\
&- 4\langle A_\ell(t)B_0\rangle\,\langle B_\ell(t)A_0\rangle\,\mathrm{Re}\langle A_\ell(t)A_0\rangle\,\mathrm{Re}\langle B_\ell(t)B_0\rangle\ .
\end{aligned}
$$

We can identify the leading behavior as

$$
\begin{aligned}
\mathrm{Re}F_{xx}(\ell,t) &\sim 1 - 2\left[(\mathrm{Im}\langle B_\ell(t)A_0\rangle)^2 + (\mathrm{Im}\langle A_\ell(t)B_0\rangle)^2\right.\\
&\qquad \left.+(\mathrm{Re}\langle A_\ell(t)A_0\rangle)^2 + (\mathrm{Re}\langle B_\ell(t)B_0\rangle)^2\right]\\
&- 4\langle A_0B_0\rangle^2\,[\mathrm{Im}\langle A_\ell(t)B_0\rangle\,\mathrm{Im}\langle B_\ell(t)A_0\rangle\\
&\qquad +\mathrm{Re}\langle A_\ell(t)A_0\rangle\,\mathrm{Re}\langle B_\ell(t)B_0\rangle]\ .
\end{aligned}
\tag{4.26}
$$

If we follow the ray $\ell/t = v$, where $|v| < c$, in the long-time limit, we can use the stationary phase approximation and obtain

$$
\begin{aligned}
\mathrm{Re}\langle A_\ell(t)A_0\rangle &\sim \sqrt{\frac{1}{2\pi\epsilon''_{k_0}t}}\cos\left(\omega_0 t - \frac{\pi}{4}\right)\ ,\\
\mathrm{Re}\langle B_\ell(t)B_0\rangle &\sim -\sqrt{\frac{1}{2\pi\epsilon''_{k_0}t}}\cos\left(\omega_0 t - \frac{\pi}{4}\right)\ ,\\
\mathrm{Im}\langle A_\ell(t)B_0\rangle &\sim -\sqrt{\frac{1}{2\pi\epsilon''_{k_0}t}}\sin\left(\omega_0 t - \theta_{k_0} - \frac{\pi}{4}\right)\ ,\\
\mathrm{Im}\langle B_\ell(t)A_0\rangle &\sim \sqrt{\frac{1}{2\pi\epsilon''_{k_0}t}}\sin\left(\omega_0 t + \theta_{k_0} - \frac{\pi}{4}\right)\ .
\end{aligned}
$$

Here k_0 is the wavevector satisfying $d\epsilon_k/dk|_{k_0} = v$, and $\omega_0 \equiv \epsilon_{k_0} - k_0 v$ is the frequency. In particular, if we fix ℓ and consider long-time limit, this effectively corresponds to $v = 0$ and gives $k_0 = \pi$ and $\theta_\pi = 0$. In this case we find that the limiting behavior of $\mathrm{Re}F_{xx}(\ell, t)$ is t^{-1} decay without oscillation, and we obtain Eq. (4.13) quoted in the main text.

To calculate $G_{xx}(\ell, t) \equiv \frac{\partial \ln C_{xx}(\ell,t)}{\partial t}$, we use

$$G_{xx}(\ell, t) = \frac{-1}{1 - \mathrm{RePf}[\Phi^{xx}_{\mathrm{NS}}]} \mathrm{Re}\left(\frac{d\mathrm{Pf}[\Phi^{xx}_{\mathrm{NS}}]}{dt} \right) , \tag{4.27}$$

where the derivative of the Pfaffian can be calculated as

$$\frac{d\mathrm{Pf}[\Phi^{xx}_{\mathrm{NS}}]}{dt} = \frac{1}{2}\mathrm{Pf}[\Phi^{xx}_{\mathrm{NS}}]\, \mathrm{Tr}\left[(\Phi^{xx}_{\mathrm{NS}})^{-1} \frac{d\Phi^{xx}_{\mathrm{NS}}}{dt} \right] . \tag{4.28}$$

The difference between results obtained using “NS” and “R” boundary conditions is very small for large enough systems.

Appendix C: Pfaffian calculation of $F_{zz}(\ell, t)$

Here we present details of the calculation of $F_{zz}(\ell, t)$. The “doubled” OTOC $\Gamma_{zz}(\ell, t; L)$, Eq. (4.14), can be written in terms of the JW fermions as

$$\begin{aligned} \Gamma_{zz}(\ell, t; L) \quad = \quad & \left\langle \left(\prod_{j=\frac{L}{2}}^{L-\ell-1} B_j(t) A_{j+1}(t) \right) \left(\prod_{j=0}^{\frac{L}{2}-\ell-1} B_j A_{j+1} \right) \right. \\ & \left. \left(\prod_{j=\frac{L}{2}}^{L-\ell-1} B_j(t) A_{j+1}(t) \right) \left(\prod_{j=0}^{\frac{L}{2}-\ell-1} B_j A_{j+1} \right) \right\rangle . \end{aligned}$$

We again need to calculate both “RS” and “N” pieces. We define $(L-2\ell)\times(L-2\ell)$ matrices

$$\begin{aligned} R^{zz}_{\mathrm{NS/R}} \quad &= \quad \begin{pmatrix} [0] & [\mathtt{AB}]^{m=1:\frac{L}{2}-\ell}_{n=0:\frac{L}{2}-\ell-1} \\ [\mathtt{BA}]^{m=0:\frac{L}{2}-\ell-1}_{n=1:\frac{L}{2}-\ell} & [0] \end{pmatrix} , \\ S^{zz}_{\mathrm{NS/R}} \quad &= \quad \begin{pmatrix} [\mathtt{AA}]^{m=\frac{L}{2}:L-\ell-1}_{n=0:\frac{L}{2}-\ell-1}(t) & [\mathtt{AB}]^{m=1+\frac{L}{2}:L-\ell}_{n=0:\frac{L}{2}-\ell-1}(t) \\ [\mathtt{BA}]^{m=\frac{L}{2}:L-\ell-1}_{n=1:\frac{L}{2}-\ell}(t) & [\mathtt{BB}]^{m=\frac{L}{2}:L-\ell-1}_{n=0:\frac{L}{2}-\ell-1}(t) \end{pmatrix} , \\ U^{zz}_{\mathrm{NS/R}} \quad &= \quad \begin{pmatrix} [\mathtt{AA}]^{m=\frac{L}{2}:L-\ell-1}_{n=0:\frac{L}{2}-\ell-1}(-t) & [\mathtt{BA}]^{m=1+\frac{L}{2}:L-\ell}_{n=0:\frac{L}{2}-\ell-1}(-t) \\ [\mathtt{AB}]^{m=\frac{L}{2}:L-\ell-1}_{n=1:\frac{L}{2}-\ell}(-t) & [\mathtt{BB}]^{m=\frac{L}{2}:L-\ell-1}_{n=0:\frac{L}{2}-\ell-1}(-t) \end{pmatrix} , \\ J^{zz} \quad &= \quad \begin{pmatrix} [\mathtt{I}] & [\mathtt{0}] \\ [\mathtt{0}] & -[\mathtt{I}] \end{pmatrix} , \end{aligned}$$

where $[\mathtt{I}]$ and $[\mathbb{0}]$ are $(\frac{L}{2}-\ell)\times(\frac{L}{2}-\ell)$ unit and zero matrices respectively. We then construct $2(L-2\ell)\times 2(L-2\ell)$ matrices

$$\begin{aligned} M^{zz}_{\text{NS/R}} &= \begin{pmatrix} R^{zz}_{\text{NS/R}} & S^{zz}_{\text{NS/R}} \\ -(S^{zz}_{\text{NS/R}})^{\text{T}} & R^{zz}_{\text{NS/R}} \end{pmatrix}, \\ N^{zz}_{\text{NS/R}} &= \begin{pmatrix} J^{zz}+R^{zz}_{\text{NS/R}} & S^{zz}_{\text{NS/R}} \\ (U^{zz}_{\text{NS/R}})^{\text{T}} & J^{zz}+R^{zz}_{\text{NS/R}} \end{pmatrix}, \end{aligned}$$

and $4(L-2\ell)\times 4(L-2\ell)$ matrix

$$\Phi^{zz}_{\text{NS/R}} = \begin{pmatrix} M^{zz}_{\text{NS/R}} & N^{zz}_{\text{NS/R}} \\ -(N^{zz}_{\text{NS/R}})^{\text{T}} & M^{zz}_{\text{NS/R}} \end{pmatrix}.$$

Finally, we also define $2(L-2\ell)\times 2L$ matrix

$$Q^{zz}_{\text{NS/R}} = \begin{pmatrix} [\mathtt{AA}]^{m=1+\frac{L}{2}:L-\ell}_{n=0:L-1}(t) & [\mathtt{AB}]^{m=1+\frac{L}{2}:L-\ell}_{n=0:L-1}(t) \\ [\mathtt{BA}]^{m=\frac{L}{2}:L-\ell-1}_{n=0:L-1}(t) & [\mathtt{BB}]^{m=\frac{L}{2}:L-\ell-1}_{n=0:L-1}(t) \\ [\mathtt{I}]^{m=0:\frac{L}{2}-\ell-1}_{n=0:L-1} & [\mathtt{AB}]^{m=1:\frac{L}{2}-\ell}_{n=0:L-1} \\ [\mathtt{BA}]^{m=0:\frac{L}{2}-\ell-1}_{n=0:L-1} & -[\mathtt{I}]^{m=0:\frac{L}{2}-\ell-1}_{n=0:L-1} \end{pmatrix}.$$

We can now compactly write the results of applying the Wick's theorem:

$$\begin{aligned} & \langle \sigma^z_{\frac{L}{2}}(t)\sigma^z_{L-\ell}(t)\sigma^z_0\sigma^z_{\frac{L}{2}-\ell}\sigma^z_{\frac{L}{2}}(t)\sigma^z_{L-\ell}(t)\sigma^z_0\sigma^z_{\frac{L}{2}-\ell}\rangle_{\text{NS/R}} \\ = \; & \text{Pf}(\Phi^{zz}_{\text{NS/R}}), \\ & \langle \sigma^z_{\frac{L}{2}}(t)\sigma^z_{L-\ell}(t)\sigma^z_0\sigma^z_{\frac{L}{2}-\ell}\sigma^z_{\frac{L}{2}}(t)\sigma^z_{L-\ell}(t)\sigma^z_0\sigma^z_{\frac{L}{2}-\ell}(-1)^{N_{\text{tot}}}\rangle_{\text{NS/R}} \\ = \; & (-1)^{\frac{L(L-1)}{2}}\text{Pf}\begin{pmatrix} M^{zz}_{\text{NS/R}} & N^{zz}_{\text{NS/R}} & Q^{zz}_{\text{NS/R}} \\ -(N^{zz}_{\text{NS/R}})^{\text{T}} & M^{zz}_{\text{NS/R}} & Q^{zz}_{\text{NS/R}} \\ -(Q^{zz}_{\text{NS/R}})^{\text{T}} & -(Q^{zz}_{\text{NS/R}})^{\text{T}} & F_{\text{NS/R}} \end{pmatrix}. \end{aligned}$$

We evaluate these numerically and combine to obtain the C_{zz} results for the spin system with periodic boundary conditions presented in the main text.

To calculate $G_{zz}(\ell,t)\equiv\frac{\partial \ln C_{zz}(\ell,t)}{\partial t}$, we use

$$G_{zz}(\ell,t) = \frac{\mp 1}{1\mp \text{Re}\sqrt{\text{Pf}[\Phi^{zz}_{\text{NS}}]}}\text{Re}\left(\frac{d\sqrt{\text{Pf}[\Phi^{zz}_{\text{NS}}]}}{dt}\right),$$

where the upper/lower sign corresponds to the upper/lower sign in $\text{Re}F_{zz} = \pm\text{Re}\sqrt{\text{Pf}[\Phi^{zz}_{\text{NS}}]}$ respectively (recall from the main text that we are calculating $\text{Pf}[\Phi^{zz}_{\text{NS}}] \approx F^2_{zz}$ and recover the sign when taking the square-root by continuity in parameters t and ℓ). We calculate the derivative of the Pfaffian in the standard way,

$$\frac{d\mathrm{Pf}[\Phi^{zz}_{\mathrm{NS}}]}{dt} = \frac{1}{2}\mathrm{Pf}[\Phi^{zz}_{\mathrm{NS}}]\,\mathrm{Tr}\left[(\Phi^{zz}_{\mathrm{NS}})^{-1}\frac{d\Phi^{zz}_{\mathrm{NS}}}{dt}\right] .$$

Again, there is essentially no difference between results from NS sector and from both sectors in the thermodynamic limit.

Appendix D: Pfaffian calculation of $F_{zx}(\ell,t)$

Here we present details of the calculation of $F_{zx}(\ell,t)$. The "doubled" OTOC $\Gamma_{zx}(\ell,t;L)$, Eq. (4.18), can be written in terms of the JW fermions as

$$\begin{aligned}\Gamma_{zx}(\ell,t;L) \;=\; & \left\langle\left(\prod_{j=L/2}^{L-\ell-1} B_j(t)A_{j+1}(t)\right)A_0A_{\frac{L}{2}-\ell}B_0B_{\frac{L}{2}-\ell}\right.\\ & \left.\left(\prod_{j=L/2}^{L-\ell-1} B_j(t)A_{j+1}(t)\right)A_0A_{\frac{L}{2}-\ell}B_0B_{\frac{L}{2}-\ell}\right\rangle .\end{aligned}$$

We define $(L-2\ell+4)\times(L-2\ell+4)$ matrices

$$M^{zx}_{\mathrm{NS/R}} = \begin{pmatrix} [\mathbb{0}] & \mathtt{[AB]}^{m=1:\frac{L}{2}-\ell}_{n=0:\frac{L}{2}-\ell-1} & \mathtt{[AA]}^{m=1+\frac{L}{2}:L-\ell}_{n=0}(t) & \mathtt{[AA]}^{m=1+\frac{L}{2}:L-\ell}_{n=\frac{L}{2}-\ell}(t) & \mathtt{[AB]}^{m=1+\frac{L}{2}:L-\ell}_{n=0}(t) & \mathtt{[AB]}^{m=1+\frac{L}{2}:L-\ell}_{n=\frac{L}{2}-\ell}(t) \\ \mathtt{[BA]}^{m=0:\frac{L}{2}-\ell-1}_{n=1:\frac{L}{2}-\ell} & [\mathbb{0}] & \mathtt{[BA]}^{m=\frac{L}{2}:L-\ell-1}_{n=0}(t) & \mathtt{[BA]}^{m=\frac{L}{2}:L-\ell-1}_{n=\frac{L}{2}-\ell}(t) & \mathtt{[BB]}^{m=\frac{L}{2}:L-\ell-1}_{n=0}(t) & \mathtt{[BB]}^{m=\frac{L}{2}:L-\ell-1}_{n=\frac{L}{2}-\ell}(t) \\ -\mathtt{[AA]}^{m=0}_{n=1+\frac{L}{2}:L-\ell}(t) & -\mathtt{[BA]}^{m=0}_{n=\frac{L}{2}:L-\ell-1}(t) & 0 & 0 & \mathtt{[AB]}^{m=0}_{n=0} & \mathtt{[AB]}^{m=0}_{n=\frac{L}{2}-\ell} \\ -\mathtt{[AA]}^{m=\frac{L}{2}-\ell}_{n=1+\frac{L}{2}:L-\ell}(t) & -\mathtt{[BA]}^{m=\frac{L}{2}-\ell}_{n=\frac{L}{2}:L-\ell-1}(t) & 0 & 0 & \mathtt{[AB]}^{m=\frac{L}{2}-\ell}_{n=0} & \mathtt{[AB]}^{m=0}_{n=0} \\ -\mathtt{[AB]}^{m=0}_{n=1+\frac{L}{2}:L-\ell}(t) & -\mathtt{[BB]}^{m=0}_{n=\frac{L}{2}:L-\ell-1}(t) & -\mathtt{[AB]}^{m=0}_{n=0} & -\mathtt{[AB]}^{m=\frac{L}{2}-\ell}_{n=0} & 0 & 0 \\ -\mathtt{[AB]}^{m=\frac{L}{2}-\ell}_{n=1+\frac{L}{2}:L-\ell}(t) & -\mathtt{[BB]}^{m=\frac{L}{2}-\ell}_{n=\frac{L}{2}:L-\ell-1}(t) & -\mathtt{[AB]}^{m=0}_{n=\frac{L}{2}-\ell} & -\mathtt{[AB]}^{m=0}_{n=0} & 0 & 0 \end{pmatrix},$$

$$N^{zx}_{\mathrm{NS/R}} = \begin{pmatrix} \mathtt{[I]} & \mathtt{[AB]}^{m=1:\frac{L}{2}-\ell}_{n=0:\frac{L}{2}-\ell-1} & \mathtt{[AA]}^{m=1+\frac{L}{2}:L-\ell}_{n=0}(t) & \mathtt{[AA]}^{m=1+\frac{L}{2}:L-\ell}_{n=\frac{L}{2}-\ell}(t) & \mathtt{[AB]}^{m=1+\frac{L}{2}:L-\ell}_{n=0}(t) & \mathtt{[AB]}^{m=1+\frac{L}{2}:L-\ell}_{n=\frac{L}{2}-\ell}(t) \\ \mathtt{[BA]}^{m=0:\frac{L}{2}-\ell-1}_{n=1:\frac{L}{2}-\ell} & -\mathtt{[I]} & \mathtt{[BA]}^{m=\frac{L}{2}:L-\ell-1}_{n=0}(t) & \mathtt{[BA]}^{m=\frac{L}{2}:L-\ell-1}_{n=\frac{L}{2}-\ell}(t) & \mathtt{[BB]}^{m=\frac{L}{2}:L-\ell-1}_{n=0}(t) & \mathtt{[BB]}^{m=\frac{L}{2}:L-\ell-1}_{n=\frac{L}{2}-\ell}(t) \\ \mathtt{[AA]}^{m=0}_{n=1+\frac{L}{2}:L-\ell}(-t) & \mathtt{[AB]}^{m=0}_{n=\frac{L}{2}:L-\ell-1}(-t) & 1 & 0 & \mathtt{[AB]}^{m=0}_{n=0} & \mathtt{[AB]}^{m=0}_{n=\frac{L}{2}-\ell} \\ \mathtt{[AA]}^{m=\frac{L}{2}-\ell}_{n=1+\frac{L}{2}:L-\ell}(-t) & \mathtt{[AB]}^{m=\frac{L}{2}-\ell}_{n=\frac{L}{2}:L-\ell-1}(-t) & 0 & 1 & \mathtt{[AB]}^{m=\frac{L}{2}-\ell}_{n=0} & \mathtt{[AB]}^{m=0}_{n=0} \\ \mathtt{[BA]}^{m=0}_{n=1+\frac{L}{2}:L-\ell}(-t) & \mathtt{[BB]}^{m=0}_{n=\frac{L}{2}:L-\ell-1}(-t) & \mathtt{[BA]}^{m=0}_{n=0} & \mathtt{[BA]}^{m=\frac{L}{2}-\ell}_{n=0} & -1 & 0 \\ \mathtt{[BA]}^{m=\frac{L}{2}-\ell}_{n=1+\frac{L}{2}:L-\ell}(-t) & \mathtt{[BB]}^{m=\frac{L}{2}-\ell}_{n=\frac{L}{2}:L-\ell-1}(-t) & \mathtt{[BA]}^{m=0}_{n=\frac{L}{2}-\ell} & \mathtt{[BA]}^{m=0}_{n=0} & 0 & -1 \end{pmatrix},$$

and combine these to form $2(L-2\ell+4)\times 2(L-2\ell+4)$ matrix

$$\Phi^{zx}_{\mathrm{NS/R}} = \begin{pmatrix} M^{zx}_{\mathrm{NS/R}} & N^{zx}_{\mathrm{NS/R}} \\ -(N^{zx}_{\mathrm{NS/R}})^{\mathrm{T}} & M^{zx}_{\mathrm{NS/R}} \end{pmatrix} ;$$

finally, we also define $(L-2\ell+4)\times 2L$ matrix

$$Q^{zx}_{\mathrm{NS/R}} \quad = \quad \begin{pmatrix} [\mathtt{AA}]^{m=1+\frac{L}{2}:L-\ell}_{n=0:L-1}(t) & [\mathtt{AB}]^{m=1+\frac{L}{2}:L-\ell}_{n=0:L-1}(t) \\ [\mathtt{BA}]^{m=\frac{L}{2}:L-\ell-1}_{n=0:L-1}(t) & [\mathtt{BB}]^{m=\frac{L}{2}:L-\ell-1}_{n=0:L-1}(t) \\ [\mathtt{I}]^{m=0}_{n=0:L-1} & [\mathtt{AB}]^{m=0}_{n=0:L-1} \\ [\mathtt{I}]^{m=\frac{L}{2}-\ell}_{n=0:L-1} & [\mathtt{AB}]^{m=\frac{L}{2}-\ell}_{n=0:L-1} \\ [\mathtt{BA}]^{m=0}_{n=0:L-1} & -[\mathtt{I}]^{m=0}_{n=0:L-1} \\ [\mathtt{BA}]^{m=\frac{L}{2}-\ell}_{n=0:L-1} & -[\mathtt{I}]^{m=\frac{L}{2}-\ell}_{n=0:L-1} \end{pmatrix} .$$

We can now write the result of applying the Wick's theorem to the calculation of Γ_{zx} as

$$\begin{aligned} &\langle \sigma^z_{\frac{L}{2}}(t)\sigma^z_{L-\ell}(t)\sigma^x_0\sigma^x_{\frac{L}{2}-\ell}\sigma^z_{\frac{L}{2}}(t)\sigma^z_{L-\ell}(t)\sigma^x_0\sigma^x_{\frac{L}{2}-\ell}\rangle_{\mathrm{NS/R}} \\ &= \mathrm{Pf}[\Phi^{zx}_{\mathrm{NS/R}}]\,, \\ &\langle \sigma^z_{\frac{L}{2}}(t)\sigma^z_{L-\ell}(t)\sigma^x_0\sigma^x_{\frac{L}{2}-\ell}\sigma^z_{\frac{L}{2}}(t)\sigma^z_{L-\ell}(t)\sigma^x_0\sigma^x_{\frac{L}{2}-\ell}(-1)^{N_{\mathrm{tot}}}\rangle_{\mathrm{NS/R}} \\ &= (-1)^{\frac{L(L-1)}{2}}\mathrm{Pf}\begin{pmatrix} M^{zx}_{\mathrm{NS/R}} & N^{zx}_{\mathrm{NS/R}} & Q^{zx}_{\mathrm{NS/R}} \\ -(N^{zx}_{\mathrm{NS/R}})^{\mathrm{T}} & M^{zx}_{\mathrm{NS/R}} & Q^{zx}_{\mathrm{NS/R}} \\ -(Q^{zx}_{\mathrm{NS/R}})^{\mathrm{T}} & -(Q^{zx}_{\mathrm{NS/R}})^{\mathrm{T}} & F_{\mathrm{NS/R}} \end{pmatrix} . \end{aligned}$$

To calculate $G_{zx}(\ell,t) \equiv \frac{\partial \ln C_{zx}(\ell,t)}{\partial t}$, we use

$$G_{zx}(\ell,t) = \frac{\mp 1}{1 \mp \mathrm{Re}\sqrt{\mathrm{Pf}[\Phi^{zx}_{\mathrm{NS}}]}}\mathrm{Re}\left(\frac{d\sqrt{\mathrm{Pf}[\Phi^{zx}_{\mathrm{NS}}]}}{dt}\right),$$

where the upper/lower signs correspond to the upper/lower sign in $\mathrm{Re}F_{zx} = \pm\mathrm{Re}\sqrt{\mathrm{Pf}[\Phi^{zx}_{\mathrm{NS}}]}$ respectively (the correct sign is determined using continuity considerations). The derivative of the Pfaffian can be calculated as $\frac{d\mathrm{Pf}[\Phi^{zx}_{\mathrm{NS}}]}{dt} = \frac{1}{2}\mathrm{Pf}[\Phi^{zx}_{\mathrm{NS}}]\mathrm{Tr}[(\Phi^{zx}_{\mathrm{NS}})^{-1}\frac{d\Phi^{zx}_{\mathrm{NS}}}{dt}]$.

Appendix E: Exact Heisenberg evolution of $\sigma^x(t)$

Following Ref. [58], we can obtain a compact expression for the Heisenberg evolution of $\sigma^x_j(t)$ under the quantum Ising Hamiltonian, Eq. (4.3), at the critical coupling $g = 1$. With this in hand, we can in fact gain more intuition about the commutator functions $C_{xx}(\ell,t)$ and $C_{zx}(\ell,t)$ at $\beta = 0$ from the operator spreading point of view. We define Majorana fermions $P_{2j} = (\prod_{j'=-\infty}^{j-1}\sigma^x_{j'})\sigma^z_j$ and $P_{2j+1} = -(\prod_{j'=-\infty}^{j-1}\sigma^x_{j'})\sigma^y_j$. (Note that these are simply related to the Majoranas in the main text and the previous appendices by $A_j = -P_{2j}$ and $B_j = iP_{2j+1}$; the convenience of P_n's is that the critical Ising model gives a Majorana chain that is invariant under translation by one Majorana, $n \longrightarrow n+1$.) We have [58]

$$\begin{aligned} P_n(t) &= \sum_k P_{n+k} J_{-k}(2t) = \sum_m P_m J_{n-m}(2t) \,, & (4.29) \\ \sigma_0^x(t) &= \sum_{m,m'} i P_m P_{m'} J_{-m+1}(2t) J_{-m'}(2t) \,, & (4.30) \end{aligned}$$

where J_n is the n-th order Bessel function of the first kind.

The summation is over all integers m and m' and this expression holds in an infinite system. We can reorganize the summation over m and m' into a summation over ordered pairs,

$$\sigma_0^x(t) = \sum_{m<m'} i P_m P_{m'} F_{m,m'}(2t) \,, \tag{4.31}$$

where

$$F_{m,m'}(2t) \equiv J_{-m+1}(2t) J_{-m'}(2t) - J_{-m'+1}(2t) J_{-m}(2t) \,. \tag{4.32}$$

Note that $F_{m,m'}(2t) = -F_{m',m}(2t)$ is antisymmetric. The summation terms in Eq. (4.30) with $m = m'$ give zero since

$$\sum_m J_{-m+1} J_{-m} = -\sum_m J_{m-1} J_m = -\sum_{\tilde{m}} J_{-\tilde{m}} J_{-\tilde{m}+1} = 0 \,,$$

where we first used the property $J_{-n} = (-1)^n J_n$ and then changed the summation variable.

Note that the operator $i P_m P_{m'}$ in terms of spin operators is basically a Pauli string of the form $\sigma^{y/z} \sigma^x \sigma^x \ldots \sigma^x \sigma^x \sigma^{y/z}$, i.e., with σ^x in the middle and σ^y or σ^z at the string ends depending on the parities of m and m'; the only exception is $i P_{2j} P_{2j+1} = -\sigma_j^x$. We can now easily see that the Heisenberg evolution of $\sigma_0^x(t)$ is composed of such Pauli-strings $i P_m P_{m'}$ with amplitudes $F_{m,m'}(2t)$. This already provides a rough idea of the "shape" of the commutator functions $C_{xx}(\ell, t)$ and $C_{zx}(\ell, t)$. Indeed, since σ_ℓ^x does not commute with $i P_m P_{m'}$ only when ℓ coincides with one of the ends of the string, we expect C_{xx} to have the "shell-like" structure [50] described in the main text. On the other hand, σ_ℓ^z does not commute with $i P_m P_{m'}$ when ℓ is anywhere inside the string, and this explains the "dome-like" structure of C_{zx}.

We can supplement these qualitative observations with precise calculations. The terms in the commutator $[\sigma_0^x(t), \sigma_\ell^x]$ are nonzero when the boundary of the string $i P_m P_{m'}$ hits site ℓ, which gives us $m = 2\ell$ or $m = 2\ell+1$ or $m' = 2\ell$ or $m' = 2\ell+1$, excluding the case $(m = 2\ell, m' = 2\ell + 1)$. The commutator function $C_{xx}(\ell, t)$ at infinite temperature is easily obtained as the Frobenius norm of $[\sigma_0^x(t), \sigma_\ell^x]$ (divided by 2). We therefore have

$$\begin{aligned} C_{xx}(\ell, t) \;&=\; 2\Bigg[\sum_{m'>2\ell+1} |F_{2\ell,m'}(2t)|^2 + \sum_{m'>2\ell+1} |F_{2\ell+1,m'}(2t)|^2 \\ &\qquad + \sum_{m<2\ell} |F_{m,2\ell}(2t)|^2 + \sum_{m<2\ell} |F_{m,2\ell+1}(2t)|^2\Bigg] . \end{aligned}$$

With such an expression in hand, we can reproduce the qualitative behavior $C_{xx}(\ell, t) \sim 1/t$ at long times inside the timelike region, $t \gg \ell/c$. Indeed, it is not difficult to see that

$$F_{m,m'}(2t) \approx \frac{1}{\pi t} \cos\left[\frac{\pi}{2}(m - m' - 1)\right] \;, \text{ for } |m|, |m'| \ll t \,, \tag{4.33}$$

while $F_{m,m'}(2t)$ decays quickly once $|m|$ or $|m'|$ exceeds number of order t. This means that the above expression for $C_{xx}(\ell, t)$ contains of order t terms of magnitude of order $1/t^2$, hence $C_{xx}(\ell, t) \sim 1/t$. A more sophisticated analysis is needed to obtain the amplitude as well as subleading terms, and the treatment in Appendix B provides an alternative derivation giving this data more directly (with the additional benefit of being easily applicable also at finite temperature). Nevertheless, we find the operator spreading analysis in the present appendix enlightening.

For the commutator function $C_{zx}(\ell, t)$, we can equivalently consider $[\sigma_0^x(t), \sigma_\ell^z]$. The nonzero contributions come from the $iP_m P_{m'}$ pieces of $\sigma_0^x(t)$ with $(m \le 2\ell, m' \ge 2\ell + 1)$. This gives us

$$C_{zx}(\ell, t) \;=\; 2 \sum_{m \le 2\ell, m' \ge 2\ell+1} |F_{m,m'}(2t)|^2 \,. \tag{4.34}$$

Using this expression, we can readily understand the finding in the main text that $C_{zx}(\ell, t)$ approaches a nonzero value at long times inside the timelike region, $t \gg \ell/c$. Indeed, from the behavior of $F_{m,m'}(2t)$ noted earlier, we can see that in the above sum there are of order t^2 terms of magnitude of order $1/t^2$, and hence the nonzero value of the sum in the long-time limit. Note that the "operator spreading" derivation here is much simpler than the formal Pfaffian derivation in Appendix D and gives us almost a closed-form expression for this commutator function at infinite temperature. On the other hand, the Pfaffian derivation has the advantage of working readily also at finite temperature.

Lastly, we can see different information "extracted" from the $\sigma^x(t)$ in other dynamical calculations discussed at the end of Sec. 4.2. For example, the dynamical correlation function at infinite temperature is simply [58]

$$\langle \sigma_0^x(t)\, \sigma_\ell^x \rangle = -F_{2\ell,2\ell+1}(2t) \approx \frac{1}{\pi t} \, . \tag{4.35}$$

We see that the origin of the specific long-time power law behavior in the dynamical correlation function and the OTOC is indeed very different from the operator spreading point of view.

4.6 Hard-core boson and Luttinger liquid models

Consider a Hamiltonian defined on lattice sites $i = -L/2+1, \ldots, L/2$, where we have assumed that the number of sites L is even for simplicity:

$$H = \sum_{i<j} J_{ij} \left[b_i^\dagger \left(e^{\mathrm{i}\pi \sum_{r=i+1}^{j-1} n_r} \right) b_j + \text{H.c.} \right] - \mu \sum_i n_i \, , \tag{4.36}$$

with open boundary conditions and real couplings J_{ij}; also, $n_i \equiv b_i^\dagger b_i$ is the boson number operator. The boson operators are hard-core bosons commuting on different sites. The choice of the Hamiltonian is such that under the JW transformation $b_j = (\prod_{r=-L/2+1}^{j-1} e^{\mathrm{i}\pi n_r}) c_j$, the Hamiltonian becomes

$$H = \sum_{i<j} J_{ij} \left(c_i^\dagger c_j + \text{H.c.} \right) - \mu \sum_i n_i \, . \tag{4.37}$$

The first model we consider is the "short-range hopping" model (various quantities defined and calculated in this model will be labeled by "I"), defined by

$$J_{ij}^{\mathrm{I}} = -\frac{v_B}{2} (\delta_{i=j-1} + \delta_{i=j+1}) \, . \tag{4.38}$$

The Hamiltonian can be diagonalized by the transformation

$$c_k = \sqrt{\frac{2}{L+1}} \sum_{j=-L/2+1}^{L/2} \sin(k\bar{j}) c_j \, , \tag{4.39}$$

where $\bar{j} \equiv j + L/2$ and $\{k = \frac{n\pi}{L+1}, \; n = 1, \ldots, L\}$. We obtain $H = \sum_k \epsilon^{\mathrm{I}}(k) c_k^\dagger c_k$, where the dispersion $\epsilon^{\mathrm{I}}(k) = -v_B \cos(k) - \mu$. The coupling is chosen such that the maximum group velocity $v_{\max} = \max|\partial \epsilon_k / \partial k| = v_B$. We choose $v_B = 1$ as our energy unit and throughout set $\hbar = 1$.

For the second model (with quantities labeled by "II,"), we artificially "straighten" the dispersion, making it as $\epsilon^{\mathrm{II}}(k) = J|k| - \mu$ for $k \in [-\pi, \pi]$. For general $k' \notin [-\pi, \pi]$, $\epsilon^{\mathrm{II}}(k') = \epsilon^{\mathrm{II}}(k)$ where $k = k' + 2\pi m$, with m some integer such that $k \in [-\pi, \pi]$. In real space, $J^{\mathrm{II}}_{ij} = \frac{2}{L+1}\sum_{k_n}(\epsilon^{\mathrm{II}}(k_n)+\mu)\sin(k_n\bar{i})\sin(k_n\bar{j})$. In the thermodynamic limit $L \longrightarrow \infty$, for points in the bulk, we have

$$J^{\mathrm{II}}_{ij} = \frac{v_B}{\pi}\frac{[(-1)^{|i-j|}-1]}{|i-j|^2} . \tag{4.40}$$

We will focus on the cases where μ is tuned such that the ground state is in the gapless phase (quasi-long-range ordered).

Finally, we will also compare the results to the Luttinger liquid model [60–62] (quantities labeled by "III"), defined as

$$H^{\mathrm{III}} = \frac{v_B}{2\pi}\int_0^L dx\left[g(\pi\hat{\Pi})^2 + \frac{1}{g}(\partial_x\hat{\theta})^2\right] , \tag{4.41}$$

where we set the characteristic velocity as v_B. As we will see later, this will indeed be the butterfly velocity. $\hat{\theta}(x)$ is related to the density operator defined as

$$n(x) = d_0 + \rho_0(x) + d_2 W(x) , \tag{4.42}$$

where $\rho_0(x) \equiv -\partial_x\hat{\theta}(x)/\pi$ and

$$W(x) \equiv e^{i2\pi d_0 x}V_{-2}(x) + e^{-i2\pi d_0 x}V_2(x) , \tag{4.43}$$

and $V_m(x) \equiv e^{im\hat{\theta}(x)}$ is the vertex operator, while $d_0 = k_F/\pi$ is the density of the system, and d_2 is some constant to be determined. $\hat{\Pi}(x)$ is the conjugate momentum to $\hat{\theta}(x)$, satisfying $[\hat{\Pi}(x), \hat{\theta}(x')] = -\mathrm{i}\,\delta(x-x')$. Since we are studying bosonic models, we will also consider the boson creation field

$$\psi^\dagger_B(x) \sim e^{\mathrm{i}\,\hat{\phi}(x)} , \tag{4.44}$$

where the field $\hat{\phi}(x)$ is the phase field defined by the relation $\hat{\Pi}(x) = -\partial_x\hat{\phi}/\pi$. To be concrete, here we use periodic boundary conditions, $\hat{\theta}(x+L) = \hat{\theta}(x)$. However, as most of our calculations will be taken in the thermodynamic limit, the choice of the boundary conditions will not matter.

The Luttinger liquid model can be diagonalized as follows. We define Fourier modes $\theta_k = \frac{1}{\sqrt{L}}\int_0^L dx e^{-ikx}\hat{\theta}(x)$ and $\Pi_k = \frac{1}{\sqrt{L}}\int_0^L dx e^{-ikx}\hat{\Pi}(x)$, and find $H^{\mathrm{III}} = \frac{v_B}{2\pi}\sum_k(\pi^2 g\Pi_{-k}\Pi_k + \frac{k^2}{g}\theta_{-k}\theta_k)$. We can identify $\omega_k = v_B|k|$ and $m = \frac{1}{\pi v_B g}$ as in a harmonic oscillator. We now define ladder operators $b_k = \sqrt{\frac{m\omega_k}{2}}(\theta_k + \frac{\mathrm{i}}{m\omega_k}\Pi_k)$ and $b^\dagger_k = \sqrt{\frac{m\omega_k}{2}}(\theta_{-k} - \frac{\mathrm{i}}{m\omega_k}\Pi_{-k})$, which satisfy canonical boson commutation relations $[b_k, b_{k'}] = 0$, $[b_k, b^\dagger_{k'}] = \delta_{k,k'}$. The Hamiltonian becomes $H^{\mathrm{III}} = \sum_k \omega_k(b^\dagger_k b_k + \frac{1}{2})$, and the fields $\hat{\theta}(x)$ and $\hat{\phi}(x)$ can be expressed as linear combinations of the eigenmode operators b_k and $b^\dagger_k$.

4.7 Hard-core boson and Luttinger liquid models: Density-density OTOC

We first consider the density-density OTOC $F_{nn}(\ell, t)$ [and the squared commutator $C_{nn}(\ell, t)$], where $n_i \equiv b_i^\dagger b_i$. The density-density OTOC in fact can be calculated analytically and relatively easily in the lattice models since the operators can be expressed using few JW fermion operators. Detailed calculations are presented in Appendix F for the lattice models and Appendix G for the Luttinger liquid model.

Density-density OTOC in the lattice models

In the lattice models, we find

$$C_{nn}(\ell, t) = |A(\ell, t)|^2 \Big([\langle n_\ell \rangle + \langle n_0 \rangle]/2 - \langle n_\ell \rangle \langle n_0 \rangle - \mathrm{Re}\left[\langle c_0^\dagger(t) c_\ell \rangle \langle c_0(t) c_\ell^\dagger \rangle \right] \Big) , \tag{4.45}$$

where

$$A(\ell, t) \equiv \int_{-\pi}^{\pi} \frac{dk}{2\pi} e^{\mathrm{i}\,(k\ell - \epsilon_k t)} \tag{4.46}$$

is a specific fermion evolution function [which appears, e.g., in the anti-commutator for the fermion fields, $\{c_0(t), c_\ell^\dagger\} = A(\ell, t)$]. At infinite temperature ($\beta = 0$), $C_{nn}(\ell, t) = \frac{1}{4}(|A(\ell, t)|^2 - |A(\ell, t)|^4)$.

For the short-range hopping model, $\epsilon_k^{\mathrm{I}} = -v_B \cos(k) - \mu$, we have

$$|A^{\mathrm{I}}(\ell, t)|^2 = J_\ell(v_B t)^2 , \tag{4.47}$$

where $J_n(t)$ is the Bessel function of order n and $v_B = v_{\max}$. We first consider behavior near the wavefront. Bessel functions have so-called "transition regions" when the order of the Bessel function and the argument are close [63], here $v_B t = \ell + O(t^{1/3})$, which corresponds precisely to the wavefront region of interest to us. In this region, we can write

$$C_{nn}^{\mathrm{I}}(\ell, t) \sim f\left[\frac{(\ell - v_B t)^{3/2}}{t^{1/2}} \right] . \tag{4.48}$$

More precisely, the asymptotic expansion for the Bessel functions needed here is taking $\ell, v_B t$ to be very large while keeping $|\ell - v_B t|/t^{1/3}$ fixed, and it can be found in Eq. (3.1) in Ref. [63]. In the regime $|\ell - v_B t|/t^{1/3} \gg 1$ this connects with the saddle-point analysis of Ref. [38], which gives

$$C_{nn}^{\mathrm{I}}(\ell, t) \sim \exp[-c \frac{(\ell - v_B t)^{3/2}}{t^{1/2}}] . \tag{4.49}$$

On the other hand, following the approach of Ref. [39], on the fixed-velocity rays $\ell(v) = vt$ with $v > v_B$ (i.e., outside the light cone), we find $C^{\mathrm{I}}_{nn}(\ell = vt, t) \sim \exp[-\lambda(v)t]$, where $\lambda \sim (v - v_B)^{3/2}$ for small $v - v_B$; the precise asymptotic for the Bessel functions needed here is the Debye's expansion [63] where we take $\ell, v_B t$ large while keeping $(\ell - v_B t)/t = v - v_B > 0$ fixed. According to Ref. [63], the transition region's asymptotic expansion is accurate for $\ell - v_B t \ll t^{2/3}$, while the Debye's expansion is accurate for $\ell - v_B t \gg t^{1/3}$, so there is an adequate overlap between the two and hence a smooth crossover from the wavefront region to the ray region. We remark that while we used the properties of the Bessel functions as appropriate for the specific dispersion $\epsilon(k) = -v_B \cos(k) - \mu$, the properties near the wavefront originate from behavior of $\epsilon(k)$ near the maximal group velocity, which is generic, and we expect qualitatively similar wavefront properties for any dispersion.

We also mention behavior at long times inside the light cone, $t \gg \ell/v_B$, which follows from the familiar long-time asymptotics of the Bessel functions: $C_{nn}(\ell, t)$ has oscillatory decay back to zero with envelope $\sim t^{-1}$. Again, the long-time behavior holds also for generetic dispersion, but here it is controlled by the extrema of $\epsilon(k)$ itself.

Turning to the long-range model, we have

$$|A^{\mathrm{II}}(\ell, t)|^2 = \frac{2}{\pi^2}\left[1 - (-1)^\ell \cos(\pi v_B t)\right] \frac{(v_B t)^2}{\left[\ell^2 - (v_B t)^2\right]^2} \,. \tag{4.50}$$

The commutator function $C_{nn}(\ell, t)$ grows as t^2 at short time, rises sharply at the wavefront, and then decays back to zero as t^{-2} inside the light cone. Moreover, the wavefront does not broaden with time. Indeed, consider $\ell = v_B t + \delta\ell$, where $\delta\ell \ll v_B t$ is the small deviation from the wavefront. In this region, we have $C^{\mathrm{II}}_{nn}(\ell, t) \sim \frac{(v_B t)^2}{(2v_B t + \delta\ell)^2(\delta\ell)^2} \sim (\delta\ell)^{-2}$, which is valid when $\delta\ell$ is $O(1)$ deviation. Comparing to the typical scaling form [38, 39] of the wavefront $C_{nn}(\ell, t) \sim f(\delta\ell/t^\alpha)$, we have $\alpha = 0$, which formally corresponds to the absence of the wavefront broadening. On the other hand, if we follow the rays $\ell = vt$, $v > v_B$, we have $C^{\mathrm{II}}_{nn}(\ell, t) \sim \frac{v_B^2}{(v^2 - v_B^2)^2 t^2}$, which decays as t^{-2} power law at long times. Therefore, we cannot define the velocity-dependent Lyapunov exponent here. This is not surprising, since the Lieb-Robinson bound does not necessarily hold in this model.

We now show that in the long-range model, outside the lightcone, the early-time (perturbative) region essentially extends to the "ray" region—more precisely, the regime where one follows rays $\ell = vt$ with $v \gg v_B$. Consider the long-range hopping model in terms of Pauli-matrices X, Y, and Z, i.e., mapping hard-core bosons spins, with $n = (1 + Z)/2$. Introducing short-hand notation $\bar{Z}_i = -Z_i$ and the string operator $\mathcal{Z}_{i,j} = \prod_{m=i}^{j} \bar{Z}_m$, we write

$$\begin{aligned} H^{\mathrm{II}} &= \frac{1}{2}\sum_{i<j} J_{ij}[X_i \mathcal{Z}_{i+1,j-1} X_j + Y_i \mathcal{Z}_{i+1,j-1} Y_j] \\ &- \frac{1}{2}\sum_{i} \mu(I_i + Z_i)\,. \end{aligned} \tag{4.51}$$

Consider the Baker-Campbell-Hausdorff expansion $W_0(t) = \sum_{n=0}^{\infty} \frac{(it)^n}{n!} L^n(W_0)$, where $L(W) \equiv [H, W]$. The power-law growth of the commutator function is determined by the lowest-order nonzero commutator $[L^n(W_0), V_\ell]$. Due to the long-range nature of the Hamiltonian H^{II}, already the first order $[L(n_0), n_\ell] = \frac{1}{4}[L(Z_0), Z_\ell]$ is nonzero. More specifically, we have

$$\begin{aligned} L(Z_0) &= \sum_{j>0} J_{0j} \mathcal{Z}_{1,j-1}(-iY_0 X_j + iX_0 Y_j) \\ &+ \sum_{j<0} J_{j0} \mathcal{Z}_{j+1,-1}(-iX_j Y_0 + iY_j X_0)\,, \end{aligned} \tag{4.52}$$

giving us (assuming $\ell > 0$ for concreteness)

$$[L(Z_0), Z_\ell] = -2J_{0,\ell} \mathcal{Z}_{1,\ell-1}(Y_0 Y_\ell + X_0 X_\ell)\,. \tag{4.53}$$

The leading contribution to the commutator function is thus

$$C_{nn}^{\mathrm{II}}(\ell, t) \approx \frac{t^2}{32}\langle |[L(Z_0), Z_\ell]|^2 \rangle = \frac{(v_B t)^2}{2\pi^2 \ell^4}[1 - (-1)^\ell]\,, \tag{4.54}$$

where in the last equation we specialized to infinite temperature for simplicity. For very short time $v_B t \ll 1$, this expression matches with the asymptotic behavior of the exact result, $C_{nn}(\ell, t) = \frac{1}{4}(|A(\ell, t)|^2 - |A(\ell, t)|^4) \approx \frac{1}{4}|A(\ell, t)|^2$ and using Eq. (4.50). In fact, we can also see that this asymptotic also extends "qualitatively" to the regime when we follow the rays $\ell = vt \gg 1$ but with $v \gg v_B$, giving us $C_{nn}^{\mathrm{II}}(\ell = vt, t) \sim v_B^2/(2\pi^2 v^4 t^2)$ (here "qualitatively" means ignoring oscillations in time, which of course such Hausdorff-Campbell-Baker expansion cannot capture).

Density-density OTOC in the Luttinger-liquid model

Here we present the result for the density-density OTOC in the Luttinger liquid, while we give the detailed calculation in Appendix G. The non-oscillating part of this OTOC was considered in Ref. [36]. We consider the density operator defined in

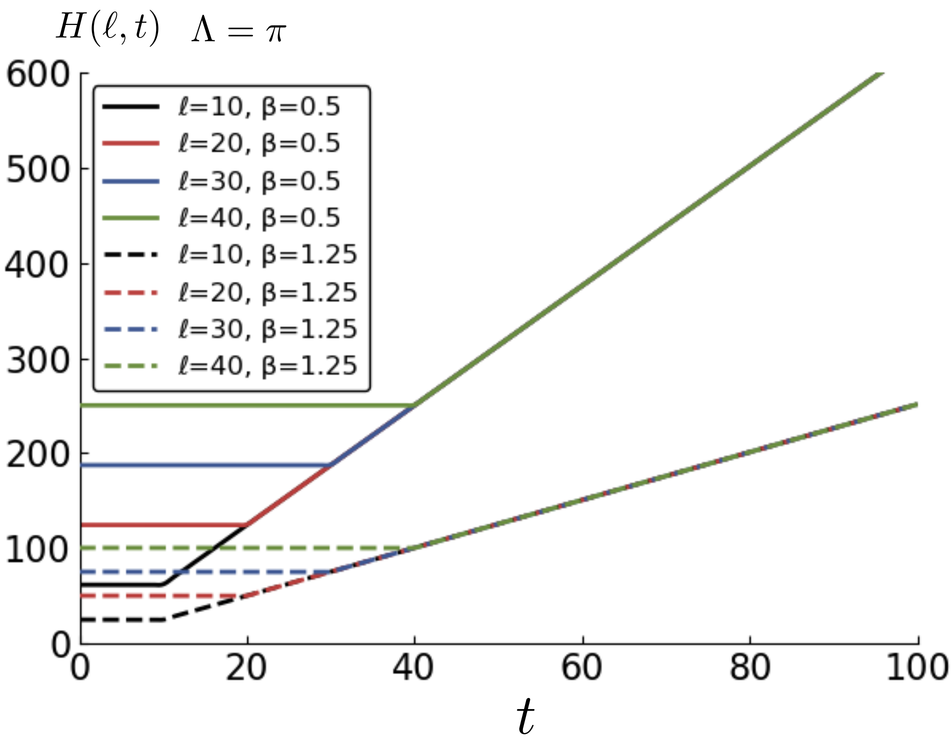

Figure 4.15: Numerical integration results for the function $H(x,t)$ entering $C_{nn}^{\mathrm{III}}(\ell,t)$, see Eqs. (4.55) and (4.57), using momentum cutoff $\Lambda=\pi$. We can see that $e^{-H(\ell,t)}$ decays exponentially inside the light cone; furthermore, for such ℓ and β, the numerical value is negligible compared to 1.

Eq. (4.42). To compare with the lattice models more closely, we choose to regularize the theory by a hard-cutoff Λ, instead of a soft cutoff $e^{-\alpha|k|}$ factor in the integration over momentum k used in Ref. [36].

The result for the commutator function is

$$\begin{aligned} C_{nn}^{\mathrm{III}}(\ell,t) &= \frac{g^2}{2\pi^4}N^2(\ell,t) \\ &+ 2d_2^4[4+2\cos(4\pi\rho_0\ell)e^{-2gH(\ell,t)}]\sin^2[2gG(\ell,t)] \\ &- d_2^2\frac{4g}{\pi^2}\cos(2\pi\rho_0\ell)e^{-2gH(\ell,t)}N(\ell,t)\sin^2[2gG(\ell,t)]\,, \end{aligned} \tag{4.55}$$

where

$$\begin{aligned} N(\ell,t) &= \int_0^\Lambda dk\, k\cos(k\ell)\sin(v_B kt) \\ &= \frac{\sin[\Lambda(v_B t-\ell)]}{2(v_B t-\ell)^2} - \frac{\Lambda\cos[\Lambda(v_B t-\ell)]}{2(v_B t-\ell)} \\ &+ \frac{\sin[\Lambda(v_B t+\ell)]}{2(v_B t+\ell)^2} - \frac{\Lambda\cos[\Lambda(v_B t+\ell)]}{2(v_B t+\ell)}, \end{aligned} \tag{4.56}$$

$$H(\ell,t) = \int_0^\Lambda \frac{dk}{k}[2f(v_B k)+1][1-\cos(k\ell)\cos(v_B kt)], \tag{4.57}$$

with $f(\epsilon) = 1/(e^{\beta\epsilon}-1)$ being Bose-Einstein distribution, and

$$G(\ell,t) = \int_0^\Lambda \frac{dk}{k}\cos(k\ell)\sin(v_B kt) \tag{4.58}$$

$$= \frac{1}{2}[\mathrm{Si}(\Lambda t_+) + \mathrm{Si}(\Lambda t_-)], \tag{4.59}$$

where $\mathrm{Si}(x) \equiv \int_0^x dy \sin(y)/y$, and we have abbreviated $t_\pm = v_B t \pm \ell$.

The above expressions are defined through the hard cutoff regularization. (For results of the soft cutoff regularization, see Ref. [36] and Appendix G and H.) First, we note that $H(\ell,t)$ is the only temperature-dependent piece; it grows linearly with ℓ outside the light cone, $t < \ell/v_B$, and grows linearly with t inside the light cone, $t > \ell/v_B$, as shown in Fig. 4.15. Therefore e^{-gH} decays exponentially when either ℓ or t are large, and can be safely neglected when discussing asymptotic behaviors.

We first consider short times, $t \ll \ell/v_B$. It is easy to see that in this regime $N^2(\ell,t)$ grows as t^2. More specifically, we have

$$\begin{aligned} N(\ell,t) &\sim v_B t \int_0^\Lambda dk\, k^2 \cos(k\ell) \\ &= v_B t \left(\frac{2\Lambda\cos(\Lambda\ell)}{\ell^2} + \frac{(-2+\ell^2\Lambda^2)\sin(\Lambda\ell)}{\ell^3} \right) . \end{aligned}$$

For the cutoff $\Lambda = \pi$ and recalling that ℓ is an integer, we have $N(\ell,t)^2 \sim (v_B t)^2/\ell^4$, which in fact matches with the short-time behavior of the long-range hopping model. However, for a generic cutoff, we would obtain the leading contribution $N(\ell,t)^2 \sim (v_B t)^2/\ell^2$.

We also need to consider the contribution from $\sin^2[2gG(\ell,t)]$ at the short time. This can be obtained from the behavior of $G(\ell,t)$, where at the short time

$$\begin{aligned} G(\ell,t) &\sim \frac{\sin(\Lambda\ell)}{\ell}v_B t \\ &- \frac{2\Lambda\ell\cos(\Lambda\ell)+(-2+\Lambda^2\ell^2)\sin(\Lambda\ell)}{6\ell^3}(v_B t)^3 \ . \end{aligned} \tag{4.60}$$

For the choice $\Lambda = \pi$, we have $\sin^2[2gG(\ell,t)] \sim 4g^2\pi^2(v_B t)^6/(9\ell^4)$; while for generic Λ, we have $\sin^2[2gG(\ell,t)] \sim 4g^2\sin^2(\Lambda\ell)(v_B t)^2/\ell^2$. We therefore see that, in general, $C_{nn}^{\text{III}}(\ell,t) \sim t^2$ at the short time, with the coefficient which is a function of ℓ whose behavior depends on the cutoff Λ, and special $\Lambda = \pi$ provides a good match with our long-range model also in the ℓ-dependence of the coefficient.

After the wavefront passes, in the infinite time limit,

$$C_{nn}^{\text{III}}(\ell,\infty) = 8d_2^4\sin^2[2gG(\ell,\infty)] \le 8d_2^4 \ . \tag{4.61}$$

For the lattice models, the commutator function is bounded by $C_{nn} \le 2$, so we choose $d_2 = 1/\sqrt{2}$ such that the bounds match between the Luttinger liquid model and the lattice models. Also noting that $G(\ell,\infty) = \pi/2$, we have $C_{nn}^{\text{III}} \to 2\sin^2(g\pi)$. For the "non-interacting" (i.e., free-fermion) model, $g = 1$ and $C_{nn}^{\text{III}} \to 0$, which agrees with results in the lattice models.

The long-time behavior of $N^2(\ell,t)$ can be obtained easily as

$$N^2(\ell,t) \sim \Lambda^2\cos^2(\Lambda v_B t)\cos^2(\Lambda\ell)/(v_B t)^2 \ .$$

To analyze $\sin^2[2gG(\ell,t)]$ at the long time, we first note the asymptotic expansion of

$$\begin{aligned} G(\ell,t) &\sim \frac{\pi}{2} - \frac{\cos(\Lambda v_B t)\cos(\Lambda\ell)}{\Lambda v_B t} \\ &- \frac{\sin(\Lambda v_B t)\cos(\Lambda\ell)}{(\Lambda v_B t)^2} \ , \end{aligned} \tag{4.62}$$

where we used that $\text{Si}(x) \sim \pi/2 - \cos(x)/x - \sin(x)/x^2 + O(x^{-3})$ at large x. We therefore have

$$\begin{aligned} \sin^2[2gG(\ell,t)] &\sim \sin^2(g\pi) - 2g\sin(2g\pi)\cos(\Lambda\ell)\frac{\cos(\Lambda v_B t)}{\Lambda v_B t} \\ &+ 4g^2\cos(2g\pi)\cos^2(\Lambda\ell)\frac{\cos^2(\Lambda v_B t)}{(\Lambda v_B t)^2} \\ &- 2g\sin(2g\pi)\cos(\Lambda\ell)\frac{\sin(\Lambda v_B t)}{(\Lambda v_B t)^2} \ . \end{aligned} \tag{4.63}$$

Therefore, for the free-fermion point $g = 1$, we have that $C^{\mathrm{III}}_{nn}(\ell, t)$ vanishes as $\sim t^{-2}$ at long times. On the other hand, if g is not an integer, we have that $C^{\mathrm{III}}_{nn}(\ell, t)$ approaches a non-zero value, with the approach $\sim t^{-1}$. The t^{-2} behavior is in fact also seen in the long-range hopping model, but not in the short-range hopping model.

Lastly, we note that the wavefront does not broaden in the Luttinger liquid model, which is also the case in the long-range hopping model. This can be seen from the fact that $C^{\mathrm{III}}_{nn}(\ell, t)$ depends on ℓ and t only via combinations $v_B t \pm \ell$. In this case, when one considers the behavior around the wavefront, writing $\ell = v_B t + \delta\ell$, the dependence on $\delta\ell$ has no scaling with time, which corresponds to the wavefront that does not broaden with time. This is expected to be general feature in relativistic theories, and it is reproduced by our long-range hopping model with the straightened dispersion curve with finite band width.

4.8 Hard-core boson models: Boson-boson OTOC

In this section, we study the OTOC in the short-range and long-range hopping models for operators $W_0 = X_0$ and $V_\ell = X_\ell$, where $X_j \equiv b_j^\dagger + b_j$ is the combination of boson creation and annihilation operators. [X_j is simply the Pauli spin matrix σ_j^x when the hard-core bosons are mapped to spin-1/2-s and is convenient since it is both Hermitian and unitary, see our discussion on Eqs. (4.1)]. The above operator becomes nonlocal in terms of the JW fermions. The calculations hence become intricate and analytical results for different asymptotic regimes are difficult to obtain. Thus we evaluate the OTOC numerically from the full analytical expression as a Pfaffian and present results here, while we present details of the setup of calculation in Appendix I. In Fig. 4.16, we show the overall picture of $C_{XX}(\ell, t)$ for both the short-range and long-range hard core boson models. We clearly observe a ballistic wavefront with butterfly velocity $v_B = 1$. Furthermore, the commutator function saturates to a non-zero value inside the light cone, which indicates that $X_0(t)$ is evolving into a nonlocal operator, spreading throughout inside the light cone. This behavior is in contrast to the density-density OTOC, where the commutator function goes back to zero deep inside the light cone. In the quantum Ising model which we studied earlier in Ref. [37], this type of operator that is non-local in terms of the JW fermions also shows saturation to a non-zero value in the commutator function.

Below, we examine in detail behavior of $C_{XX}(\ell, t)$ in different regimes.

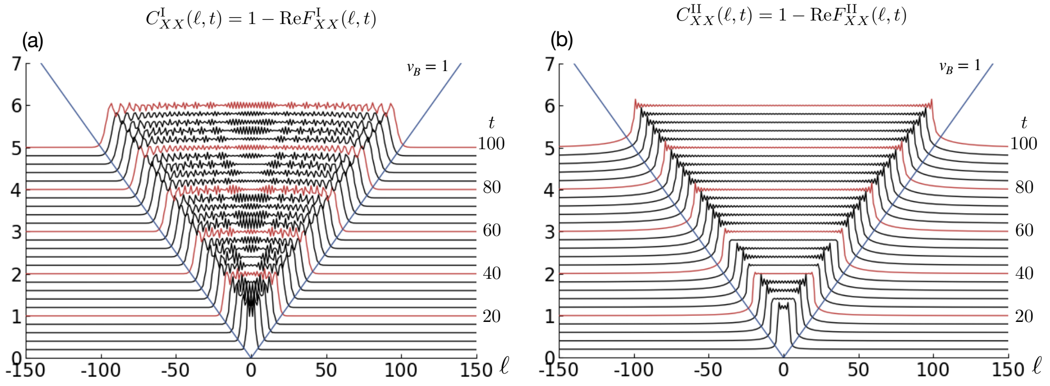

Figure 4.16: The overall picture of $C_{XX}(\ell, t)$ calculated in (a) model I and (b) model II, with $L = 512$, $\beta = 0$, and $J = 1$. (At infinite temperature, the systems are at half-filling for any μ.) We have shifted each trace by $0.05t$ to create a 3D-like visualization; also, for every time t that is a multiple of 20, we plot the trace with red color for easy reference. The saturation to a non-zero value inside the light cone is a characteristic of scrambling; it indicates that $X_0(t)$ evolves into a nonlocal operator, in contrast to the time-evolved density operator.

Velocity-dependent Lyapunov exponent and wavefront broadening analysis in the short-range hopping model

In the short-range hopping model, it is well understood that in the early-time regime, the commutator function has a position dependent power-law growth which can be understood from the Hausdorff-Campbell-Baker expansion [35–38] (see also Table 4.1). We therefore skip the discussion of this regime in the short-range hopping model and focus on the behavior around the wavefront.

References [38] and [39] proposed that for the noninteracting free fermion models, the wavefront broadens as $t^{1/3}$. This can be verified by either examining the long-time behavior along different fixed-velocity rays $\ell = vt$ with $v > v_B$, or by studying scaling collapse of $C(\ell, t)$ near the wavefront. In Fig. 4.17(a), we show the $t^{1/3}$ broadening by the scaling collapse analysis. Furthermore, in Fig. 4.17(b), we extracted the velocity-dependent Lyapunov exponent, which shows $(v - v_B)^{3/2}$ scaling, corresponding to the proposed $t^{1/3}$ wavefront broadening. Note that, unlike the case of the density-density OTOC (or OTOCs composed of few fermion operators considered in Refs. [38] and [39]), the boson-boson OTOC does not have a simple analytical expression where the saddle-point analysis can be applied easily. However, the wavefront broadening still has the same characteristic behavior despite the presence of the fermionic strings. Finally, we note that our numerical results

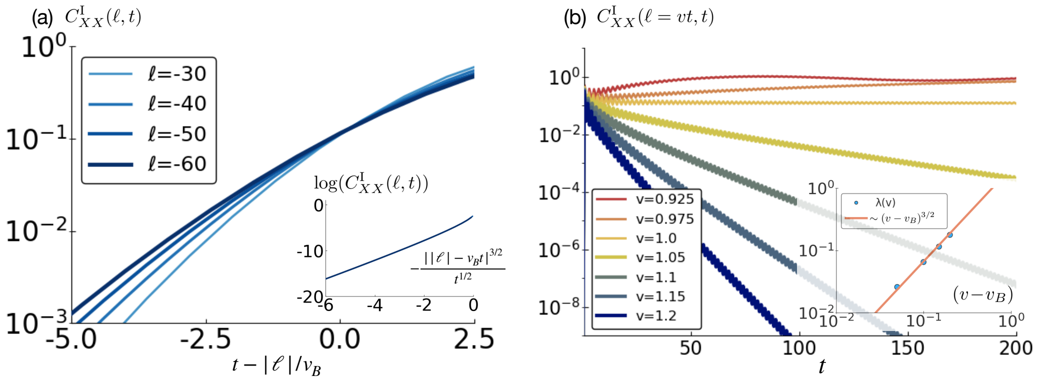

Figure 4.17: (a) The commutator function $C^{\mathrm{I}}_{XX}(\ell, t)$ of the short-range model around the wave front, for several ℓ (negative ℓ correspond to points to the left of the origin in our chain with sites labeled $-L/2+1,\dots,0,\dots,L/2$; the string that runs from the left boundary is shorter for these points than for positive ℓ). The systems size is $L = 512$ and the inverse temperature is $\beta = 0$. Inset: scaling collapse demonstrating that around the wavefront, $C^{I}_{XX}(\ell = vt, t) \sim \exp[-\lambda(\ell - v_B t)^{3/2}/t^{1/2}]$. (b) The commutator function $C^{I}_{XX}(\ell = vt, t)$ along different rays $\ell = vt$, for the same system as in panel (a). Inset: the velocity-dependent Lyapunov exponent extracted by fitting the numerical data to $C(\ell = vt, t) = A\exp[-\lambda(v)t]$. For velocities close to the butterfly velocity but outside the light cone, $v > v_B$, we observe the relation $\lambda(v) \sim (v - v_B)^{3/2}$.

show that the above descriptions are essentially temperature independent.

From early-time region to early-growth region in the long-range hopping model

The situation with the wavefront broadening in the long-range hopping model is rather different from the short-range model, as we have already seen in the density-density OTOC. In Fig. 4.18, we plot $C^{\mathrm{II}}_{XX}(\ell, t)$ for different fixed ℓ. In this case, as we will argue in more detail below, the perturbative (Hausdorff-Baker-Campbell) expansion gives us t^2 power-law growth at short time due to the long-range hopping; this is shown in the inset of Fig. 4.18. Also, the early-time region connects to the early-growth region near the wavefront rather abruptly. In fact, one can identify an $O(1)$ window around the wavefront where the t^2 growth stops and transits into the early-growth region. We therefore conclude that in the long-range hopping model, the wavefront has little to no broadening.

We now provide the details of the early-time region. Recall the Hamiltonian H^{II} in the spin variables written in Eq. (4.51). In the early-time (perturbative) regime, consider the expansion $X_0(t) = \sum_{n=0}^{\infty} \frac{(it)^n}{n!} L^n(X_0)$, where $L(A) \equiv [H, A]$. The power-law growth of the commutator function is determined by the lowest-order nonzero commutator $[L^n(X_0), X_\ell]$. Since H^{II} is long-ranged, $n = 1$ immediately "connects" X_0 and X_ℓ, giving us t^2 growth. However, there are in fact many terms that contribute to the amplitude of the t^2 growth. By writing out

$$\begin{aligned} L(X_0) &= -i \sum_{i<0,j>0} J_{ij} \mathcal{Z}_{i+1,-1} Y_0 \mathcal{Z}_{1,j-1} (X_i X_j + Y_i Y_j) \\ &+ i \sum_{j>0} J_{0j} \mathcal{Z}_{0,j-1} Y_j + i \sum_{i<0} J_{i0} Y_i \mathcal{Z}_{i+1,0} - i\mu Y_0 \,, \end{aligned}$$

we have (assuming $\ell > 0$ for concreteness)

$$\begin{aligned} &[L(X_0), X_\ell] = -2 J_{0,\ell} \mathcal{Z}_{0,\ell} \\ &-2 \sum_{i<0,j>\ell} J_{ij} \mathcal{Z}_{i+1,-1} Y_0 \mathcal{Z}_{1,\ell-1} Y_\ell \mathcal{Z}_{\ell+1,j-1} (X_i X_j + Y_i Y_j) \\ &+2 \sum_{j>\ell} J_{0j} \mathcal{Z}_{0,\ell-1} Y_\ell \mathcal{Z}_{\ell+1,j-1} Y_j + 2 \sum_{i<0} J_{i\ell} Y_i \mathcal{Z}_{i+1,-1} Y_0 \mathcal{Z}_{1,\ell} \,. \end{aligned}$$

The leading order is therefore

$$C^{\mathrm{II}}_{XX}(\ell, t) \sim 4t^2 \Big(\sum_{i<0,j>\ell} J_{ij}^2 + \sum_{j>\ell} J_{0j}^2 + J_{0,\ell}^2/2 \Big) \,, \tag{4.64}$$

where in the thermodynamic limit $J_{ij}^2 = \frac{2v_B^2}{\pi^2} \frac{[1-(-1)^{i-j}]}{|i-j|^4}$. Hence, we estimate $C_{XX}(\ell, t) \sim \frac{t^2}{\ell^2}(1 + O(\ell^{-1}))$, which is valid for $v_B t \ll 1 \ll \ell$. (Note that unlike the density-density OTOC, the early-time region does not extend into the "ray" region.)

Long-time behavior of boson-boson OTOC

Since a simple expression for $F_{XX}(\ell, t)$ is not easily obtainable, we study the long-time behavior numerically. Figure 4.19 plots the long time behavior of $F_{XX}(\ell, t)$ in the short-range hopping model and the long-range hopping model. It is clear that both cases show power-law decay. For the short-range model, we conclude that the power-law is close to $t^{-1/2}$, with the system size $L = 512$ already having little finite size effect. On the other hand, for the long-range model, we observe much stronger finite size effect (which is indeed expected). For example, for $L = 512$, we see the power-law is close to $t^{-0.75}$, while it is close to $t^{-0.85}$ for our largest size $L = 1024$ shown in Fig. 4.18(b). Extracting the power-law exponent numerically is thus challenging due to the finite-size effect, as well as due to the mixing with other power-laws and the presence of the oscillations. We conjecture that in the thermodynamic limit, the power-law approach is t^{-1}, as predicted in the Luttinger liquid model, see Sec. 4.9.

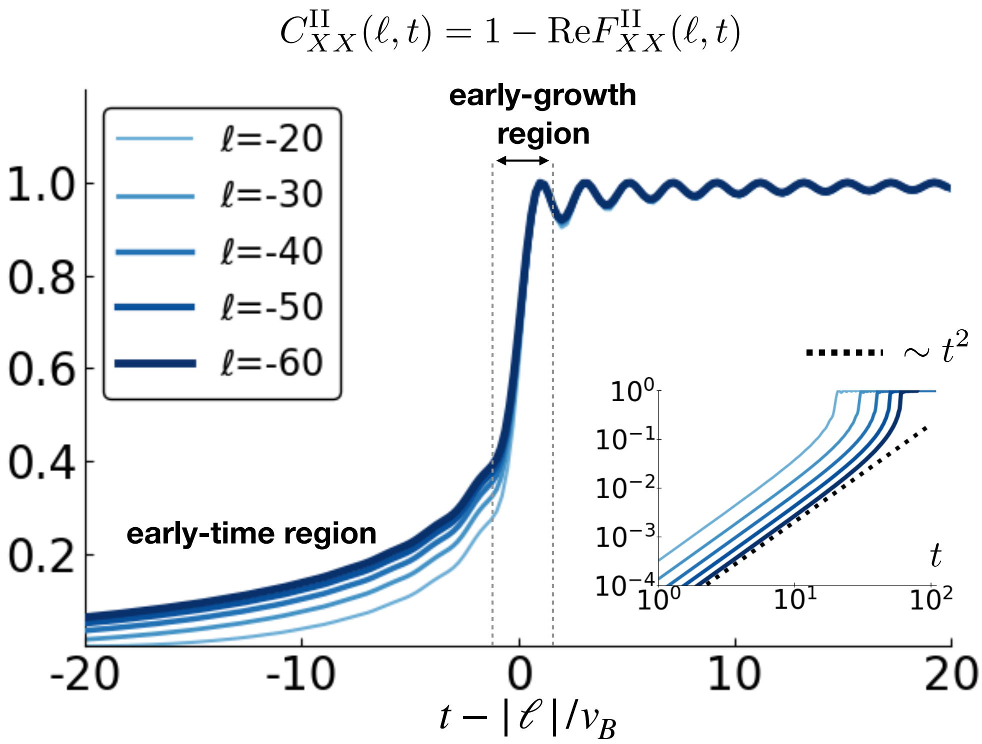

Figure 4.18: The commutator function $C_{XX}(\ell, t)$ in the long-range hopping model for several fixed ℓ. One can see that the early-time HCB region connects to the early-growth region rather abruptly. The window of the early-growth region always stays as $O(1)$. Inset: demonstration of the t^2 power-law growth in the HCB region.

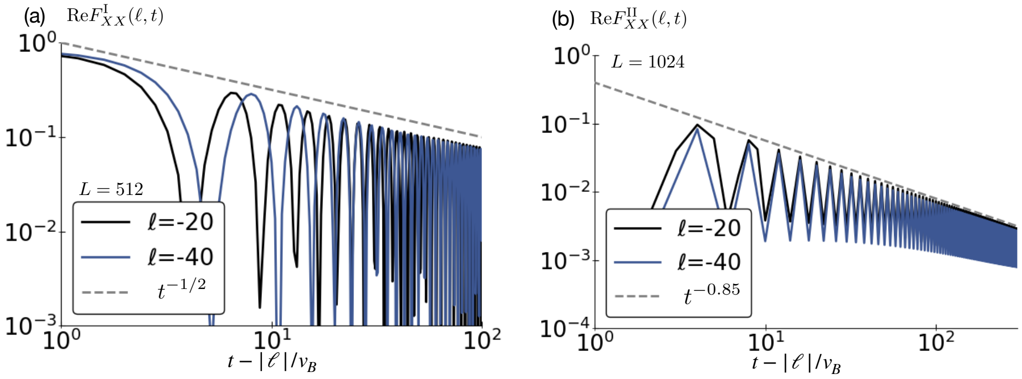

Figure 4.19: The long-time power-law decay $t^{-\alpha}$ of $\mathrm{Re}F_{XX}(\ell, t)$ in (a) the short-range hopping model and (b) the long-range hopping model. The numerical results suggest that the exponents are close to $\alpha^{\mathrm{I}} \approx 0.5$ and $\alpha^{\mathrm{II}} \approx 0.85$, respectively. However, we conjecture that α^{II} approaches 1 in the thermodynamic limit (see the text).

To conclude, we see that the long-time power-law depends on the nature of the quasiparticle dispersion, and is different between the generic case corresponding to short-range hopping and the completely straightened case corresponding to the specific long-range hopping. Interestingly, in the quantum Ising case which we studied in Ref. [37], similar "chaotic" OTOC (i.e., OTOC for operator that contains string operator in terms of the JW fermions) shows yet a different $t^{-0.25}$ power law; understanding this and the power law in the nearest-neighbor hard-core boson hopping model are outstanding questions.

4.9 Luttinger liquid model: Boson-boson OTOC

In this section, we discuss the calculation of the boson-boson OTOC in the Luttinger liquid model and the agreements and disagreements with the ones obtained in the lattice models. Here we consider the operator $X(x,t) = c(e^{i\phi(x,t)} + e^{-i\phi(x,t)})$, which resembles the sum of the boson creation and annihilation operators as considered in the previous section. The constant c will be fixed later. We again consider the commutator function $C_{XX}(\ell,t) = \frac{1}{2}\langle [X(\ell,t), X(0,0)]^\dagger [X(\ell,t), X(0,0)]\rangle$. To calculate it, we consider the Schwinger function in the Euclidean path integral [abbreviating $r_i = (x_i, \tau_i)$]

$$\begin{aligned} F^E_{XX}(\{r_i\}) &= \langle X(r_1)X(r_2)X(r_3)X(r_4)\rangle \\ &= \sum_{p_i=\pm, \sum_i p_i = 0} \langle e^{i(\sum_{i=1}^4 p_i \phi_i)}\rangle \\ &= \sum_{p_i=\pm, \sum_i p_i = 0} \exp\left[\frac{1}{2g}\sum_{i<j} p_i p_j K(r_i - r_j)\right], \end{aligned} \tag{4.65}$$

where

$$\begin{aligned} K(r) &\equiv \int_0^\Lambda \frac{dk}{k} 2f(v_B k)[1-\cos(kx)\cosh(v_B k\tau)] \\ &+ \int_0^\Lambda \frac{dk}{k}[1-\cos(kx)e^{-v_B k|\tau|}], \end{aligned} \tag{4.66}$$

with $f(\epsilon) = 1/(e^{\beta\epsilon} - 1)$ denoting the Bose-Einstein distribution function. Again, to compare with the lattice systems at finite temperature, we choose to regularize the theory with a hard cutoff Λ. The $|\tau|$ symbol is to be understood as $|\tau| = \tau$ if $\mathrm{Re}(\tau) > 0$ and $|\tau| = -\tau$ if $\mathrm{Re}(\tau) < 0$. To obtain the functions in the real time, we need the analytical continuations $\lim_{\epsilon\to 0^+} K(x, \tau \to \pm\epsilon + it) = H(x,t) \mp iG(x,t)$, where $H(x,t)$ and $G(x,t)$ are defined in Eqs. (4.57) and (4.58), respectively.

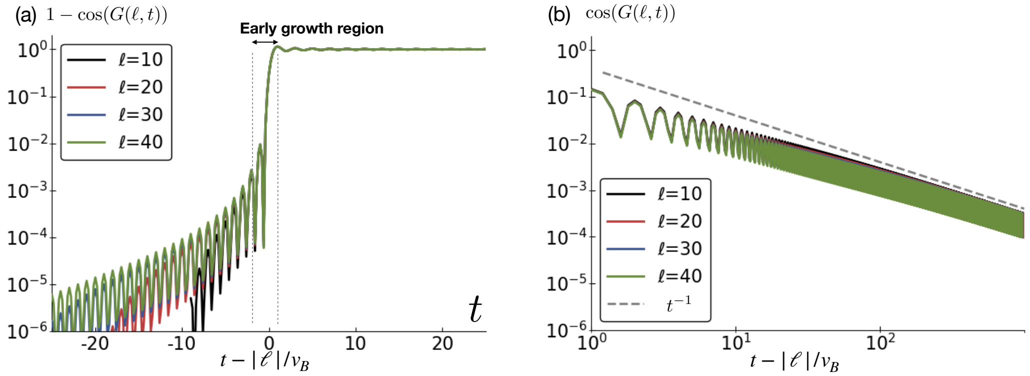

Figure 4.20: (a) The dominant part of the commutator function $C^{\mathrm{III}}_{XX}(\ell,t) \approx 1-\cos[G(\ell,t)]$ in the Luttinger model with $g=1$ ("free-fermion" value). (b) The long-time approach is described by the t^{-1} power law.

Using suitable combinations of the analytical continuations, we have

$$C^{\mathrm{III}}_{XX}(\ell,t) = c^4\left[8+4e^{-\frac{2}{g}H(\ell,t)}\right]\sin^2\left[\frac{G(\ell,t)}{2g}\right] . \tag{4.67}$$

We can fix the constant c as follows. The factor $e^{-2H(\ell,t)/g}$ decays exponentially to zero at long time. Therefore, the limiting value of the commutator function inside the light cone is $C^{\mathrm{III}}_{XX}(\ell,t\to\infty) = 8c^4\sin^2[G(\ell,\infty)/(2g)] \le 8c^4$. For the lattice models, $C_{XX}(\ell,t) \le 2$. We then fix $c = 1/\sqrt{2}$ so that the maximal possible value matches with the lattice models.

The integral that gives $G(x,t)$ in Eq. (4.58) is convergent even if we set $\Lambda=\infty$. In this case, $G(x,t) = \frac{\pi}{4}(\mathrm{sign}(v_Bt-x)+\mathrm{sign}(v_Bt+x)) \longrightarrow \frac{\pi}{2}$ when $t\longrightarrow\infty$. This means that $C_{XX}(\ell,t)\longrightarrow 1$ inside the light cone, which coincide with the result in the lattice models. If we put the cutoff at $\Lambda=\infty$, the wavefront becomes a step function, and the long time behavior is described by $\exp[-2H(x,t)/g]$ (which in fact approaches zero when $\Lambda\longrightarrow\infty$). A more realistic approach (i.e., closer to the lattice models) is to have a finite cutoff Λ. As we will see, introducing the finite cutoff indeed changes the behavior $C_{XX}(\ell,t)$ around the wavefront and its asymptote in the long time.

Figure 4.20 shows results with finite cutoff $\Lambda=\pi$ for the case with the Luttinger parameter $g=1$ (which corresponds to non-interacting fermions). In the figure, we ignored the $\exp[-2H(\ell,t)/g]$ since it is numerically negligible and does not affect the behavior of $C_{XX}(\ell,t)$, as explained in Fig. 4.15. One can see that the presence of the finite cutoff indeed modifies the shape of the wavefront (early-growth region), which is no longer the simple step function. However, the time window of the early-growth is always $O(1)$, which is indeed similar to the case of the lattice model with long-range hopping. Moreover, in this case as well the wavefront does not broaden, which can be also seen from the fact that $C^{\mathrm{III}}_{XX}(\ell, t)$ is a function of $v_B t \pm \ell$ only. Making a more detailed comparison of Fig. 4.20(a) and

$$G(\ell, t) \approx \pi/4 + \mathrm{Si}[\Lambda(v_B t - \ell)]/2 \tag{4.68}$$

in this early-growth region, $v_B t \sim \ell \gg 1$, we note that the shape of the wavefront is indeed converging as ℓ increases. The precipitous drop when going away from the wavefront for $v_B t < \ell$ but still in the early growth region is due to numerical "accident:" here $G(\ell, t)$ oscillates around 0, hence the strong drop in $1 - \cos[G(\ell, t)]$, and the next largest value happens to be small by accident.

Before the wavefront is reached, $C_{XX}(\ell, t)$ has a fixed power-law growth $\sim t^2$ for any ℓ, which is also similar to the early-time (perturbative) region in the long-ranged hopping hard-core boson model. To be more specific, recalling the early time behavior of $G(\ell, t)$ in Eq. (4.60), similarly we have $\sin^2[G(\ell, t)/(2g)] \sim \pi^2 (v_B t)^6/(36 g^2 \ell^4)$ for the choice $\Lambda = \pi$; while for a generic Λ, we have

$$\sin^2[G(\ell, t)/(2g)] \sim \sin^2(\Lambda \ell)(v_B t)^2/(4 g^2 \ell^2) \,.$$

Note that in this case, one has to choose generic cut-off to match the early-time growth power law in the long-range hopping model.

We note that the long-time power-law approach is also due to the presence of the finite cutoff. Recalling the long-time behavior of $G(\ell, t)$ in Eq. (4.62), we have

$$\begin{aligned} \sin^2\left[\frac{G(\ell,t)}{2g}\right] \;&\sim\; \sin^2\left(\frac{\pi}{4g}\right) - \sin\left(\frac{\pi}{2g}\right)\cos(\Lambda\ell)\frac{\cos(\Lambda v_B t)}{2g(\Lambda v_B t)} \\ &+\; \cos\left(\frac{\pi}{2g}\right)\cos^2(\Lambda\ell)\frac{\cos^2(\Lambda v_B t)}{4g^2(\Lambda v_B t)^2} \\ &-\; \sin\left(\frac{\pi}{2g}\right)\cos(\Lambda\ell)\frac{\sin(\Lambda v_B t)}{2g(\Lambda v_B t)^2} \,. \end{aligned} \tag{4.69}$$

Therefore, for general $g \neq 1/(2m)$, where m is some integer, we have $C^{\mathrm{III}}_{XX}(\ell, t) \sim t^{-1}$ at long time; this includes the non-interacting model $g = 1$ [in the special cases with $g = 1/(2m), m \in \mathbb{Z}$, we have $C^{\mathrm{III}}_{XX}(\ell, t) \sim t^{-2}$]. We speculate that this agrees with the long-range hard-core boson model in the thermodynamic limit. We therefore see that, while not in all the details, the Luttinger liquid model can capture a great deal of the OTOC behavior in the long-range hopping hardcore boson model.

Density-density OTOC	Early-time	Wavefront Broadening	Long time approach
Model I	$t^{2\ell}/(\ell!)^2$	$t^{\frac{1}{3}}$	t^{-1}
Model II	t^2/ℓ^4	No (i.e., t^0)	t^{-2}
Model III(a)	t^2/ℓ^4	No	t^{-2}
Model III(b)	t^2/ℓ^2	No	t^{-2}

Boson-boson OTOC	Early-time	Wavefront Broadening	Long time approach
Model I	$t^{2\ell}/(\ell!)^2$	$t^{\frac{1}{3}}$	$t^{-\frac{1}{2}}$
Model II	t^2/ℓ^2	No	t^{-1}
Model III(a)	t^6/ℓ^4	No	t^{-1}
Model III(b)	t^2/ℓ^2	No	t^{-1}

Table 4.1: Summary of the main results for the three models in the different regimes. Model I is the nearest-neighbor lattice model; model II is the long-range hopping lattice model; and model III is the continuum Luttinger liquid model. The results for model III are quoted with the Luttinger parameter $g = 1$ corresponding to noninteracting fermions and (a) cutoff $\Lambda = \pi$ and (b) generic cutoff $\Lambda \neq \pi$.

4.10 Discussions of the results in the Hard-core boson and the Luttinger liquid models

We studied the OTOCs in the hard-core boson models with short-range hopping and with long-range hopping where we artificially straighten the fermionic quasiparticle dispersion. We compared these models to the Luttinger-liquid model with hard cutoff regularization, which mimics the finite band width in the lattice models.

The density-density commutator function exhibits "non-scrambling" behavior (i.e., it approaches zero in the long-time limit) in all three models. In the short-range hopping model, the wavefront broadens as $t^{1/3}$, which can be verified using the asymptotic properties of the Bessel functions in the so-called "transition region." On the other hand, in the long-range hopping model and the Luttinger-liquid model, we find that the wavefront does not broaden; there is also no well-defined "exponential growth" (i.e., "butterfly effect") regime since the wavefront width is finite (and the width is also cutoff-dependent in the Luttinger-liquid model).

Before the wavefront reaches, the long-range model and the Luttinger-liquid model both show t^2 growth. The t^2 growth in the long-range model can be understood using the perturbative early-time expansion and is due to the fact that all sites "talk" to each other via the long-range couplings. The coefficient of the t^2 growth as a function of ℓ can be carried out according to the perturbative expansion. The fact that we find similar early-time behavior in the Luttinger-liquid model suggests that it should be regarded as representing bosons with long-range couplings. We therefore see that this “light-cone leakage" phenomenon [64] might be a very general feature for long-range models. The short-range model, on the other hand, shows position-dependent power-law growth in the early-time regime described by the perturbative expansion. After the wavefront passes, both the long-range model and the Luttinger-liquid model show t^{-2} decay, while the short-range model shows t^{-1} decay.

Turning to the boson-boson commutator function, the calculations are more complex in the lattice models (since the boson operator contains a string operator when expressed in terms of the JW fermions) and require numerical calculations, while they are still analytically tractable in the Luttinger-liquid model. We find that the boson-boson commutator function shows saturation inside the light cone in all free models. Such a characteristic “scrambling” behavior reflects the fact that the boson operator turns into a highly nonlocal operator under the Heisenberg evolution. In the short-range hopping model, we found the $t^{1/3}$ wavefront broadening by wavefront scaling collapse and by extracting the velocity-dependent Lyapunov exponent. In the long-range hopping model, we find a nonbroadening wavefront, which is also the case in the Luttinger-liquid model; in both cases, one cannot define a parametrically large window to describe the wavefront behavior asymptotically [while the sharp onset in the Luttinger-liquid model in Fig. 4.20 is reminiscent of an exponentially growing wavefront, we emphasize that this is a numerical accident for the simple function describing the wavefront at long times, Eq. (4.68)]. As far as the wavefront broadening is concerned, in all free models, the boson-boson and density-density OTOCs thus show similar broadening behavior. After the wavefront passes, the boson-boson OTOC approaches its limiting value as t^{-1} in the long-range model and the Luttinger-liquid model, while the approach is $t^{-0.5}$ in the short-range model.

We thus see that, despite the integrability of the models, different operators can still show different behaviors in the OTOC. It was argued that in rational conformal theories, the $t = \infty$ values of the OTOCs are solely determined by the topological data associated with the operators in the models [65]. While we do not expect the full conformal symmetry in the lattice models at finite temperature, the topological data might still be present, resulting in the same $t = \infty$ values of the OTOCs independent of the details of the dynamics. On the other hand, the character of the wavefront broadening and the long-time power-law approach depends on the details of the dispersion relations of the quasiparticles. In particular, one lesson from our study is that the conformal field theories cannot be used to described such properties of short-range models at finite temperatures.

Lastly, we mention some outstanding questions. While a seemingly simple description appears to exist for the boson-boson OTOC results, we could not acquire a more analytical understanding due to its intricacy. Thus, it will indeed be valuable if one can obtain some analytical understanding regarding the long-time asymptotic or the wavefront behavior, which we only obtained numerically. We have also shown the feasibility of reconciling the OTOCs of the hard-core boson model with a completely straightened quasiparticle dispersion to the OTOCs in the linear-Luttinger liquid. It may therefore be possible to match the behavior of OTOCs of the short-range boson model and of a "nonlinear" Luttinger liquid (i.e., theory that includes some "band curvature" effects) [66], which is worth pursuing. The quasiparticle description behind the systems we studied in this paper are noninteracting fermions. Another question is how the details of the OTOC change when one adds interactions, and what role the integrability plays. A recent work [67] has shown that in an interacting integrable Floquet system, the OTOCs have diffusive wavefront broadening, similar to the random unitary circuit model. On the other hand, little is known for integrable Hamiltonian systems that do not have a description in terms of free particles (e.g., models where the Jordan-Wigner fermions are interacting). A robust study on such systems such as the XXZ chain will be valuable for a deeper understanding of OTOCs and operator spreading in high-energy, quantum-information, and condensed-matter communities.

Appendix F: Calculation of the density-density OTOC in the lattice models

Here we present detailed calculations for the density-density OTOC in the short-range and long-range hopping models. Directly calculating the "commutator-squared" $|[n_0(t), n_\ell]|^2$ using the Hamiltonian formalism and the explicit Heisenberg evolution of the operators is in fact easier than calculating the expanded four terms individually. However, here we will carry out the calculations using path-integral formalism and obtain all the terms individually. Such approach parallels OTOC calculations in field theories, and the Luttinger liquid model is one example that we want to compare and contrast.

We define

$$\begin{aligned} C_{nn}(\ell, t) &= \frac{1}{2}\langle [n_0(t), n_\ell]^\dagger [n_0(t), n_\ell]\rangle \\ &= \frac{1}{2}\left[F_1(\ell,t) + F_2(\ell,t) - F_3(\ell,t) - F_4(\ell,t)\right] , \end{aligned}$$

where

$$\begin{aligned} F_1(\ell, t) &= \langle n_\ell \, n_0(t) \, n_0(t) \, n_\ell\rangle , \\ F_2(\ell, t) &= \langle n_0(t) \, n_\ell \, n_\ell \, n_0(t)\rangle , \\ F_3(\ell, t) &= \langle n_0(t) \, n_\ell \, n_0(t) \, n_\ell\rangle , \\ F_4(\ell, t) &= \langle n_\ell \, n_0(t) \, n_\ell \, n_0(t)\rangle . \end{aligned}$$

Now consider the Jordan-Wigner fermion model formulated in the Euclidean path integral over Grassmann fields, $Z = \int \mathfrak{D}[\bar{\eta}, \eta] e^{-S[\bar{\eta},\eta]}$, where

$$S = \int_0^\beta d\tau \sum_{ij} \bar{\eta}_i [\delta_{ij}\partial_\tau + J_{ij}]\eta_j . \tag{4.70}$$

The standard method of calculating OTOC is to calculate the Schwinger functions and do the analytical continuation to the Wightmann functions. Consider the Schwinger function

$$F^{(E)}(\ell; \tau_1, \tau_2, \tau_3, \tau_4) = \langle T_\tau \{n_\ell(\tau_1) n_\ell(\tau_2) n_0(\tau_3) n_0(\tau_4)\}\rangle . \tag{4.71}$$

The required Wightmann functions are obtained by

$$\begin{aligned} F_1(\ell, t) &= F^{(E)}(\ell; \epsilon_1, \epsilon_4, \epsilon_2 + it, \epsilon_3 + it) , \\ F_2(\ell, t) &= F^{(E)}(\ell; \epsilon_2, \epsilon_3, \epsilon_1 + it, \epsilon_4 + it) , \\ F_3(\ell, t) &= F^{(E)}(\ell; \epsilon_2, \epsilon_4, \epsilon_1 + it, \epsilon_3 + it) , \\ F_4(\ell, t) &= F^{(E)}(\ell; \epsilon_1, \epsilon_3, \epsilon_2 + it, \epsilon_4 + it) , \end{aligned}$$

where the ϵ_i's are taken to the limit of 0^+ in the order of $\epsilon_1 > \epsilon_2 > \epsilon_3 > \epsilon_4 > 0$. The Schwinger function is in fact an eight-point fermion correlation function

$$\begin{aligned} F^{(E)}(\ell; \tau_1, \tau_2, \tau_3, \tau_4) &= \langle \eta_\ell(\tau_1)\eta_\ell(\tau_2)\eta_0(\tau_3)\eta_0(\tau_4)\bar{\eta}_\ell(\tau_1 + \delta)\bar{\eta}_\ell(\tau_2 + \delta)\bar{\eta}_0(\tau_3 + \delta)\bar{\eta}_0(\tau_4 + \delta)\rangle \\ &= \det \begin{bmatrix} \langle n_\ell\rangle & \langle \eta_\ell(\tau_1)\bar{\eta}_\ell(\tau_2)\rangle & \langle \eta_\ell(\tau_1)\bar{\eta}_0(\tau_3)\rangle & \langle \eta_\ell(\tau_1)\bar{\eta}_0(\tau_4)\rangle \\ \langle \eta_\ell(\tau_2)\bar{\eta}_\ell(\tau_1)\rangle & \langle n_\ell\rangle & \langle \eta_\ell(\tau_2)\bar{\eta}_0(\tau_3)\rangle & \langle \eta_\ell(\tau_2)\bar{\eta}_0(\tau_4)\rangle \\ \langle \eta_0(\tau_3)\bar{\eta}_\ell(\tau_1)\rangle & \langle \eta_0(\tau_3)\bar{\eta}_\ell(\tau_2)\rangle & \langle n_0\rangle & \langle \eta_0(\tau_3)\bar{\eta}_0(\tau_4)\rangle \\ \langle \eta_0(\tau_4)\bar{\eta}_\ell(\tau_1)\rangle & \langle \eta_0(\tau_4)\bar{\eta}_\ell(\tau_2)\rangle & \langle \eta_0(\tau_4)\bar{\eta}_0(\tau_3)\rangle & \langle n_0\rangle \end{bmatrix} . \end{aligned}$$

Note that in the first line, δ is a positive infinitesimal smaller than all ϵ_i, i.e., $\delta < \epsilon_i$, $i = 1, \ldots, 4$; in the second line, δ has been taken to be 0^+.

We can now obtain the Wightmann functions. We have

$$\begin{aligned} F_1 &= \det \begin{bmatrix} \langle n_\ell \rangle & \langle n_\ell \rangle - 1 & -\langle c_\ell c_0^\dagger(t) \rangle & -\langle c_\ell c_0^\dagger(t) \rangle \\ \langle n_\ell \rangle & \langle n_\ell \rangle & \langle c_0^\dagger(t) c_\ell \rangle & \langle c_0^\dagger(t) c_\ell \rangle \\ \langle c_\ell^\dagger c_0(t) \rangle & -\langle c_0(t) c_\ell^\dagger \rangle & \langle n_0 \rangle & \langle n_0 \rangle - 1 \\ \langle c_\ell^\dagger c_0(t) \rangle & -\langle c_0(t) c_\ell^\dagger \rangle & \langle n_0 \rangle & \langle n_0 \rangle \end{bmatrix} , \\ &= \langle n_\ell \rangle \langle n_0 \rangle + \langle n_\ell \rangle |A(\ell, t)|^2 - |\langle c_0(t)^\dagger c_\ell \rangle|^2 , \end{aligned} \tag{4.72}$$

where $A(\ell, t) = \langle c_\ell^\dagger c_0(t) + c_0(t) c_\ell^\dagger \rangle = \frac{1}{L} \sum_k e^{ik\ell - i\epsilon(k)t}$ is just the fermion evolution function. Note that it is completely independent of the temperature.

Next, we have

$$\begin{aligned} F_2 &= \det \begin{bmatrix} \langle n_\ell \rangle & \langle n_\ell \rangle - 1 & \langle c_0^\dagger(t) c_\ell \rangle & -\langle c_\ell c_0^\dagger(t) \rangle \\ \langle n_\ell \rangle & \langle n_\ell \rangle & \langle c_0^\dagger(t) c_\ell \rangle & -\langle c_\ell c_0^\dagger(t) \rangle \\ -\langle c_0(t) c_\ell^\dagger \rangle & -\langle c_0(t) c_\ell^\dagger \rangle & \langle n_0 \rangle & \langle n_0 \rangle - 1 \\ \langle c_\ell^\dagger c_0(t) \rangle & \langle c_\ell^\dagger c_0(t) \rangle & \langle n_0 \rangle & \langle n_0 \rangle \end{bmatrix} , \\ &= \langle n_\ell \rangle \langle n_0 \rangle + \langle n_0 \rangle |A(\ell, t)|^2 - |\langle c_0(t)^\dagger c_\ell \rangle|^2 , \end{aligned} \tag{4.73}$$

and

$$\begin{aligned} F_3 &= \det \begin{bmatrix} \langle n_\ell \rangle & \langle n_\ell \rangle - 1 & \langle c_0^\dagger(t) c_\ell \rangle & -\langle c_\ell c_0^\dagger(t) \rangle \\ \langle n_\ell \rangle & \langle n_\ell \rangle & \langle c_0^\dagger(t) c_\ell \rangle & \langle c_0^\dagger(t) c_\ell \rangle \\ -\langle c_0(t) c_\ell^\dagger \rangle & -\langle c_0(t) c_\ell^\dagger \rangle & \langle n_0 \rangle & \langle n_0 \rangle - 1 \\ \langle c_\ell^\dagger c_0(t) \rangle & -\langle c_0(t) c_\ell^\dagger \rangle & \langle n_0 \rangle & \langle n_0 \rangle \end{bmatrix} , \\ &= (|A(\ell, t)|^2 + 1)(\langle n_\ell \rangle \langle n_0 \rangle + \langle c_0^\dagger(t) c_\ell \rangle \langle c_0(t) c_\ell^\dagger \rangle) \\ &- A(\ell, t) \langle c_0^\dagger(t) c_\ell \rangle . \end{aligned} \tag{4.74}$$

Finally, we use

$$\begin{aligned} F_4 = F_3^* &= (|A(\ell, t)|^2 + 1)(\langle n_\ell \rangle \langle n_0 \rangle + \langle c_\ell^\dagger c_0(t) \rangle \langle c_\ell c_0^\dagger(t) \rangle) \\ &- A^*(\ell, t) \langle c_\ell^\dagger c_0(t) \rangle . \end{aligned} \tag{4.75}$$

Combining everything, we have

$$\begin{aligned} C_{nn}(\ell, t) &= |A(\ell, t)|^2 \Big\{ (\langle n_\ell \rangle + \langle n_0 \rangle)/2 - \langle n_\ell \rangle \langle n_0 \rangle \\ &\qquad - \mathrm{Re}[\langle c_0^\dagger(t) c_\ell \rangle \langle c_0(t) c_\ell^\dagger \rangle] \Big\} . \end{aligned} \tag{4.76}$$

It is easy to see that the most important part of $C_{nn}(\ell, t)$ is the temperature-independent factor $|A(\ell, t)|^2$. Indeed, the first line in the $\{\ldots\}$ is a non-zero constant [equal to $d(1 - d)$ where d is the density], while the second line decays both in separation ℓ and in time t.

Appendix G: Calculation of the density-density OTOC in the Luttinger liquid model

In this section, we present detailed calculations for the density-density OTOC. The non-oscillation component of the density-density OTOC was calculated in Ref. [36]. In fact, it is the dominant contribution for $C_{nn}(\ell, t)$. Here, for the completeness, we also include the $q = 2k_F$ component of $C_{nn}(\ell, t)$ and use the path-integral formalism instead of the Hamiltonian formalism.

The density operator in consideration is defined in Sec. 4.6. Here we repeat the definition for reader's convenience.

$$n(x) = d_0 + \rho_0(x) + d_2 W(x)\,, \tag{4.77}$$

where $\rho_0(x) \equiv -\partial_x \hat{\theta}(x)/\pi$ and

$$W(x) \equiv e^{i2\pi d_0 x} V_{-2}(x) + e^{-i2\pi d_0 x} V_2(x)\,, \tag{4.78}$$

with the abbreviation $V_m(x) \equiv e^{im\hat{\theta}(x)}$, $d_0 = k_F/\pi$ denoting the density, and d_2 is some constant determined by microscopic details of the model.

We therefore have

$$\begin{aligned} C_{nn}(\ell, t) &= C_{\rho_0\rho_0}(\ell, t) + d_2^4 C_{WW}(\ell, t) \\ &+ d_2^2 C_{\rho_0 W}(\ell, t) + d_2^2 C_{W\rho_0}(\ell, t) \\ &+ d_2^2 C_{\rho_0\rho_0 WW}(\ell, t) + d_2^2 C_{\rho_0 WW\rho_0}(\ell, t)\,, \end{aligned} \tag{4.79}$$

where we have abbreviated

$$\begin{aligned} C_{\rho_0\rho_0 WW}(\ell, t) &\equiv \frac{1}{2}\langle [\rho_0(x,t), \rho_0(0)]^\dagger [W(x,t), W(0)]\rangle + \text{H.c.}\,, \\ C_{\rho_0 WW\rho_0}(\ell, t) &\equiv \frac{1}{2}\langle [\rho_0(x,t), W(0)]^\dagger [W(x,t), \rho_0(0)]\rangle + \text{H.c.}\,. \end{aligned}$$

To calculate the various commutator functions, we first consider the Schwinger functions and then analytically continue to the desired combinations.

First, we consider $C_{\rho_0\rho_0}(\ell, t)$. Abbreviating $r \equiv (x, \tau)$, we define (with the hard-cutoff Λ)

$$\begin{aligned} D(r) &= \int_0^\Lambda dk k 2 f_B(v_B k) \cosh(v_B k \tau) \cos(kx) \\ &+ \int_0^\Lambda dk k \cos(kx) e^{-|\tau| v k}\,. \end{aligned} \tag{4.80}$$

(For the soft-cutoff version, one integrates k from 0 to ∞ with an extra factor $e^{-\alpha k}$.) We in fact have $\partial_{x_1}\partial_{x_2}\langle\theta_1\theta_2\rangle = gD(r_{12})/2$, where we have abbreviated $\theta_j \equiv \theta(r_j)$ and $r_{ij} \equiv (x_i - x_j, \tau_i - \tau_j)$. We then consider the Schwinger function

$$\begin{aligned} F_{\rho_0\rho_0} &\equiv \pi^{-4}\langle\theta_1\theta_2\theta_3\theta_4\rangle \\ &= \frac{g^2}{4\pi^4}[D(r_{12})D(r_{34}) + D(r_{13})D(r_{24}) + D(r_{14})D(r_{23})]\,, \end{aligned} \tag{4.81}$$

by Wick's theorem. To obtain the functions after analytical continuation, we have

$$D(x, \tau \to it \pm 0^+) = M(x,t) \mp iN(x,t)\,, \tag{4.82}$$

where

$$\begin{aligned} M(x,t) &= \int_0^\Lambda dkk[2f_B(v_Bk) + 1]\cos(kx)\cos(v_Bkt) \\ N(x,t) &= \int_0^\Lambda dkk\cos(kx)\sin(v_Bkt)\,. \end{aligned} \tag{4.83}$$

We also note that $D(0) = 0$ and $N(x,-t) = -N(x,t)$. (Again, one can also consider the soft-cutoff regularization, with integrand $k = 0$ to ∞ with an extra factor $e^{-\alpha k}$.)

We therefore obtain $C_{\rho_0\rho_0}(\ell,t)$ via analytical continuation (with the order $\epsilon_1 > \epsilon_2 > \epsilon_3 > \epsilon_4 \to 0$) as

$$\begin{aligned} 2C_{\rho_0\rho_0}(\ell,t) &= F_{\rho_0\rho_0}(x_1 = x_4 = 0, x_2 = x_3 = x; \tau_1 = \epsilon_1, \tau_2 = \epsilon_2 + it, \tau_3 = \epsilon_3 + it, \tau_4 = \epsilon_4) \\ &+ F_{\rho_0\rho_0}(x_1 = x_4 = x, x_2 = x_3 = 0; \tau_1 = \epsilon_1 + it, \tau_2 = \epsilon_2, \tau_3 = \epsilon_3, \tau_4 = \epsilon_4 + it) \\ &- F_{\rho_0\rho_0}(x_1 = x_3 = x, x_2 = x_4 = 0; \tau_1 = \epsilon_1 + it, \tau_2 = \epsilon_2, \tau_3 = \epsilon_3 + it, \tau_4 = \epsilon_4) \\ &- F_{\rho_0\rho_0}(x_1 = x_3 = 0, x_2 = x_4 = x; \tau_1 = \epsilon_1, \tau_2 = \epsilon_2 + it, \tau_3 = \epsilon_3, \tau_4 = \epsilon_4 + it) \\ &= \frac{g^2}{\pi^4}N^2(x,t)\,. \end{aligned} \tag{4.84}$$

For the soft-cutoff version, we have

$$N(x,t) = \frac{\alpha(vt - x)}{[(vt-x)^2 + \alpha^2]^2} + \frac{\alpha(vt + x)}{[(vt+x)^2 + \alpha^2]^2}\,, \tag{4.85}$$

hence recovering the result in Ref. [36]. For the hard-cutoff version, we have Eq. (4.56) in the main text.

Next we calculate $C_{WW}(\ell,t)$. The Schwinger function to consider in this case is

$$\begin{aligned} F_{WW} &= \langle\exp(2i(p_1\theta_1 + p_2\theta_2 + p_3\theta_3 + p_4\theta_4))\rangle \\ &= \exp[2g\sum_{i<j} p_ip_jK(r_{ij})]\,, \end{aligned} \tag{4.86}$$

and the analytical continuation $K(x, \tau = it \pm 0^+) = H(x,t) \mp iG(x,t)$. We expand

$$\begin{aligned} C_{WW}(\ell,t) &= C_{V_2V_{-2}}(\ell,t) + C_{V_{-2}V_2}(\ell,t) \\ &+ C_{V_{-2}V_{-2}}(\ell,t) + C_{V_2V_2}(\ell,t) \\ &+ e^{-i4\pi\rho_0\ell}C_a(\ell,t) \\ &+ e^{i4\pi\rho_0\ell}C_b(\ell,t)\,, \end{aligned} \tag{4.87}$$

where

$$\begin{aligned} C_a(\ell,t) &= \frac{1}{2}\langle [V_{-2}(\ell,t), V_2(0)]^\dagger [V_2(\ell,t), V_{-2}(0)]\rangle \\ C_b(\ell,t) &= \frac{1}{2}\langle [V_2(\ell,t), V_{-2}(0)]^\dagger [V_{-2}(\ell,t), V_2(0)]\rangle\ . \end{aligned}$$

Suitable combinations of the analytical continuations give us

$$\begin{aligned} C_{V_{-2}V_2}(\ell,t) &= C_{V_{-2}V_2}(\ell,t) = C_{V_{-2}V_{-2}}(\ell,t) = C_{V_2V_2}(\ell,t) \\ &= 2\sin^2(2gG(\ell,t))\,, \end{aligned} \tag{4.88}$$

and

$$\begin{aligned} C_a(\ell,t) &= C_b(\ell,t) \\ &= 2\exp[-8gH(\ell,t)]\sin^2[2gG(\ell,t)]\ . \end{aligned}$$

So we have

$$C_{WW}(\ell,t) = 2[4 + 2\cos(4\pi\rho_0\ell)\exp(-8gH)]\sin^2(2gG)\ .$$

Note that for the soft-cutoff version,

$$G(\ell,t) = \frac{1}{2}(\arctan(\frac{vt+\ell}{\alpha}) + \arctan(\frac{vt-\ell}{\alpha}))\,, \tag{4.89}$$

recovering the result of $C_{V_{-2}V_2}(\ell,t)$ in Ref. [36].

Finally, we present the calculations of $C_{n_0w}(\ell,t)$, $C_{Wn_0}(\ell,t)$, $C_{\rho_0\rho_0WW}(\ell,t)$, $C_{\rho_0WW\rho_0}(\ell,t)$. The relevant Schwinger function in this case is

$$\begin{aligned} F_{\rho_0\rho_0WW} &= \pi^{-2}\partial_{x_1}\partial_{x_2}\langle\theta_1\theta_2W(r_3)W(r_4)\rangle\ . \\ &= \frac{g}{\pi^2}D(r_{12})\exp[2gF(r_{34})]\cos(2\pi\rho_0x_{34}) \end{aligned} \tag{4.90}$$

We therefore obtain, upon analytical continuations,

$$\begin{aligned} C_{\rho_0W}(\ell,t) &= C_{W\rho_0}(\ell,t) = 0 \\ C_{\rho_0\rho_0WW}(\ell,t) &= \frac{-4g}{\pi^2}\cos(2\pi\rho_0\ell)e^{-2gH}N(\ell,t)\sin^2(2gG(\ell,t)) \\ C_{\rho_0WW\rho_0}(\ell,t) &= 0\ . \end{aligned}$$

Collecting all the pieces, we obtain the result Eq. (4.55) in the main text.

Appendix H: Comparison of $G(\ell, t)$ in hard-cutoff and soft-cutoff regularizations

For the readers' benefit, here we collect and compare the behavior of the function $G(\ell, t)$ in different regions of interest for the two regularization schemes. We denote $G(\ell, t; \Lambda)$ the function defined via the hard-cutoff regularization and given in Eq. (4.58), while $G(\ell, t; \alpha)$ is the function defined via the soft-cutoff regularization, given in Ref. [36] or Eq. (4.89).

In the short-time region $t \ll 1/(v_B \Lambda)$ or $t \ll \alpha/v_B$, we have the behavior

$$\begin{aligned} G(\ell, t; \Lambda) &\sim v_B t \frac{\sin(\Lambda \ell)}{\ell} \\ &+ (v_B t)^3 \frac{2\Lambda\ell \cos(\Lambda\ell) + (-2 + \Lambda^2\ell^2)\sin(\Lambda\ell)}{6\ell^3} ; \\ G(\ell, t; \alpha) &\sim v_B t \frac{\alpha}{\alpha^2 + \ell^2} - (v_B t)^3 \frac{\alpha(\alpha^2 - 3\ell^2)}{3(\alpha^2 + \ell^2)^3} . \end{aligned}$$

In the region where one follows the rays $\ell = vt$, and $v > v_B$, or around the wavefront,

$$\begin{aligned} G(\ell, t; \Lambda) &\sim \frac{\pi}{4} + \frac{1}{2}\mathrm{Si}[\Lambda(v_B t - \ell)] ; \\ G(\ell, t; \alpha) &\sim \frac{\pi}{4} + \frac{1}{2}\arctan\left(\frac{v_B t - \ell}{\alpha}\right) , \end{aligned}$$

both showing non-broadening wavefront behavior.

Finally, in the long-time region, $t \gg \ell/v_B$,

$$\begin{aligned} G(\ell, t; \Lambda) &\sim \frac{\pi}{2} - \frac{\cos(\Lambda v_B t)\cos(\Lambda\ell)}{\Lambda v_B t} \\ &- \frac{\sin(\Lambda v_B t)\cos(\Lambda\ell)}{(\Lambda v_B t)^2} ; \\ G(\ell, t; \alpha) &\sim \frac{\pi}{2} - \frac{\alpha}{v_B t} + O(t^{-3}) . \end{aligned}$$

We therefore see that in all the cases of interest, the hard-cutoff and soft-cutoff expressions are not qualitatively different except for oscillating factors for the hard cutoff. We used the hard cutoff to compare with our fully controlled lattice calculation in the long-range hopping model, since such cutoff mimics the finite band width in the lattice models.

Appendix I: Calculation of the boson-boson OTOC in the hard-core boson models

To compute the commutator function, it suffices to calculate the OTOC $F_{XX}(\ell, t) = \langle X_0(t) X_\ell(0) X_0(t) X_\ell(0) \rangle$. For simplicity, we denote the left end-point of the lattice as $e \equiv -L/2+1$. Defining the fermions $A_j = c_j^\dagger + c_j$ and $B_j = c_j^\dagger - c_j$, we can express

$$\begin{aligned} F_{XX}(\ell,t) = \langle (A_e(t) \quad \dots \quad & A_0(t) B_e(t) \dots B_{-1}(t) \\ A_e \quad \dots \quad & A_\ell B_e \dots B_{\ell-1})^2 \rangle \,, \end{aligned} \tag{4.91}$$

and calculate it by Wick's theorem.

We need the following two-point correlation functions involving operators A and B:

$$\begin{aligned} \langle A_n(t) A_m \rangle &= -\langle B_n(t) B_m \rangle \\ &= \frac{2}{L+1} \sum_k \sin(kn) \sin(km) \\ &\times \ [\cos(\epsilon_k t) - i \sin(\epsilon_k t) \tanh(\frac{\beta \epsilon_k}{2})] \,, \\ \langle A_n(t) B_m \rangle &= -\langle B_n(t) A_m \rangle \\ &= \frac{2}{L+1} \sum_k \sin(kn) \sin(km) \\ &\times \ [\cos(\epsilon_k t) \tanh(\frac{\beta \epsilon_k}{2}) - i \sin(\epsilon_k t)] \,, \end{aligned}$$

where the summation is running through the set $k = p\pi/(L+1), p = 1 \dots L$.

We define $[\mathtt{AA}](t)^{n=a:b}_{m=c:d}$ as a matrix with matrix elements $\langle A_n(t) A_m \rangle$, having row index n from a to b and column index m from c to d, and similarly for $[\mathtt{AB}](t)$, $[\mathtt{BA}](t)$, and $[\mathtt{BB}](t)$. We will need also $t = 0$ correlation functions $[\mathtt{AB}](0)$ and $[\mathtt{BA}](0)$, which we will denote as $[\mathtt{AB}]$ and $[\mathtt{BA}]$, i.e., by simply omitting the time argument. We also denote the identity matrix as $[\mathtt{I}]$ and the zero matrix as $[\mathbb{0}]$, with their sizes specified implicitly according to the context.

Now define matrices

$$S = \begin{pmatrix} [\mathbb{0}] & [\mathtt{AB}]^{n=e:0}_{m=e:-1} & [\mathtt{AA}](t)^{n=e:0}_{m=e:\ell} & [\mathtt{AB}](t)^{n=e:0}_{m=e:\ell-1} \\ - & [\mathbb{0}] & [\mathtt{BA}](t)^{n=e:-1}_{m=1:\ell} & [\mathtt{BB}](t)^{n=e:-1}_{m=1:\ell-1} \\ - & - & [\mathbb{0}] & [\mathtt{AB}]^{n=e:0}_{m=e:-1} \\ - & - & - & [\mathbb{0}] \end{pmatrix},$$

where the rest of the matrix elements are defined such that $S^T = -S$, and

$$R = \begin{pmatrix} [\mathtt{I}] & [\mathtt{AB}]^{n=e:0}_{m=e:-1} & [\mathtt{AA}](t)^{n=e:0}_{m=e:\ell} & [\mathtt{AB}](t)^{n=e:0}_{m=e:\ell-1} \\ [\mathtt{BA}]^{n=e:-1}_{m=e:0} & -[\mathtt{I}] & [\mathtt{BA}](t)^{n=e:-1}_{m=1:\ell} & [\mathtt{BB}](t)^{n=e:-1}_{m=1:\ell-1} \\ [\mathtt{AA}](-t)^{n=e:\ell}_{m=e:0} & [\mathtt{AB}](-t)^{n=e:\ell}_{m=e:-1} & [\mathtt{I}] & [\mathtt{AB}]^{n=e:0}_{m=e:-1} \\ [\mathtt{BA}](-t)^{n=e:\ell-1}_{m=e:0} & [\mathtt{BB}](-t)^{n=e:\ell-1}_{m=e:-1} & [\mathtt{BA}]^{n=e:\ell-1}_{m=1:\ell} & -[\mathtt{I}] \end{pmatrix}.$$

Using Wick's theorem, we then have

$$F_{XX} = \mathrm{Pf}\begin{bmatrix} S & R \\ -R^T & S \end{bmatrix}, \tag{4.92}$$

where Pf[Q] evaluates the Pfaffian of an antisymmetric matrix Q.

References

[1] A. I. Larkin, and Y. N. Ovchinnikov, "Quasiclassical method in the theory of superconductivity", Sov. Phys. JETP **28**, 1200–1205 (1969).

[2] Alexei Kitaev, "A Simple Model of Quantum Holography", Talk at KITP (2015).

[3] A. Kitaev, and S. J. Suh, "The soft mode in the sachdev-ye-kitaev model and its gravity dual", J. High Energ. Phys. **2018**, 183 (2018).

[4] J. Maldacena, S. H. Shenker, and D. Stanford, "A bound on chaos", J. High Energ. Phys. **2016**, 106 (2016).

[5] J. S. Cotler, D. Ding, and G. R. Penington, "Out-of-time-order operators and the butterfly effect", Ann. Phys. **396**, 318–333 (2018).

[6] T. Scaffidi, and E. Altman, "Semiclassical Theory of Many-Body Quantum Chaos and Its Bound", arXiv:1711.04768.

[7] I. L. Aleiner, L. Faoro, and L. B. Ioffe, "Microscopic Model of Quantum Butterfly Effect: Out-of-Time-Order Correlators and Traveling Combustion Waves", Ann. Phys. **375**, 378–406 (2016).

[8] A. Bohrdt, C. B. Mendl, M. Endres, and M. Knap, "Scrambling and Thermalization in a Diffusive Quantum Many-Body System", New J. Phys. **19**, 063001 (2017).

[9] Y. Werman, S. A. Kivelson, and E. Berg, "Quantum Chaos in an Electron-Phonon Bad Metal", arXiv:1705.07895.

[10] H. Shen, P. Zhang, R. Fan, and H. Zhai, "Out-of-Time-Order Correlation at a Quantum Phase Transition", Phys. Rev. B **96**, 054503 (2017).

[11] D. Chowdhury, and B. Swingle, "Onset of Many-Body Chaos in the O(N) Model", Phys. Rev. D **96**, 065005 (2017).

[12] A. A. Patel, and S. Sachdev, "Quantum Chaos on a Critical Fermi Surface", Proc. Natl. Acad. Sci. **114**, 1844–1849 (2017).

[13] A. A. Patel, D. Chowdhury, S. Sachdev, and B. Swingle, "Quantum Butterfly Effect in Weakly Interacting Diffusive Metals", Phys. Rev. X **7**, 031047 (2017).

[14] B. Dóra, and R. Moessner, "Out-of-Time-Ordered Density Correlators in Luttinger Liquids", Phys. Rev. Lett. **119**, 026802 (2017).

[15] Y. Huang, Y.-L. Zhang, and X. Chen, “Out-of-Time-Ordered Correlators in Many-Body Localized Systems”, Ann. Phys. **529**, 1600318–n/a (2017).

[16] B. Swingle, and D. Chowdhury, “Slow Scrambling in Disordered Quantum Systems”, Phys. Rev. B **95**, 060201 (2017).

[17] X. Chen, T. Zhou, D. A. Huse, and E. Fradkin, “Out-of-time-order correlations in many-body localized and thermal phases”, Annalen der Physik **529**, 1600332 (2017).

[18] R. Fan, P. Zhang, H. Shen, and H. Zhai, “Out-of-Time-Order Correlation for Many-Body Localization”, Sci. Bull. **62**, 707–711 (2017).

[19] K. Slagle, Z. Bi, Y.-Z. You, and C. Xu, “Out-of-Time-Order Correlation in Marginal Many-Body Localized Systems”, Phys. Rev. B **95**, 165136 (2017).

[20] E. B. Rozenbaum, S. Ganeshan, and V. Galitski, “Lyapunov Exponent and Out-of-Time-Ordered Correlator’s Growth Rate in a Chaotic System”, Phys. Rev. Lett. **118**, 086801 (2017).

[21] K. Hashimoto, K. Murata, and R. Yoshii, “Out-of-Time-Order Correlators in Quantum Mechanics”, J. High Energ. Phys. **2017**, 138 (2017).

[22] I. Kukuljan, S. Grozdanov, and T. Prosen, “Weak Quantum Chaos”, Phys. Rev. B **96**, 060301 (2017).

[23] S. H. Shenker, and D. Stanford, “Black Holes and the Butterfly Effect”, J. High Energ. Phys. **2014**, 67 (2014).

[24] D. A. Roberts, and D. Stanford, “Diagnosing Chaos Using Four-Point Functions in Two-Dimensional Conformal Field Theory”, Phys. Rev. Lett. **115**, 131603 (2015).

[25] P. Hosur, X.-L. Qi, D. A. Roberts, and B. Yoshida, “Chaos in Quantum Channels”, J. High Energ. Phys. **2016**, 4 (2016).

[26] N. Yunger-Halpern, “Jarzynski-like Equality for the out-of-Time-Ordered Correlator”, Phys. Rev. A **95**, 012120 (2017).

[27] N. Yunger Halpern, B. Swingle, and J. Dressel, “Quasiprobability behind the Out-of-Time-Ordered Correlator”, Phys. Rev. A **97**, 042105 (2018).

[28] D. A. Roberts, D. Stanford, and L. Susskind, “Localized Shocks”, J. High Energ. Phys. **2015**, 51 (2015).

[29] C. W. von Keyserlingk, T. Rakovszky, F. Pollmann, and S. L. Sondhi, “Operator Hydrodynamics, OTOCs, and Entanglement Growth in Systems without Conservation Laws”, Phys. Rev. X **8**, 021013 (2018).

[30] A. Nahum, J. Ruhman, S. Vijay, and J. Haah, “Quantum Entanglement Growth Under Random Unitary Dynamics”, Phys. Rev. X **7**, 031016 (2017).

[31] A. Nahum, S. Vijay, and J. Haah, “Operator Spreading in Random Unitary Circuits”, Phys. Rev. X **8**, 021014 (2018).

[32] V. Khemani, A. Vishwanath, and D. A. Huse, “Operator Spreading and the Emergence of Dissipative Hydrodynamics under Unitary Evolution with Conservation Laws”, Phys. Rev. X **8**, 031057 (2018).

[33] T. Rakovszky, F. Pollmann, and C. W. von Keyserlingk, “Diffusive Hydrodynamics of Out-of-Time-Ordered Correlators with Charge Conservation”, Phys. Rev. X **8**, 031058 (2018).

[34] A. Chapman, and A. Miyake, “Classical simulation of quantum circuits by dynamical localization: analytic results for pauli-observable scrambling in time-dependent disorder”, Phys. Rev. A **98**, 012309 (2018).

[35] D. A. Roberts, and B. Swingle, “Lieb-Robinson and the Butterfly Effect”, Phys. Rev. Lett. **117**, 091602 (2016).

[36] B. Dóra, and R. Moessner, “Out-of-Time-Ordered Density Correlators in Luttinger Liquids”, Phys. Rev. Lett. **119**, 026802 (2017).

[37] C.-J. Lin, and O. I. Motrunich, “Out-of-Time-Ordered Correlators in a Quantum Ising Chain”, Phys. Rev. B **97**, 144304 (2018).

[38] S. Xu, and B. Swingle, “Accessing Scrambling Using Matrix Product Operators”, arXiv:1802.00801.

[39] V. Khemani, D. A. Huse, and A. Nahum, “Velocity-dependent lyapunov exponents in many-body quantum, semiclassical, and classical chaos”, Phys. Rev. B **98**, 144304 (2018).

[40] J. Maldacena, S. H. Shenker, and D. Stanford, “A Bound on Chaos”, J. High Energ. Phys. **2016**, 106 (2016).

[41] A. Kitaev, and S. J. Suh, “The Soft Mode in the Sachdev-Ye-Kitaev Model and Its Gravity Dual”, J. High Energ. Phys. **2018**, 183 (2018).

[42] I. L. Aleiner, L. Faoro, and L. B. Ioffe, “Microscopic Model of Quantum Butterfly Effect: Out-of-Time-Order Correlators and Traveling Combustion Waves”, Ann. Phys. **375**, 378–406 (2016).

[43] Y. Gu, X.-L. Qi, and D. Stanford, “Local Criticality, Diffusion and Chaos in Generalized Sachdev-Ye-Kitaev Models”, J. High Energ. Phys. **2017**, 125 (2017).

[44] X. Chen, T. Zhou, and C. Xu, “Measuring the distance between quantum many-body wave functions”, Journal of Statistical Mechanics: Theory and Experiment **2018**, 073101 (2018).

[45] S. Sachdev, *Quantum Phase Transitions*, 2nd ed. (Cambridge University Press, 2011).

[46] D. Rossini, S. Suzuki, G. Mussardo, G. E. Santoro, and A. Silva, “Long Time Dynamics Following a Quench in an Integrable Quantum Spin Chain: Local versus Nonlocal Operators and Effective Thermal Behavior”, Phys. Rev. B **82**, 144302 (2010).

[47] P. Calabrese, F. H. L. Essler, and M. Fagotti, “Quantum Quench in the Transverse Field Ising Chain I: Time Evolution of Order Parameter Correlators”, J Stat. Mech. Theory Exp. **2012**, P07016 (2012).

[48] F. H. L. Essler, and M. Fagotti, “Quench Dynamics and Relaxation in Isolated Integrable Quantum Spin Chains”, J. Stat. Mech. **2016**, 064002 (2016).

[49] V. Khemani, A. Vishwanath, and D. A. Huse, “Operator Spreading and the Emergence of Dissipative Hydrodynamics under Unitary Evolution with Conservation Laws”, Phys. Rev. X **8**, 031057 (2018).

[50] D. A. Roberts, and B. Swingle, “Lieb-Robinson and the Butterfly Effect”, Phys. Rev. Lett. **117**, 091602 (2016).

[51] X. Chen, T. Zhou, and C. Xu, “Measuring the Distance between Quantum Many-Body Wave Functions”,

[52] B. M. McCoy, E. Barouch, and D. B. Abraham, “Statistical Mechanics of the xy Model. IV. Time-Dependent Spin-Correlation Functions”, Phys. Rev. A **4**, 2331–2341 (1971).

[53] H. Capel, and J. Perk, “Autocorrelation Function of the X-Component of the Magnetization in the One-Dimensional XY-Model”, Phys. A **87**, 211–242 (1977).

[54] J. Perk, and H. Capel, “Time-Dependent Xx-Correlation Functions in the One-Dimensional XY-Model”, Phys. A **89**, 265–303 (1977).

[55] J. Perk, H. Capel, G. Quispel, and F. Nijhoff, “Finite-Temperature Correlations for the Ising Chain in a Transverse Field”, Phys. A **123**, 1–49 (1984).

[56] A. R. Its, A. G. Izergin, V. E. Korepin, and N. A. Slavnov, “Temperature Correlations of Quantum Spins”, Phys. Rev. Lett. **70**, 1704–1706 (1993).

[57] J. H. H. Perk, and H. Au-Yang, “New Results for the Correlation Functions of the Ising Model and the Transverse Ising Chain”, J. Stat. Mech. **135**, 599–619 (2009).

[58] U. Brandt, and K. Jacoby, “Exact Results for the Dynamics of One-Dimensional Spin-Systems”, Z. Für Phys. B Condens. Matter **25**, 181–187 (1976).

[59] C.-J. Lin, and O. I. Motrunich, “Quasiparticle Explanation of the Weak-Thermalization Regime under Quench in a Nonintegrable Quantum Spin Chain”, Phys. Rev. A **95**, 023621 (2017).

[60] F. D. M. Haldane, “’Luttinger Liquid Theory’ of One-Dimensional Quantum Fluids. I. Properties of the Luttinger Model and Their Extension to the General 1D Interacting Spinless Fermi Gas”, J. Phys. C Solid State Phys. **14**, 2585 (1981).

[61] F. D. M. Haldane, “Effective Harmonic-Fluid Approach to Low-Energy Properties of One-Dimensional Quantum Fluids”, Phys. Rev. Lett. **47**, 1840–1843 (1981).

[62] T. Giamarchi, *Quantum Physics in One Dimension* (Clarendon Press, Dec. 2003).

[63] F. W. J. Olver, “Some New Asymptotic Expansions for Bessel Functions of Large Orders”, Math. Proc. Camb. Philos. Soc. **48**, 414–427 (1952).

[64] D. J. Luitz, and Y. Bar Lev, “Emergent locality in systems with power-law interactions”, Phys. Rev. A **99**, 010105 (2019).

[65] Y. Gu, and X.-L. Qi, “Fractional Statistics and the Butterfly Effect”, J. High Energ. Phys. **2016**, 129 (2016).

[66] A. Imambekov, T. L. Schmidt, and L. I. Glazman, “One-Dimensional Quantum Liquids: Beyond the Luttinger Liquid Paradigm”, Rev. Mod. Phys. **84**, 1253–1306 (2012).

[67] S. Gopalakrishnan, “Operator Growth and Eigenstate Entanglement in an Interacting Integrable Floquet System”, Phys. Rev. B **98**, 060302 (2018).

Chapter 5

QUANTUM MANY-BODY SCAR STATES

Understanding quantum thermalization in isolated systems has attracted a lot of attention, due to both developments in cold atom experiments and fundamental theoretical interest. The eigenstate thermalization hypothesis (ETH) has emerged as a paradigmatic mechanism for quantum thermalization [1, 2]. ETH postulates that a generic many-body system thermalizes at the level of individual eigenstates: eigenstates at the same energy density give the same expectation values of “local-enough" observables. The strong version of the ETH requires this on *every* eigenstate. While an analytical proof is elusive, many numerical studies provided strong corroborations [3–6]. However, some systems showed atypical dynamics [7, 8] due to special low-energy states [9–11].

A recent Rydberg cold atom experiment [12] hinted at a new scenario, where the system exhibited atypical quench dynamics starting from a charge density wave (CDW) state at effective temperature $T = \infty$. In contrast, a uniform initial state with the same energy density showed the expected thermalization behavior. References [13, 14] proposed that this phenomenon is related to the presence of special eigenstates–*quantum many-body scar states*–which violate the ETH in the otherwise thermal spectrum, analogous to the nonergodic single-particle scar wavefunctions inside the chaotic single-particle spectrum [15].

Another nonintegrable system hosting nonthermal eigenstates is the Affleck-Lieb-Kennedy-Tasaki model [16]. Reference [17] constructed families of exact eigenstates in this model. Using matrix product states (MPS), furthermore, Ref. [18] showed that these exact eigenstates with a finite energy density have logarithmic entanglement scaling in the subsystem size. These papers thus provided an important analytical demonstration of exact scar states that violate the ETH [19]. Other works [20, 21] also proposed a special construction to embed nonthermal eigenstates into the many-body spectrum.

Remarkably, in the same Rydberg atom Hamiltonian studied in Refs. [12–14, 22, 23], we have discovered some exact scar states with a *finite bond dimension* at energy density corresponding to $T = \infty$. Our exact MPS description shows that these exact scar states have constant entanglement scaling and are, hence, even more “nonthermal” than the exact scar states at a finite energy density in Refs. [17, 18]. Furthermore, these exact scar states break the lattice translation symmetry, despite being at $T = \infty$. Thus, the strong ETH is violated in the Rydberg atom chain. Using a “single-mode approximation” (SMA) and generaizing it to a “multimode approximation" (MMA) on top of our exact scar states, we also find good approximations to nearby scar states, potentially relating the existence of other scar states to our exact states.

5.1 Constrained Hilbert space and the PXP model

Consider Rydberg atoms on a chain with L sites, and denote $|0\rangle$ as the atomic ground state and $|1\rangle$ as the Rydberg excitation. The Rydberg blockade prohibits states with $|\dots 11 \dots\rangle$ on any two neighboring sites [12]. Despite the resulting non-tensor-product structure of the Hilbert space, one can still have the ETH concept [24].

The dynamics of this system is described by the so-called PXP model:

$$H = \sum_{j=2}^{L-1} P_{j-1} X_j P_{j+1} + H_1 + H_L \, , \tag{5.1}$$

where $P = |0\rangle\langle 0|$ is the projector to the Rydberg atom ground state and $X = |0\rangle\langle 1| + |1\rangle\langle 0|$ describes transitions between the ground and excited states. (Previous works [25–28] studied low-energy states of related Hamiltonians.) For periodic boundary conditions (PBC), we have $H_1 = P_L X_1 P_2$ and $H_L = P_{L-1} X_L P_1$, while for open boundary conditions (OBC), $H_1 = X_1 P_2$ and $H_L = P_{L-1} X_L$. For PBC, the Hamiltonian has translation symmetry T_x and inversion symmetry I, while for OBC, there is only inversion symmetry relative to the midpoint, $I : j \to L - j + 1$. Furthermore, one can define “particle-hole transformation” $C_{\text{ph}} = \prod_j Z_j$, where $Z = |1\rangle\langle 1| - |0\rangle\langle 0|$. This satisfies $C_{\text{ph}} H C_{\text{ph}}^{-1} = -H$, which guarantees that the spectrum is symmetric around zero energy; moreover, the intertwining of C_{ph} with the inversion symmetry produces exponentially many zero-energy eigenstates [14, 29].

The above Hamiltonian, despite its simple appearance, is not trivially solvable. While its level-spacing statistics indicates its nonintegrability [14], a recent work [23] has suggested that it could be a deformation from some integrable Hamiltonian.

Inspired by Ref. [17], we inspected entanglement spectra of eigenstates of the PXP model for OBC and discovered eigenstates at $E = \pm\sqrt{2}$ with a finite bond dimension. We then reverse-engineered a simple MPS representation for these eigenstates and further identified two more exact eigenstates with $E = 0$ for OBC and two exact eigenstates at $E = 0$ for PBC. Hence, these states analytically demonstrate that the PXP Hamiltonian violates the strong ETH and are therefore *exact* quantum many-body scar states.

5.2 Exact scar states in the periodic boundary condition

These eigenstates exist for even L (assumed throughout) and are expressed using MPSs. We define 2×3 and 3×2 matrices

$$B^0 = \begin{pmatrix} 1 & 0 & 0 \\ 0 & 1 & 0 \end{pmatrix}, \quad B^1 = \sqrt{2}\begin{pmatrix} 0 & 0 & 0 \\ 1 & 0 & 1 \end{pmatrix}, \tag{5.2}$$

$$C^0 = \begin{pmatrix} 0 & -1 \\ 1 & 0 \\ 0 & 0 \end{pmatrix}, \quad C^1 = \sqrt{2}\begin{pmatrix} 1 & 0 \\ 0 & 0 \\ -1 & 0 \end{pmatrix}. \tag{5.3}$$

Two (unnormalized) exact scar states for PBC can be expressed as

$$|\Phi_1\rangle = \sum_{\{\sigma\}} \mathrm{Tr}[B^{\sigma_1} C^{\sigma_2} \dots B^{\sigma_{L-1}} C^{\sigma_L}] |\sigma_1 \dots \sigma_L\rangle, \tag{5.4}$$

and $|\Phi_2\rangle = T_x|\Phi_1\rangle$, where $\sigma_j = 0$ or 1. The wavefunctions satisfy the constraints since $B^1C^1 = 0_{2\times2}$ and $C^1B^1 = 0_{3\times3}$. Since these states are at $E = 0$, their effective temperature is $T = \infty$.

The norm of the states is $\langle\Phi_i|\Phi_i\rangle = 3^{L_b} + 2 + (-1)^{L_b}$, where $L_b \equiv L/2$. The two states are not orthogonal and have overlap $\langle\Phi_1|\Phi_2\rangle = 2[(\sqrt{2}-1)^{L_b} + (-1)^{L_b}(\sqrt{2}+1)^{L_b}]$; however, they are linearly independent for $L_b > 3$ [for $L_b \leq 3$, we happen to have $|\Phi_2\rangle = (-1)^{L_b}|\Phi_1\rangle$]. For $L_b > 3$, the states $|\Phi_{1,2}\rangle$ in fact break the translation symmetry T_x, while by construction they are invariant under T_x^2. One can form degenerate states $|\Phi_{K=0/\pi}\rangle = |\Phi_1\rangle \pm |\Phi_2\rangle$ that carry definite momenta 0 and π, which can be viewed as a finite-size signature of the T_x breaking that appears in the thermodynamic limit.

Proof of exact scar states in PBC

Here we prove that $H|\Phi_1\rangle = 0$. To prove this, it is easier to work in the blocked reformulation of the Hamiltonian: We block two sites $2b-1, 2b$ into one "block-site", with allowed block states (00), (10), and (01) denotes as O, L, and R respectively; the Rydberg constraint further disallows configurations with RL on consecutive blocks. The number of blocks is $L_b = L/2$, and recall that throughout we assume that L

is even. In the blocked representation, the Hamiltonian can be written as a sum of two-body terms:

$$\begin{aligned} H &= \sum_{b=1}^{L_b} h_{b,b+1} \,, \\ h_{b,b+1} &= (|R\rangle\langle O| + |O\rangle\langle R|)_b \otimes (I - |L\rangle\langle L|)_{b+1} \\ &\quad + (I - |R\rangle\langle R|)_b \otimes (|L\rangle\langle O| + |O\rangle\langle L|)_{b+1} \,. \end{aligned} \tag{5.5}$$

The state $|\Phi_1\rangle$ can be written in the blocked representation as an MPS of bond dimension 2, namely

$$|\Phi_1\rangle = \sum_{\{s\}} \mathrm{Tr}[A^{s_1} \dots A^{s_{L_b}}] |s_1 \dots s_{L_b}\rangle \,, \tag{5.6}$$

where we have introduced blocked matrices $A^{(\sigma_1\sigma_2)} = B^{\sigma_1} C^{\sigma_2}$. Explicitly,

$$A^O = \begin{pmatrix} 0 & -1 \\ 1 & 0 \end{pmatrix} \,, \quad A^R = \begin{pmatrix} \sqrt{2} & 0 \\ 0 & 0 \end{pmatrix} \,, \quad A^L = \begin{pmatrix} 0 & 0 \\ 0 & -\sqrt{2} \end{pmatrix} \,. \tag{5.7}$$

One can easily check that $A^R A^L = 0$, so the state satisfies the Rydberg constraint between the blocks. Interestingly, these matrices also satisfy $A^L A^R = 0$, so this state also disallows LR on consecutive blocks.

We first examine how the genuinely two-body part of the Hamiltonian term $h_{b,b+1}$, namely $h^{(2)}_{b,b+1} \equiv -(|R\rangle\langle O| + |O\rangle\langle R|)_b \otimes (|L\rangle\langle L|)_{b+1} - (|R\rangle\langle R|)_b \otimes (|L\rangle\langle O| + |O\rangle\langle L|)_{b+1}$ operates on $|\Phi_1\rangle$. The special property $A^R A^L = 0$ leaves us only the part $-(|R\rangle\langle O|)_b \otimes (|L\rangle\langle L|)_{b+1} - (|R\rangle\langle R|)_b \otimes (|L\rangle\langle O|)_{b+1}$. It is easy to check that the matrices also satisfy $A^O A^L + A^R A^O = 0$, and hence we conclude that $h^{(2)}_{b,b+1}|\Phi_1\rangle = 0$.

We now collect the one-body parts of the Hamiltonian and after convenient grouping obtain:

$$H' = \sum_{b=1}^{L_b} \Big(|R\rangle\langle O| + |O\rangle\langle R| + |L\rangle\langle O| + |O\rangle\langle L| \Big)_b \,. \tag{5.8}$$

Consider action of a term associated with block b on $|\Phi_1\rangle$:

$$\Big(|R\rangle\langle O| + |O\rangle\langle R| + |L\rangle\langle O| + |O\rangle\langle L| \Big)_b |\Phi_1\rangle = \sum_{\{s\}} \mathrm{Tr}[A^{s_1} \dots F^{s_b} \dots A^{s_{L_b}}] |s_1 \dots s_{L_b}\rangle \,, \tag{5.9}$$

where

$$F^O = \begin{pmatrix} \sqrt{2} & 0 \\ 0 & -\sqrt{2} \end{pmatrix} \,, \quad F^R = F^L = \begin{pmatrix} 0 & -1 \\ 1 & 0 \end{pmatrix} \,. \tag{5.10}$$

Therefore, we have

$$H|\Phi_1\rangle = H'|\Phi_1\rangle = \sum_{b=1}^{L_b} \sum_{\{s\}} \mathrm{Tr}[A^{s_1} \dots F^{s_b} \dots A^{s_{L_b}}]|s_1 \dots s_{L_b}\rangle \,. \tag{5.11}$$

It is easy to verify that $F^s = XA^s - A^s X$, where $X = \frac{1}{\sqrt{2}}\sigma_x$. Substituting this in Eq. (5.11), we therefore see that $H|\Phi_1\rangle = 0$. The fact that $|\Phi_2\rangle$ is also an eigenstate follows from the translational invariance of the Hamiltonian: $H|\Phi_2\rangle = HT_x|\Phi_1\rangle = T_x H|\Phi_1\rangle = 0$.

It is instructive to see an alternative proof how the sum of the one-body terms H' annihilates Φ_1 (which will be also useful later for developing intuition about our single-mode approximation constructed on top of $|\Phi_1\rangle$). To this end, we first transform to the basis diagonalizing the one-body terms. On each block-site, the eigenvalues are $\sqrt{2}$, $-\sqrt{2}$, and 0, and the corresponding eigenvectors are

$$\begin{aligned}
|\mathbf{+}\rangle_b &\equiv \frac{1}{2}\left(|R\rangle + |L\rangle + \sqrt{2}|O\rangle\right)_b \,, \\
|\mathbf{-}\rangle_b &\equiv \frac{1}{2}\left(|R\rangle + |L\rangle - \sqrt{2}|O\rangle\right)_b \,, \\
|\mathbf{0}\rangle_b &\equiv \frac{1}{\sqrt{2}}\left(|R\rangle - |L\rangle\right)_b \,.
\end{aligned} \tag{5.12}$$

Hence we have

$$H' = \sqrt{2}\sum_{b=1}^{L_b}\left(|\mathbf{+}\rangle\langle\mathbf{+}| - |\mathbf{-}\rangle\langle\mathbf{-}|\right)_b = \sqrt{2}(N_{\mathbf{+}} - N_{\mathbf{-}})\,, \tag{5.13}$$

where $N_{\pm} \equiv \sum_{b=1}^{L_b}(|\pm\rangle\langle\pm|)_b$ simply count numbers of **+** vs **—** states on the block-site lattice.

In the new basis, we can write $|\Phi_1\rangle$ as an MPS with matrices

$$\begin{aligned}
A^{\pm} &= V\frac{1}{2}\left(A^R + A^L \pm \sqrt{2}A^O\right)V^{-1}\,, \\
A^{\mathbf{0}} &= V\frac{1}{\sqrt{2}}\left(A^R - A^L\right)V^{-1}\,,
\end{aligned}$$

where it was also convenient to perform an additional gauge transformation with $V = \frac{1}{\sqrt{2}}\begin{pmatrix} 1 & 1 \\ 1 & -1 \end{pmatrix}$. The resulting matrices are

$$A^{\mathbf{+}} = \begin{pmatrix} 0 & \sqrt{2} \\ 0 & 0 \end{pmatrix}, \quad A^{\mathbf{-}} = \begin{pmatrix} 0 & 0 \\ \sqrt{2} & 0 \end{pmatrix}, \quad A^{\mathbf{0}} = \begin{pmatrix} 1 & 0 \\ 0 & 1 \end{pmatrix}. \tag{5.14}$$

Using properties $(A^{\mathbf{+}})^2 = (A^{\mathbf{-}})^2 = 0$, $A^{\mathbf{+}}A^{\mathbf{-}} = \mathrm{diag}(2,0)$, and the fact that $A^{\mathbf{0}}$ is identity matrix, it is now easy to expand $|\Phi_1\rangle$ in the $\pm, \mathbf{0}$ basis. In particular, we see that for basis vectors with non-trivial contributions to $|\Phi_1\rangle$, each $\mathbf{+}$ must be followed by $\mathbf{-}$, with possibly intervening $\mathbf{0}$'s in any number. This immediately implies that in each such basis vector we have $N_+ = N_-$; hence, $|\Phi_1\rangle$ is indeed annihilated by the sum of the one-body terms H'.

It is interesting to note that there is a precise relation between our exact eigenstate $|\Phi_1\rangle$ in the blocked representation and the celebrated AKLT state in a spin-1 chain. Specifically, we can perform the following gauge transformation

$$\begin{aligned}\mathrm{Tr}[A^{s_1}A^{s_2}A^{s_3}A^{s_4}\dots] &= \mathrm{Tr}[A^{s_1}UU^{-1}A^{s_2}A^{s_3}UU^{-1}A^{s_4}\dots]\\ &= \mathrm{Tr}[(A')^{s_1}(A'')^{s_2}(A')^{s_3}(A'')^{s_4}\dots]\end{aligned}$$

with $U = \sigma^x$ Pauli matrix and $(A')^s = A^sU$, $(A'')^s = U^{-1}A^s$. The matrices $(A')^s$ are precisely the matrices used in an MPS representation of the AKLT state with identification $s = O, R, L$ as $S_z = 0, 1, -1$ in the spin-1 chain, while the matrices $(A'')^s$ become the same as $(A')^s$ after a unitary transformation on the physical states that interchanges L and R states. Unfortunately, the Hamiltonians in the Rydberg problem and in the AKLT problem appear to be drastically different. Most notably, the Rydberg Hamiltonian has a nontrivial translation symmetry T_x by one Rydberg atom, while the AKLT Hamiltonian "knows" only about T_x^2 which is the simple translation symmetry by one block in the blocked variables. Also, the AKLT Hamiltonian has continuous spin rotation symmetry and is a sum of local terms that individually annihilate the AKLT state, which is not the case for the Rydberg Hamiltonian and our exact eigenstate. So far, we have not been able to utilize knowledge about the AKLT Hamiltonian in the Rydberg problem.

Calculations of norms and overlaps of $|\Phi_1\rangle$ and $|\Phi_2\rangle$

Calculations with the MPS state $|\Phi_1\rangle$ simplify in the blocked representation introduced previously. They heavily use the associated transfer matrix defined as

$$E_A = \sum_s (A^s)^* \otimes A^s = \begin{pmatrix} 2 & 0 & 0 & 1\\ 0 & 0 & -1 & 0\\ 0 & -1 & 0 & 0\\ 1 & 0 & 0 & 2 \end{pmatrix}, \tag{5.15}$$

and we immediately get

$$E_A^m = \frac{1}{2}\begin{pmatrix} 1+3^m & 0 & 0 & -1+3^m \\ 0 & 1+(-1)^m & -1+(-1)^m & 0 \\ 0 & -1+(-1)^m & 1+(-1)^m & 0 \\ -1+3^m & 0 & 0 & 1+3^m \end{pmatrix} . \tag{5.16}$$

The norm of the state is $\langle\Phi_1|\Phi_1\rangle = \mathrm{Tr}[E_A^{L_b}] = 3^{L_b}+2+(-1)^{L_b}$. Since $|\Phi_2\rangle = T_x|\Phi_1\rangle$, we have $\langle\Phi_2|\Phi_2\rangle = \langle\Phi_1|\Phi_1\rangle$.

To calculate the overlap between $|\Phi_1\rangle$ and $|\Phi_2\rangle$ used in the main text, it is convenient to introduce blocked matrices $D^{(\sigma_1\sigma_2)} = C^{\sigma_1}B^{\sigma_2}$. Specifically,

$$D^O = \begin{pmatrix} 0 & -1 & 0 \\ 1 & 0 & 0 \\ 0 & 0 & 0 \end{pmatrix}, \quad D^R = \begin{pmatrix} -\sqrt{2} & 0 & -\sqrt{2} \\ 0 & 0 & 0 \\ 0 & 0 & 0 \end{pmatrix}, \quad D^L = \begin{pmatrix} \sqrt{2} & 0 & 0 \\ 0 & 0 & 0 \\ -\sqrt{2} & 0 & 0 \end{pmatrix} . \tag{5.17}$$

To calculate $\langle\Phi_1|\Phi_2\rangle$, we need the transfer matrix

$$E_{AD} = \sum_s (A^s)^* \otimes D^s = \begin{pmatrix} \sqrt{2}D^R & -D^O \\ D^O & -\sqrt{2}D^L \end{pmatrix} , \tag{5.18}$$

which is a 6×6 matrix with eigenvalues $-\sqrt{2}-1$, $-\sqrt{2}-1$, 0, 0, $\sqrt{2}-1$, and $\sqrt{2}-1$. We therefore obtain $\langle\Phi_1|\Phi_2\rangle = \mathrm{Tr}[E_{AD}^{L_b}] = 2[(\sqrt{2}-1)^{L_b} + (-1)^{L_b}(\sqrt{2}+1)^{L_b}]$.

Translation symmetry breaking and symmetry properties

Let us examine properties of the state $|\Phi_1\rangle$ (properties of $|\Phi_2\rangle$ simply follow). First, the breaking of T_x in this state cannot be detected by any one-site observable, since the one-site reduced density matrices are the same for all sites, $\rho^{\text{one-site}} = \frac{2}{3}|0\rangle\langle 0| + \frac{1}{3}|1\rangle\langle 1|$ in the thermodynamic limit. In particular, for the Rydberg excitation number $n_j = |1\rangle\langle 1|$, we have $\langle\Phi_1|n_j|\Phi_1\rangle/\langle\Phi_1|\Phi_1\rangle = \frac{1}{3}$. This violates the ETH, since, at $T = \infty$, the Gibbs ensemble predicts $\langle n_j\rangle_{T=\infty} = (1+\phi^2)^{-1} \approx 0.2764$, where $\phi = (1+\sqrt{5})/2$ is the golden ratio.

On the other hand, two-site observables can detect the T_x breaking, as can be seen from the corresponding reduced density matrices for subsystems $[1,2]$ and $[2,3]$ in the $|\Phi_1\rangle$ state:

$$\rho_{[1,2]}^{\text{two-site}} = \frac{1}{3}(|00\rangle\langle 00| + |01\rangle\langle 01| + |10\rangle\langle 10|) , \tag{5.19}$$

$$\rho_{[2,3]}^{\text{two-site}} = \frac{1}{3}(|00\rangle\langle 00| + |01\rangle\langle 01| + |10\rangle\langle 10|) - \frac{1}{9}(|01\rangle\langle 10| + |10\rangle\langle 01|) . \tag{5.20}$$

In particular, we see that $|0_j 1_{j+1}\rangle\langle 1_j 0_{j+1}| + \text{H.c.}$ has expectation value 0 for j odd and $-2/9$ for j even.

Obtaining the one-site reduced density matrix of the exact states in PBC is a simple exercise in MPS calculations. For concreteness, let us consider $|\Phi_1\rangle$. We define generalized transfer matrices $E_B^{\sigma\sigma'} \equiv (B^\sigma)^* \otimes B^{\sigma'}$ and $E_C^{\sigma\sigma'} \equiv (C^\sigma)^* \otimes C^{\sigma'}$. The ordinary transfer matrices E_B and E_C defined earlier are related to these as $E_B = \sum_\sigma E_B^{\sigma\sigma}$ and $E_C = \sum_\sigma E_C^{\sigma\sigma}$. We can now obtain the matrix elements of the one-site density matrix on the odd sites as $\langle\sigma'|\rho_{[1]}^{\text{one-site}}|\sigma\rangle = \text{Tr}[E_B^{\sigma\sigma'} E_C E_A^{L_b-1}]/\text{Tr}[E_A^{L_b}]$. We find

$$\rho_{[1]}^{\text{one-site}} = \frac{2\cdot 3^{L_b-1} + 1 + (-1)^{L_b}}{Z}|0\rangle\langle 0| + \frac{3^{L_b-1}+1}{Z}|1\rangle\langle 1|\,, \tag{5.21}$$

where $Z = 3^{L_b} + 2 + (-1)^{L_b}$ On the even sites, the matrix elements are given as

$$\langle\sigma'|\rho_{[2]}^{\text{one-site}}|\sigma\rangle = \text{Tr}[E_B E_C^{\sigma\sigma'} E_A^{L_b-1}]/\text{Tr}[E_A^{L_b}]\,. \tag{5.22}$$

It is easy to verify that we indeed have $\rho_{[1]}^{\text{one-site}} = \rho_{[2]}^{\text{one-site}}$. For even L_b, the one-site density matrix is $\rho_{[1]}^{\text{one-site}} = \rho_{[2]}^{\text{one-site}} = \frac{2}{3}|0\rangle\langle 0| + \frac{1}{3}|1\rangle\langle 1|$; while for odd L_b, it is essentially the same but with an exponentially small correction.

For the two-site reduced density matrix on sites 1 and 2, the matrix elements are given as $\langle\sigma_1'\sigma_2'|\rho_{[1,2]}^{\text{two-site}}|\sigma_1\sigma_2\rangle = \text{Tr}[E_A^{(\sigma_1\sigma_2)(\sigma_1'\sigma_2')} E_A^{L_b-1}]/\text{Tr}[E_A^{L_b}]$, where $E_A^{(\sigma_1\sigma_2)(\sigma_1'\sigma_2')} = (A^{(\sigma_1\sigma_2)})^* \otimes A^{(\sigma_1'\sigma_2')}$, giving us

$$\begin{aligned}\rho_{[1,2]}^{\text{two-site}} =& \frac{3^{L_b-1}+(-1)^{L_b}}{Z}|00\rangle\langle 00| + \frac{3^{L_b-1}+1}{Z}(|01\rangle\langle 01| + |10\rangle\langle 10|)\\ &+\frac{-1+(-1)^{L_b}}{3Z}(|01\rangle\langle 10| + |10\rangle\langle 01|)\,.\end{aligned} \tag{5.23}$$

On sites 2 and 3, the matrix elements of the two-site reduced density matrix are $\langle\sigma_2'\sigma_3'|\rho_{[2,3]}^{\text{two-site}}|\sigma_2\sigma_3\rangle = \text{Tr}[E_B E_D^{(\sigma_2\sigma_3)(\sigma_2'\sigma_3')} E_C E_A^{L_b-2}]/\text{Tr}[E_A^{L_b}]$, where $E_D^{(\sigma_2\sigma_3)(\sigma_2'\sigma_3')} \equiv (C^{\sigma_2}B^{\sigma_3})^* \otimes (C^{\sigma_2'}B^{\sigma_3'})$. We find

$$\begin{aligned}\rho_{[2,3]}^{\text{two-site}} =& \frac{3^{L_b-1}+(-1)^{L_b}}{Z}|00\rangle\langle 00| + \frac{3^{L_b-1}+1}{Z}(|01\rangle\langle 01| + |10\rangle\langle 10|)\\ &+\frac{1-3^{L_b-2}}{Z}(|01\rangle\langle 10| + |10\rangle\langle 01|)\,.\end{aligned} \tag{5.24}$$

As discussed, one-site observables cannot detect translation symmetry breaking, while the two-site observable $|0_j 1_{j+1}\rangle\langle 1_j 0_{j+1}| + \text{H.c.}$ can detect the T_x breaking. Another common observable in experiment and numerical studies—"domain wall number" P_jP_{j+1}—has expectation value $1/3$ for any j (and $L \to \infty$) and hence does not detect the translation symmetry breaking. Interestingly, the Gibbs ensemble in the thermodynamic limit gives $\langle P_jP_{j+1}\rangle_{T=\infty} = \phi/(\phi+2) \approx 0.4472$, which again directly shows the non-ETH behavior of $|\Phi_1\rangle$.

For L even, the inversion $I : j \to L - j + 1$ is relative to a bond center and is not broken. In the MPS representation, we have

$$I|\Phi_1\rangle = \sum_{\{\sigma\}} \mathrm{Tr}[B_I^{\sigma_1} C_I^{\sigma_2} \dots B_I^{\sigma_{L-1}} C_I^{\sigma_L}] |\sigma_1 \dots \sigma_L\rangle\,, \tag{5.25}$$

where $B_I^{\sigma} \equiv [C^{\sigma}]^T$ and $C_I^{\sigma} \equiv [B^{\sigma}]^T$. Consider now a 2×2 matrix $X_I \equiv i\sigma_y$ and a 3×3 matrix $Y_I \equiv \mathrm{diag}(-1,-1,1)$. These satisfy $X_I B_I^{\sigma} Y_I^{-1} = B^{\sigma}$ and $Y_I C_I^{\sigma} X_I^{-1} = -C^{\sigma}$ and give us an MPS gauge transformation that proves $I|\Phi_1\rangle = (-1)^{L_b}|\Phi_1\rangle$. For $|\Phi_2\rangle \equiv T_x|\Phi_1\rangle$, note that since $IT_x = T_x^{-1}I$ and $T_x^2|\Phi_i\rangle = |\Phi_i\rangle$, we have $I|\Phi_2\rangle = (-1)^{L_b}|\Phi_2\rangle$.

While C_{ph} is not a symmetry of H, our states are in fact eigenstates of C_{ph}. Indeed, in terms of MPS,

$$C_{\mathrm{ph}}|\Phi_1\rangle = \sum_{\{\sigma\}} \mathrm{Tr}[B_c^{\sigma_1} C_c^{\sigma_2} \dots B_c^{\sigma_{L-1}} C_c^{\sigma_L}] |\sigma_1 \dots \sigma_L\rangle\,, \tag{5.26}$$

where $B_c^0 = -B^0$, $B_c^1 = B^1$, $C_c^0 = -C^0$, and $C_c^1 = C^1$. Consider a 2×2 matrix $X_c \equiv \sigma_z$ and a 3×3 matrix $Y_c \equiv \mathrm{diag}(-1,1,-1)$. Then applying the gauge transformation $X_c B_c^{\sigma} Y_c^{-1} = B^{\sigma}$, $Y_c C_c^{\sigma} X_c^{-1} = -C^{\sigma}$ proves $C_{\mathrm{ph}}|\Phi_1\rangle = (-1)^{L_b}|\Phi_1\rangle$. For $|\Phi_2\rangle$, noting that $C_{\mathrm{ph}}T_x = T_x C_{\mathrm{ph}}$, we conclude that $C_{\mathrm{ph}}|\Phi_2\rangle = (-1)^{L_b}|\Phi_2\rangle$.

5.3 Exact scar states in the open boundary condition

We also found exact scar states for OBC with the same bulk MPSs. Defining "boundary vectors" $v_1 = (1,1)^T$ and $v_2 = (1,-1)^T$, we can write four exact scar states

$$|\Gamma_{\alpha,\beta}\rangle = \sum_{\{\sigma\}} v_\alpha^T B^{\sigma_1} C^{\sigma_2} \dots B^{\sigma_{L-1}} C^{\sigma_L} v_\beta |\sigma_1 \dots \sigma_L\rangle\,, \tag{5.27}$$

where $\alpha, \beta \in \{1,2\}$. The eigenenergies are $E = 0$ for $|\Gamma_{\alpha,\alpha}\rangle$, $E = \sqrt{2}$ for $|\Gamma_{1,2}\rangle$, and $E = -\sqrt{2}$ for $|\Gamma_{2,1}\rangle$.

Proof of exact eigenstates in OBC

Here we prove that $|\Gamma_{\alpha,\beta}\rangle$ are eigenstates in OBC. In this case, the Hamiltonian in the blocked form is

$$H = \sum_{b=1}^{L_b-1} h_{b,b+1} + h_{\text{left}} + h_{\text{right}} \,,$$
$$h_{\text{left}} = (|L\rangle\langle O| + |O\rangle\langle L|)_{b=1} \,, h_{\text{right}} = (|R\rangle\langle O| + |O\rangle\langle R|)_{b=L_b} \,, \tag{5.28}$$

with the "bulk" $h_{b,b+1}$ given in Eq. (5.5).

We can write the states in the blocked representation as

$$|\Gamma_{\alpha,\beta}\rangle = \sum_{\{s\}} v_\alpha^T A^{s_1} \dots A^{s_{L_b}} v_\beta |s_1 \dots s_{L_b}\rangle \,.$$

Similar to the case in PBC, the genuinely two-body part of $h_{b,b+1}$ annihilates these states, $h^{(2)}_{b,b+1}|\Gamma_{\alpha,\beta}\rangle = 0$. We therefore have

$$H|\Gamma_{\alpha,\beta}\rangle = H'|\Gamma_{\alpha,\beta}\rangle = \sum_{b=1}^{L_b} \sum_{\{s\}} v_\alpha^T A^{s_1} \dots F^{s_b} \dots A^{s_{L_b}} v_\beta |s_1 \dots s_{L_b}\rangle \,, \tag{5.29}$$

where H' is the sum of one-body terms defined in Eq. (5.8), and matrices F^s are defined in Eq. (5.10). We can again substitute $F^s = XA^s - A^s X$, with $X = \frac{1}{\sqrt{2}}\sigma^x$, and obtain

$$\begin{aligned} H|\Gamma_{\alpha,\beta}\rangle &= \sum_{\{s\}} (v_\alpha^T X A^{s_1} \dots A^{s_{L_b}} v_\beta - v_\alpha^T A^{s_1} \dots A^{s_{L_b}} X v_\beta) |s_1 \dots s_{L_b}\rangle \\ &= -\frac{1}{\sqrt{2}}[(-1)^\alpha - (-1)^\beta]|\Gamma_{\alpha,\beta}\rangle \,, \end{aligned} \tag{5.30}$$

where in the last equality we used $X = X^T$ and $X v_\alpha = -(-1)^\alpha \frac{1}{\sqrt{2}} v_\alpha$. Thus, $|\Gamma_{1,1}\rangle$ and $|\Gamma_{2,2}\rangle$ are eigenstates with energy 0, while $|\Gamma_{1,2}\rangle$ and $|\Gamma_{2,1}\rangle$ have energy $\sqrt{2}$ and $-\sqrt{2}$ respectively.

It is interesting to note that $\Gamma_{\alpha,\beta}$ are also eigenstates of H' defined in Eq. (5.8). From the diagonalization of H' in Eq. (5.13), any eigenstate of H' must have energy which is an integer multiple of $\sqrt{2}$. However, the fact that $H|\Gamma_{\alpha,\beta}\rangle = H'|\Gamma_{\alpha,\beta}\rangle$ only guarantees that $H'|\Gamma_{\alpha,\beta}\rangle$ satisfy the Rydberg constraints, and we needed additional arguments to show that $|\Gamma_{\alpha,\beta}\rangle$ are eigenstates of H'.

As an alternative proof, we can also write the OBC states $|\Gamma_{\alpha,\beta}\rangle$ in the $\pm, \mathbf{0}$ basis introduced in Eq. (5.12). Convenient MPS matrices in this basis are given in

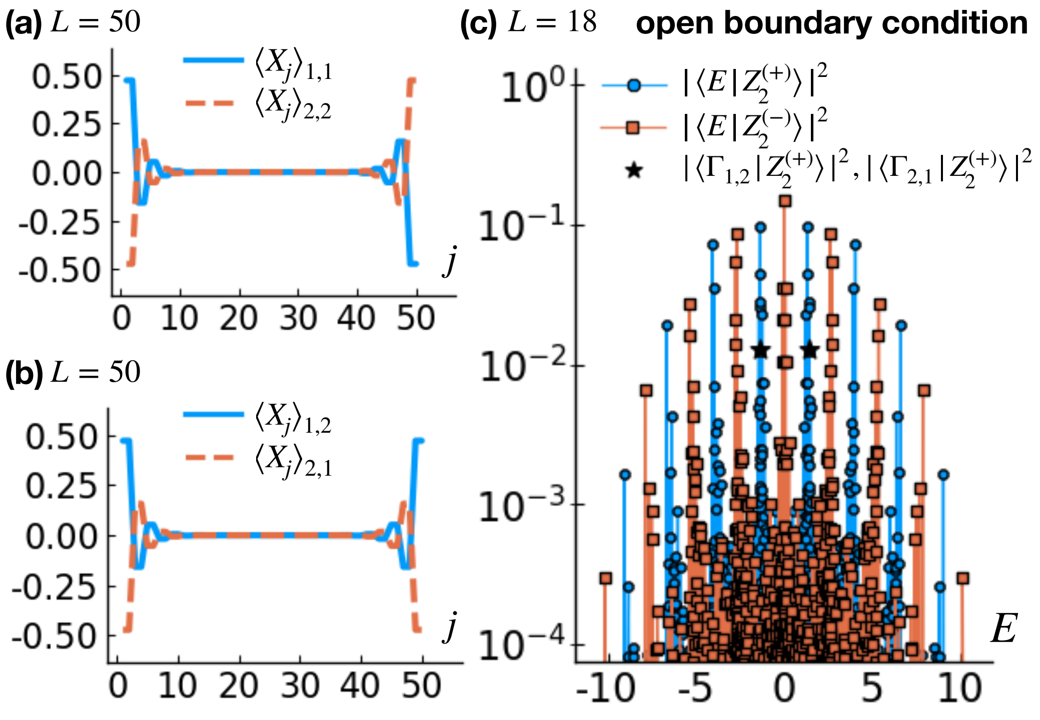

Figure 5.1: (a)(b) Energy density profiles $\langle X_j \rangle_{\alpha,\beta}$ in the four exact eigenstates $|\Gamma_{\alpha,\beta}\rangle$ in the OBC system of size $L = 50$. (c)Towers of the Z_2 scar states for OBC found in ED. The positions of the exact scar states $|\Gamma_{1,2}\rangle$ and $|\Gamma_{2,1}\rangle$ are marked with stars.

Eq. (5.14), and the corresponding termination vectors (obtained using the gauge transformation that produced the convenient matrices) are $\tilde{v}_1 = V v_1 = (\sqrt{2}, 0)^T$ and $\tilde{v}_2 = V v_2 = (0, \sqrt{2})^T$. It is now easy to see that for a product basis vector to be present in the expansion of $|\Gamma_{\alpha,\beta}\rangle$, the leftmost non-$\mathbf{0}$ block-site must have $\mathbf{+}$ if $\alpha = 1$ and $\mathbf{-}$ if $\alpha = 2$, while the rightmost non-$\mathbf{0}$ site must have $\mathbf{-}$ if $\beta = 1$ and $\mathbf{+}$ if $\beta = 2$. Similar to the case in PBC, properties $(A^{\mathbf{+}})^2 = (A^{\mathbf{-}})^2 = 0$ and $A^{\mathbf{0}} = 1$ imply that the $\mathbf{+}$'s and $\mathbf{-}$'s must alternate while allowing intervening $\mathbf{0}$'s. Hence, we conclude that $N_{\mathbf{+}} - N_{\mathbf{-}} = 0$ for the $|\Gamma_{\alpha,\alpha}\rangle$ states, while $N_{\mathbf{+}} - N_{\mathbf{-}} = 1$ or -1 for the $|\Gamma_{1,2}\rangle$ or $|\Gamma_{2,1}\rangle$ respectively, which reproduces the eigenvalues under H' obtained earlier.

Edge excitations in the OBC exact scar states

It is interesting to examine the energy density profiles. Figures 5.1(a) and 5.1(b) show $\langle X_j \rangle_{\alpha,\beta} \equiv \langle \Gamma_{\alpha,\beta} | X_j | \Gamma_{\alpha,\beta} \rangle / \langle \Gamma_{\alpha,\beta} | \Gamma_{\alpha,\beta} \rangle$ in each state. We can see that there are localized "energy lumps" at the edges of the chain. The profiles decay exponentially into the bulk with decay length $2\ln(3)$. The integrated energy over each lump is

$\sqrt{2}/2$ or $-\sqrt{2}/2$ depending on the termination, which can be thought as representing different "edge states."

It is an easy exercise in MPS calculations to obtain expectation values of the local energy $\langle X_j \rangle_{\alpha,\beta} \equiv \langle \Gamma_{\alpha,\beta} | X_j | \Gamma_{\alpha,\beta} \rangle / \langle \Gamma_{\alpha,\beta} | \Gamma_{\alpha,\beta} \rangle$ in the OBC exact eigenstates. The essential ingredients are generalized transfer matrices $E_{XB} = B^0 \otimes B^1 + B^1 \otimes B^0$ and $E_{XC} = C^0 \otimes C^1 + C^1 \otimes C^0$, as well as ordinary transfer matrices $E_B = B^0 \otimes B^0 + B^1 \otimes B^1$ and $E_C = C^0 \otimes C^0 + C^1 \otimes C^1$, where we have already used the fact that all our matrices B^σ, C^σ are real. Note that $E_B E_C = E_A$, which is the transfer matrix used in the blocked formulation and given in Eq. (5.15). We also define boundary vectors $e_\alpha = v_\alpha \otimes v_\alpha$, where $\alpha = 1, 2$ (here also using that our vectors v_α are real). Parameterizing our terminations as $v_\alpha = (1, (-1)^{\alpha-1})$, $\alpha = 1, 2$, we obtain the norms as

$$\langle \Gamma_{\alpha,\beta} | \Gamma_{\alpha,\beta} \rangle = e_\alpha^T E_A^{L_b} e_\beta = 2\Big[(-1)^{L_b+\alpha+\beta} + 3^{L_b}\Big] \,. \tag{5.31}$$

For the energy calculations, at site $j = 2b - 1$, $b = 1 \ldots L_b$, we have

$$\langle \Gamma_{\alpha,\beta} | X_j | \Gamma_{\alpha,\beta} \rangle = e_\alpha^T E_A^{b-1} E_{XB} E_C E_A^{L_b - b} e_\beta \,,$$

while at site $j = 2b$, we have

$$\langle \Gamma_{\alpha,\beta} | X_j | \Gamma_{\alpha,\beta} \rangle = e_\alpha^T E_A^{b-1} E_B E_{XC} E_A^{L_b - b} e_\beta \,.$$

We obtain

$$\begin{aligned}\langle X_{2b-1} \rangle_{\alpha,\beta} =& \langle X_{2b} \rangle_{\alpha,\beta} \\ =& \frac{\sqrt{2}}{1 + (-1)^{L_b+\alpha+\beta} 3^{-L_b}} \Big[(-1)^\alpha (-1)^b 3^{-b} + (-1)^\beta (-1)^{L_b - b} 3^{-L_b + b - 1}\Big] \,.\end{aligned} \tag{5.32}$$

These are plotted in Fig. 5.1. Interestingly, we can relate these states that differ by their terminations only at one edge by an action of a local two-site operator near that edge. For example,

$$|\Gamma_{1,2}\rangle = \mathbf{1}_{[1,\ldots,L-2]} \otimes \Big(\frac{1}{\sqrt{2}} |00\rangle\langle 01| - \frac{1}{\sqrt{2}} |00\rangle\langle 10| + |01\rangle\langle 01| - |10\rangle\langle 10|\Big)_{[L-1,L]} |\Gamma_{1,1}\rangle \,.$$

(However, note that the operator achieving this is not unique.)

It is easy to check that the expectation value of the total energy $\langle H \rangle_{\alpha,\beta} = \sum_{j=1}^L \langle X_j \rangle_{\alpha,\beta}$ is 0 if $\alpha = \beta$, while $\langle H \rangle_{1,2} = \sqrt{2}$ and $\langle H \rangle_{2,1} = -\sqrt{2}$. In fact, the states are exact eigenstates and these expectation values are the corresponding eigenvalues, as we showed in Sec. 5.3.

Symmetry properties of the OBC exact scar states

The symmetry properties of $|\Gamma_{\alpha,\beta}\rangle$ can be derived in a similar fashion as for PBC. In particular, we have $I|\Gamma_{1,2}\rangle = (-1)^{L_b-1}|\Gamma_{1,2}\rangle$ and $I|\Gamma_{2,1}\rangle = (-1)^{L_b-1}|\Gamma_{2,1}\rangle$; while $I|\Gamma_{1,1}\rangle = (-1)^{L_b}|\Gamma_{2,2}\rangle$ and $I|\Gamma_{2,2}\rangle = (-1)^{L_b}|\Gamma_{1,1}\rangle$. Under the inversion,

$$I|\Gamma_{\alpha,\beta}\rangle = \sum_{\{\sigma\}} v_\beta^T B_I^{\sigma_1} C_I^{\sigma_2} \dots B_I^{\sigma_{L-1}} C_I^{\sigma_L} v_\alpha |\sigma_1 \dots \sigma_L\rangle \, . \tag{5.33}$$

Recall that $v_1 = (1,1)^T$ and $v_2 = (1,-1)^T$. We can perform the same gauge transformation as in PBC using matrices X_I and Y_I. The boundary vectors transform as $X_I v_1 = v_2$ and $X_I v_2 = -v_1$, and using also $X_I^{-1} = X_I^T$, we conclude that $I|\Gamma_{1,2}\rangle = (-1)^{L_b-1}|\Gamma_{1,2}\rangle$ and $I|\Gamma_{2,1}\rangle = (-1)^{L_b-1}|\Gamma_{2,1}\rangle$; while $I|\Gamma_{1,1}\rangle = (-1)^{L_b}|\Gamma_{2,2}\rangle$ and $I|\Gamma_{2,2}\rangle = (-1)^{L_b}|\Gamma_{1,1}\rangle$.

As for the particle-hole transformation, we obtain $C_{\text{ph}}|\Gamma_{1,2}\rangle = (-1)^{L_b}|\Gamma_{2,1}\rangle$ and $C_{\text{ph}}|\Gamma_{1,1}\rangle = (-1)^{L_b}|\Gamma_{2,2}\rangle$. The fact that $|\Gamma_{1,2}\rangle$ and $|\Gamma_{2,1}\rangle$ are eigenstates of I means that they can be nondegenerate, which is what we found in exact diagonalization (ED). As expected, these $E = \pm\sqrt{2}$ scar states are related by C_{ph}. Since they are nondegenerate, their finite bond dimensions are not related to the exponential degeneracy of the $E = 0$ sector. Their existence again demonstrates the violation of the ETH, even without worrying about potential subtleties in the degenerate space [29].

5.4 Entanglement entropies of the exact scar states

We can also calculate entanglement in $|\Gamma_{\alpha,\beta}\rangle$ for any cut and system size [18, 30]. To obtain the entanglement spectrum for the states $|\Gamma_{\alpha,\beta}\rangle$, we follow the procedure in Refs. [17, 18, 30]. First, we consider the entanglement cut between the sites $2b$ and $2b+1$. We form 2×2 Gram matrix $\mathcal{L}_{2\times 2}$ reshaped from $e_\alpha^T E_A^b$ and 2×2 Gram matrix $\mathcal{R}_{2\times 2}$ reshaped from $E_A^{L_b-b} e_\beta$, and then obtain an effective matrix

$$\mathcal{S}_{2\times 2} = \frac{\mathcal{L}_{2\times 2}\mathcal{R}_{2\times 2}}{\langle\Gamma_{\alpha,\beta}|\Gamma_{\alpha,\beta}\rangle} = \frac{1}{2}\begin{pmatrix} 1 & \frac{(-1)^{\alpha+1}3^{L_b-b}+(-1)^{\beta+1}3^b}{(-1)^{L_b+\alpha+\beta}+3^{L_b}} \\ \frac{(-1)^{\alpha+1}3^{L_b-b}+(-1)^{\beta+1}3^b}{(-1)^{L_b+\alpha+\beta}+3^{L_b}} & 1 \end{pmatrix} \tag{5.34}$$

whose eigenvalues are the same as eigenvalues of the reduced density matrix. We therefore obtain the entanglement spectrum as

$$s_{1,2} = \frac{1}{2}\left(1 \pm \frac{(-1)^{\alpha+1}3^{L_b-b} + (-1)^{\beta+1}3^b}{(-1)^{L_b+\alpha+\beta} + 3^{L_b}}\right) \, . \tag{5.35}$$

For large subsystem size b and in the thermodynamic limit, e.g., where we take $L_b \to \infty$, $b \to \infty$, while fixing the ratio $b/L_b = f < 1$, or where we take

$L_b \to \infty$ first and then $b \to \infty$, the entanglement spectrum approaches $s_{1,2} \to 1/2$ independent of the terminations.

For the entanglement cut between sites $2b+1$ and $2b+2$, we need 3×3 Gram matrix $\mathcal{L}_{3\times3}$ reshaped from $e_\alpha^T E_A^b E_B$ and 3×3 Gram matrix $\mathcal{R}_{3\times3}$ reshaped from $E_C E_A^{L_b-b-1} e_\beta$. The effective matrix that reproduces the entanglement spectrum is

$$\mathcal{S}_{3\times3} = \frac{\mathcal{L}_{3\times3}\mathcal{R}_{3\times3}}{\langle\Gamma_{\alpha,\beta}|\Gamma_{\alpha,\beta}\rangle} = \frac{1}{3^{L_b} + (-1)^{L_b+\alpha+\beta}}$$
$$\times \begin{pmatrix} \frac{5}{6}\cdot 3^{L_b} + \frac{1}{2}\cdot(-1)^{L_b+\alpha+\beta} & \frac{1}{6}\cdot(-1)^{1+b}[(-1)^{\alpha}\cdot 3^{L_b-b} + 9\cdot(-1)^{L_b+\beta}\cdot 3^{b}] & -3^{L_b-1} \\ \frac{1}{2}\cdot(-1)^{1+b}[(-1)^{\alpha}\cdot 3^{L_b-b} + (-1)^{L_b+\beta}\cdot 3^{b}] & \frac{1}{6}\cdot 3^{L_b} + \frac{1}{2}\cdot(-1)^{L_b+\alpha+\beta} & (-1)^{b+\alpha}\cdot 3^{L_b-b-1} \\ 3^{L_b-1} & (-1)^{1+\beta+L_b-b}\cdot 3^{b} & 0 \end{pmatrix}. \tag{5.36}$$

The entanglement spectrum at any finite L_b, b can be obtained from the eigenvalues of the above matrix. For large b and in the thermodynamic limit, we have

$$\mathcal{S} \to \begin{pmatrix} \frac{5}{6} & 0 & -\frac{1}{3} \\ 0 & \frac{1}{6} & 0 \\ \frac{1}{3} & 0 & 0 \end{pmatrix}, \tag{5.37}$$

which gives the entanglement spectrum 2/3, 1/6 and 1/6.

Therefore, in the thermodynamic limit, across a cut between C_{2b} and B_{2b+1} (bond-dimension $D = 2$ cut), we have the squared Schmidt values 1/2 and 1/2, which gives the von Neumann entanglement entropy $S_{\text{vN}}^{\text{OBC},D=2} = \ln 2$. Cutting instead across B_{2b+1} and C_{2b+2} ($D = 3$), the squared Schmidt values are 2/3, 1/6, and 1/6, and $S_{\text{vN}}^{\text{OBC},D=3} = -\frac{2}{3}\ln(\frac{2}{3}) - \frac{1}{3}\ln(\frac{1}{6}) \approx 0.868$.

For the states $|\Phi_i\rangle$ in PBC and a large subregion, there are two entanglement cuts, and the entanglement entropy will be the sum of the OBC entropies associated with each cut (and will remain finite in the thermodynamic limit). We can then predict that for the states $|\Phi_{K=0/\pi}\rangle$, the entanglement entropy will be $S_{\text{vN}}^{\text{PBC}} = S_{\text{vN}}^{\text{OBC},D=2} + S_{\text{vN}}^{\text{OBC},D=3} + \ln 2 \approx 2.254$.

5.5 Single mode approximation and multimode approximations for other primary scar states

Turner *et. al.* [13, 14] focused on the PXP model with PBC and identified a set of quantum many-body scar states (called Z_2 scar states) through the overlap of eigenstates $|E\rangle$ with the CDW states $|Z_2\rangle = |10\ldots10\rangle$ or $|Z_2'\rangle = |01\ldots01\rangle$. The most prominent such scar states have the largest overlap and the smallest

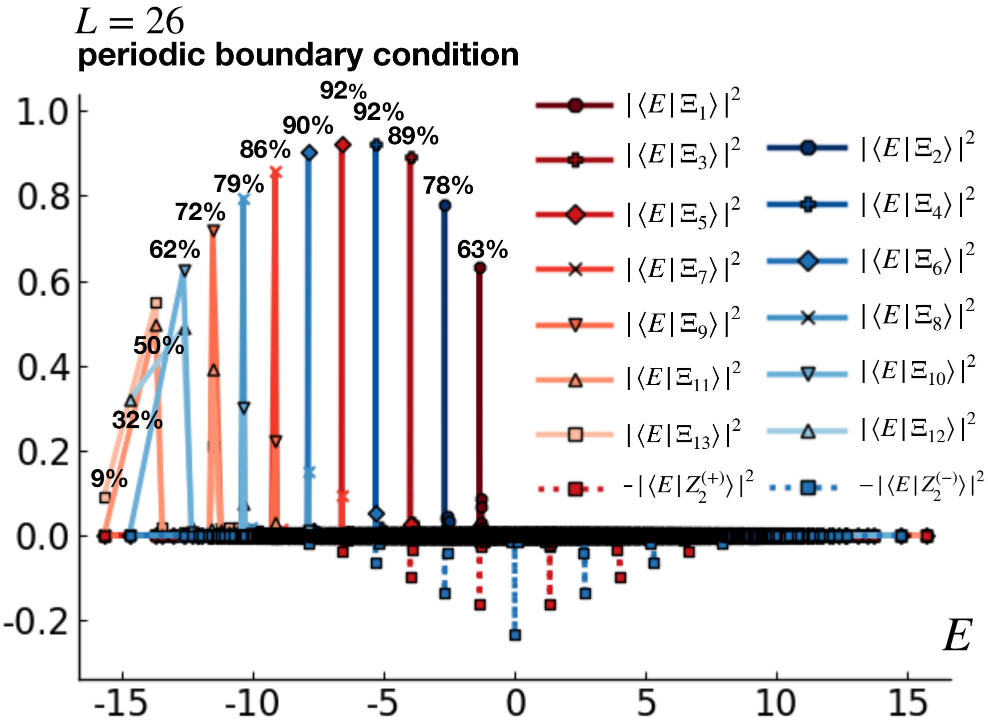

Figure 5.2: Overlaps of the SMA and MMA wavefunctions with the eigenstates in the PBC system with $L = 26$. We also list the overlaps with the primary Z_2 scar states. The Z_2 scar states are identified through the overlaps with the $|Z_2^{(+)}\rangle$ or $|Z_2^{(-)}\rangle$ states (for more clarity, we show negatives of these overlaps).

entanglement entropy compared to nearby states, but there are also “bands" (or “towers") of weaker scar states close to each primary one. (See also Fig. 1.3.) The consecutive primary scar states have an almost equal energy separation of ≈ 1.33. The scar states and this frequency were proposed to be responsible for the strong oscillations observed in quenches from the $|Z_2\rangle$ state.

It is convenient to consider states $|Z_2^{(\pm)}\rangle = (|Z_2\rangle \pm |Z_2'\rangle)/\sqrt{2}$, which have inversion quantum numbers $I = 1$ and $I = -1$ and carry momenta $K = 0$ and $K = \pi$ respectively, if in PBC. For L_b even, the Z_2 scar states at energy $E \approx 0$ are found to have $I = 1$ (and $K = 0$ in PBC), while for L_b odd they have $I = -1$ (and $K = \pi$). For a fixed L_b, I (and K in PBC) alternate between these values when going from one primary scar state to the next (and are the same within the band of weaker scar states associated with each primary state). This is illustrated in Figs. 5.1(c) and 5.2.

Turner *et. al.* [13, 14] proposed to approximate the primary scar states using “forward scattering approximation" (FSA) starting from the Z_2 state. We propose an alternative picture starting from our exact $E = 0$ states.

First, we note that our exact $E = 0$ scar states are, in fact, representative of the nearby scar states. For instance, at $L = 26$, the nearby $E \approx \pm 1.34$ scar states have average Rydberg excitation number $\langle E|n_j|E\rangle \approx 0.3476$ while $\langle \Phi_{K=\pi}|n_j|\Phi_{K=\pi}\rangle \approx 0.3355$. Second, we note that for OBC, the exact scar states $|\Gamma_{1,2}\rangle$ and $|\Gamma_{2,1}\rangle$, while not being the primary Z_2 scar states, belong to the first non-zero-energy towers of scar states, as shown in Fig. 5.1(c). Furthermore, we can understand these exact $E = \pm\sqrt{2}$ scar states as "edge excitations" on top of the $E = 0$ states $|\Gamma_{\alpha,\alpha}\rangle$. We therefore conjecture that for the PBC system as well, the nearby scar states can be understood as quasiparticle excitations on top of the "vacuum" $|\Phi_i\rangle$.

Motivated by these observations, we construct variational wavefunctions using SMA [31, 32] and generalize it to MMA on top of our exact $|\Phi_i\rangle$ states and aimed to capture the nearby scar states. We start with the following SMA wavefunction $|\Xi_1\rangle = [|M_1\rangle - (-1)^{L_b} T_x |M_1\rangle]/\xi_1$, where

$$|M_1\rangle = \sum_{\{\sigma\}} \sum_{b=1}^{L_b} \mathrm{Tr}[B^{\sigma_1} C^{\sigma_2} \ldots M^{\sigma_{2b-1}\sigma_{2b}} \ldots C^{\sigma_L}] |\sigma_1 \ldots \sigma_L\rangle, \tag{5.38}$$

and ξ_1 provides normalization $\langle \Xi_1|\Xi_1\rangle = 1$. The matrices

$$M^{00} = \begin{pmatrix} 1 & 0 \\ 0 & 1 \end{pmatrix}, \; M^{01} = \begin{pmatrix} \mu_1 & 0 \\ \mu_2 & 0 \end{pmatrix}, \; M^{10} = \begin{pmatrix} 0 & 0 \\ -\mu_2 & \mu_1 \end{pmatrix}$$

are chosen such that the wavefunction satisfies the Rydberg-blockaded constraint and $I|M_1\rangle = (-1)^{L_b - 1}|M_1\rangle$, hence $I|\Xi_1\rangle = (-1)^{L_b-1}|\Xi_1\rangle$ (see Ref. [**zotero-1083**]). We have also chosen the translation quantum number of $|\Xi_1\rangle$ to be $(-1)^{L_b-1}$, which matches the symmetry sector of the first $E \neq 0$ scar state overlapping with the Z_2 CDW. To make $|\Xi_1\rangle$ as close to an eigenstate as possible, we minimize the energy variance $\sigma_H^2(\mu_1, \mu_2) = \langle \Xi_1|H^2|\Xi_1\rangle - \langle \Xi_1|H|\Xi_1\rangle^2$ at fixed L. At $L = 26$, we find optimal parameters $\mu_1 = -1.0876$ and $\mu_2 = -0.6344$, which give $\sigma_H^2 = 0.0263$ and the average energy $\langle \Xi_1|H|\Xi_1\rangle = -1.3147$. Remarkably, the optimized state has over 63% overlap with the primary Z_2 scar state at $E \approx -1.3386$ found in ED, as shown in Fig. 5.2. It is easy to check that $\mu_1' = -\mu_1, \mu_2' = \mu_2$ gives $|\Xi_1'\rangle = (-1)^{L_b-1} C_{\mathrm{ph}} |\Xi_1\rangle$, which captures the scar state with $E \approx 1.3386$.

To capture other primary scar states and support our picture of quasiparticle excitations, we examine the following MMA wavefunctions

$$|\Xi_n\rangle = [|M_n\rangle + (-1)^{L_b+n} T_x |M_n\rangle]/\xi_n\,, \tag{5.39}$$

where

$$|M_n\rangle = \sum_{\{\sigma\}} \sum_{b_1,\ldots,b_n=1}^{L_b}{}' \operatorname{Tr}[B^{\sigma_1}C^{\sigma_2}\ldots M^{\sigma_{2b_1-1}\sigma_{2b_1}}\ldots$$
$$\ldots M^{\sigma_{2b_n-1}\sigma_{2b_n}}\ldots B^{\sigma_{L-1}}C^{\sigma_L}]|\sigma_1\ldots\sigma_L\rangle\,, \tag{5.40}$$

and the summation is constrained to have all b_i distinct and ξ_n is the normalization factor. Such an $|M_n\rangle$ describes some n-particle scattering state and is the most primitive construction where we simply try hard-core exclusion of the particles. For simplicity, we will take M from the optimization of $|\Xi_1\rangle$. Moreover, $|\Xi_n\rangle$ has quantum numbers $T_x = (-1)^{L_b+n}$ and $I = (-1)^{L_b+n}$, matching the symmetry structure of the Z_2 scar states. Unexpectedly, Fig. 5.2 shows that the overlaps of such simplest MMA wavefunctions and the primary scar states become better with more quasiparticles, up to about $n \approx L_b/2$, while for larger n the overlaps start to decrease. The poorer performance for $n > L_b/2$ is not surprising: For example, for $n = L_b$, the state $|M_{L_b}\rangle = \bigotimes_{b=1}^{L_b} |0\rangle_{2b-1}(|0\rangle+\mu_1|1\rangle)_{2b}+\bigotimes_{b=1}^{L_b}(|0\rangle+\mu_1|1\rangle)_{2b-1}|0\rangle_{2b}-\bigotimes_{b=1}^{L_b} |0\rangle|0\rangle$, therefore $|\Xi_{L_b}\rangle \sim |M_{L_b}\rangle$ but has spontaneous T_x symmetry breaking and is only a crude approximation to the true nondegenerate fully symmetric ground state. Our MMA states with n close to L_b are similarly expected to be only crude approximations to the actual primary scar states and are seen to be spread over several nearby scar states. On the other hand, the performance of the states with $n < L_b/2$ is truly remarkable. Typically, when adding more quasiparticles without further optimizations, such MMA states become worse with the number of particles added, while our MMA have better overlaps with the primary scar states. Furthermore, our MMA states perform better than the FSA states for $2 \le n \simeq L_b/2$. For reference, at $L = 26$, the FSA states have overlap 69% with the scar states $E \approx \pm 1.33$ and 68% − 72%, overlaps on the consecutive primary scar states respectively. This suggests that our exact eigenstates at $E = 0$ provide a better starting point for understanding the scar states in the PXP model.

Let us further discuss these results. $|\Xi_1\rangle$ and $|\Xi_1'\rangle \sim C_{\text{ph}}|\Xi_1\rangle$ can be viewed as representing "elementary quasiparticles" with energies $\epsilon_- \approx -1.31$ and $\epsilon_+ = -\epsilon_-$; these particles also carry inversion quantum number -1. It is then natural to expect strong oscillations with frequency ϵ_+ in observables that flip the inversion quantum number. (Observables in experiment and numerics that do not flip I will show frequency $2\epsilon_+$.) Indeed, even though the overlaps of the Z_2 initial state with the primary scar states decrease exponentially with the system size, the "quasiparticle creation operators" can also act on many more states, always "adding" roughly $\epsilon_\pm$.

This argument resembles the quasiparticle explanation [9] of strong oscillations in the "weak thermalization" regime in Ref. [7], where the initial state happened to be near the ground state. The differences here are that the initial Z_2 state is at $T = \infty$ but is "close" to our special eigenstates $|\Phi_i\rangle$, and that the quasiparticles here can carry both positive and negative energies.

By the repeated application of the SMA construction that gave us the $|\Xi_1\rangle$ and $|\Xi_1'\rangle$ states, we also expect additional states with energies $E \approx (n_+ - n_-)\epsilon_+, n_+, n_- \in \mathbb{N}$. We have demonstrated the $(n_+, n_-) = (0, n)$ branch explicitly in Fig. 5.2. Interestingly, the same energy $m\epsilon_+$ can be obtained in multiple ways, which may explain the bands of weaker scar states near the primary states.

Further details of SMA for the $E \approx \pm 1.33$ scar states with $I = (-1)^{L_b - 1}$

For ease of reference, we remind the construction and then explain more details behind it: $|\Xi_1\rangle = (|M_1\rangle - (-1)^{L_b} T_x |M_1\rangle)/\xi_1$, where ξ_1 provides normalization $\langle \Xi_1 | \Xi_1 \rangle = 1$ and

$$|M_1\rangle = \sum_{b=1}^{L_b} \mathrm{Tr}[B^{\sigma_1} C^{\sigma_2} \dots M^{\sigma_{2b-1}\sigma_{2b}} \dots B^{\sigma_{L-1}} C^{\sigma_L}] |\sigma_1 \dots \sigma_L\rangle \, , \tag{5.41}$$

with

$$M^{00} = \begin{pmatrix} 1 & 0 \\ 0 & 1 \end{pmatrix} , \quad M^{01} = \begin{pmatrix} \mu_1 & 0 \\ \mu_2 & 0 \end{pmatrix} , \quad M^{10} = \begin{pmatrix} 0 & 0 \\ -\mu_2 & \mu_1 \end{pmatrix} , \quad M^{11} = 0_{2\times 2} \, .$$

We have chosen the "excitation" matrices M to satisfy $M^{01} B^1 = 0_{2\times 3}$ and $C^1 M^{10} = 0_{3\times 2}$ so that the wavefunction automatically satisfies the Rydberg blockade constraint. Furthermore, we have required that the matrices give the inversion quantum number opposite to the exact $E = 0$ eigenstate $|\Phi_1\rangle$: By examining the action of I on $|M_1\rangle$ in the MPS language similar to Eq. (5.25) and utilizing the same gauge transformation used in the discussion after Eq. (5.25), we see that the desired inversion quantum number is achieved by requiring $X_I M_I^s X_I^{-1} = M^s$, where $M_I^{00} \equiv (M^{00})^T, M_I^{01} \equiv (M^{10})^T, M_I^{10} \equiv (M^{01})^T$. Satisfying these conditions leads to the ansatz with two parameters μ_1 and μ_2 shown above. In principle, the SMA wavefunction has a "gauge redundancy", i.e., property that $M^{\sigma_1\sigma_2} \to M^{\sigma_1\sigma_2} + [W, B^{\sigma_1} C^{\sigma_2}]$ does not change $|M_1\rangle$ for arbitrary 2×2 matrix W. We need to consider this redundancy to find the set of truly independent parameters. In the present case, it happens that the above ansatz for the excitation matrices has independent parameters already. Hence, the gauge redundancy does not reduce the number of the independent parameters. The optimal parameters are obtained by minimizing the energy fluctuation $\sigma_H^2 \equiv \langle \Xi_1 | H^2 | \Xi_1 \rangle - \langle \Xi_1 | H | \Xi_1 \rangle^2$. The resulting optimal state is presented in Fig. 5.3.

We also note that by choosing $\mu_1' = -\mu_1$ and $\mu_2' = \mu_2$, we can obtain the opposite-energy counterpart, $|\Xi_1'\rangle \sim C_{\text{ph}} |\Xi_1\rangle$. This can be seen using the gauge transformation introduced in the discussion of the action of C_{ph} on the exact eigenstate $|\Phi_1\rangle$ and noting that the corresponding excitation matrices satisfy $(M')^s = X_c M_c^s X_c^{-1}$, where $M_c^{00} \equiv M^{00}, M_c^{01} \equiv -M^{01}, M_c^{10} \equiv -M^{10}$.

Finally, we can provide some intuition for the energetics of the SMA ansatz by working in the blocked language used in Sec. 5.2 utilizing the $\pm, \mathbf{0}$ basis introduced in Eq. (5.12). Recall that in this basis $|\Phi_1\rangle$ is conveniently written using MPS matrices in Eq. (5.14). We can easily obtain excitation matrices in this representation by following the same steps that produced Eq. (5.14); we find

$$M^{\mathbf{+}} = \frac{\mu_1 + \sqrt{2}}{2} \begin{pmatrix} 1 & 0 \\ 0 & 1 \end{pmatrix}, M^{\mathbf{-}} = \frac{\mu_1 - \sqrt{2}}{2} \begin{pmatrix} 1 & 0 \\ 0 & 1 \end{pmatrix}, M^{\mathbf{0}} = \frac{1}{\sqrt{2}} \begin{pmatrix} \mu_2 & \mu_1 + \mu_2 \\ \mu_1 - \mu_2 & -\mu_2 \end{pmatrix}. \tag{5.42}$$

We can now examine a wavefunction obtained by placing such an excitation on one block-site b. The wavefunction has a part with $s_b = \mathbf{+}$, originating from $M^{\mathbf{+}}$, which on the rest of the system is basically $\text{Tr}[AA\dots A]$ and hence contains only configurations with equal numbers of $\mathbf{+}$ and $\mathbf{-}$ block-sites. Hence, this part is an eigenstate of H' introduced in Sec. 5.2, see Eqs. (5.8) and (5.13), with eigenvalue $\sqrt{2}$. Similarly, a part of the wavefunction with $s_b = \mathbf{-}$, originating from $M^{\mathbf{-}}$, on the rest of the system contains only configurations with equal numbers of $\mathbf{+}$ and $\mathbf{-}$ block-sites; hence, this part is an eigenstate of H' with eigenvalue $-\sqrt{2}$. Note that the amplitudes of the two parts are proportional to $(\mu_1 + \sqrt{2})/2$ and $(\mu_1 - \sqrt{2})/2$ respectively, and for the optimal parameters $\mu_1 \approx -1.09$, $\mu_2 \approx -0.63$ used in the main text, the latter amplitude is significantly larger.

We now examine a part of the wavefunction with $s_b = \mathbf{0}$, originating from $M^{\mathbf{0}}$, which we further subdivide as follows. The upper-left subpart $\mu_2/\sqrt{2}$ in $M^{\mathbf{0}}$ by itself requires that on the rest of the system we have equal numbers of $\mathbf{+}$'s and $\mathbf{-}$'s, and the first such site to the right of b must be $\mathbf{+}$. Similarly, the lower-right subpart $-\mu_2/\sqrt{2}$ in $M^{\mathbf{0}}$ by itself requires that on the rest of the system we have equal numbers of $\mathbf{+}$'s and $\mathbf{-}$'s, and the first such site to the right of b must be $\mathbf{-}$. Each of these cases gives an eigenstate of H' with eigenvalue 0. Next, the lower-left subpart $(\mu_1 - \mu_2)/\sqrt{2}$ in $M^{\mathbf{0}}$ by itself requires configurations on the rest of the system to be of the form $\ldots \mathbf{+} \ldots \mathbf{-} \ldots \mathbf{+} \ldots$, where "$\ldots$" can contain any number of $\mathbf{0}$'s. Such configurations contain one more $\mathbf{+}$ compared to $\mathbf{-}$, which gives an eigenstate of H' with eigenvalue $\sqrt{2}$. Similarly, the upper-right subpart $(\mu_1 + \mu_2)/\sqrt{2}$ in $M^{\mathbf{0}}$ by itself requires configurations on the rest of the system to be of the form $\ldots \mathbf{-} \ldots \mathbf{+} \ldots \mathbf{-} \ldots$, i.e., contain one less $\mathbf{+}$ compared to $\mathbf{-}$, which gives an eigenstate of H' with eigenvalue $-\sqrt{2}$.

We can now use the fact that the expectation value of H in this wavefunction coincides with the expectation value of H', since the genuinely two-body parts in the writing of H in Sec. 5.2 connect to outside of the Rydberg-constrained Hilbert space. (As a side remark, we can obtain the action of H on this wavefunction by first acting with H' and then projecting into the Rydberg Hilbert space; in particular, one can see that such an excitation wavefunction is no longer exact eigenstate of H.) By examining contributions to the expectation value of H' from the above parts of the wavefunction, we can roughly understand the value of the trial energy ≈ -1.31 obtained using these excitation matrices in the main text. Also, we can see that changing the sign of μ_1 gives a trial state with opposite energy, in agreement with the formal argument using C_{ph} given earlier.

Note that in the main text we formed plane wave superpositions of such localized excitations, and in the analysis here we are not attempting a quantitative match with the numerical results. Also note that while this analysis provides a rough intuition for the trial energies, in the main text we optimized the SMA ansatz by *minimizing the variance*, for which we have less intuition. Nevertheless, the above arguments provide an approximate picture where adding an excitation is like acting with a ladder operator raising or lowering eigenvalues of H' in Eq. (5.13), and developing this picture more precisely may provide a better understanding of the scar states in the PXP model away from $E = 0$.

SMA for the $E \approx \pm 2.66$ scar states with $I = (-1)^{L_b}$

While we showed the multi-mode approximation (MMA) to capture other Z_2 scar states, here we can also try to use the SMA but with the symmetry quantum numbers $T_x = (-1)^{L_b}$ and $I = (-1)^{L_b}$. Specifically, we can write an SMA wavefunction with such quantum numbers as $|\tilde{\Xi}_1\rangle = (|\tilde{M}_1\rangle + (-1)^{L_b} T_x |\tilde{M}_1\rangle)/\tilde{\xi}_1$, where again $\tilde{\xi}_1$ is the normalization factor and $|\tilde{M}_1\rangle$ has the same form as in Eq. (5.41) but with matrices

$$\tilde{M}^{00} = \begin{pmatrix} \sqrt{2} & -\sqrt{2}\tilde{\mu}_1 \\ \sqrt{2}\tilde{\mu}_1 & -\sqrt{2} \end{pmatrix}, \quad \tilde{M}^{01} = \begin{pmatrix} -\tilde{\mu}_1 & 0 \\ -1 & 0 \end{pmatrix}, \quad \tilde{M}^{10} = \begin{pmatrix} 0 & 0 \\ -1 & \tilde{\mu}_1 \end{pmatrix}.$$

Similarly to the construction of $|M_1\rangle$, we have chosen the matrices $\tilde{M}^s$ to satisfy $\tilde{M}^{01}B^1 = 0_{2\times 3}$ and $C^1\tilde{M}^{10} = 0_{3\times 2}$ but with $X_I\tilde{M}^s_I X_I^{-1} = -\tilde{M}^s$ to give the same inversion quantum number as $|\Phi_i\rangle$. We have also used the SMA gauge redundancy, $\tilde{M}^{\sigma_1\sigma_2} \longrightarrow \tilde{M}^{\sigma_1\sigma_2} + [W, B^{\sigma_1}C^{\sigma_2}]$, to identify the truly independent parameters. Finally, the number of the independent parameters was reduced by one by requiring $|\tilde{M}_1\rangle$ to be orthogonal to $|\Phi_1\rangle$ in the thermodynamic limit (we did not need to do this for $|M_1\rangle$ since it has different inversion quantum number and is automatically orthogonal to $|\Phi_1\rangle$).

The optimal parameter $\tilde{\mu}_1$ is obtained by minimizing the energy fluctuation; using system of length $L = 26$, we find $\tilde{\mu}_1 = 0.89285$, $\langle\tilde{\Xi}_1|H|\tilde{\Xi}_1\rangle = -2.4572$ and $\langle\tilde{\Xi}_1|H^2|\tilde{\Xi}_1\rangle - \langle\tilde{\Xi}_1|H|\tilde{\Xi}_1\rangle^2 = 0.3219$. To obtain the positive energy counterpart, we can choose $\tilde{\mu}_1' = -\tilde{\mu}_1$, which gives $|\tilde{\Xi}_1'\rangle \sim C_{\text{ph}}|\tilde{\Xi}_1\rangle$ (the argument is essentially identical to that for $|\Xi_1'\rangle \sim C_{\text{ph}}|\Xi_1\rangle$ at the end of the previous subsection). The overlap of $|\tilde{\Xi}_1\rangle$ with the eigenstates is plotted in Fig. 5.3. While this state still has majority of the weight on the primary scar state with $E \approx -2.66$, the overlap is significantly worse than the multi-particle ansatz $|\Xi_2\rangle$ presented in the main text. The wavefunction $|\tilde{\Xi}_1\rangle$ can be loosely viewed as a bound state of two quasiparticles, while $|\Xi_2\rangle$ can be viewed as a scattering state of two quasiparticles. These results suggest that the scar states are better understood as essentially free quasiparticle states rather than bound states of quasiparticles.

“Bond-dimension-3" SMA

The SMA wavefunctions $|\Xi_1\rangle$ and $|\tilde{\Xi}_1\rangle$ are constructed by “exciting" the matrices B and C consecutively, where the “quasiparicle excitation" matrix M has bond-dimension 2. We therefore call these wavefunctions “bond-dimension-2" ansatzes. On the other hand, one can also think of excitations on consecutive matrices C and B, which will give the quasiparticle excitation matrix with bond-dimension 3. Such ansatzes will have more variational parameters and can potentially be better approximations. The bond-dimension-3 SMA capturing the $E \approx \pm 1.33$ scar states with quantum numbers $T_x = (-1)^{L_b-1}$ and $I = (-1)^{L_b-1}$ is $|\Upsilon_1\rangle =$

$(|N_1\rangle - (-1)^{L_b} T_x |N_1\rangle)/\upsilon_1$, where υ_1 is the normalization factor and

$$|N_1\rangle = \sum_{b=1}^{L_b} \mathrm{Tr}[B^{\sigma_1} C^{\sigma_2} \ldots B^{\sigma_{2b-1}} N^{\sigma_{2b}\sigma_{2b+1}} C^{\sigma_{2b+2}} \ldots B^{\sigma_{L-1}} C^{\sigma_L}] |\sigma_1 \ldots \sigma_L\rangle \,, \quad (5.43)$$

with

$$N^{00} = \begin{pmatrix} 1+\sqrt{2}\,\nu_7 & 0 & 2\sqrt{2}\,\nu_6 \\ 0 & 1-\sqrt{2}\,\nu_7 & 2\sqrt{2}\,\nu_5 \\ -2\sqrt{2}\,\nu_6 & 2\sqrt{2}\,\nu_5 & \nu_1 \end{pmatrix}, \quad N^{01} = \begin{pmatrix} \nu_2 & 2\nu_6 & \nu_2 \\ \nu_6+\nu_7 & \nu_3 & \nu_6+\nu_7 \\ \nu_2-\nu_5 & \nu_4 & \nu_2-\nu_5 \end{pmatrix},$$

$$N^{10} = \begin{pmatrix} \nu_2 & \nu_6+\nu_7 & -\nu_2-\nu_5 \\ 2\nu_6 & \nu_3 & -\nu_4 \\ -\nu_2 & -\nu_6-\nu_7 & \nu_2+\nu_5 \end{pmatrix}.$$

We obtained these matrices by requiring $N^{01}C^1 = 0_{3\times 2}$, $B^1 N^{10} = 0_{2\times 3}$ to ensure the Rydberg constraints. To obtain the desired inversion quantum number, we also required $Y_I N_I^s Y_I^{-1} = N^s$, where $N_I^{00} \equiv (N^{00})^T$, $N_I^{01} \equiv (N^{10})^T$, $N_I^{10} \equiv (N^{01})^T$, and Y_I is the matrix for the gauge transformation used in our discussion of I. Finally, we also used the SMA gauge redundancy, $N^{\sigma_1\sigma_2} \longrightarrow N^{\sigma_1\sigma_2} + [W, C^{\sigma_1} B^{\sigma_2}]$, to find truly independent parameters as shown above. For system size $L = 26$, we find the optimal parameters $\nu_1 = 0.507183$, $\nu_2 = 0.60202$, $\nu_3 = 0.625366$, $\nu_4 = 0.264115$, $\nu_5 = -0.00128607$, $\nu_6 = 0.0228075$, and $\nu_7 = 0.42342$. The trial energy is $\langle \Upsilon_1 | H | \Upsilon_1 \rangle = 1.3396$ and the energy fluctuation is $\langle \Upsilon_1 | H^2 | \Upsilon_1 \rangle - \langle \Upsilon_1 | H | \Upsilon_1 \rangle^2 = 0.007201$, which is a more accurate approximation than the $|\Xi_1\rangle$ SMA state in the main text. We can see from Fig. 5.3 that the overlap with the primary Z_2 scar state with energy $E \approx 1.33$ is 66%, which is higher than the bond-dimension-2 ansatz $|\Xi_1\rangle$. To obtain the negative energy counterpart, one can simply change the signs of $\nu_{2,3,5}$ and obtain $|\Upsilon_1'\rangle \sim C_{\mathrm{ph}} |\Upsilon_1\rangle$, which is deduced by applying the discussion of C_{ph} and using $(N')^s = Y_c N_c^s Y_c^{-1}$, where $N_c^{00} \equiv N^{00}$, $N_c^{01} \equiv -N^{01}$, $N_c^{10} \equiv -N^{10}$.

Similarly, we can construct the bond-dimension-3 SMA in the symmetry sector $T_x = (-1)^{L_b}$ and $I = (-1)^{L_b}$ as $|\tilde{\Upsilon}_1\rangle = (|\tilde{N}_1\rangle + (-1)^{L_b} T_x |\tilde{N}_1\rangle)/\tilde{\upsilon}_1$, where $\tilde{\upsilon}_1$ is the normalization factor and $|\tilde{N}_1\rangle$ has the same form as in Eq. (5.43) but with matrices

$$\tilde{N}^{00} = \begin{pmatrix} 0 & 2\sqrt{2} & 2\sqrt{2}\,\tilde{\nu}_4 \\ -2\sqrt{2} & 0 & 2\sqrt{2}\,\tilde{\nu}_3 \\ 2\sqrt{2}\,\tilde{\nu}_4 & -2\sqrt{2}\,\tilde{\nu}_3 & 0 \end{pmatrix}, \quad \tilde{N}^{01} = \begin{pmatrix} -1 & -2\tilde{\nu}_4 & -1 \\ \tilde{\nu}_4 & \tilde{\nu}_1 & \tilde{\nu}_4 \\ -1+\tilde{\nu}_3 & \tilde{\nu}_2 & -1+\tilde{\nu}_3 \end{pmatrix},$$

$$\tilde{N}^{10} = \begin{pmatrix} 1 & -\tilde{\nu}_4 & -1-\tilde{\nu}_3 \\ 2\tilde{\nu}_4 & -\tilde{\nu}_1 & \tilde{\nu}_2 \\ -1 & \tilde{\nu}_4 & 1+\tilde{\nu}_3 \end{pmatrix}.$$

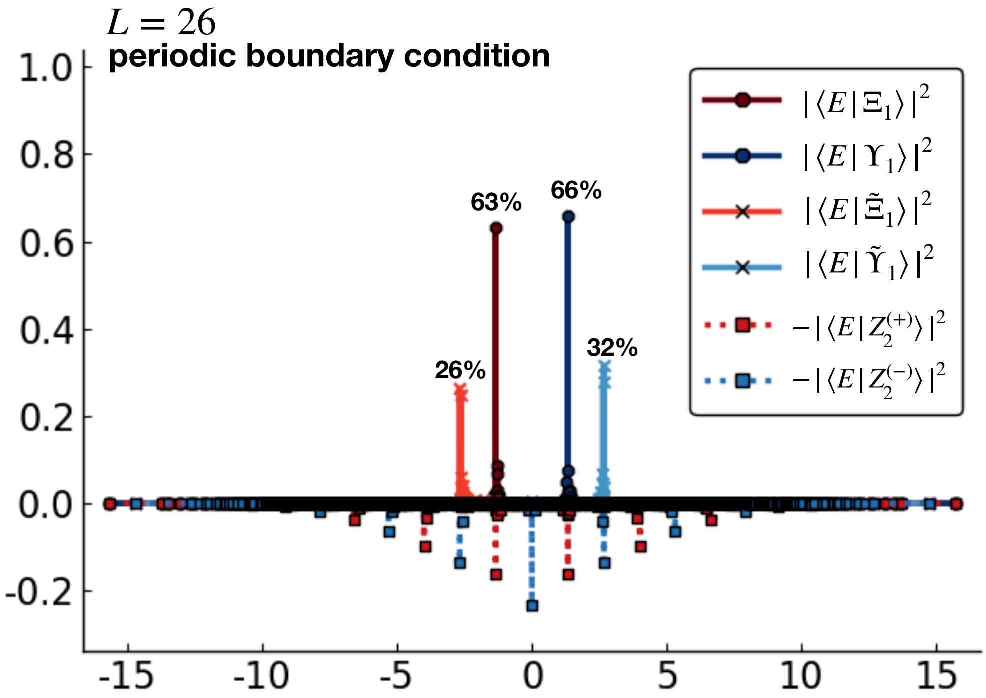

Figure 5.3: Overlaps of the SMA wavefunctions with eigenstates in the PBC chain of length $L = 26$. Here the SMA wavefunctions are constructed using "bond-dimension 2" ($|\Xi_1\rangle$ and $|\tilde{\Xi}_1\rangle$) and "bond-dimension 3" ($|\Upsilon_1\rangle$ and $|\tilde{\Upsilon}_1\rangle$) ansatzes, with choices producing different symmetry sectors. The red lines and the non-tilde states label the $K = 0$, $I = 1$ sector; while the blue lines and the tilded states label the $K = \pi$, $I = -1$ sector.

In addition to satisfying the Rydberg constraint and giving the inversion quantum number $I = (-1)^{L_b}$, the matrices are chosen such that $|\tilde{\Upsilon}_1\rangle$ is orthogonal to $|\Phi_1\rangle$ in the thermodynamic limit. Using system size $L = 26$, we find the optimal parameters $\tilde{v}_1 = 2.59334$, $\tilde{v}_2 = 1.48065$, $\tilde{v}_3 = 0.0615383$, and $\tilde{v}_4 = -0.992914$, with the trial energy $\langle\tilde{\Upsilon}_1|H|\tilde{\Upsilon}_1\rangle = 2.5594$, and energy fluctuation $\langle\tilde{\Upsilon}_1|H^2|\tilde{\Upsilon}_1\rangle - \langle\tilde{\Upsilon}_1|H|\tilde{\Upsilon}_1\rangle^2 = 0.18591$. To obtain the corresponding negative-energy trial state $|\tilde{\Upsilon}_1'\rangle \sim C_{\mathrm{ph}}|\tilde{\Upsilon}_1\rangle$, one changes the signs of $\tilde{v}_2$ and $\tilde{v}_4$. We again see from Fig. 5.3 that the overlap with the Z_2 primary scar state at $E \approx 2.66$ is higher than the bond-dimension-2 ansatz $|\tilde{\Xi}_1\rangle$, but significantly worse than the MMA wavefunction $|\Xi_2\rangle$.

In fact, we can again construct the corresponding "bond-dimension-3" MMA wavefunctions: $|\Upsilon_n\rangle = (|N_n\rangle + (-1)^{L_b+n} T_x |N_n\rangle)/\upsilon_n$, where

$$|N_n\rangle = \sum_{b_1,\ldots,b_n=1}^{L_b}{}' \operatorname{Tr}[B^{\sigma_1} C^{\sigma_2} \ldots N^{\sigma_{2b_1}\sigma_{2b_1+1}} \ldots N^{\sigma_{2b_n}\sigma_{2b_n+1}} \ldots B^{\sigma_{L-1}} C^{\sigma_L}] |\sigma_1 \ldots \sigma_L\rangle \,, \tag{5.44}$$

the summation is constrained to have all b_i distinct, and υ_n is the normalization factor. We take the N matrices from the optimal result of $|\Upsilon_1\rangle$ and examine the overlaps of $|\Upsilon_n\rangle$ with the eigenstates, in particular, with the Z_2 primary scar states in Fig. 5.4. Similar to the bond-dimension-2 results presented in the main text, these bond-dimension-3 MMA wavefunctions have symmetry quantum numbers $T_x = I = (-1)^{L_b+n}$ and, remarkably, capture the primary scar states with even higher fidelity with more quasiparticles, up to $n \approx L_b/4$. In this case, even the ground state and the primary scar states near the ground state are approximated fairly well compared to the results from the bond-dimension-2 ansatzes $|\Xi_n\rangle$.

Comparison with the forward scattering approximation

Here we follow Refs. [13, 14] to construct the foward scattering approximation (FSA) and compare with our alternative picture. Our main goal is to compare performance of our multi-mode approximations (MMA) on top of the exact $E = 0$ states and the FSA, in order to argue that our exact states and approximate quasiparticle constructions on top of these are relevant for the Z_2 scar states. In the FSA, one constructs a “variational" subspace, where one starts from $|Z_2\rangle \equiv |10\ldots10\rangle$ and operates with $H^+ \equiv \sum_{j\in\text{even}} P_{j-1}\sigma_j^+ P_{j+1} + \sum_{j\in\text{odd}} P_{j-1}\sigma_j^- P_{j+1}$ to form basis vectors $|n\rangle = (H^+)^n|Z_2\rangle/\|(H^+)^n|Z_2\rangle\|$ for $n = 0, 1, \ldots, L$. It is easy to see that $|L\rangle = |Z_2'\rangle \equiv |01\ldots01\rangle$. One then projects the full Hamiltonian into this subspace and obtains an effective Hamiltonain H_{FSA}, which is an $(L+1)\times(L+1)$ matrix with basis $|n\rangle$. By construction, H_{FSA} is bidiagonal. Diagonalzing $H_{\text{FSA}} = S E_{\text{FSA}} S^\dagger$, one obtains “variational" energies $E_{\text{FSA},i}$ and approximate wavefunctions $|\text{FSA}_i\rangle = \sum_{n=0}^{L} S_{ni}|n\rangle$, where $i = 0, 1, \ldots, L$.

We show the overlaps between the FSA wavefunctions and the eigenstates, $|\langle E|\text{FSA}_i\rangle|^2$, for $i = 0, 1, \ldots, L$ in Fig. 5.5. We also quote the overlap values on the “matching” primary Z_2 scar states, i.e., between $|\text{FSA}_i\rangle$ and the i-th primary scar state, with both sets of states assumed ordered by energy. In general, the FSA provides very good approximations for the primary Z_2 scar states, and, in particular, an extremely good approximation for the ground state and the scar state closest to the ground state.

It is interesting to note that the FSA variational space and the FSA states $|\text{FSA}_i\rangle$

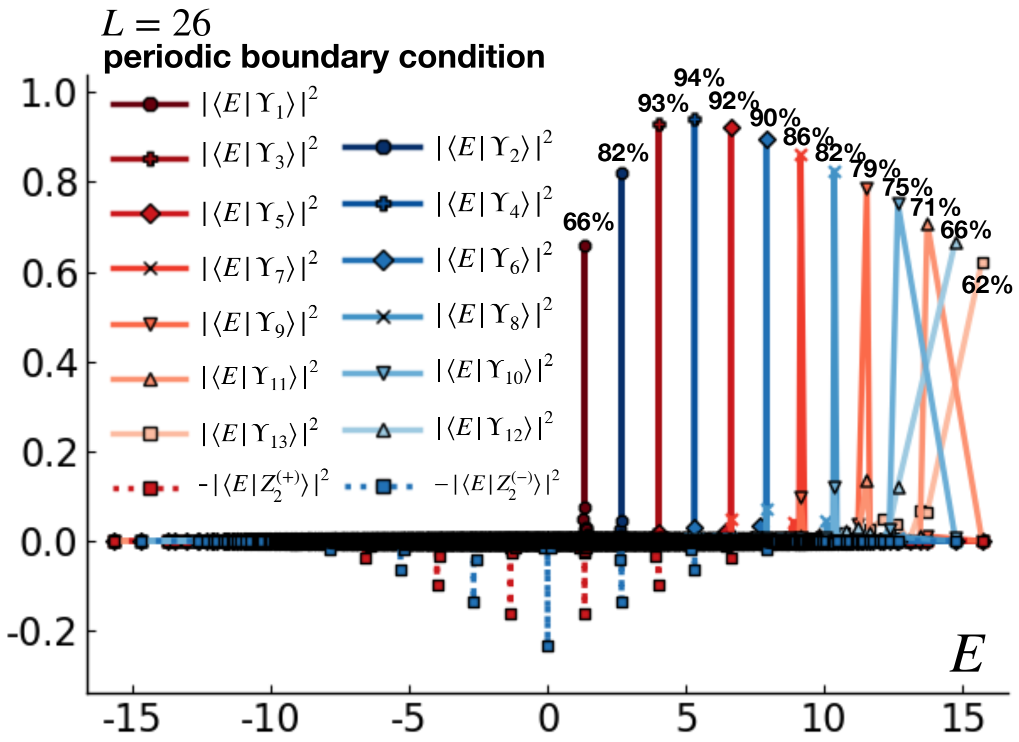

Figure 5.4: Overlaps between the MMA wavefunctions $|\Upsilon_n\rangle$ with eigenstates in the PBC chain with $L = 26$. The quasiparticle N matrices are chosen from the optimal “bond-dimension 3" SMA wavefunction. These wavefunctions represent the simplest scattering states of the quasiparticles with hard-core exclusions.

generated by the above procedure do not respect the translation and inversion symmetries of the Hamiltonian. Instead, they mix the $K = 0$, $I = 1$ and $K = \pi$, $I = -1$ sectors. However, each individual $|\text{FSA}_i\rangle$ state generally has a very high weight on a particular symmetry sector. In principle, one can fix this completely by including the symmetry-related counterparts in the variational basis, but we have not done such an embellishment and only followed the original procedure in Refs. [13, 14]. On the other hand, our trial SMA and MMA wavefunctions are constructed with definite symmetry quantum numbers from the outset.

Size dependence of the bipartite entanglement entropy of SMA and MMA

In this section, we discuss the bipartite entanglement entropy scaling of the SMA and MMA wavefunctions comparing with the ED results. In Fig. 5.6, we show the bipartite entanglement entropy at small system sizes reachable by ED, obtained for chains in PBC for dividing the system into halves. For the primary scar states at

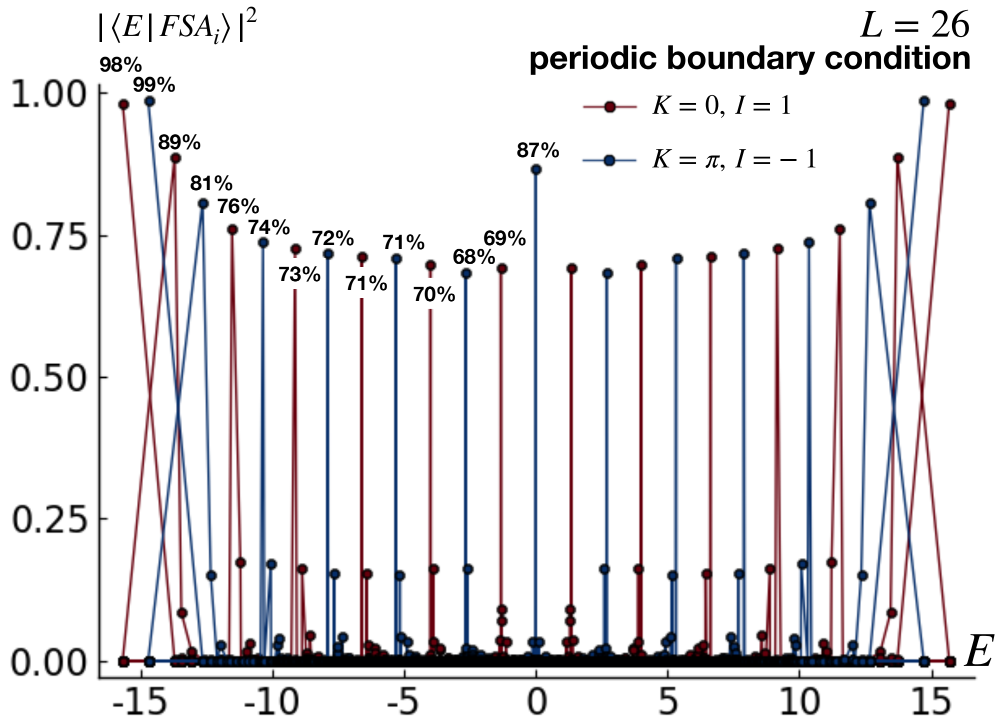

Figure 5.5: Overlaps between the FSA wavefunctions, $|\text{FSA}_i\rangle$, $i = 0, 1, \ldots, L$, and the eigenstates in the PBC chain with $L = 26$. The red lines are in the $K = 0$, $I = 1$ sector, while the blue lines are in the $K = \pi$, $I = -1$ sector. $|\text{FSA}_i\rangle$ has the largest overlap with the i-th Z_2 scar state, and this value is listed for easy reference for $i = 0, 1, \ldots, L/2$.

$E \approx -1.33$ and $E \approx -2.66$, their entanglement entropies show seeming logarithmic scaling, and are conjectured in Ref. [14] to have such scaling in the thermodynamic limit. On the other hand, the “vacuum" wavefunction of the quasiparticles, $|\Xi_0\rangle \equiv [|\Phi_1\rangle + (-1)^{L_b}|\Phi_2\rangle]/\xi_0$ (i.e., properly normalized exact $E = 0$ eigenstate with appropriate 0 or π momentum depending on $L_b = L/2$), has constant entanglement scaling in the thermodynamic limit with the saturation value $S \approx 2.254$, see the main text for details. Since they add only a finite number of quasiparticles, the SMA and MMA wavefunctions $|\Xi_1\rangle$ and $|\Xi_2\rangle$ are also expected to have constant entanglement scaling in the thermodynamic limit. However, as we can see from Fig. 5.6, the vacuum $|\Xi_0\rangle$ and the SMA and MMA $|\Xi_{1,2}\rangle$ wavefunctions also show apparent logarithmic entanglement scaling and bound the entanglement of the primary scar states at the available small system sizes. It is also noteworthy that in our SMA and MMA wavefunctions, adding quasiparticles in fact decreases the entanglement

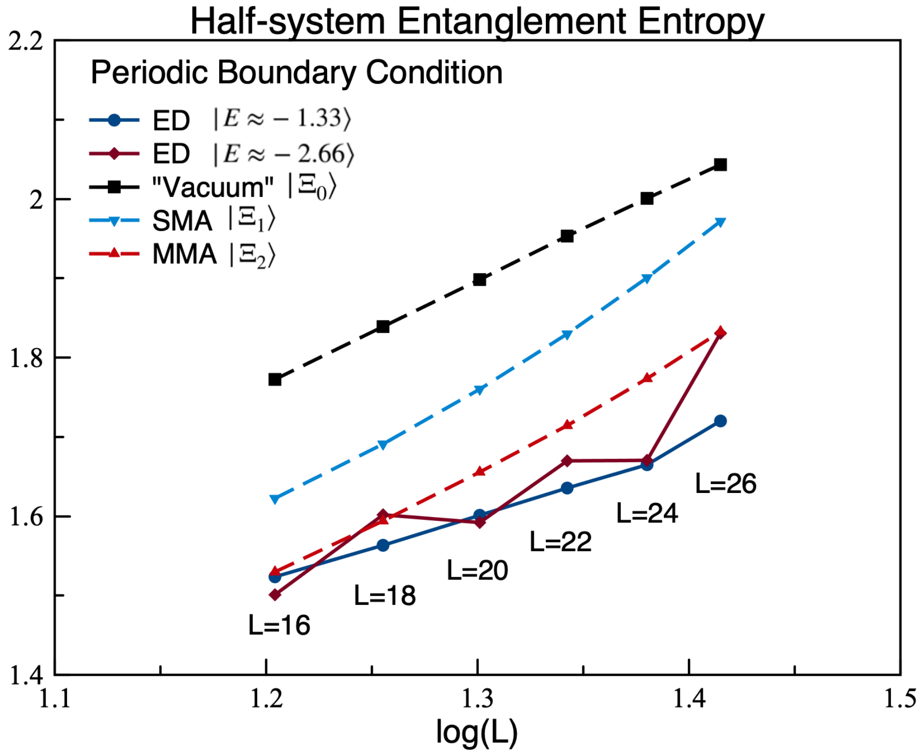

Figure 5.6: Bipartite entanglement entropies of the exact eigenstates and the variational SMA and MMA states. The primary scar states with $E \approx -1.33$ and $E \approx -2.66$ show what appears to be logarithmic scaling for the available system sizes L. The “vacuum" $|\Xi_0\rangle \equiv [|\Phi_1\rangle + (-1)^{L_b}|\Phi_2\rangle]/\xi_0$ (i.e., exact $E = 0$ wavefunction with appropriate momentum) and the SMA/MMA $|\Xi_1\rangle$ and $|\Xi_2\rangle$ are expected to have constant entanglement scaling at large L, while they also show apparent logarithmic scaling at these small system sizes. Note that for the optimal SMA and MMA we found, adding quasiparticles in fact decreases the entnaglement entropies.

entropy; this is contrary to common intuition about adding quasiparticles on top of a ground state, but it can happen in formal MPS states and depends on the properties of the “excitation” matrices.

If the SMA and MMA wavefunctions are qualitatively true asymptotic descriptions for the primary scar states, then the seeming logarithmic entanglement scaling of the ED results could be simply finite-size effect, and to see such constant scaling behavior, one may need to go to much larger system sizes. However, while the statements about our exact $E = 0$ scar states are exact, the SMA and MMA wavefunctions are only approximations to the ED scars. One needs to study if it is possible to construct convergent improvements of the SMA and MMA states and their true properties in the thermodynamic limit, which is a non-trivial question given the surrounding eigenstates forming apparently thermal background. We hope that addressing this question will help understanding stability of the scar states in the thermodynamic limit and in the presence of generic perturbations, while the presented entanglement data is meant to show that the available system sizes are still not sufficient to distinguish between constant or logarithmic entanglement scaling in the primary scar states.

Diagonalizing the Hamiltonian in the variational space spanned by $|\Xi_n\rangle$

While increasing the number of variational parameters is one way to improve the ansatzes, we can also improve the trial states starting with $|\Xi_n\rangle$ in the same spirit as the FSA improves on the states constructed using $(H^+)^n|Z_2\rangle$. That is, we can treat the span of $|\Xi_n\rangle, n = 1, \ldots, L_b$ as the “variational subspace" and project the Hamiltonian into this variational space (recall that $L_b = L/2$, and here n runs over the negative-energy MMA states). More specifically, we obtain an $L_b \times L_b$ effective Hamiltonian H_{eff} with matrix elements $[H_{\text{eff}}]_{nm} = \langle \Xi_n|H|\Xi_m\rangle$ and the overlap matrix B with matrix elements $[B]_{nm} = \langle \Xi_n|\Xi_m\rangle$. (Note that these matrices in fact are in block-diagonal form due to the symmetries.) We then solve the generalized eigenvalue problem $H_{\text{eff}}\vec{v}^{(i)} = \lambda_i B\vec{v}^{(i)}$, obtaining the improved wavefunctions $\sum_{n=1}^{L_b} \vec{v}_n^{(i)}|\Xi_n\rangle$, for $i = 1, \ldots, L_b$.

Figure 5.7 shows the overlap between the improved trial states and the eigenstates at $L = 26$. We see that the improvements are mainly on the approximations on the scar states close to the ground state and the ground state; while the approximations to the scar states close to the middle of the spectrum are not affected much. This is expected, since, as one can see from a careful inspection of Fig. 2 in the main text, $|\Xi_n\rangle$'s with $n \gtrsim L_b/2$ have high weights on usually two primary scar states. The diagonalization procedure within this variational subspace therefore can be better isolated and improve approximations to the corresponding scar states.

To conclude, we see that, qualitatively, the primary scar states can be well understood as free quasiparticles, at least for our finite system sizes. An immediate question is if such a description survives for much larger sizes or even in the thermodynamic limit. We already see that some systematic improvements of the approximations can be achieved by increasing the number of variational parameters, as in the bond-dimension-3 SMA or allowing superpositions of the MMA states as in the present section. Some immediate improvements could be achieved also by allowing the variational parameters to vary in each individual MMA state rather than simply

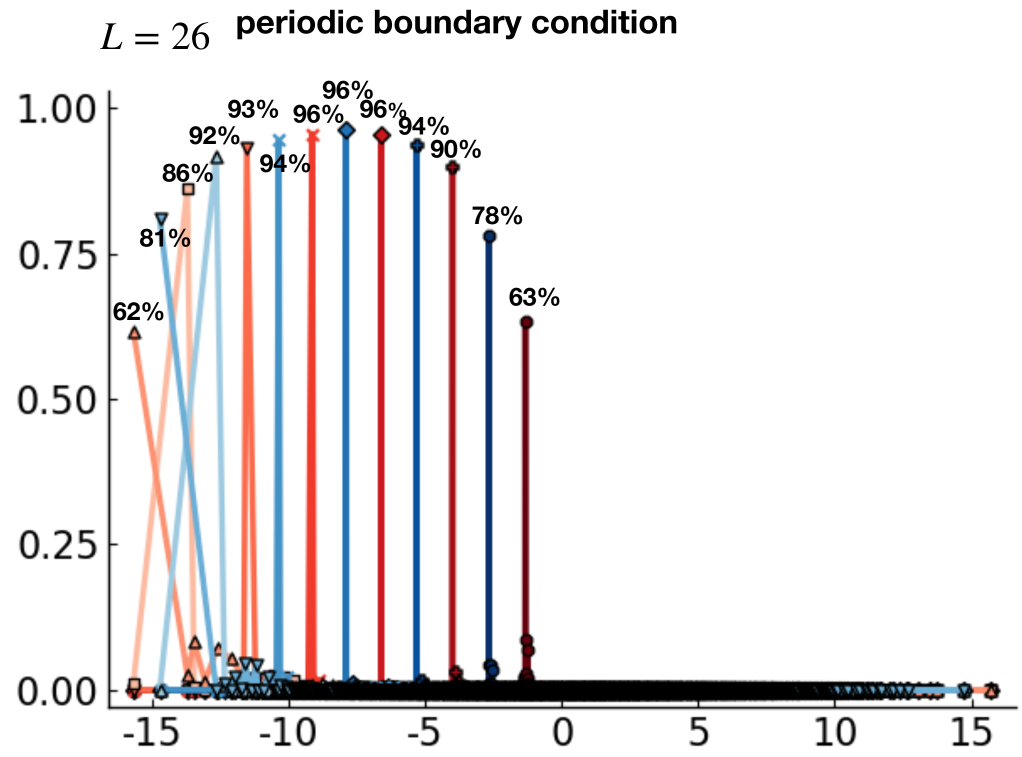

Figure 5.7: Improving the “bond-dimension 2" multiparticle wavefunction by diagonalizing the projected Hamiltonian in the “variational subspace" $\{|\Xi_n\rangle|, n = 1\dots13\}$. Such procedure improves the approximations on the ground states and scar states near the ground state.

using the values from the optimal SMA state, and by allowing superpositions of different families of the already constructed states, such as the SMA $|\tilde{\Xi}_1\rangle$ and the MMA $|\Xi_2\rangle$ for the $E \approx -2.66$ scar states, etc. A more systematic approach is to increase the excitation block size and study convergence to the exact scar states. In particular, we hope that this can tell whether the scar states truly survive in the thermodynamic limit even when they do not have exact closed-form expressions as happens in more fine-tuned models. This is left for future work.

5.6 Outlook

We discovered exact scar states in the Rydberg-blockaded atom chain at $T = \infty$ that explicitly violate the strong ETH and have constant entanglement scaling in the subsystem size. Our exact states show translation symmetry breaking, which implies twofold degeneracy for PBC. The exact scar states for OBC have the same bulk as for PBC and can have different edge terminations leading to different eigenenergies, including nondegenerate energies.

By constructing quasiparticles on top of the exact scar states, we capture the primary Z_2 scar states with high fidelity. Systematic improvements for capturing the primary scar states, as well as study bands of weaker scar states are therefore warranted. For example, even for the SMA, is there a convergent construction that reproduces the first primary Z_2 scar state and proves its ETH-violating properties? It is also interesting to understand the pattern of scar states in the PXP model more generally and how it compares with other instances of exact scar states [17, 18, 20]. Studying additional models with exact scar states and their stability to perturbations would be beneficial for both of these questions. We leave such explorations for future work.

References

[1] J. M. Deutsch, "Quantum statistical mechanics in a closed system", Phys. Rev. A **43**, 2046–2049 (1991).

[2] M. Srednicki, "Chaos and quantum thermalization", Phys. Rev. E **50**, 888–901 (1994).

[3] M. Rigol, V. Dunjko, V. Yurovsky, and M. Olshanii, "Relaxation in a Completely Integrable Many-Body Quantum System: An Ab Initio Study of the Dynamics of the Highly Excited States of 1D Lattice Hard-Core Bosons", Phys. Rev. Lett. **98**, 050405 (2007).

[4] M. Rigol, V. Dunjko, and M. Olshanii, "Thermalization and its mechanism for generic isolated quantum systems", Nature **452**, 854–858 (2008).

[5] H. Kim, T. N. Ikeda, and D. A. Huse, "Testing whether all eigenstates obey the eigenstate thermalization hypothesis", Phys. Rev. E **90**, 052105 (2014).

[6] J. R. Garrison, and T. Grover, "Does a Single Eigenstate Encode the Full Hamiltonian?", Phys. Rev. X **8**, 021026 (2018).

[7] M. C. Bañuls, J. I. Cirac, and M. B. Hastings, "Strong and Weak Thermalization of Infinite Nonintegrable Quantum Systems", Phys. Rev. Lett. **106**, 050405 (2011).

[8] M. Kormos, M. Collura, G. Takács, and P. Calabrese, "Real-time confinement following a quantum quench to a non-integrable model", Nat. Phys. **13**, 246–249 (2016).

[9] C.-J. Lin, and O. I. Motrunich, "Quasiparticle explanation of the weak-thermalization regime under quench in a nonintegrable quantum spin chain", Phys. Rev. A **95**, 023621 (2017).

[10] A. J. A. James, R. M. Konik, and N. J. Robinson, “Nonthermal States Arising from Confinement in One and Two Dimensions”, Phys. Rev. Lett. **122**, 130603 (2019).

[11] N. J. Robinson, A. J. A. James, and R. M. Konik, “Signatures of rare states and thermalization in a theory with confinement”, arXiv:1808.10782.

[12] H. Bernien, S. Schwartz, A. Keesling, H. Levine, A. Omran, H. Pichler, S. Choi, A. S. Zibrov, M. Endres, M. Greiner, V. Vuletić, and M. D. Lukin, “Probing many-body dynamics on a 51-atom quantum simulator”, Nature **551**, 579–584 (2017).

[13] C. J. Turner, A. A. Michailidis, D. A. Abanin, M. Serbyn, and Z. Papić, “Weak ergodicity breaking from quantum many-body scars”, Nat. Phys. **14**, 745–749 (2018).

[14] C. J. Turner, A. A. Michailidis, D. A. Abanin, M. Serbyn, and Z. Papić, “Quantum scarred eigenstates in a Rydberg atom chain: Entanglement, breakdown of thermalization, and stability to perturbations”, Phys. Rev. B **98**, 155134 (2018).

[15] E. J. Heller, “Bound-State Eigenfunctions of Classically Chaotic Hamiltonian Systems: Scars of Periodic Orbits”, Phys. Rev. Lett. **53**, 1515–1518 (1984).

[16] I. Affleck, T. Kennedy, E. H. Lieb, and H. Tasaki, “Rigorous results on valence-bond ground states in antiferromagnets”, Phys. Rev. Lett. **59**, 799–802 (1987).

[17] S. Moudgalya, S. Rachel, B. A. Bernevig, and N. Regnault, “Exact excited states of nonintegrable models”, Phys. Rev. B **98**, 235155 (2018).

[18] S. Moudgalya, N. Regnault, and B. A. Bernevig, “Entanglement of exact excited states of Affleck-Kennedy-Lieb-Tasaki models: Exact results, many-body scars, and violation of the strong eigenstate thermalization hypothesis”, Phys. Rev. B **98**, 235156 (2018).

[19] O. Vafek, N. Regnault, and B. A. Bernevig, “Entanglement of Exact Excited Eigenstates of the Hubbard Model in Arbitrary Dimension”, SciPost Phys **3**, 043 (2017).

[20] N. Shiraishi, and T. Mori, “Systematic Construction of Counterexamples to the Eigenstate Thermalization Hypothesis”, Phys. Rev. Lett. **119**, 030601 (2017).

[21] T. Mori, and N. Shiraishi, “Thermalization without eigenstate thermalization hypothesis after a quantum quench”, Phys. Rev. E **96**, 022153 (2017).

[22] W. W. Ho, S. Choi, H. Pichler, and M. D. Lukin, “Periodic Orbits, Entanglement, and Quantum Many-Body Scars in Constrained Models: Matrix Product State Approach”, Phys. Rev. Lett. **122**, 040603 (2019).

[23] V. Khemani, C. R. Laumann, and A. Chandran, “Signatures of integrability in the dynamics of Rydberg-blockaded chains”, Phys. Rev. B **99**, 161101 (2019).

[24] A. Chandran, M. D. Schulz, and F. J. Burnell, "The eigenstate thermalization hypothesis in constrained Hilbert spaces: a case study in non-Abelian anyon chains", Phys. Rev. B **94**, 235122 (2016).

[25] S. Sachdev, K. Sengupta, and S. M. Girvin, "Mott insulators in strong electric fields", Phys. Rev. B **66**, 075128 (2002).

[26] P. Fendley, K. Sengupta, and S. Sachdev, "Competing density-wave orders in a one-dimensional hard-boson model", Phys. Rev. B **69**, 075106 (2004).

[27] I. Lesanovsky, "Many-Body Spin Interactions and the Ground State of a Dense Rydberg Lattice Gas", Phys. Rev. Lett. **106**, 025301 (2011).

[28] I. Lesanovsky, "Liquid Ground State, Gap, and Excited States of a Strongly Correlated Spin Chain", Phys. Rev. Lett. **108**, 105301 (2012).

[29] M. Schecter, and T. Iadecola, "Many-body spectral reflection symmetry and protected infinite-temperature degeneracy", Phys. Rev. B **98**, 035139 (2018).

[30] J. I. Cirac, D. Poilblanc, N. Schuch, and F. Verstraete, "Entanglement spectrum and boundary theories with projected entangled-pair states", Phys. Rev. B **83**, 245134 (2011).

[31] J. Haegeman, B. Pirvu, D. J. Weir, J. I. Cirac, T. J. Osborne, H. Verschelde, and F. Verstraete, "Variational matrix product ansatz for dispersion relations", Phys. Rev. B **85**, 100408(R) (2012).

[32] J. Haegeman, S. Michalakis, B. Nachtergaele, T. J. Osborne, N. Schuch, and F. Verstraete, "Elementary Excitations in Gapped Quantum Spin Systems", Phys. Rev. Lett. **111**, 080401 (2013).